



# Experimental and numerical investigation of the mechanical behaviour of dissimilar arc and spot welds of advanced high strength steels

Thibaut Huin

## ► To cite this version:

Thibaut Huin. Experimental and numerical investigation of the mechanical behaviour of dissimilar arc and spot welds of advanced high strength steels. Materials. Université de Lyon, 2017. English. NNT : 2017LYSEI055 . tel-01921591

**HAL Id: tel-01921591**

**<https://theses.hal.science/tel-01921591>**

Submitted on 13 Nov 2018

**HAL** is a multi-disciplinary open access archive for the deposit and dissemination of scientific research documents, whether they are published or not. The documents may come from teaching and research institutions in France or abroad, or from public or private research centers.

L'archive ouverte pluridisciplinaire **HAL**, est destinée au dépôt et à la diffusion de documents scientifiques de niveau recherche, publiés ou non, émanant des établissements d'enseignement et de recherche français ou étrangers, des laboratoires publics ou privés.



N°d'ordre NNT : 2017LYSEI055

**THESE de DOCTORAT DE L'UNIVERSITE DE LYON**  
opérée au sein de  
**L'Institut National des Sciences Appliquées de Lyon**

**Ecole Doctorale N° EDA 034**  
**Matériaux de Lyon**

**Spécialité de doctorat : Matériaux**

Soutenue publiquement le 04/07/2017, par :  
**Thibaut Huin**

---

**Experimental and numerical  
investigation of the mechanical  
behaviour of dissimilar arc and spot  
welds of advanced high strength steels**

---

Devant le jury composé de :

Simar, Aude	Professeur	UC Louvain	Président
Gourgues-Lorenzon, Anne-Françoise	Professeur	Mines Paristech	Rapporteur
Bergheau, Jean-Michel	Professeur	ENISE	Rapporteur
Zollinger, Julien	Maître de conférence	Mines Nancy	Examineur
Fabrègue, Damien	Professeur	INSA Lyon	Directeur de thèse
Dancette, Sylvain	Maître de conférence	INSA Lyon	Co-directeur de thèse
Dupuy, Thomas	Ingénieur-Docteur	ArcelorMittal	Examineur





## Département FEDORA – INSA Lyon - Ecoles Doctorales – Quinquennal 2016-2020

SIGLE	ECOLE DOCTORALE	NOM ET COORDONNEES DU RESPONSABLE
<b>CHIMIE</b>	<b>CHIMIE DE LYON</b> <a href="http://www.edchimie-lyon.fr">http://www.edchimie-lyon.fr</a> Sec : Renée EL MELHEM Bat Blaise Pascal 3 <sup>e</sup> étage <a href="mailto:secretariat@edchimie-lyon.fr">secretariat@edchimie-lyon.fr</a> Insa : R. GOURDON	<b>M. Stéphane DANIELE</b> Institut de Recherches sur la Catalyse et l'Environnement de Lyon IRCÉLYON-UMR 5256 Équipe CDFA 2 avenue Albert Einstein 69626 Villeurbanne cedex <a href="mailto:directeur@edchimie-lyon.fr">directeur@edchimie-lyon.fr</a>
<b>E.E.A.</b>	<b>ELECTRONIQUE, ELECTROTECHNIQUE, AUTOMATIQUE</b> <a href="http://edeea.ec-lyon.fr">http://edeea.ec-lyon.fr</a> Sec : M.C. HAVGOUDOUKIAN <a href="mailto:Ecole-Doctorale.eea@ec-lyon.fr">Ecole-Doctorale.eea@ec-lyon.fr</a>	<b>M. Gérard SCORLETTI</b> Ecole Centrale de Lyon 36 avenue Guy de Collongue 69134 ECULLY Tél : 04.72.18 60.97 Fax : 04 78 43 37 17 <a href="mailto:Gerard.scorletti@ec-lyon.fr">Gerard.scorletti@ec-lyon.fr</a>
<b>E2M2</b>	<b>EVOLUTION, ECOSYSTEME, MICROBIOLOGIE, MODELISATION</b> <a href="http://e2m2.universite-lyon.fr">http://e2m2.universite-lyon.fr</a> Sec : Sylvie ROBERJOT Bât Atrium - UCB Lyon 1 04.72.44.83.62 Insa : H. CHARLES <a href="mailto:secretariat.e2m2@univ-lyon1.fr">secretariat.e2m2@univ-lyon1.fr</a>	<b>M. Fabrice CORDEY</b> CNRS UMR 5276 Lab. de géologie de Lyon Université Claude Bernard Lyon 1 Bât Géode 2 rue Raphaël Dubois 69622 VILLEURBANNE Cédex Tél : 06.07.53.89.13 <a href="mailto:cordey@univ-lyon1.fr">cordey@univ-lyon1.fr</a>
<b>EDISS</b>	<b>INTERDISCIPLINAIRE SCIENCES-SANTE</b> <a href="http://www.ediss-lyon.fr">http://www.ediss-lyon.fr</a> Sec : Sylvie ROBERJOT Bât Atrium - UCB Lyon 1 04.72.44.83.62 Insa : M. LAGARDE <a href="mailto:secretariat.ediss@univ-lyon1.fr">secretariat.ediss@univ-lyon1.fr</a>	<b>Mme Emmanuelle CANET-SOULAS</b> INSERM U1060, CarMeN lab, Univ. Lyon 1 Bâtiment IMBL 11 avenue Jean Capelle INSA de Lyon 696621 Villeurbanne Tél : 04.72.68.49.09 Fax : 04 72 68 49 16 <a href="mailto:Emmanuelle.canet@univ-lyon1.fr">Emmanuelle.canet@univ-lyon1.fr</a>
<b>INFOMATHS</b>	<b>INFORMATIQUE ET MATHEMATIQUES</b> <a href="http://infomaths.univ-lyon1.fr">http://infomaths.univ-lyon1.fr</a> Sec : Renée EL MELHEM Bat Blaise Pascal, 3 <sup>e</sup> étage Tél : 04.72. 43. 80. 46 Fax : 04.72.43.16.87 <a href="mailto:infomaths@univ-lyon1.fr">infomaths@univ-lyon1.fr</a>	<b>M. Luca ZAMBONI</b> Bâtiment Braconnier 43 Boulevard du 11 novembre 1918 69622 VILLEURBANNE Cedex Tél : 04 26 23 45 52 <a href="mailto:zamboni@maths.univ-lyon1.fr">zamboni@maths.univ-lyon1.fr</a>
<b>Matériaux</b>	<b>MATERIAUX DE LYON</b> <a href="http://ed34.universite-lyon.fr">http://ed34.universite-lyon.fr</a> Sec : Marion COMBE Tél: 04-72-43-71-70 –Fax : 87.12 Bat. Direction <a href="mailto:ed.materiaux@insa-lyon.fr">ed.materiaux@insa-lyon.fr</a>	<b>M. Jean-Yves BUFFIERE</b> INSA de Lyon MATEIS Bâtiment Saint Exupéry 7 avenue Jean Capelle 69621 VILLEURBANNE Cedex Tél : 04.72.43 71.70 Fax 04 72 43 85 28 <a href="mailto:Ed.materiaux@insa-lyon.fr">Ed.materiaux@insa-lyon.fr</a>
<b>MEGA</b>	<b>MECANIQUE, ENERGETIQUE, GENIE CIVIL, ACOUSTIQUE</b> <a href="http://mega.universite-lyon.fr">http://mega.universite-lyon.fr</a> Sec : Marion COMBE Tél: 04-72-43-71-70 –Fax : 87.12 Bat. Direction <a href="mailto:mega@insa-lyon.fr">mega@insa-lyon.fr</a>	<b>M. Philippe BOISSE</b> INSA de Lyon Laboratoire LAMCOS Bâtiment Jacquard 25 bis avenue Jean Capelle 69621 VILLEURBANNE Cedex Tél : 04.72 .43.71.70 Fax : 04 72 43 72 37 <a href="mailto:Philippe.boisse@insa-lyon.fr">Philippe.boisse@insa-lyon.fr</a>
<b>ScSo</b>	<b>ScSo*</b> <a href="http://recherche.univ-lyon2.fr/scso/">http://recherche.univ-lyon2.fr/scso/</a> Sec : Viviane POLSINELLI Brigitte DUBOIS Insa : J.Y. TOUSSAINT Tél : 04 78 69 72 76 <a href="mailto:viviane.polsinelli@univ-lyon2.fr">viviane.polsinelli@univ-lyon2.fr</a>	<b>M. Christian MONTES</b> Université Lyon 2 86 rue Pasteur 69365 LYON Cedex 07 <a href="mailto:Christian.montes@univ-lyon2.fr">Christian.montes@univ-lyon2.fr</a>

\*ScSo : Histoire, Géographie, Aménagement, Urbanisme, Archéologie, Science politique, Sociologie, Anthropologie

---

*To Farès...*

# Remerciements

Tout d'abord, j'adresse mes sincères remerciements aux membres du jury pour avoir accepté d'évaluer mon travail de thèse : Madame Anne-Françoise Gourgues-Lorenzon et Monsieur Jean-Michel Bergheau qui m'ont fait l'honneur de rapporter cette thèse, Madame Aude Simar qui a accepté de présider le jury de thèse ainsi que Julien Zollinger qui a participé de près au projet.

Ensuite, je souhaite remercier mes directeur de thèse Damien Fabrègue et Sylvain Dancette pour leur encadrement durant ces trois années.

Je remercie également ArcelorMittal de m'avoir fait confiance pour ce projet de thèse, et plus particulièrement Thomas Dupuy et Mohamed Bouzekri pour leur encadrement.

Je tiens à remercier également les nombreuses personnes que j'ai eu la chance de cotoyer au centre de recherche de Maizières-lès-Metz. Je pense en particulier à l'équipe soudage mais également aux personnes d'autres équipes qui ont été disponibles et de bon conseil (Pascal, Laurent entre autre). Je remercie tout particulièrement les membres du service pour la bonne ambiance: Tarik, Jérôme, Alexandre, Régis, Savine, Robin, les autres membres du service, les nombreux stagiaires. J'en profite pour remercier les stagiaires qui ont travaillé sur mon projet : Elise et Lina.

Je souhaite faire une mention spéciale à l'équipe métal du laboratoire Mateis, dans laquelle la bonne humeur et la bienveillance sont omniprésentes. Que ce soit les permanents ou les nombreux thésards qui se succèdent d'années en années, l'entente et toujours aussi bonne. Je tiens également à remercier plus personnellement les permanents toujours prêts à rendre service (Carole, Jérôme, les Joël, Florian (pour les bières), Michel, Patrice, Christophe, Stéphanie, Jean-Yves, Carole, Xavier, Jonathan, Sophie, Eric, Julien, Véronique et surtout le plus important : Frida).

Maintenant, je tiens à remercier les nombreux thésards du labo pour le soutien, les conseils, les sorties, les pauses café et tout le reste. Les anciens qui m'ont accueilli: Paul, Aude, Antoine, Vincent, Benoît. Les moins anciens avec qui j'ai partagé énormément de bons moments et de souvenirs (Kfet ou pire): Willian, Juan, Seb (collègue de pause café), Josselin, Morgane.

## Remerciements

---

Un gros merci à Mélanie, thésarde de ma génération, pour tout ce qu'on a partagé ensemble (notamment la biafine), ce fut un plaisir de travailler avec toi.

Un gros merci également aux plus jeunes pour leur bonne humeur et les nombreuses sorties ensemble: Victor, Oriane, Théo, Gwen, Aléthéa, Aurélien, Julie, Justine, Alexis, Gabriel, François, Amine, Ning, Zak, Yacine etc... (désolé pour les pourrissages de bureaux, c'était la tradition)

Je tiens maintenant à remercier ma famille pour son soutien et pour m'avoir supporter pendant la thèse, et particulièrement mon papa pour avoir contribué grandement à l'encadrement de la thèse et ma maman pour l'organisation de la journée de soutenance (pot).

Je veux également remercier Adeline qui a réussi à me supporter pendant ces trois ans et qui a toujours été là pour moi <3.

Je veux aussi remercier mes amis de Nancy ou de Lyon qui m'ont donné de la force: Charly, Rom, Alexis, Gaut', Faf', Aymeric, Chris, Héri, Seb etc...

# Abstract

Nowadays, ecological policy encourages carmakers to reduce the global vehicle weight. Fine steel sheets assemblies with different thickness optimizing each part of the assembly are used and steelmakers develop steels which are more and more resistant namely Advanced High Strength Steel (AHSS) with a good compromise between mechanical strength and ductility (stamping). During the mechanical tests of heterogeneous AHSS welding, unusual fracture modes are observed, in particular along the interface between the Heat Affected Zone (HAZ) and the Fusion Zone or molten zone (FZ). These fractures generally occur with lower strength than expected for these welding.

The objectives of the study are to understand fracture mechanisms during mechanical testing and create a mechanical FE model is developed to be able to predict mechanical strength of the welded assemblies.

Firstly, a study of heterogeneous welding constituted of two well-known steel grades of ArcelorMittal aims at understanding failure mechanism and parameters affecting the failure modes. Different configurations are studied with thickness. FE model is built with mechanical response identified of each zone (base materials, heat affected zones and fusion zone), using ArcelorMittal models and experimental data. Failure criteria based on ductile damage taking into account the influence of the triaxiality are used and some cohesive elements are used to simulate interfacial failure. Two configurations of mechanical testing in the case of Resistance Spot Welding (cross tension and tensile shear tests) are considered. Model predictions were very accurate with experimental failure modes and strengths.

Then, this FE modelling method was successfully applied to a highly heterogeneous spot welding case including a new third generation low density AHSS concept with high aluminum and manganese content. Failure modes and strengths obtained were comparable. Moreover, FE modelling method was applied on more complex configurations, in particular on a triple thick spot welded assembly. The robustness of the model to predict partial failure modes and strengths of a triple thick spot weld has been demonstrated. In addition, FE modelling methodology was extended to another welding type: arc welding. In this case, two sheets are welded in ab overlap configuration with a filler wire. FE model allows predicting the failure zone and strength of welded assembly.

**Keywords:** resistance spot welding, arc welding, dissimilar welding, automotive high strength steel, cross tension, tensile shear, failure mode, ductile damage, FE modelling, microstructure, low density steel, martensitic steel.



# Contents

<b>Liste des ecoles doctorales</b>	<b>i</b>
<b>Remerciements</b>	<b>iii</b>
<b>Abstract</b>	<b>v</b>
<b>Contents</b>	<b>vii</b>
<b>List of Figures</b>	<b>xi</b>
<b>List of Tables</b>	<b>xxiii</b>
<b>Introduction</b>	<b>xxv</b>
<b>1 Literature Review</b>	<b>1</b>
1.1 Generalities . . . . .	1
1.1.1 Steels for automotive industry . . . . .	2
1.1.2 Resistance spot welding . . . . .	7
1.1.3 Arc Welding . . . . .	16
1.2 Mechanical behaviour of spot welds under quasi-static loading . . . . .	18
1.2.1 Spot weld behaviour . . . . .	18
1.2.2 Mechanical behaviour of homogeneous AHSS spot welds . . . . .	23
1.2.3 Mechanical behaviour of heterogeneous AHSS spot welds . . . . .	26
1.3 Modelling of spot welded assemblies mechanical behaviour . . . . .	28
1.3.1 Analytical models . . . . .	28
1.3.2 Finite element models . . . . .	31
1.4 Conclusion . . . . .	37
<b>2 Experimental results of heterogeneous welding (Usibor1500/DP600)</b>	<b>39</b>
2.1 Materials and welding configurations . . . . .	40
2.1.1 Materials . . . . .	40
2.1.2 Welding configurations . . . . .	41
2.2 Spot weldability . . . . .	42
2.3 Failure modes . . . . .	46
2.3.1 Cross tension tests . . . . .	47
2.3.2 Tensile shear tests . . . . .	50
2.4 Failure strength . . . . .	56



2.4.1	Cross tension strength . . . . .	56
2.4.2	Tensile shear strength . . . . .	58
2.5	Discussion . . . . .	60
2.5.1	Liquid metal splash influence on cross tension performance . . . . .	60
2.5.2	Positive deviation of cross tension failure load with dissimilar thickness	61
2.5.3	Dissimilar thickness effect in tensile shear . . . . .	63
2.6	Arc welding . . . . .	63
2.6.1	Configurations . . . . .	64
2.6.2	Microstructures . . . . .	64
2.6.3	Failure Modes . . . . .	66
2.6.4	Failure strengths . . . . .	67
2.7	Conclusion . . . . .	67
<b>3</b>	<b>Experimental results of highly heterogeneous welding (Duplex/DP600)</b>	<b>69</b>
3.1	Materials and welding configurations . . . . .	70
3.1.1	Materials . . . . .	70
3.1.2	Duplex steelmaking . . . . .	70
3.1.3	Microstructures . . . . .	74
3.1.4	Welding configurations . . . . .	75
3.2	Spot weldability . . . . .	76
3.2.1	Welding range . . . . .	76
3.2.2	Heat affected zone microstructures . . . . .	78
3.3	Failure modes . . . . .	85
3.3.1	Cross tension tests . . . . .	86
3.3.2	Tensile shear tests . . . . .	92
3.4	Failure strengths . . . . .	96
3.4.1	Cross tension strengths . . . . .	96
3.4.2	Tensile shear strengths . . . . .	98
3.5	Discussion . . . . .	100
3.5.1	Aluminum effect on performance . . . . .	100
3.5.2	Ferrite layer formation . . . . .	101
3.6	Arc welding . . . . .	106
3.6.1	Configurations . . . . .	106
3.6.2	Microstructures . . . . .	107
3.6.3	Mechanical tests . . . . .	110
3.7	Conclusion . . . . .	111
<b>4</b>	<b>Finite Element modelling of heterogeneous spot welds mechanical behaviour</b>	<b>113</b>
4.1	FE modelling methodology . . . . .	113
4.1.1	Spot weld zone discretization . . . . .	114
4.1.2	Elastic-plastic strain hardening law . . . . .	118
4.1.3	Ductile damage failure criterion . . . . .	121
4.1.4	Cohesive zones implementation . . . . .	126
4.2	Heterogeneous welding model . . . . .	127
4.2.1	Cross tension test results . . . . .	127

4.2.2	Tensile shear test results . . . . .	136
4.2.3	Discussion . . . . .	144
4.3	Highly heterogeneous welding model . . . . .	145
4.3.1	Cross tension test results . . . . .	145
4.3.2	Tensile shear test results . . . . .	146
4.3.3	Discussion . . . . .	148
4.4	Conclusion . . . . .	148
<b>5</b>	<b>Finite Element model: limitation and potential</b>	<b>151</b>
5.1	FE model limitation . . . . .	151
5.1.1	Solver influence . . . . .	151
5.1.2	Mesh size dependency . . . . .	154
5.1.3	Boundary conditions influence . . . . .	154
5.1.4	Mass scaling influence . . . . .	158
5.2	FE model potential . . . . .	159
5.2.1	Triple-sheet spot welded assembly modelling . . . . .	159
5.2.2	Arc welds FE modelling . . . . .	165
5.3	Conclusion . . . . .	169
	<b>Conclusion</b>	<b>171</b>
	<b>References</b>	<b>175</b>



# List of Figures

1.1	Formability of flat steels for automotive application [KEE 04]. . . . .	2
1.2	Schematic microstructure of DP steel. . . . .	4
1.3	Microstructure of DP600 steel using Nital 1% reagent and 250 °C annealing for 2 hours (Ferrite is pink phase, and martensite is blue one). . . . .	4
1.4	Formability of DP steels for automotive application [KEE 04]. . . . .	5
1.5	Formability of MS steels for automotive application [KEE 04]. . . . .	5
1.6	Microstructure of Usibor1500 (22MnB5) boron steel using Nital 1% reagent (fully martensitic). . . . .	6
1.7	Typical Duplex structure; gray phases are austenite and blue phases are ferrite [BAR 14] . . . . .	7
1.8	Different steps of the welding process. . . . .	8
1.9	Scheme of a spot weld cross section showing the molten nugget, the HAZ and the base material. . . . .	9
1.10	Maximal temperature reached during the spot welding process as a function of the position in the spot weld and related to the Fe-C phase diagram [ZHA 06]. . . . .	10
1.11	Influence of the difference of alloying elements concentration on the formation of fusion zone. . . . .	12
1.12	Destructive tests on spot welds according to [NIS 82]. . . . .	13
1.13	Schematic representation of the plug ratio in the case of Partial Interfacial Failure (PIF). . . . .	14
1.14	Different failure modes identified by AWS [GOU 05]. . . . .	15
1.15	Welding range definition with the weld diameter according to Blondeau [BLO 01]. . . . .	16
1.16	Schematic representation of arc welding according to Anderson [AND 01]. . . . .	16
1.17	Schematic representation of the five arc welding designs according to Minnick [MIN 07]. . . . .	17
1.18	Illustration of arc welding mechanical test: a) schematic representation and b) picture of a sample in the tensile test machine. . . . .	18
1.19	Typical hardness profile between GA780DP and 22MnB5 after RSW with tempering in the 22MnB5 HAZ according to [CHO 11]. . . . .	20
1.20	Welding parameters influence on nugget size: a) Intensity current and holding time effect on nugget diameter according to Pouranvari and al. [POU 07] and b) Intensity current effect on nugget diameter of similar and dissimilar DP spot welds according to Hernandez and al. [HER 08]. . . . .	21

1.21	Nugget size influence on spot weld performance: a) Lap shear peak load versus fusion zone size for DP800 welds according to Sun and al. [SUN 08]. b) Changes in spot weld strength due to welding current of 780 MPa cold-rolled steel sheet according to Sakuma and al. [SAK 03]. . . . .	21
1.22	Nugget size prediction compared to experiments using FE modelling according to: a) Srikunwong and al. [SRI 05] and b) Shen and al. [SHE 10]. .	22
1.23	Cross tension test: a) Load-deflection curves according to [LEE 05a], b) Pull-Out in the nugget border and c) the corresponding ductile sheared fracture surface according to [CHA 03a]. . . . .	23
1.24	Tensile shear test: a) Load-deflection curves according to [LEE 05a], b) Pull-Out in the base material according to [ZUN 97] and c) ductile fracture surface according to [CHA 03a]. . . . .	24
1.25	Interfacial failure during TSS test: a) Schematic stress dispersion in the spot weld according to [POU 07], b) Pull-Out in the base material according to [TAO 08]. . . . .	24
1.26	Partial Interfacial failure: a) micrograph of DP980 spot welds in cross tension according to Dancette and al. [DAN 11a], b) macroscopic visual aspect and c) micrograph of final failure occurred both in the weld nugget and the base metal (M800GI 2.0 mm) according to Bouzekri and al. [BOU 10]. . . .	25
1.27	Improvement of weldability of TRIP steels by use of in-situ pre and post-heat treatments according to Cretteur and al. [CRE 02]: a) optimised welding cycle comparison with standard welding cycle, b) CTS improvement and c) TSS improvement. . . . .	26
1.28	Micrographs and sketch of nugget shifting because of: a) sheet thicknesses according to Marashi and al. [MAR 10] and b) steel grades heterogeneity (high difference of thermal conductivities) according to Wei and al. [WEI 16].	27
1.29	Micrograph of A5052 aluminium alloy and DP600 steel spot weld cross section according to Chen and al. [CHE 16]. . . . .	28
1.30	Button pull out failure mode: a) Schematic of failure surface $A_f$ according to Dancette [DAN 09] and b) Stress distribution around button according to Chao [CHA 03b]. . . . .	29
1.31	Full interfacial failure mode: a) Schematic of failure surface $A_f$ according to Dancette [DAN 09] and b) Stress distribution around button according to Chao [CHA 03a]. . . . .	29
1.32	a) Mode I stress intensity factor in a spot weld notch root and b) critical nugget diameter for failure mode transition according to Chao [CHA 03a]. .	30
1.33	Stress distribution during tensile shear test according to Abid and al. [ADI 04]: a) S11 stress singularity at the notch root and b) S11 stress distribution in the sheet thickness. . . . .	32
1.34	Discretization in many zones of the spot weld: a) according to Yang and al. [YAN 08] and b) according to Mahelle and al. [MAH 07]. . . . .	32
1.35	Comparison between experiments and simulation of load-displacement response and failure mode: a) cross tension according to Kosnan and al. [KOS 14] and b) tensile shear according to Nielsen [NIE 08]. . . . .	34

1.36	Cohesive zones in spot weld modelling according to Dancette and al. [DAN 12]: a) Bilinear mode I cohesive zone model at the faying surface, b) load-displacement curves and c) failure type for the homogeneous 1.5 mm weld assembly. . . . .	35
1.37	Model of crack propagation in DP600GI spot weld according to Lacroix and al. [LAC 15]: a) Crack front and fractured area at different stages of the wedge indentation, b) comparison of experimental results and simulation, load (F) and crack advance vs. wedge displacement, c) load (F) and crack opening angle (CTOA) vs. crack advance. . . . .	35
1.38	Model of DP600 steel and low carbon steel heterogeneous spot weld under tensile shear load according to Long and al. [LON 16], comparative result of load versus displacement and failure mode: a) interfacial failure, b) button pull out failure. . . . .	36
1.39	Model of 22MnB5 press hardened steel and micro alloyed high strength low-alloy steel heterogeneous spot weld according to Burget and Sommer [BUR 13]: a) Zone discretization and mesh, b) various loading modes applied. . . . .	36
1.40	Model of 22MnB5 press hardened steel and micro alloyed high strength low-alloy steel heterogeneous spot weld under tensile shear loading according to Burget and Sommer [BUR 13]: a) experimental and simulated load-displacement curves comparison, b) experimental and simulated failure mode comparison. . . . .	37
1.41	Comparison of experimental and simulated of the dissimilar DP980-TRIP980 button pull out failed spot welds according to Noh and al. [NOH 17]: a) failure strength under lap-shear test, b) failure strength under U-shape test, c) failure modes under lap-shear test and d) failure mode under U-shape test. . . . .	38
2.1	Optical view of a) Usibor1500 fully martensitic microstructure and b) DP600 microstructure (ferrite is white phase and martensite is dark phase). . . . .	40
2.2	Mechanical properties of DP600 and Usibor1500 steel grades (Uniaxial ISO tensile test). . . . .	41
2.3	Spot welding configurations. . . . .	42
2.4	Arc welding configurations. . . . .	42
2.5	Spot welding intensity range of the four welded configurations. . . . .	43
2.6	Chemical etching of a spot weld with a) Bechet-Beaujard reagent and b) Nital 3% reagent. . . . .	44
2.7	Spot weld metallographic cross sections for DB and DD configurations at the three positions in the welding range (Usibor1500 is always the upper sheet): a) DB lower end, b) DB middle position, c) DB upper end, d) DD lower end, e) DD middle position; and f) DD upper end. . . . .	45
2.8	Spot weld hardness profiles for DB (Usibor1500 2.0 mm-DP600 2.0 mm) and DC (Usibor1500 2.0 mm-DP600 1.2 mm) configurations: a) DB hardness profile, b) DC hardness profile, c) DB metallographic cross-section and d) DC metallographic cross-section. . . . .	46
2.9	Spot weld failure modes: Button Pull-Out (BPO), Partial Interfacial Failure (PIF), Full Interfacial Failure (FIF), Partial Dome Failure (PDF), and Total Dome Failure (TDF). . . . .	47

2.10	Spot weld cross tension failure modes for the four configurations (DA, DB, DC and DD) for the three welding intensities. . . . .	48
2.11	Main failure modes encountered during Cross Tension tests (macroscopic visual aspect): a) PIF, b) BPO, and c) BPO + PDF. . . . .	48
2.12	Beginning of expulsion in the DC configuration at the upper end of the welding range promoting partial dome failure: metallographic cross section before a) and after b) the cross tension test. . . . .	49
2.13	Scanning Electron Microscopy (SEM) fracture surfaces in cross tension of Button Pull-Out failure mode. . . . .	50
2.14	Scanning Electron Microscopy (SEM) fracture surfaces in cross tension of Interfacial failure mode. . . . .	51
2.15	Splash angle along button periphery. . . . .	51
2.16	Scanning Electron Microscopy (SEM) fracture surfaces in cross tension of Partial Dome failure mode. . . . .	52
2.17	Spot weld tensile shear failure modes for the four configurations (DA, DB, DC and DD) and the three welding intensities. . . . .	53
2.18	Main failure modes encountered during Tension Shear tests (macroscopic visual aspect): a) FIF, b) BPO and c) TDF. . . . .	53
2.19	Scanning Electron Microscopy (SEM) fracture surfaces in tensile shear of Button Pull-Out failure mode. . . . .	54
2.20	Scanning Electron Microscopy (SEM) fracture surfaces in cross tension of Full Interfacial Failure mode. . . . .	55
2.21	Scanning Electron Microscopy (SEM) fracture surfaces in cross tension of Total Dome Failure mode. . . . .	56
2.22	Cross tension failure load (CTS) as a function of weld diameter and welding assembly: Usibor1500 and DP600 heterogeneous welding configurations with similar thickness. $\alpha$ in daN/mm <sup>2</sup> . . . . .	58
2.23	Cross tension failure load (CTS) as a function of weld diameter and welding assembly: Usibor1500 and DP600 heterogeneous welding configurations. $\alpha$ in daN/mm <sup>2</sup> . . . . .	59
2.24	Cross tension failure load (CTS) as a function of weld diameter and welding assembly: Usibor1500 and DP600 homogeneous welding configurations compared with the dissimilar 1.5 mm Usibor1500/1.5 mm DP600. $\alpha$ in daN/mm <sup>2</sup> . . . . .	60
2.25	Tensile shear failure load (TSS) as a function of weld diameter and welding assembly. . . . .	61
2.26	DA configuration spot weld: a) Metallographic cross-section at the upper end of the welding range after cross tension, highlighting two possible values of diameter (plug or weld). b) DA failure loads as a function of diameter, with a possible horizontal shift of the upper end spot welds when considering the effective plug diameter instead of the full weld diameter. . . . .	62
2.27	Nugget shift schema. . . . .	63
2.28	Arc weld failure modes: a) Base material failure, b) and c) HAZ failure, d) Molten zone failure and e) Border zone failure . . . . .	64

2.29	Arc weld hardness profiles for DA (Usibor1500 2.0 mm-Usibor1500 1.5 mm) and DB (Usibor1500 1.5 mm-Usibor1500 2.0 mm) configurations: a) DA hardness profile, b) DB hardness profile, c) DA metallographic cross-section and d) DB metallographic cross-section. . . . .	65
2.30	Arc weld failure modes: a) DA configuration (thicker upside) and b) DB configuration (thicker downside). . . . .	67
3.1	Hot rolled steel microstructures: a) Duplex 4Al and b) Duplex 8Al. . . . .	71
3.2	Cold rolling tests a) Duplex 4Al, b) Duplex 8Al, c) delamination of Duplex 4Al and d) delamination and cracking of Duplex 8Al. . . . .	72
3.3	Cold rolled steel microstructures: a) Duplex 4Al and b) Duplex 8Al. . . . .	73
3.4	Mechanical properties of Duplex steel grades before and after homogenizing annealing (Uniaxial ISO tensile test). . . . .	74
3.5	Microstructure of DP600 base material: a) confocal microscopy observation and b) SEM observation. . . . .	75
3.6	Microstructure of Duplex base materials: a) confocal microscopy observation of Duplex 4Al, b) SEM observation of Duplex 4Al, c) confocal microscopy observation of Duplex 8Al and d) SEM observation of Duplex 8Al. . . . .	76
3.7	Spot welding intensity range of the two welded configurations. . . . .	77
3.8	Spot weld metallographic cross sections of Duplex 4Al/DP600 spot welds at the three positions in the welding range (Duplex 4Al is always the upper sheet): a) lower end, b) middle position, c) upper end. . . . .	78
3.9	Spot weld metallographic cross sections of Duplex 8Al/DP600 spot welds at the three positions in the welding range (Duplex 8Al is always the upper sheet): a) lower end, b) middle position, c) upper end. . . . .	79
3.10	Spot weld hardness profiles for Duplex 4Al/DP600 and Duplex 8Al/DP600 configurations: a) Duplex 4Al hardness profile, b) Duplex 8Al hardness profile, c) Duplex 4Al metallographic cross-section and d) Duplex 8Al metallographic cross-section. . . . .	80
3.11	Microstructure of Duplex 4Al heat affected zone with scanning microscopy a) Laser (confocal) and b) Electron (SEM). . . . .	80
3.12	Microstructure of Duplex 8Al heat affected zone with scanning microscopy: a) Laser (confocal), b) Laser zoom on HAZ (confocal) and c) Electron zoom on HAZ (SEM). . . . .	81
3.13	Microstructure of the Ferrite Layer with scanning microscopy of Duplex 8Al/DP600 spot weld: a) Laser (confocal) and b) Electron (SEM). . . . .	81
3.14	Hardness profile (Hv0.1 with 50 $\mu$ m indent spacing) of HAZ a) Duplex 4Al HAZ, b) Duplex 8Al HAZ and c) Interface between DP600 HAZ and Nugget (melted DP600 and Duplex 8Al) (ferrite layer). . . . .	82
3.15	Analysed zone with EBSD. . . . .	83
3.16	Microstructure of Duplex 8Al HAZ a) alpha Band contrast map, b) Forward-scattered Electron (FSD) image with pseudo backscatter colours. . . . .	83
3.17	Inverse Pole Figures (IPF) of Duplex 8Al HAZ: a) along X axis, b) along Y axis and c) along Z axis. . . . .	84
3.18	Zoom on Duplex 8Al HAZ a) observed zone, b) FSD image and IPF Y, c) FSD image and phase identification. . . . .	84



3.19	Zoom on the interface between DP600 HAZ and nugget of Duplex 8Al/DP600 spot weld: a) observed zone, b) FSD image and IPF Y and c) FSD image and phase identification. . . . .	85
3.20	Scanning laser observations of dark inclusions in the nugget of Duplex 4Al/DP600 spot welds. . . . .	85
3.21	Dark inclusion in the nugget: a) SEM view, b) Fe distribution, c) Mn distribution, d) Al distribution, e) Zn distribution and f) O distribution. . .	86
3.22	Spot weld cross tension failure modes of Duplex 4Al/DP600 spot welds for the three welding intensities: a) lower end, b) middle position, c) upper end.	88
3.23	Spot weld Cross tension failure modes of Duplex 8Al/DP600 spot welds for the three welding intensities: a) lower end, b) middle position, c) upper end.	89
3.24	Failure modes encountered during Cross Tension tests on Duplex 4Al (macroscopic visual aspect): a) lower end, b) middle position, c) upper end. . . .	89
3.25	Failure mode encountered during Cross Tension tests on Duplex 8Al (macroscopic visual aspect): a) Duplex 8Al sheet, b) DP600 sheet. . . . .	90
3.26	Duplex 4Al/DP600 spot weld Total Dome Failure (Duplex 4Al side) zones SEM fractographs. . . . .	91
3.27	Duplex 4Al/DP600 spot weld Partial Dome Failure zones SEM fractographs.	91
3.28	Duplex 8Al/DP600 spot weld Total Dome Failure (DP600 side) zones SEM fractographs. . . . .	92
3.29	Spot weld Tensile Shear failure modes of Duplex 4Al/DP600 spot welds for middle and upper end welding intensities. . . . .	94
3.30	Failure modes encountered during Tensile Shear tests on Duplex 4Al (macroscopic visual aspect): a) lower end, b) middle position, c) upper end. . . .	94
3.31	Spot weld Tensile Shear failure modes of Duplex 8Al/DP600 spot welds for middle end welding intensity. . . . .	95
3.32	Duplex 4Al / DP600 spot weld Total Dome Failure (DP600 side) zones SEM fractographs. . . . .	95
3.33	Duplex 4Al / DP600 spot weld Total Dome Failure (Duplex 4Al side) zones SEM fractographs. . . . .	96
3.34	Duplex 4Al / DP600 spot weld Partial Dome Failure (Duplex 4Al side) zones SEM fractograph. . . . .	97
3.35	Cross tension failure load (CTS) as a function of weld diameter and welding assembly: Duplex (with different aluminium contents) and DP600 heterogeneous welding configurations. $\alpha$ in daN/mm <sup>2</sup> . . . . .	98
3.36	Tensile shear failure load (TSS) as a function of weld diameter and welding assembly. . . . .	99
3.37	Cross tension failure load (CTS) as a function of weld diameter and welding assembly: Duplex (with different aluminium content) and DP600 heterogeneous welding configurations compared to the more unfavorable configuration of Usibor1500/DP600. $\alpha$ in daN/mm <sup>2</sup> . . . . .	100
3.38	Tensile Shear failure load (TSS) as a function of weld diameter and welding assembly: Duplex (with different aluminium content) and DP600 heterogeneous welding configurations compared to the more unfavorable configuration of Usibor1500/DP600. . . . .	101

3.39	Ferrite layer (white phase) micrographic observations: a) Duplex 4Al/DP600, b) Duplex 8Al/DP600 (nugget is at top side and DP600 HAZ at the bottom side). . . . .	102
3.40	Concentration profile of C at the interface of 3.8 Si% steel/0.5 Si% steel . .	102
3.41	Simulated interfaces: a) Duplex 4Al/DP600 and b) Duplex 8Al/DP600. . .	103
3.42	Interface of Duplex 4Al/DP600 assembly: a) micrographic view and b) C mapping (EPMA). . . . .	104
3.43	Interface of Duplex 8Al/DP600 assembly: a) micrographic view and b) C mapping (EPMA). . . . .	104
3.44	Concentration profile of C at the interfaces of Duplex 4Al/DP600 and Duplex 8Al/DP600 assemblies. . . . .	105
3.45	Failure propagation in the ferrite layer. . . . .	106
3.46	Zoom on the failure propagation in the ferrite layer. . . . .	106
3.47	Overlap arc welding of hot rolled Duplex 8Al steel sheets using G3Si wire. .	107
3.48	Arc weld hardness profiles for Duplex 4Al and Duplex 8Al configurations: a) Duplex 4Al hardness profile, b) Duplex 8Al hardness profile, c) Duplex 4Al metallographic cross-section and d) Duplex 8Al metallographic cross-section.	108
3.49	Hardness of Duplex 8Al arc welding in the Fusion Zone (red triangles correspond to the highest hardness values, orange squares to the intermediate hardness values and yellow circles to the lowest). . . . .	108
3.50	Duplex 4Al arc welding microstructures: a) base material, b) HAZ, c) interface HAZ/molten zone, d) molten zone (fusion zone). . . . .	109
3.51	Duplex 8Al arc welding microstructures: a) base material, b) HAZ, c) interface HAZ/molten zone, d) molten zone (fusion zone). . . . .	110
3.52	Failure modes of arc welds: a) Duplex 4Al and b) Duplex 8Al. . . . .	111
3.53	Fractography of failed surfaces: a) and b) on Duplex 4Al arc weld, c) and d) on Duplex 8Al arc weld. . . . .	112
3.54	Tensile shear behaviour of Duplex 4Al and 8Al arc weld assemblies (Two samples for each configuration). . . . .	112
4.1	Micro-hardness profile on a Usibor1500/DP600 spot weld with the corresponding micrograph. . . . .	114
4.2	Minimal discretization for heterogeneous Usibor1500/DP600 spot weld behaviour. . . . .	115
4.3	Micro-hardness profile on Duplex8Al/DP600 spot weld with the corresponding micrograph. . . . .	115
4.4	Minimal discretization for heterogeneous Duplex 8Al/DP600 spot weld behaviour. . . . .	116
4.5	Minimal symmetry of heterogeneous spot weld mechanical tests with the loading conditions: a) spot weld quarter in cross section and b) half spot weld in tensile shear. . . . .	116
4.6	Mesh of a cross tension model. . . . .	117
4.7	Comparison of elastic-plastic constitutive behaviours using the Gleeble + Swift-Voce and the SCCA methodologies: a) on the quenched Usibor1500 HAZ and b) on the tempered Usibor1500 HAZ. . . . .	120

4.8	Elastic-plastic strain hardening law for each zones of a Usibor1500/DP600 spot weld (with same sheets thickness) established by SCCA model [ARL 13].	121
4.9	Elastic-plastic strain hardening law for each zones of a Duplex 8Al/DP600 spot weld (with same sheets thickness) established by SCCA model [ARL 13] for DP600 steel zones and by fitting Swift-Voce model on tensile test for Duplex 8Al steel zone. . . . .	122
4.10	Considered criterion identification on Usibor1500 steel. . . . .	123
4.11	Stress triaxiality dependent effective damage initiation strain for damage initiation criterion of Usibor1500 base material. . . . .	124
4.12	Damage evolution in Abaqus: a) stress-strain curve with progressive damage degradation and b) linear definition of damage evolution based on plastic displacement. . . . .	125
4.13	Cohesive zone implementation in spot weld FE models: a) Traction separation law of cohesive elements, b) cohesive zone at the sheets interface of Usibor1500/DP600 spot welds and c) cohesive zones at the sheets interface of Duplex 8Al/DP600 spot welds and at the DP600 HAZ and fusion zone interface. . . . .	126
4.14	Usibor1500/DP600 spot welding configurations. . . . .	127
4.15	Comparison between experimental and simulation response in cross tension of Usibor1500 1.2 mm/DP600 1.2 mm spot weld (DA) at the lower end intensity: a) load-displacement curves and b) failure mode. . . . .	128
4.16	Comparison between experimental and simulation response in cross tension of Usibor1500 1.2 mm/DP600 1.2 mm spot weld (DA) at middle intensity: a) load-displacement curves and b) failure mode. . . . .	128
4.17	Comparison between experimental and simulation response in cross tension of Usibor1500 1.2 mm/DP600 1.2 mm spot weld (DA) at the upper end intensity: a) load-displacement curves and b) failure mode. . . . .	129
4.18	Comparison between experimental and simulation response in cross tension of Usibor1500 2 mm/DP600 2 mm spot weld (DB) at the lower end intensity: a) load-displacement curves and b) failure mode. . . . .	130
4.19	Comparison between experimental and simulation response in cross tension of Usibor1500 2 mm/DP600 2 mm spot weld (DB) at middle intensity: a) load-displacement curves and b) failure mode. . . . .	130
4.20	Comparison between experimental and simulation response in cross tension of Usibor1500 2 mm/DP600 2 mm spot weld (DB) at the upper end intensity: a) load-displacement curves and b) failure mode. . . . .	131
4.21	Comparison between experimental and simulation response in cross tension of Usibor1500 2 mm/DP600 2 mm spot weld (DB) at the upper end intensity: a) load-displacement curves and b) equivalent plastic strain before slope change and c) equivalent plastic strain after slope change. . . . .	131
4.22	Comparison between experimental and simulation response in cross tension of Usibor1500 2 mm/DP600 1.2 mm spot weld (DC) at the lower end intensity: a) load-displacement curves and b) failure mode. . . . .	132
4.23	Comparison between experimental and simulation response in cross tension of Usibor1500 2 mm/DP600 1.2 mm spot weld (DC) at middle intensity: a) load-displacement curves and b) failure mode. . . . .	132

4.24	Comparison between experimental and simulation response in cross tension of Usibor1500 2 mm/DP600 1.2 mm spot weld (DC) at the upper end intensity: a) load-displacement curves and b) failure mode. . . . .	133
4.25	Comparison between experimental and simulation response in cross tension of Usibor1500 1.2 mm/DP600 2 mm spot weld (DD) at the lower end intensity: a) load-displacement curves and b) failure mode. . . . .	134
4.26	Comparison between experimental and simulation response in cross tension of Usibor1500 1.2 mm/DP600 2 mm spot weld (DD) at middle intensity: a) load-displacement curves and b) failure mode. . . . .	134
4.27	Comparison between experimental and simulation response in cross tension of Usibor1500 1.2 mm/DP600 2 mm spot weld (DD) at the upper end intensity: a) load-displacement curves and b) failure mode. . . . .	135
4.28	Comparison between experimental and simulation response in tensile shear of Usibor1500 1.2 mm/DP600 1.2 mm spot weld (DA) at the lower end intensity: a) load-displacement curves and b) failure mode. . . . .	137
4.29	Comparison between experimental and simulation response in tensile shear of Usibor1500 1.2 mm/DP600 1.2 mm spot weld (DA) at middle intensity: a) load-displacement curves and b) failure mode. . . . .	137
4.30	Comparison between experimental and simulation response in tensile shear of Usibor1500 1.2 mm/DP600 1.2 mm spot weld (DA) at the upper end intensity: a) load-displacement curves and b) failure mode. . . . .	138
4.31	Comparison between experimental and simulation response in tensile shear of Usibor1500 2 mm/DP600 2 mm spot weld (DB) at the lower end intensity: a) load-displacement curves and b) failure mode. . . . .	139
4.32	Comparison between experimental and simulation response in tensile shear of Usibor1500 2 mm/DP600 2 mm spot weld (DB) at middle intensity: a) load-displacement curves and b) failure mode. . . . .	139
4.33	Comparison between experimental and simulation response in tensile shear of Usibor1500 2 mm/DP600 2 mm spot weld (DB) at the upper end intensity: a) load-displacement curves and b) failure mode. . . . .	140
4.34	Comparison between experimental and simulation response in tensile shear of Usibor1500 2 mm/DP600 1.2 mm spot weld (DC) at the lower end intensity: a) load-displacement curves and b) failure mode. . . . .	140
4.35	Comparison between experimental and simulation response in tensile shear of Usibor1500 2 mm/DP600 1.2 mm spot weld (DC) at middle intensity: a) load-displacement curves and b) failure mode. . . . .	141
4.36	Comparison between experimental and simulation response in tensile shear of Usibor1500 2 mm/DP600 1.2 mm spot weld (DC) at the upper end intensity: a) load-displacement curves and b) failure mode. . . . .	141
4.37	Comparison between experimental and simulation response in tensile shear of Usibor1500 1.2 mm/DP600 2 mm spot weld (DD) at the lower end intensity: a) load-displacement curves and b) failure mode. . . . .	142
4.38	Comparison between experimental and simulation response in tensile shear of Usibor1500 1.2 mm/DP600 2 mm spot weld (DD) at middle intensity: a) load-displacement curves and b) failure mode. . . . .	142

4.39	Comparison between experimental and simulation response in tensile shear of Usibor1500 1.2 mm/DP600 2 mm spot weld (DD) at the upper end intensity: a) load-displacement curves and b) failure mode. . . . .	143
4.40	Comparison between experimental and simulation response in cross tension of Duplex 8Al 1.2 mm/DP600 1.2 mm spot weld at the lower end intensity: a) load-displacement curves and b) failure mode. . . . .	145
4.41	Comparison between experimental and simulation response in cross tension of Duplex 8Al 1.2 mm/DP600 1.2 mm spot weld at middle intensity: a) load-displacement curves and b) failure mode. . . . .	146
4.42	Comparison between experimental and simulation response in cross tension of Duplex 8Al 1.2 mm/DP600 1.2 mm spot weld at the upper end intensity: a) load-displacement curves and b) failure mode. . . . .	146
4.43	Comparison between experimental and simulation response in tensile shear of Duplex 8Al 1.2 mm/DP600 1.2 mm spot weld at the lower end intensity: a) load-displacement curves and b) failure mode. . . . .	147
4.44	Comparison between experimental and simulation response in tensile shear of Duplex 8Al 1.2 mm/DP600 1.2 mm spot weld at middle intensity: a) load-displacement curves and b) failure mode. . . . .	147
4.45	Comparison between experimental and simulation response in tensile shear of Duplex 8Al 1.2 mm/DP600 1.2 mm spot weld at the upper end intensity: a) load-displacement curves and b) failure mode. . . . .	147
5.1	Implicit and Explicit solvers Load-Displacement response of Usibor1500 2 mm/DP600 2 mm configuration: a) in cross tension and b) in tensile shear.	152
5.2	Implicit and Explicit solvers Load-Displacement response of Usibor1500 1.2 mm/DP600 2 mm configuration: a) in cross tension and b) in tensile shear. . . . .	153
5.3	Implicit and Explicit solvers Load-Displacement response of Duplex 8Al 1.2 mm/DP600 1.2 mm configuration: a) in cross tension and b) in tensile shear. . . . .	153
5.4	Usibor1500 2 mm/DP600 2 mm middle intensity configuration with different mesh size: a) coarse 0.3 mm b) intermediate 0.2 mm and c) fine 0.1 mm. . .	154
5.5	Usibor1500 2 mm/DP600 2 mm middle intensity configuration with three different mesh sizes: a) Comparison of Load-Displacement responses and b) Comparison of the failure modes. . . . .	155
5.6	Usibor1500 2 mm/DP600 2 mm middle intensity configuration with six different velocities (2, 5 (ref), 10, 20, 30 and 40, in $\text{m s}^{-1}$ ). . . . .	156
5.7	Internal and Kinetic energies comparison of Usibor1500 2 mm/DP600 2 mm middle intensity configuration with two different velocities: a) $5 \text{ m s}^{-1}$ (ref) and b) $30 \text{ m s}^{-1}$ . . . . .	157
5.8	Amplitude forms to apply a progressive increase of velocity (ramp and smooth step). . . . .	157
5.9	FE model Load-Displacement response curves for two different types of boundary condition amplitude (ramp and smooth step). . . . .	158

5.10	Usibor1500 2 mm/DP600 2 mm middle intensity configuration with three different mass scaling on elements (no mass scaling, mass scaling factor 10 and mass scaling factor 100).	159
5.11	Usibor2000 1.5 mm/DP780 1.5 mm triple-sheet spot weld assembly cross section for three welding intensities: a) lower end 4.5 kA, b) middle 5.8 kA and c) upper end 7.0 kA.	160
5.12	Usibor2000 1.5 mm/DP780 1.5 mm triple-sheet spot weld assembly micro-hardness tests on cross section for lower end intensity configuration: a) micro hardness profile and identified zones, b) corresponding cross section micrograph with hardness indents.	161
5.13	Discretization for dissimilar Usibor2000 1.5 mm/ DP780 1.5 mm triple-sheet spot weld FE model.	162
5.14	Elastic-plastic strain hardening law for each zones of Usibor2000 1.5 mm/DP780 1.5 mm triple-sheet spot weld established by SCCA model [ARL 13].	162
5.15	Minimal symmetry of Usibor2000/DP780 triple-sheet heterogeneous spot weld mechanical tests with the loading conditions: spot weld quarter in cross section.	163
5.16	Mesh of Usibor2000/DP780 triple-sheet heterogeneous spot weld models in cross tension for three welding intensity configurations: a) lower end, b) middle and c) upper end.	164
5.17	Comparison between experimental and simulation response in cross tension of Usibor2000 1.5 mm/DP780 1.5 mm triple-sheet spot weld at lower end intensity: a) load-displacement curves and b) failure mode.	164
5.18	Comparison between experimental and simulation response in cross tension of Usibor2000 1.5 mm/DP780 1.5 mm triple-sheet spot weld at middle intensity: a) load-displacement curves and b) failure mode.	164
5.19	Comparison between experimental and simulation response in cross tension of Usibor2000 1.5 mm/DP780 1.5 mm triple-sheet spot weld at upper end intensity: a) load-displacement curves and b) failure mode.	165
5.20	Hardness profiles of Usibor1500 2.0 mm/Usibor1500 1.5 mm arc weld and Usibor1500 2.0 mm/DP600 2 mm spot weld: a) and b) hardness profiles, c) and d) metallographic cross-sections.	166
5.21	Discretization for dissimilar Usibor1500 (2.0 mm/1.5 mm) arc weld FE model.	167
5.22	Elastic-plastic strain hardening law for each zones of Usibor1500 2.0 mm/1.5 mm arc weld established by SCCA model [ARL 13].	167
5.23	Experimental and simulated Load-Elongation responses of dissimilar thicknesses Usibor1500 arc welds: a) 2.0 mm/1.5 mm configuration and b) 1.5 mm/2.0 mm configuration.	168
5.24	Failure modes comparison between experiments and FE simulation of dissimilar thicknesses Usibor1500 arc welds: a) and b) 2.0 mm/1.5 mm and 1.5 mm/2.0 mm configurations experimental failure modes, c) and d) 2.0 mm/1.5 mm and 1.5 mm/2.0 mm configurations simulated failure modes.	169
5.25	Experimental data and failure mode zones as function as nugget diameter and sheet thickness: a) First proposed discretization and b) another example of discretization.	173



# List of Tables

1.1	Weld zones and the related maximal temperatures reached ( $T_{fusion}$ is the fusion temperature). . . . .	11
2.1	Chemical composition of steel grades (x 0.001 wt%). . . . .	41
2.2	Welding parameters, p=0.02 s. . . . .	43
2.3	Cross tension failure modes. . . . .	47
2.4	Tensile shear failure modes. . . . .	52
2.5	Cross tension failure loads (daN, average of three tests). . . . .	57
2.6	Tensile shear failure loads (daN, average of three tests). . . . .	59
2.7	Arc welding parameters . . . . .	64
2.8	Arc welding failure strengths (MPa, average of five tests). . . . .	67
3.1	Chemical composition of steel grades (x 0.001wt%) . . . . .	70
3.2	Hot rolling parameters . . . . .	71
3.3	Mechanical properties of Duplex steel grades in the final state (Uniaxial ISO tensile test). . . . .	74
3.4	Welding parameters (Duplex is welded with DP600 in both cases), p=0.02 s. 76	
3.5	Cross tension failure modes of Duplex 4Al 1.2 mm / DP600 1.2 mm spot welds (First three samples were welded with DP600 (1) and three others with DP600 (2)). . . . .	87
3.6	Cross tension failure modes for the two types of configuration. . . . .	87
3.7	Tensile shear failure modes. . . . .	93
3.8	Cross tension failure loads (daN, average of six tests for Duplex 4Al and three for Duplex 8Al). . . . .	97
3.9	Tensile Shear failure loads (daN, average three samples). . . . .	98
3.10	Arc welding parameters . . . . .	107
4.1	SCCA fresh martensite model parameters. . . . .	119
4.2	SCCA tempered martensite model parameters. . . . .	120
4.3	Identified damage initiation strain using Considere criterion for the different zones of a Usibor1500/DP600 spot weld. . . . .	122
4.4	Identified damage initiation strain using Considere criterion for the different zones of a Duplex 8Al/DP600 spot weld. . . . .	123
4.5	Identified effective plastic displacement at fracture for the different zones of a Usibor1500/DP600 spot weld. . . . .	125



4.6	Identified effective plastic displacement at fracture for the different zones of a Duplex 8Al/DP600 spot weld. . . . .	125
4.7	Identified parameter values of the three cohesive zones in the three directions (direction 1 is the stack direction, orthogonal to cohesive zone). $\sigma_{max}$ in MPa and $\Gamma$ in $\text{kJ m}^{-2}$ . . . . .	127
4.8	Experimental failure modes and their agreement with FE prediction for each Usibor1500/DP600 spot weld configuration in cross tension. . . . .	135
4.9	Experimental failure strengths and their agreement with FE prediction for each Usibor1500/DP600 spot weld configuration in cross tension. . . . .	136
4.10	Experimental failure modes and their agreement with FE prediction for each Usibor1500/DP600 spot weld configuration in tensile shear. . . . .	143
4.11	Experimental failure strengths and their agreement with FE prediction for each Usibor1500/DP600 spot weld configuration in tensile shear. . . . .	144
4.12	Experimental failure modes and their agreement with FE prediction for Duplex 8Al/DP600 spot weld configurations in cross tension. . . . .	146
4.13	Experimental failure modes and their agreement with FE prediction for Duplex 8Al/DP600 spot weld configurations in tensile shear. . . . .	148
5.1	Chemical composition of DP780 and Usibor2000 steel grades (x 0.001 wt%).	160
5.2	Welding parameters for triple sheet Usibor2000/DP780 assembly, p=0.02 s.	160
5.3	Identified damage initiation strain using Considere criterion criterion and effective plastic displacement at fracture for the different zones of a Usibor2000/DP780 spot weld. . . . .	163
5.4	Identified parameter values of the three cohesive zones in the three directions (direction 1 is the stack direction, orthogonal to cohesive zone). $\sigma_{max}$ in MPa and $\Gamma$ in $\text{kJ m}^{-2}$ . . . . .	163
5.5	Identified damage initiation strain using Considere criterion and effective plastic displacement at fracture for the different zones of a Usibor1500 arc weld. . . . .	168

# Introduction

Nowadays, carmakers have to satisfy more and more drastic environmental standards. These standards aim at reducing the vehicle greenhouse gas emissions, but also gas produced during car manufacturing. This policy leads carmakers to reduce the vehicle weight, and particularly the body in white (BIW) which represents more than 70% of the total car weight. Moreover, equally severe safety standards have to be taken into account to guaranty user protection in case of accident. These two major issues lead carmakers to develop new and stronger materials in order to lighten the structure on one hand and to strengthen it on the other hand.

Carmakers are using thin steel sheets of different grades and thicknesses for joined assemblies depending on their role in the structure. To do so, they develop new steel grades with a good compromise between strength and ductility. Automotive High Strength Steels (AHSS) development correspond to this requirement.

On the other hand, Resistance Spot Welding (RSW) is a widely used welding process in the automotive industry, mainly for the assembly of body in whites (BIW). This process exhibits many advantages: it is very fast, cost-effective, without any material added and particularly adapted to steel which is the main material used in vehicle structures. On average, a car contains between 4000 and 5000 spot welds.

Automotive High Strength Steels (AHSS) are more and more engaged in safety parts of BIW because of their high mechanical properties and low density. Joining AHSS with more conventional steels is a particular challenge for steelmakers but it allows to absorb large amounts of energy in case of crash. Heterogeneous welding of two steel sheets with different grades creates peculiar features in the weld, especially in the fusion zone microstructure, on the weld geometry (nugget shift in resistance spot welding) and on the appearance of brittle zones which could lead to easier weld failure with low strength.

The weldability of ferritic steels has been widely studied in the last decades and allows to establish actual standards used in the automotive industry. The development of more alloyed and technical steels like AHSS has raised many questions on the welding process. AHSS spot welds are characterized by rather low strength and unconventional failure modes such as partial interfacial or dome failures during cross tension and tensile shear mechanical tests.

The goal of this PhD is thus to get a netter understanding of the behaviour of this highly heterogeneous welds and to develop a modelling approach to permit the prediction of the strength and failure mode of such welds.

In order to introduce the various concepts used in the experimental and simulation parts of this study, chapter 1 of this manuscript is dedicated to a literature review. In a first

section, experimental aspects of welding and mechanical testing are being addressed. A presentation of the studied steel family and welding processes is done. Then, mechanical tests used to characterize welds and failure modes are presented. The state of the art in terms of mechanical behaviour understanding for AHSS homogeneous as well as for heterogeneous spot welds is presented. Finally, simple analytical models, then Finite Element models for spot welded assemblies mechanical behaviour are introduced with different modelling approach of failure.

In chapter 2, heterogeneous welding assemblies of Usibor1500 and DP600 AHSS are studied. Base materials and their microstructures are characterized and the different welding configurations are presented. The weldability of these steel grades is analysed and their heat affected zones (HAZ) characterized. Then, the mechanical test results of these welded assemblies are presented and more particularly their failure modes and strengths in order to understand failure mechanisms. Finally, key parameters influencing the failure mode and strength are discussed.

Chapter 3 of the manuscript focuses on the highly heterogeneous welding assembly of DP600 with a Duplex steel (low density ferrite-austenite concept under development). Steel making, metallurgical concept, microstructures and mechanical properties of Duplex steels are presented. Then, the weldability of Duplex steels with DP600 steel are studied. A fine characterization of HAZ and fusion zones of the welded assemblies is carried out in order to identify the zones whose mechanical behaviour needs to be discretized. Lastly, failure modes and strengths of welds are discussed.

In chapter 4, a Finite Element (FE) methodology for spot weld mechanical testing is presented. First, zones discretization is explained based on micro-hardness tests and microstructure observations. Elastic-plastic behaviour identification procedure and ductile damage criterion are described. Cohesive zone implementation to predict interfacial failure is also presented. Then, a comparative study between experimental and simulated results of failure modes and strengths is carried out in the case of heterogeneous welding (Usibor1500/DP600 spot welds). Finally, a comparative study in the case of highly heterogeneous assemblies (Duplex/DP600 spot welds) is also presented.

Chapter 5 focuses on the limitations and potentialities of the model described in the chapter 4. Solver influence is firstly presented. Then, a parametric study is carried out to highlight the mesh size and boundary conditions influence. FE model potential is discussed by presenting two extended cases of modelling. Triple sheets assemblies of Usibor2000 and DP780 steels are presented by comparing experimental and simulated failure strengths and modes on the whole welding range. Subsequently, the FE model is extended to another welding process: namely arc welding. Usibor1500 arc welds are modelled and compared to experimental results.

# Chapter 1

## Literature Review

### Contents

<b>1.1</b>	<b>Generalities</b>	<b>1</b>
1.1.1	Steels for automotive industry	2
1.1.2	Resistance spot welding	7
1.1.3	Arc Welding	16
<b>1.2</b>	<b>Mechanical behaviour of spot welds under quasi-static loading</b>	<b>18</b>
1.2.1	Spot weld behaviour	18
1.2.2	Mechanical behaviour of homogeneous AHSS spot welds	23
1.2.3	Mechanical behaviour of heterogeneous AHSS spot welds	26
<b>1.3</b>	<b>Modelling of spot welded assemblies mechanical behaviour</b>	<b>28</b>
1.3.1	Analytical models	28
1.3.2	Finite element models	31
<b>1.4</b>	<b>Conclusion</b>	<b>37</b>

### 1.1 Generalities

Steel has for long been the material of choice for carmakers worldwide. The use of steel has allowed automotive manufacturers to achieve desired standards of strength and safety for their vehicles at relatively low costs compared to other materials. However, reducing the weight of automobiles has become an extremely important consideration for carmakers. To achieve this goal, steel makers developed new steels with imposed mechanical properties and lower weight but they have to assemble them to others grades. Resistance spot welding (RSW) is a joining process for metal sheets where opposing forces and current are applied on several steel sheets. Resistance spot welding is the predominant joining process in automotive industry for assembling automotive bodies and large components. Typically, a car body contains about 5000 spot welds joining two or more sheets of different thicknesses [RIV 04].

## 1.1.1 Steels for automotive industry

### 1.1.1.1 Automotive steels

Automotive steels can be classified in several different ways. One of them is a metallurgical designation providing some process information and giving three main product groups:

- Conventional ferritic automotive steels for stamping: Interstitial Free (IF), Al-killed,
- Mild steels: High Strength Low Alloyed (HSLA), Bake Hardening (BH), Isotropic steels (IS),
- Automotive High Strength Steels (AHSS) : Dual Phase (DP), Transformation Induced Plasticity (TRIP), Twinning Induced Plasticity (TWIP), Press-Hardening Steels (PHS), 3rd generation (high strength high formability HSHF, quenching and partitioning Q&P, etc...).

The balance between strength and elongation of flat steels for automotive application is collected on the figure 1.1.

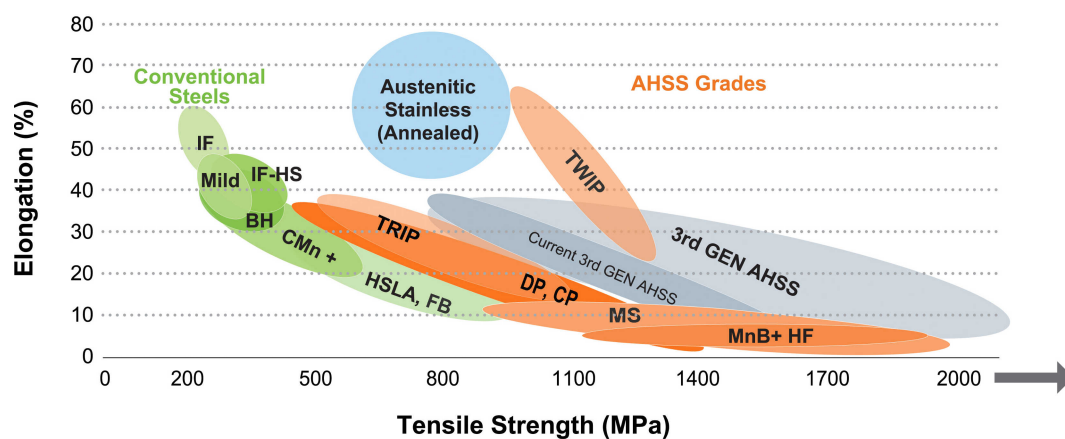


Figure 1.1: Formability of flat steels for automotive application [KEE 04].

The first group contains two main concepts: Mild steels, low strength Interstitial-Free (IF) steels. Mild steels have an essentially ferritic microstructure. IF steels have ultra-low carbon levels designed for low yield strengths and high work hardening exponents. These steels are designed to have more stretchability than Mild steels. Some grades of IF steels are strengthened by a combination of solid solution elements, precipitation of carbides and/or nitrides, and grain refinement. A common element added to increase strength is phosphorous (a solid solution strengthener). The higher strength grades of IF steel type are widely used for structural applications.

The second group is globally represented by four main concepts: High Strength Low Alloyed (HSLA), Bake Hardening (BH), Isotropic steels (IS) and high strength Interstitial-Free (IF) steels. HSLA steels are strengthened primarily by micro-alloying elements contributing to fine carbide precipitation and grain-size refinement. BH steels have a basic ferritic microstructure and are strengthened primarily by solid solution strengthening. A unique feature of these steels is the chemistry and processing designed to keep carbon in solution during steelmaking and then allowing this carbon to come out of solution during

paint baking. This increases the yield strength of the formed part. IS steels have a basic ferritic type of microstructure.

The last group is the more famous: one Automotive High Strength Steels (AHSS). It contains many steel concepts: Dual Phase (DP), Transformation Induced Plasticity (TRIP), Press Hardened Steels (PHS), Twinning Induced Plasticity (TWIP), Ferritic-Bainitic (FB), Martensitic (MS). Since the metallurgy and processing of AHSS grades are somewhat novel compared to conventional steels, they are described here to provide a baseline understanding of the link between their remarkable mechanical properties and their processing. Advanced High-Strength Steels (AHSS) are complex, sophisticated materials, with carefully selected chemical compositions and multiphase microstructures resulting from precisely controlled heating and cooling processes. Various strengthening mechanisms are employed to achieve a range of strength, ductility, toughness, and fatigue properties. These steels have been designed to exhibit light weight and to meet the challenges of today's vehicles for stringent safety regulations, emissions reduction, solid performance, at affordable costs.

The AHSS family includes Dual Phase (DP), Ferritic-Bainitic (FB), Martensitic (MS), Transformation-Induced Plasticity (TRIP), Hot-Formed (HF), and Twinning-Induced Plasticity (TWIP). These first and second generation AHSS grades are uniquely qualified to meet the functional performance demands of certain parts. For example, DP and TRIP steels are excellent in the crash zones of the car for their high energy absorption. For structural elements of the passenger compartment, extremely high-strength steels, such as Martensitic and boron-based Press Hardened Steels (PHS) result in improved safety performance. Recently there has been increased funding and research for the development of the "3<sup>rd</sup> generation" of AHSS. These steels provide an improved strength-ductility combinations compared to present grades, with a potential for more efficient joining capabilities, at lower costs. These grades will exhibit unique microstructures to achieve the desired properties.

This work will focus on the welding of three AHSS concepts:

- Dual Phase (DP)
- Press-Hardened Steels (PHS)
- Duplex (3<sup>rd</sup> AHSS generation)

#### 1.1.1.2 Dual Phase steels

DP steels consist of a ferritic matrix containing a hard martensitic second phase in the form of islands. Increasing the volume fraction of hard second phases generally increases the strength. DP (ferrite plus martensite) steels are produced by controlled cooling from the austenite domain (in hot-rolled products) or from the two-phase ferrite plus austenite phase (for continuously annealed cold-rolled and hot-dip coated products) to transform some austenite to ferrite before a rapid cooling transforms the remaining austenite to martensite. Due to the production process, small amount of other phases (Bainite and Retained Austenite) may be present.

Depending on the composition and process route, steels requiring enhanced capability to resist cracking on a stretched edge (as typically measured by hole expansion capacity) can have a microstructure containing significant quantities of bainite. Figure 1.2 shows a

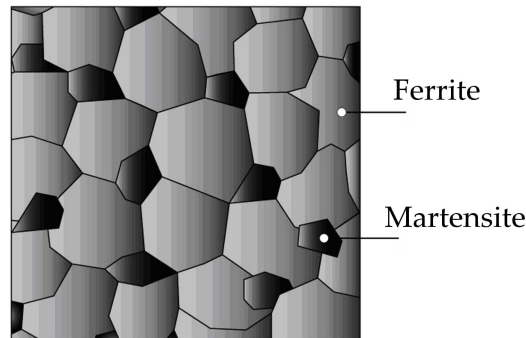


Figure 1.2: Schematic microstructure of DP steel.

schematic microstructure of DP steel, which contains ferrite and martensite islets. Figure 1.3 shows a real microstructure of a DP600 after Nital 1% chemical etching and heat treatment to reveal the intergranular martensite (blue). The soft ferrite phase is generally continuous, giving these steels excellent ductility. When these steels deform, strain is concentrated in the lower-strength ferrite phase surrounding the islands of martensite, creating the unique high initial work-hardening rate (n-value) exhibited by these steels. The work hardening rate combined with the excellent elongation creates DP steels with much higher ultimate tensile strengths than conventional steels of similar yield strength.

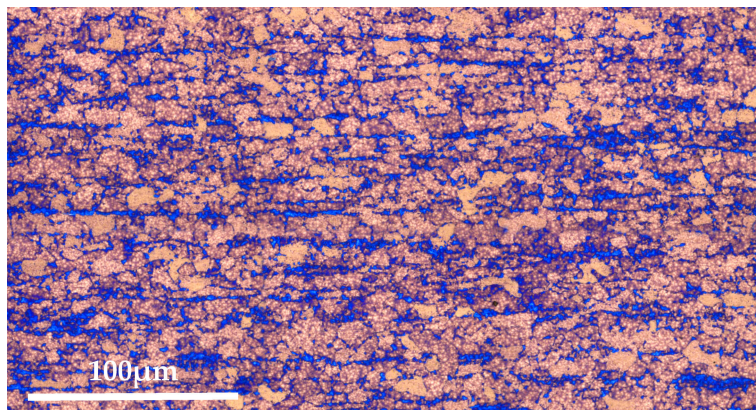


Figure 1.3: Microstructure of DP600 steel using Nital 1% reagent and 250 °C annealing for 2 hours (Ferrite is pink phase, and martensite is blue one).

The DP steels hardenability is ensured thanks to carbon, manganese, silicon, chromium, molybdenum, vanadium or nickel. Different DP steels exist following the chemical composition, controlling the ferrite fraction. Moreover, DP steels high grades have precipitates which contribute to hardening. These steels allow a lightening of automotive products by their high mechanical resistance (figure 1.4).

#### 1.1.1.3 Press hardened martensitic steels

The implementation of press-hardening applications and the utilization of hardenable steels are promising alternatives for optimized part geometries with complex shapes and no spring back issues. Boron-based hot-forming steels (between 0.001wt% and 0.005wt%

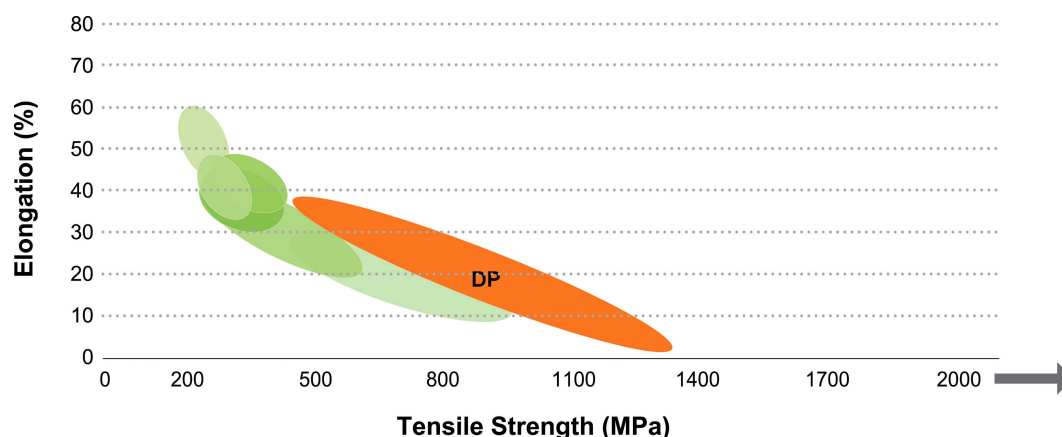


Figure 1.4: Formability of DP steels for automotive application [KEE 04].

boron) have been in use since the 1990s for body-in-white construction. A typical minimum temperature of 850 °C must be maintained during the forming process (austenitization) followed by a cooling rate greater than 50 °C s<sup>-1</sup> to ensure that the desired mechanical properties are achieved. The final microstructure of Hot Formed (HF) steel is similar to Martensite. Stress-strain curves after quenching are similar to martensitic (MS) steels. The MS steels are characterized by a martensitic matrix containing small amounts of ferrite and/or bainite. Within the group of multiphase steels, MS steels provide the highest strengths, up to 2000 MPa ultimate tensile strength (figure 1.5). MS steels are often subjected to post-quench tempering to improve ductility, and can provide adequate formability even at extremely high strengths.

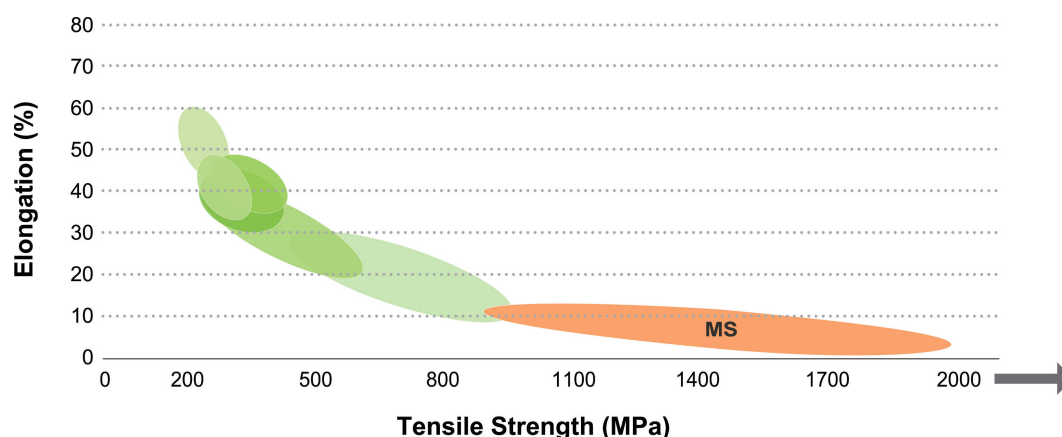


Figure 1.5: Formability of MS steels for automotive application [KEE 04].

Usibor1500 (22MnB5 as received before press hardening) belongs to this family. Due to full martensitic microstructure (figure 1.6), its mechanical strength is very high (~1500 MPa). Usibor1500 and 22MnB5 are hot formed grades intended for use in automobile structural and safety components like front and rear bumper beams, door reinforcements, windscreen upright, B-pillar reinforcements or floor and roof reinforcements.

The very high mechanical strength of the final part enables to achieve weight savings of 30 % to 50 % compared to conventional cold forming grades. The main advantages of



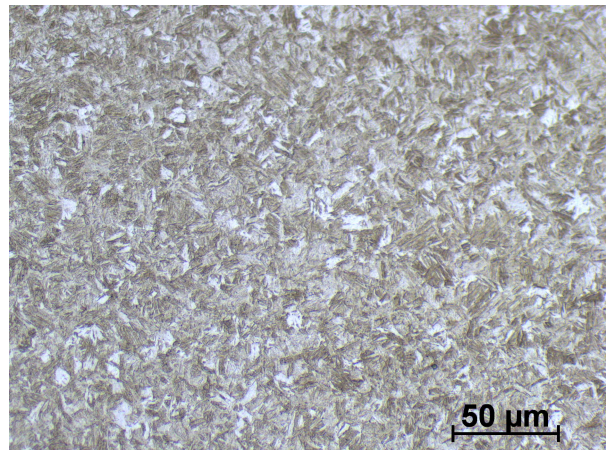


Figure 1.6: Microstructure of Usibor1500 (22MnB5) boron steel using Nital 1% reagent (fully martensitic).

Usibor1500 and 22MnB5 are:

- Ability to achieve complex geometry in both the direct process (forming in austenitic state) and the indirect process (good cold formability). Their very good hot formability makes it possible to offer steel solutions that integrate several functions (elimination of reinforcement parts and assemblies).
- Total absence of spring back.
- Uniform mechanical properties obtained in the part.
- High fatigue strength (Usibor1500) and impact resistance, allowing substantial weight reduction

#### 1.1.1.4 Third AHSS generation: Duplex

The third and last type of AHSS concept is under development and belongs to the 3<sup>rd</sup> AHSS generation. The current aim in the development of 3rd generation steels for automotive applications is to increase strength keeping at least the same formability (High Strength High Formability HSHF). Several concepts like carbide free bainite, medium manganese steels or others could bring an important reduction in the weight of vehicles. Driving forces for these developments are strict European Union regulations concerning CO2 emissions for the coming years and also alternative materials. However in this philosophy there is a hidden limit dictated by structural rigidity concepts. Therefore an optimal concept would be one which brings a lower density, in addition to an increased strength at iso-formability. This is the key issue behind the concept of Duplex lightweight steels, a reduced density through aluminium additions. Duplex concept consists in adding manganese (Mn) and aluminium (Al) to obtain a typical Duplex structure, austenite and ferrite (figure 1.7).

An evaluation showed that Duplex steels is a very stable concept concerning processing which could reach a lightening potential of 20 % in comparison to a DP600 at iso-formability. This weight saving is obtained in two ways:

- Decreasing the steel sheet thickness by increasing mechanical properties of Duplex



Figure 1.7: Typical Duplex structure; gray phases are austenite and blue phases are ferrite [BAR 14]

compared to DP600

- Reducing the steel density by adding light alloying elements (e.g. aluminium). However there are still several challenges to solve before these grades could be available on the market.

## 1.1.2 Resistance spot welding

### 1.1.2.1 Principle

Developed by Pr. Thomson in 1877, Resistance Spot Welding (RSW) process is a low cost welding technique predominantly used in automotive industry. For instance, a car body has between 3000-5000 spot welds. It is an appropriate welding technique for joining thin sheets having a thickness varying from 0.5 mm to 4 mm [CAZ 89].

RSW has two advantages, it is a low cost and very fast process. Resistance welding creates a joint welded by Joule effect by injecting a high intensity current (several kA following materials and sheet thicknesses) between two or more steel sheets held in contact by two electrodes (principally copper alloys, Cu-Cr, Cu-Zr or Cu-Cr-Zr). The supplied heat leads to the formation of a molten nugget, which solidifies when the current is stopped. The heat produced  $H$  during the process is defined by:

$$H = \int_0^{t_0} R \times I^2 dt \quad (1.1)$$

where  $R$  is the sum of resistances ( $\Omega$ ) encountered in the system,  $I$  is the current intensity (A),  $t_0$  is the phenomenon duration (s) and  $t$  is the time variable (s).

The typical encountered resistance is around hundreds of  $\mu\Omega$ , and the applied voltage is several Volts [ZHA 06]. The intensity current can be, either Direct Current (DC) or Alternative Current (AC), and may be applied by specific welding cycles (alternating hot and cold times).

A compression force is applied during welding process, ensuring the steel sheets clamping before current application and holding during and after the heating phase. This stress

is around hundreds of daN, depending on the sheets thickness. A typical spot welding cycle (figure 1.8) consists of four main stages [SRI 05]:

- The squeezing time: pressure is exerted via electrodes on the metal sheets in intimate contact until the force becomes stable. In the ArcelorMittal laboratory, only the top electrode is moving whereas the bottom electrode is fixed.
- The welding time: due to the current flow through the electrode tips and the pieces to be welded an important amount of heat is supplied by Joule effect at the interface of metal sheets. There are two steps in the welding time: firstly, the contact resistance between the two sheets is the higher, that leads to a high Joule effect and supplied heat at this location. Then the contact resistance highly decreases when temperature increases. The released heat leads to the melting of metal sheets.
- The holding time: once the current stopped, the nugget solidifies whereas the pressure is maintained. The heat is evacuated via the electrodes which are water cooled via conduction in the steel sheets. The metallurgical phases quality and the spot weld mechanical behaviour directly depend on the holding time.
- The electrode unloading: at the end of welding process cycle, the top electrode goes up.

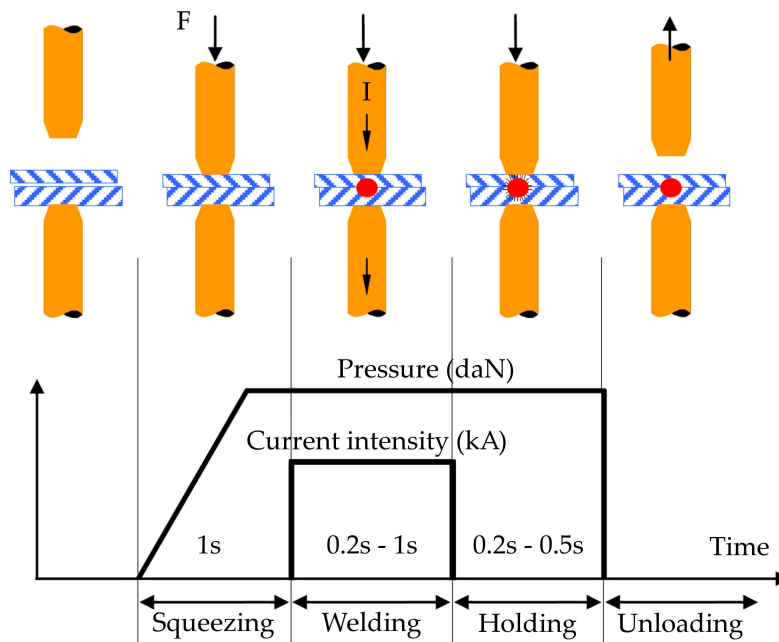


Figure 1.8: Different steps of the welding process.

Basically, a set of parameters are directly affecting the weld quality [SRI 05]:

- The pressure exerted by the electrodes,  $F$  (daN). Depending on the mechanical behavior of the metal to be welded and also on the thickness of steel sheets, it generally varies from 200 daN to 600 daN;
- The current intensity,  $I$  (kA) is a very important parameter, because it directly influences the amount of heat generated by Joule effect as mentioned above. The used intensity is either single-phase alternative current (AC-50Hz) or medium frequency

direct current (MFDC-1000 Hz). The intensity current generally varies from 5 kA to 15 kA;

- The welding time (periods): generally it is about 10-50 periods for a 50 Hz frequency, i.e. 0.2 s-1 s. Following the standards, it directly depends on the steel sheets nature and thickness. In case of high sheet thicknesses or high mechanical strengths, the current could be pulsed alternating between hot time (with current) and cold time (without current);
- The holding time (periods) necessary for solidification and heat dissipation;
- The geometry of electrodes, often truncated cone shaped with an hemispheric active face to control the contact surface size. Indeed, the electrodes have a major role on three aspects: mechanical (process pressure), electrical (current), and thermal (cooling).

### 1.1.2.2 Spot weld geometry

Figure 1.9 is a schematic representation of a spot weld cross section including electrodes axis. The spot weld geometry generally shows three particularities:

- An assembly discontinuity;
- The presence of a notch root likely to induces stress concentration in case of mechanical load.
- Indents on external faces of the assembly due to electrode force.

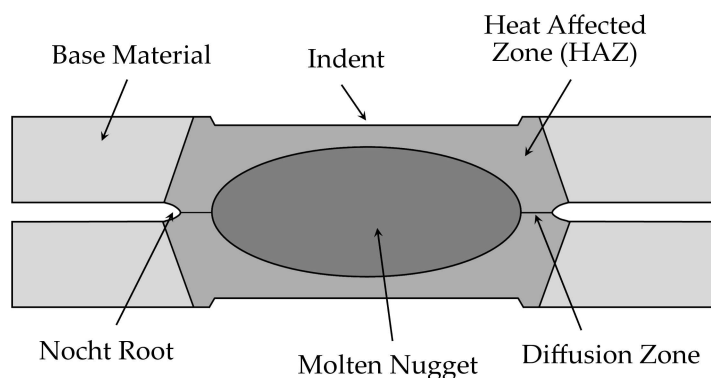


Figure 1.9: Scheme of a spot weld cross section showing the molten nugget, the HAZ and the base material.

Generally, three main zones could be described. The first is the molten nugget (or fusion zone) corresponding to the zone where steel was liquid during process then was quickly cooled down to room temperature. The molten nugget firstly solidifies at the nugget periphery by germination of a solid phase then by growth of elongated grains (called dendrites) along the normal direction of the solidification front. Nugget solidification ends at the centre with the formation of equiaxed grains. Main solidification defects, like shrinkage cavities, are located in this zone.

The second zone is the Heat Affected Zone (HAZ), corresponding to the zone where initial microstructure was affected by the thermal cycle of the welding process. Usually,

the heat affected zone is defined by a zone which underwent temperature from 700 °C up to the melting temperature.

Finally, the last zone corresponds to the base material, where the microstructure has not been modified by the welding thermal cycle.

The observed microstructures on a spot weld result from phase transformations under fast heating and cooling conditions. Therefore, a microstructural characterization after welding is only giving partial information on the thermal cycle undergone by the materials. The three main parameters influencing the final spot weld microstructure are:

- The maximal temperature reached locally,
- the cooling rate,
- chemical composition of steel.

The heating and cooling rates during the welding process do not permit to use the phase diagram to predict final microstructures in the spot welds. However, the phase diagram is generally used to approximate the obtained microstructures. Zhang and Senkara [ZHA 06] used the Iron-Carbon diagram to establish a correlation between the maximal temperature locally reached during the welding process ( $T_{max}$ ) and the different observed microstructures after welding (figure 1.10).

The cooling rate is the second main parameter affecting the final microstructure of spot welds. It differs following the location in the spot weld and according the sheet thicknesses, and is in the order of thousand degrees per second. In some cases, using thermocouples wisely positioned around the spot weld allows to evaluate the cooling rate, but this can interfere with the process.

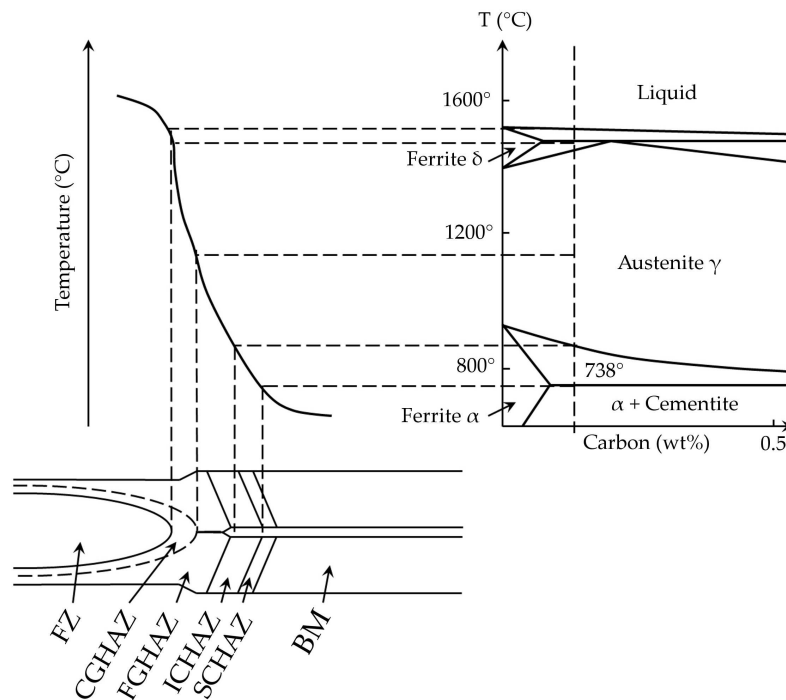


Figure 1.10: Maximal temperature reached during the spot welding process as a function of the position in the spot weld and related to the Fe-C phase diagram [ZHA 06].

A finer decomposition of weld zones based on maximal temperature and the resulting microstructure can be listed as follows (and summarized in table 1.1).

Zone	Abbreviation	Temperature
Fusion Zone	FZ	$T_{fusion} < T_{max}$
Coarse Grain HAZ	CGHAZ	$Ac_3 \ll T_{max} < T_{fusion}$
Fine Grain HAZ	FGHAZ	$Ac_3 < T_{max} \ll T_{fusion}$
Intercritical HAZ	ICHAZ	$Ac_1 < T_{max} < Ac_3$
Subcritical HAZ	SCHAZ	$T_{max} < Ac_1$

Table 1.1: Weld zones and the related maximal temperatures reached ( $T_{fusion}$  is the fusion temperature).

- **Fusion Zone (FZ):** In this zone, the maximal temperature reached is higher than the melting temperature of steel ( $T_{melting}$ ). The observed microstructure after cooling is dendritic, coarse at the nugget centre and thinner at the nugget boundary. Moreover, interdendritic segregation is generally observed. This zone is a mixture of the two (or more) steel sheets.
- **Coarse Grain HAZ (CGHAZ):** This zone corresponds to the zone which reached a maximal temperature between about 1100 °C and the melting temperature. During welding time, austenite grain coarsening occurs providing an important hardenability and quenchability to this zone. The observed microstructure after cooling is generally martensitic and homogeneous.
- **Fine Grain HAZ (FGHAZ):** the maximal temperature reached is between about  $Ac_3$  and  $\sim 1100$  °C. Following the Iron-Carbon phase diagram, austenitization is complete in this zone. During welding time, the new austenite microstructure, inhomogeneous and particularly thin, substitutes the initial one. After cooling, the observed microstructure is generally a little bainitic and martensitic with limited heterogeneities.
- **InterCritical HAZ (ICHAZ):** In this zone, the maximal temperature reached is between  $Ac_1$  and  $Ac_3$ . The partial austenitization (coexistence of  $\alpha$  ferrite and  $\gamma$  austenite) leads to important microstructure changes.
- **SubCritical HAZ (SCHAZ):** This zone corresponds to the zone which reached a maximal temperature between about 600 °C and  $Ac_1$ . Generally, no effect is observed on the grain size, but some metallurgical changes can already occur depending on the initial state. For martensitic steel, tempering can occur in this zone.

In the case of heterogeneous spot welding, the nugget may be asymmetric with respect to the interface between the two sheets. The formation of the nugget is governed by three main physical factors:

- bulk resistivity ( $R$  in  $\Omega m$ ),
- thermal conductivity ( $K$  in  $W m^{-1} K^{-1}$ ),
- melting point ( $T_{liquidus}$  in °C)

These three factors are strongly depending on the alloys composition. Consequently, when the alloying elements content increases, the bulk resistivity also increases. Since the

conductivity is the inverse of the resistivity, it will decrease.

Concerning the melting point, it decreases when the alloying elements content increases. Therefore, the higher the difference in terms of alloying elements concentration between the two pieces to be welded, the higher the difference between their melting points, bulk resistivities and their thermal conductivities. As depicted in figure 1.11, the higher the difference in alloying elements, the more asymmetric the nugget will be with respect to the interface between the two sheets A and B. Hence, it is observed that the nugget is shifted towards the most alloyed sheet as observed by Russo Spena [RUS 16] and Krajcarz [KRA 10].

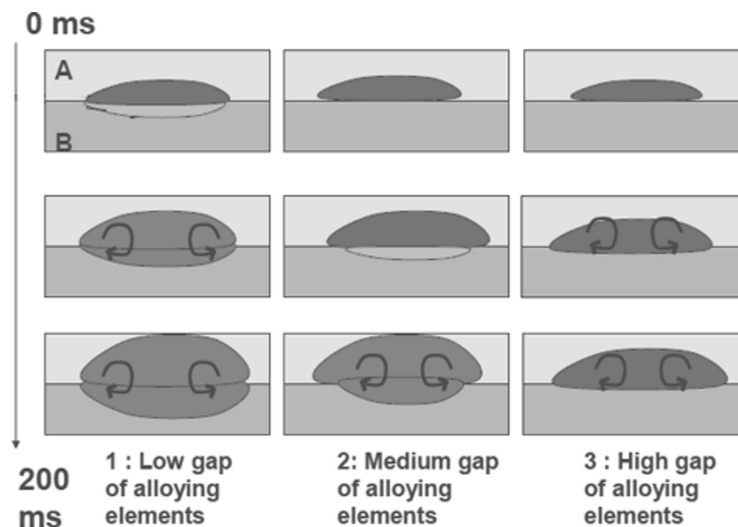


Figure 1.11: Influence of the difference of alloying elements concentration on the formation of fusion zone.

Three cases can be distinguished:

- The melting starts at the interface A/B and the molten zone is homogenized due to the convection phenomena;
- The fusion occurs firstly in the most alloyed sheet because of its lower melting point and after in the second one;
- The fusion takes place only in the most alloyed sheet. Subsequently, the dissolution of the sheet B by the liquid metal A occurs. Dissolution starts at the grain boundaries because of their high energy and inhomogeneity compared to the rest of the microstructure [AHM 06].

### 1.1.2.3 Mechanical testing

There are many destructive tests to characterize spot welds as shown in figure 1.12. Cross tension test and tensile shear test are commonly used in the automotive industry to characterize the quasi static mechanical behaviour of spot welds. These tests allow to measure the load needed to break a spot weld and observe the failure mode. The ultimate load at failure is called cross tension strength (CTS) for the cross tension test and tensile shear strength (TSS) for the tensile shear test. Note that despite the name, CTS and TSS are “load” quantities (in Newton) and not stresses (load per unit area).

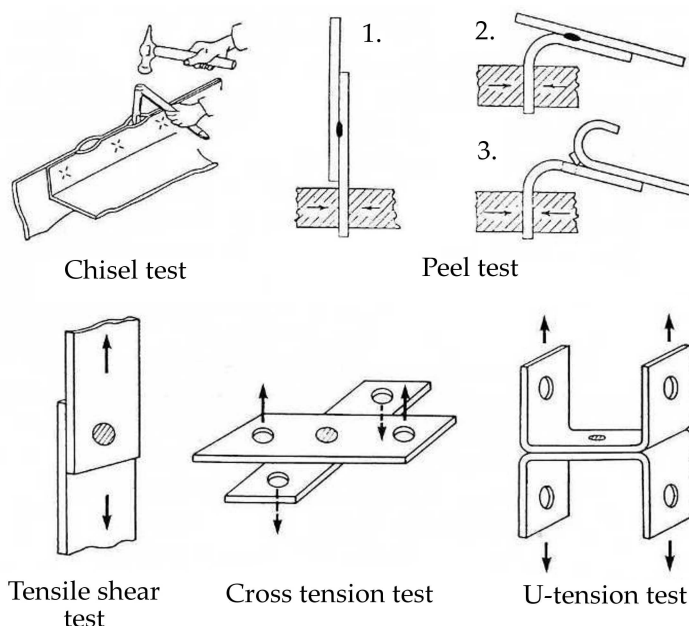


Figure 1.12: Destructive tests on spot welds according to [NIS 82].

The geometry of these two tests (among others) are detailed in figure 1.12. In both cases, three main failure modes are observed:

- The Button Pull-Out (BPO): one of the steel sheets fails around of the spot weld. The sheet has a hole and the other one has a Button.
- On the contrary, failure could occur at the interface between the two steel sheets. This is called Full Interfacial Failure (FIF).
- Between these two extreme cases, a small button surrounded by damaged area at the sheets interface may be obtained. This failure mode is called Partial Interfacial Failure (PIF). When Partial Interfacial Failure occurs, a Plug Ratio (PR) is defined corresponding to the ratio between the button diameter ( $d_b$ ) and the weld diameter ( $d_w$ ) as shown in equation 1.2 and in figure 1.13.

$$PR = d_b/d_w \quad (1.2)$$

Thus, a PR equal to 0 corresponds to Full Interfacial Failure and a PR equal to 1 to Button Pull-Out. Intermediate values of PR correspond to Partial Interfacial Failure (PIF).

Beyond these three main failure modes, the American Welding Society (AWS) has collected a total of eight different failure modes, where Button Pull-Out (BPO) and Full Interfacial Failure (FIF) are the two extreme modes [GOU 05]. The eight modes, represented in figure 1.14, are described as following:

- **mode 1** failure: This is the Button Pull-Out (BPO) failure mode previously defined. This has been the conventionally accepted failure mode for mild steels.
- **mode 2** failure: defined as a partial-thickness fracture and partial-button pull. In this mode, a button of at least 20% of the area is pulled from the opposing sheet.



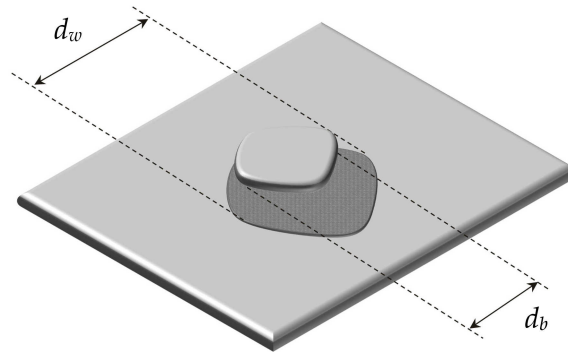


Figure 1.13: Schematic representation of the plug ratio in the case of Partial Interfacial Failure (PIF).

The weld nugget shows no evidence of failure.

- **mode 3** failure: also known as a partial-thickness fracture. Failure occurs in the HAZ around the weld nugget, but not through the nugget itself. In some case, it is related to Total Dome Failure (TDF).
- **mode 4** failure: defined as a partial-thickness fracture, partial-button pull, and partial-interfacial fracture in which the weld nugget partially separates.
- **mode 5** failure: a Partial Interfacial Failure (PIF), partial-button pull, and a partial weld nugget separation.
- **mode 6** failure: a combined partial-thickness and Partial Interfacial Failure. It is characterized by a fracture through at least 20% of part of the mating sheet thickness, as well as weld nugget separation.
- **mode 7** failure: this is a complete fracture of the weld nugget along the faying surface plane. It corresponds to the Full Interfacial Failure (FIF).
- **mode 8** failure: showing no fusion of the parent materials. This occurs when the sheets separate and show no evidence of nugget formation.

Characterizing failure modes in this way allows them to be ranked in terms of severity and provides a tool for analysing mechanical performance as a function of failure mode severity. Once it is correlated with mechanical performance, this failure mode ranking system can be used to assess spot weld quality in AHSS.

Only the mode 1, 5 and 7 are commonly observed on former steel generations, but the use of multiphased steels produces more and more of the intermediate (and usually undesired) failure modes (2, 3, 4, 6), even if the load bearing capacity of the spot welds remain acceptable.

#### 1.1.2.4 Weldability range

The weldability range represents the welding intensity current interval in which the spot welds are acceptable. The acceptability of a spot weld differs according to the different standards, but the most usual criteria are:

- welding/button diameter, a minimal diameter is generally imposed;

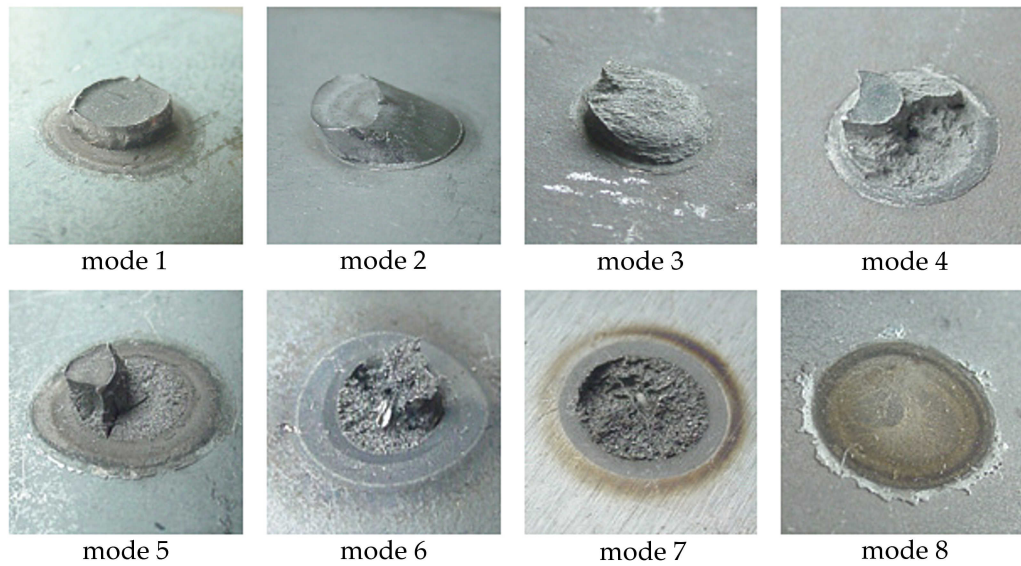


Figure 1.14: Different failure modes identified by AWS [GOU 05].

- failure mode, a spot weld is often defined as acceptable when the failure mode is a Button Pull-Out (BPO);
- spot weld strength, acceptable spot welds need to have a strength higher than a critical value.

In the ISO 18278-2 (2004) standard [ISO 04], a minimal button diameter is imposed (4 mm for sheets with a thickness under 1.3 mm and 6 mm for a thickness equal or higher than 1.3 mm). Moreover, welding parameters (electrode diameter, electrode force, welding time, holding time) are also set by the standard according to steel sheet thicknesses, UTS and coating.

For given welding parameters, there is a minimal intensity to create a molten nugget at the sheets interface. Below this intensity, steel sheets are not welded, but could possibly be bonded by diffusion or by coating brazing. Above this intensity, during mechanical tests (CTS or TSS), Full Interfacial Failure (FIF) is generally observed for low intensity. When the current intensity increases, Button Pull Out (BPO) tends to be the main failure mode [WIL 79] [FER 98].

When the button diameter reaches the minimal diameter given by standards, the minimal intensity for acceptable welding is identified and corresponds to the lower boundary of the welding range ( $I_{min}$ ). Later, when the intensity is increasing, there is a intensity for which the nugget growth reaches the notch root producing liquid metal expulsion at the interface because of the electrode force (also called splashing). This phenomenon determines the upper boundary of weldability domain ( $I_{max}$ ). The weldability domain is illustrated in figure 1.15.

Other standards have different definitions of the minimal button diameter:

- $d_{bmin} = 4\sqrt{e}$ , following the Japanese Standards Association [JSA 89],
- $d_{bmin} = 5\sqrt{e}$ , following the American Welding Society [PET 06],

where  $e$  is the steel sheet thickness in mm.

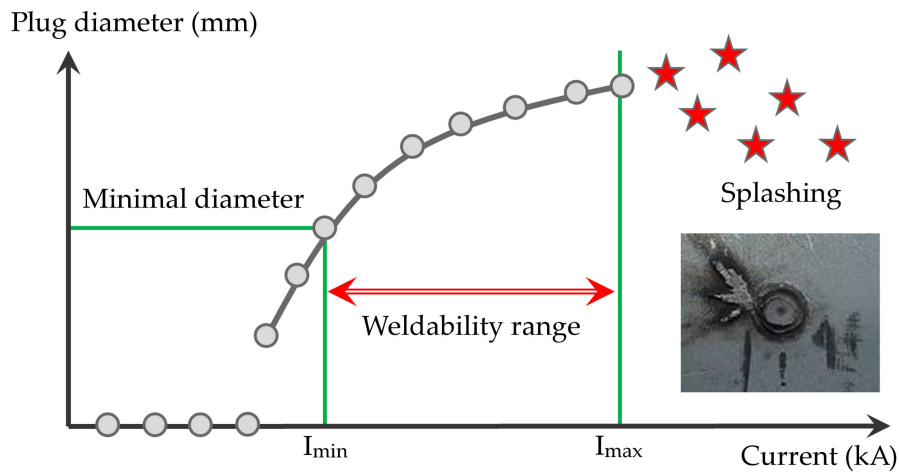


Figure 1.15: Welding range definition with the weld diameter according to Blondeau [BLO 01].

### 1.1.3 Arc Welding

#### 1.1.3.1 Principle

Arc welding is a welding process using a welding power supply to create an electric arc between an electrode and the base material in order to melt the metals at the welding point. The welding region is usually protected by some shielding gas. Arc welding processes may be manual, semi-automatic, or fully automated. First developed at the end of the 19th century, arc welding became commercially important in shipbuilding during the Second World War. Today it remains an important process for the fabrication of steel structures and vehicles, especially the Gas Metal Arc Welding process.

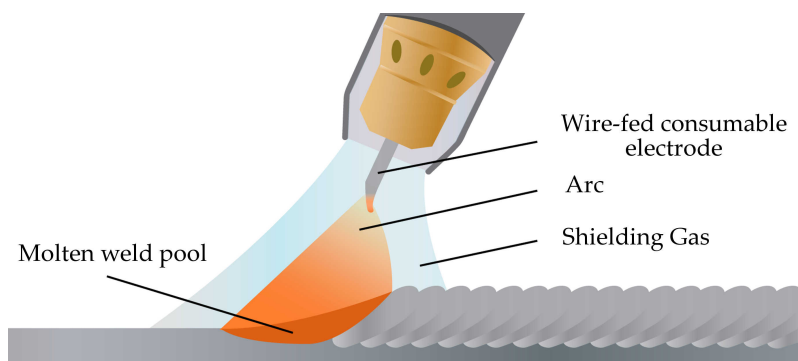


Figure 1.16: Schematic representation of arc welding according to Anderson [AND 01].

Arc welding in the steel industry mainly requires a filler wire to weld the two steel sheets (see figure 1.16). During the arc welding process, almost the same zones as in spot welding appear around the welding area. The three main zones are:

- fusion zone (molten zone or weld bead) which is a mixture of filler wire with molten base material. The lower the fusion temperature of the base material the more the base material is diluted (which may affect the fusion zone chemical composition and

properties);

- HAZ modified by thermal cycle during welding process;
- base material with initial microstructure and mechanical properties.

There are five main parameters in the arc welding process, with varying influence on the weld bead geometry. These parameters are:

- Current intensity and tension: it controls the weld bead size and its penetration in the steel sheet. Welders generally refer to guidelines to estimate the right current to use and adapt it depending of the welding geometry obtained. In fact it corresponds to an welding energy;
- Distance between the electrode and the steel sheet: this distance directly affects the energy quantity (heat) transmitted into the joint. The distance needs to be wisely chosen to prevent spatter and energy loss;
- Torch angle: there are in fact two torch angles, the work angle and the travel angle. The work angle is the angle between the joint cross section and the torch (ideally  $90^\circ$ , to transmit a maximum of energy into the joint). The travel angle is the angle between torch and line of travel (around  $10^\circ$ , to give a better control of weld bead penetration).
- Welding and filler speed: an optimal welding speed needs to be identified for arc welding. If the torch move is too slow, the weld bead will be too large because of molten filler wire quantity. Moreover, too much heat is going into the joint. On the contrary, if the torch speed is too high, the weld size will be too small because of low molten filler wire quantity brought.
- Gas nature: Usually used to protect the weld area from oxygen and water vapour, different gas or gas mixture could be use for arc welding. The gas nature could affect the weld quality by changing the number of inclusion in the weld bead. Shielding gas composition has a high effect on the arc stability according to Gadallah [GAD 12].

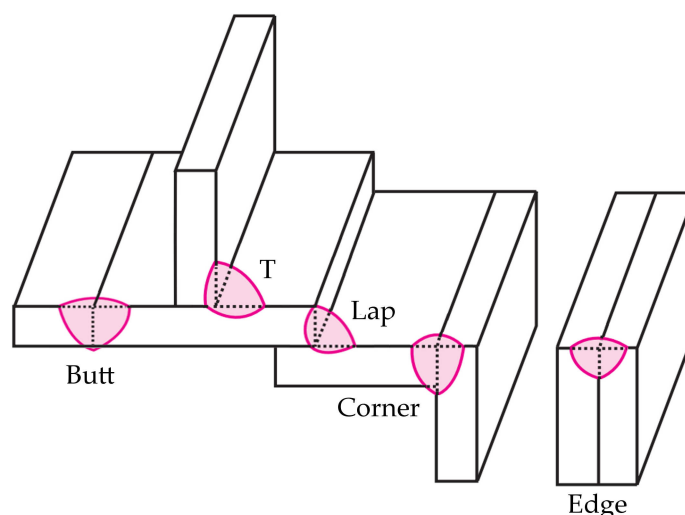


Figure 1.17: Schematic representation of the five arc welding designs according to Minnick [MIN 07].

The American Welding Society defines a joint as “the manner in which materials fit

together”. Following this definition, there are five basic types of arc weld joints (figure 1.17):

- Butt joint;
- T-joint;
- Lap joint;
- Corner joint;
- Edge joint.

### 1.1.3.2 Mechanical testing

Generally, laboratory joints are welded in two types: butt and lap. These weld geometries allow better mechanical characterisation by tensile tests. Weld joint are cut in several samples with a constant width (between 25 mm and 50 mm).

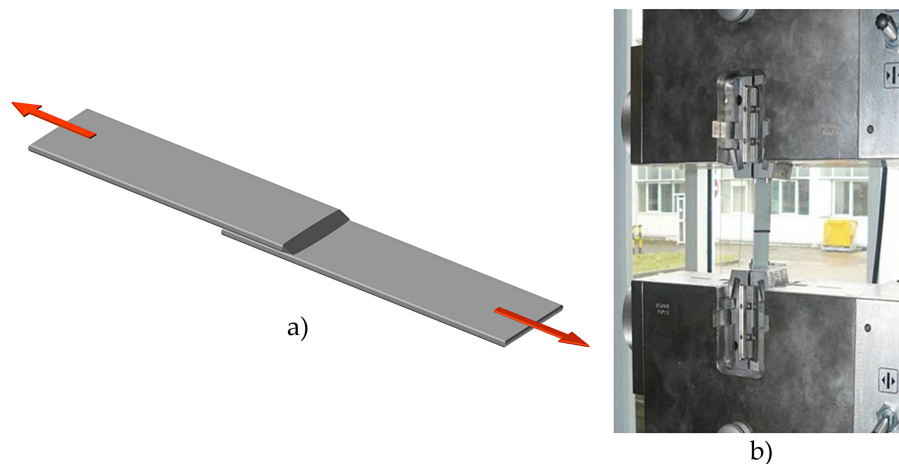


Figure 1.18: Illustration of arc welding mechanical test: a) schematic representation and b) picture of a sample in the tensile test machine.

In the case of overlap weld type, the tensile tests performed on arc welds are similar to the TSS test of Resistance Spot Welding (RSW) however there is no symmetry. The description of arc welding tensile test is illustrated in figure 1.18.

As in RSW testing, the load and displacement are recorded during the test until failure. After the mechanical test, investigations are undertaken to identify the failure mode. As in RSW testing, failure could occur in different zones of the weld (base material, HAZ, fusion zone), implying different failure modes.

## 1.2 Mechanical behaviour of spot welds under quasi-static loading

### 1.2.1 Spot weld behaviour

The AHSS weldability generally shows some particularities compared to ferritic steel welding because of the high strength of sheets, of their higher resistivity due to alloying elements

and of their hardenability (brittleness of formed phases). The main consequence of these particularities is that AHSS spot weld failure modes tend to partial or full interfacial failure.

These particularities induce a modification of welding parameters, in particular an increase of electrode force, an adjustment of welding and holding time to control the thermal cycle and the use of pre and post treatments ([JON 81], [CHU 02], [SHI 04] and [IIS 06]). These treatments could modify in particular the toughness or promote blunt shape in the notch root limiting the stress concentration.

Gould and Workman [GOU 98] summarized the conditions favouring interfacial failure:

- High stress triaxiality, in particular when weld diameter is small;
- Brittleness of notch root and nugget microstructures (carbon content);
- Presence of cavities in the nugget periphery, preferential path of crack propagation.

The first condition is essentially related to mechanical consideration due to spot weld geometry and loading type whereas the two others are closely related to steel grade (chemical composition).

### 1.2.1.1 Chemical composition effect on failure mode

Many authors studied the failure mode sensitivity to chemical composition ([NIS 82], [MOO 89], [FER 98], [MAR 05], [GOU 98], [RAD 12]). These studies generally proposed a "carbon equivalent" formulation to take into account the hardenability effect of elements like carbon, silica or the manganese and segregation effect of elements like phosphorus or sulphur during welding. The most used formulation was proposed by Nishi [NIS 82]:

$$C_{eq} = C + \frac{Si}{30} + \frac{Mn}{20} + 2 \cdot P + 4 \cdot S \quad (1.3)$$

where the chemical composition is in mass percentage.

This relationship was obtained on a hundred of cold rolled steel sheets with a thickness of 0.8 mm, identical welding parameters except for the welding intensity current which was adapted to obtain a constant welding diameter and the holding time (5 or 25 periods). Thus, depending on the chosen holding time, a critical  $C_{eq}$  allows to distinguish spot welds failing in a interfacial mode or in a button pull out mode.

Nowadays, AHSS ultimate tensile strengths are higher and higher. This is obtained thanks to chemical composition, and more precisely to carbon content in the steels. Carbon is used to obtain very hard and resistant phase such as martensite in the steel. However during the welding process, martensite undergoes particular thermal cycles. Thus, in the sub critical HAZ (SCHAZ) where the temperature reached is under  $A_{c1}$ , a tempering of initial martensite occurs. It leads to a softening of this zone. This phenomenon is visible on steel grades containing at least 10 % of martensite (UTS over 800 MPa) in particular in Dual Phase (DP) steels as observed by [BIR 12], [SUN 06], [KHA 08], [HER 08], [DAN 11b] and [POU 12].

The phenomenon of tempering is higher when the base material carbon content increases. 22MnB5 Boron steel belongs to the press hardened martensitic steel and has a high carbon content which leads to a fully martensitic microstructure after process. The welding of these steels induces the apparition of a hardness drop in the sub critical

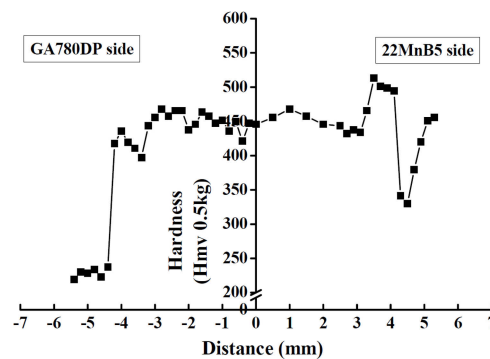


Figure 1.19: Typical hardness profile between GA780DP and 22MnB5 after RSW with tempering in the 22MnB5 HAZ according to [CHO 11].

HAZ, where hardness is around 300 Hv compared to the base material and the HAZ (over  $A_{c3}$ ) where hardness is between 450 Hv and 500 Hv as observed by [CHO 10], [JON 11], [CHO 11] and [HUI 16].

In some cases, the softening in sub critical HAZ can promote the necking during mechanical tests and promote the pull out failure mode but the spot weld strength is decreased at the same time.

### 1.2.1.2 Welding process effect

The geometrical parameters of weld assemblies are known to directly influence their mechanical response. Among these parameters, the weld nugget diameter and the corresponding sheet thickness are among the most important and strongly affect the mechanical behaviour of spot welds. Numerous authors use them directly to express the spot weld strength like [JON 81], [SAK 03], [POU 07], [SUN 08], and [HER 08].

Many authors observed the intensity current influence on the nugget diameter. Pouranvari and al. [POU 07] and Hayat [HAY 10] state that increasing weld current and weld time increase weld nugget diameter (figure 1.20.a). However, they also observed the weld nugget diameter remains constant for higher welding current and welding time. Hernandez and al. [HER 08] also show the effect of increasing current on weld size on three similar and dissimilar welding configurations of DP600 and DP780 (figure 1.20.b). In high current intensities, the nugget diameter tends to a maximal diameter.

As shown by Sakuma and al. [SAK 03], Pouranvari and al. [POU 07], Sun and al. [SUN 08] and many other authors, the nugget diameter is the main parameter influencing the spot weld strength, regardless if a cross tension test or a tensile shear test is performed. Pouranvari and al. [POU 07] and Sun and al. [SUN 08] worked on tensile shear test. While Pouranvari and al. [POU 07] stated that nugget size is the most important controlling parameter determining stress distribution in the weld nugget interface and its circumference, Sun and al. [SUN 08] observed that welds of DP800 and TRIP800 steels with larger fusion zone size typically generate higher peak loads and energy absorption levels. Sakuma and al. [SAK 03] observed the performance of similar welding of two different grades varying their thickness. In addition to studying tensile shear performance, they also studied the cross tension test. Indeed, the weld performances were highly dependent



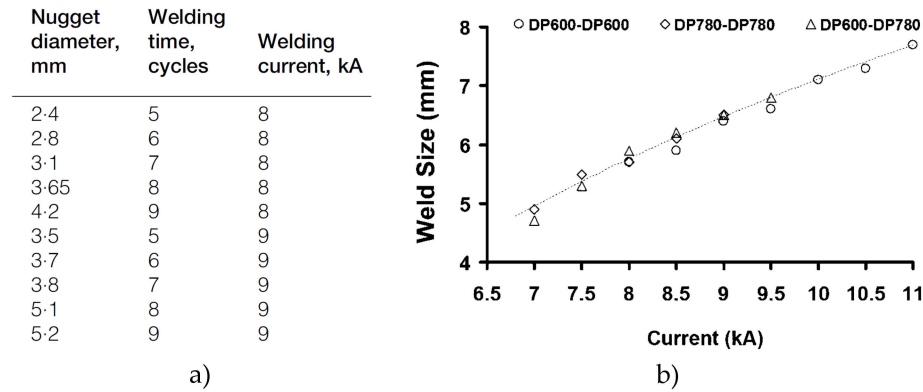


Figure 1.20: Welding parameters influence on nugget size: a) Intensity current and holding time effect on nugget diameter according to Pouranvari and al. [POU 07] and b) Intensity current effect on nugget diameter of similar and dissimilar DP spot welds according to Hernandez and al. [HER 08].

on the fusion zone size as shown in figure 1.21.b.

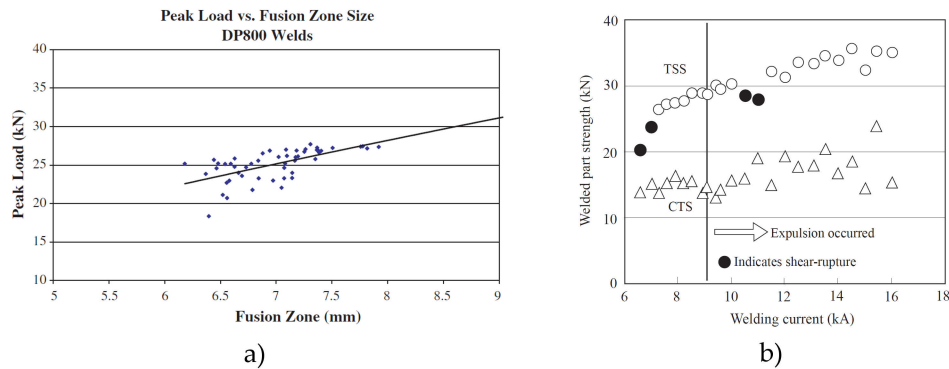


Figure 1.21: Nugget size influence on spot weld performance: a) Lap shear peak load versus fusion zone size for DP800 welds according to Sun and al. [SUN 08]. b) Changes in spot weld strength due to welding current of 780 MPa cold-rolled steel sheet according to Sakuma and al. [SAK 03].

Nugget size directly controlling the spot weld performance, many authors used numerical modelling to simulate the welding process and predict the nugget shape and size. Luo and al. [LUO 09] performed a regression modelling and process analysis of resistance spot welding to evaluate the influential parameters on nugget formation. They concluded that the welding process effects on nugget size are not linear and it is important to pay more attention to process variables in order to obtain the best spot weld design. In this context, Sriunwong and al. [SRI 03] [SRI 05], Eisazadeh and al. [EIS 10], Shen and al. [SHE 10] and Moshayedi and al. [MOS 12] proposed coupled thermal-electro-mechanical Finite Element (FE) models for predicting temperature distribution and spot nugget size in a spot welded steel joint. Sriunwong and al. [SRI 03] established a robust FE modelling procedure which allows to understand the effect of welding parameters on nugget



formation in the case of two and three sheets assembly (figure 1.22). Eisazadeh and al. [EIS 10] and Moshayedi and al. [MOS 12] observed that when the welding time increases, temperature of the faying surface of sheets rises quickly until this area is melted and the nugget is formed, as also described by Krajcarz and al. [KRA 10]. Moreover, Eisazadeh and al. [EIS 10] also stated that increasing the load on the electrodes decreases the nugget size because it increases the contact surface area. Shen and al. [SHE 10] used a coupled thermal-electro-mechanical FE model to study the influence of initial gap between DP600 steel sheets on nugget formation and expulsion. They found that increasing initial gap spacing quickly rises the temperature of sheets and the weld nugget can form earlier.

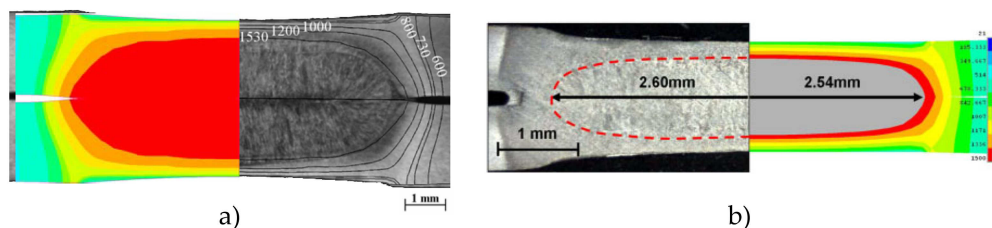


Figure 1.22: Nugget size prediction compared to experiments using FE modelling according to: a) Srikunwong and al. [SRI 05] and b) Shen and al. [SHE 10].

In addition to the tempering in the SCHAZ presented previously, some authors also insist on the role of steel microstructure in the spot weld zones like Tweed and al. [TWE 87], Gould and al. [GOU 98], Lambert-Perlade and al. [LAM 04b] [LAM 04a] Hernandez and al. [HER 08], Pouranvari and al. [POU 09], Dancette and al. [DAN 11b], Krajcarz and al. [KRA 13] and Alizadeh and al. [ALI 14].

During the welding process, the fusion zone is solidified very quickly creating a particular equiaxed microstructure in the nugget. Alizadeh and al. [ALI 14] observed that presence of martensite and  $\delta$ -ferrite in the nugget of martensitic stainless steel spot welds leads to interfacial failure. Krajcarz and al. [KRA 13] also observed interfacial failures in the nugget, but related it to the high number density of particles originating from rapid solidification facilitating the crack initiation in the nugget.

Hernandez and al. [HER 08] and Pouranvari and al. [POU 09] focused on the fusion zone in the case of dissimilar welding of two steel grades, where the two steel sheets are diluted. They observed that hardness difference between HAZ and fusion zone added to the nugget solidification orientation could lead to interfacial failures. Dancette and al. [DAN 11b] observed that the decrease in cooling rate after electrodes removal is expected to favour an auto-tempering of the martensite in formation.

Some authors focused on the micromechanics of encountered phases in spot welds such as martensite and bainite. Tweed and al. [TWE 87] studied the micromechanisms of the failure in C-Mn weld joints and developed a model for cleavage. Lambert-Perlade and al. [LAM 04b] also observed and modelled the micromechanisms of cleavage in high strength low alloy (HSLA) steel HAZ. Gourgues [GOU 03] focused on the relationship between microstructure and cleavage crack propagation, highlighting the role of former austenite grain size in the crack propagation.

## 1.2.2 Mechanical behaviour of homogeneous AHSS spot welds

### 1.2.2.1 Failure mode mechanism

Failure mode and strength are two significant characteristics of spot weld behaviour. For a mechanical test, these two characteristics are almost systematically used to define the weldability of a steel. TSS and CTS tests are widely used in the automotive industry (in laboratory). In the first one, the interface between the two steel sheets is subjected to shear and stress triaxiality in the notch root is relatively low. On the contrary, in the second one, stress triaxiality is very high because the notch root is loaded in opening mode. Many authors were interested in failure mechanism understanding of spot welds [ZUN 97], [LIN 02], [CHA 03a], [LAN 04], [LEE 05a], [MAH 07] and [LEE 05b] in particular to propose a model for predicting the failure strength.

When the nugget diameter is high enough, the important resultant load at weld centre induces a pull out failure mode by ductile failure in the sheet thickness around the nugget. This case is observed by Zuniga and Sheppard [ZUN 97] during peel test on HSLA steel, by Chao [CHA 03a] and Lee [LEE 05a], or by Lin [LIN 02]. It is also observed by Langrand [LAN 04] and Mahelle [MAH 07] for complex loads, but with a dominating normal load.

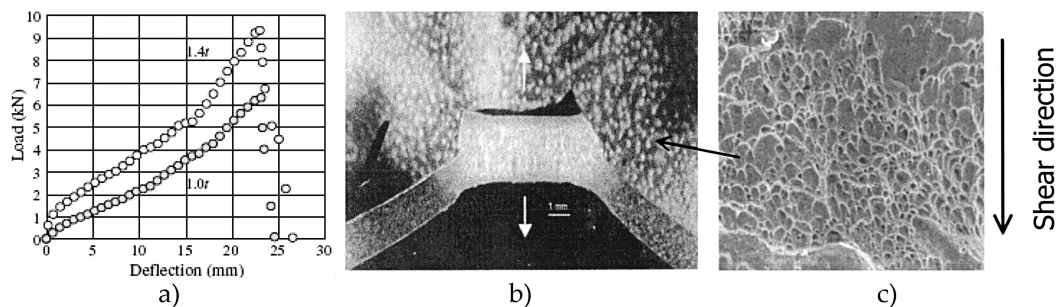


Figure 1.23: Cross tension test: a) Load-deflection curves according to [LEE 05a], b) Pull-Out in the nugget border and c) the corresponding ductile sheared fracture surface according to [CHA 03a].

Ductile sheared surfaces illustrated in figure 1.23 are typical of the button pull out failure mode. Zuniga [ZUN 97] observes that the exact location of pull out is between the Fine Grain HAZ (FGHAZ) and the molten nugget border. He also observes that crack propagation along the thickness occurs just before reaching the maximal strength (figure 1.23.a).

However, when the dominating load is tangential in the spot weld, like in the tensile shear tests, the failure is generally located in the base material with huge plastic strain (necking) or in the HAZ with ductile surfaces (figure 1.24). In this case, the maximal strength is obtained when failure is initiated in the necking zone. The progressive loss of strength corresponds to steel sheet tearing around spot weld (figure 1.24.a).

Interfacial failure mode (FIF) generally appears when nugget diameters are small or when steel sheet are thick. This failure mode could be obtained during the two types of test (CTS and TSS). In the case of CTS test (or peel test), the interfacial failure occurs by opening of notch root and propagation in the nugget. However, during TSS tests, failure occurs by shearing of the interface by tangential load. Williams and Jones

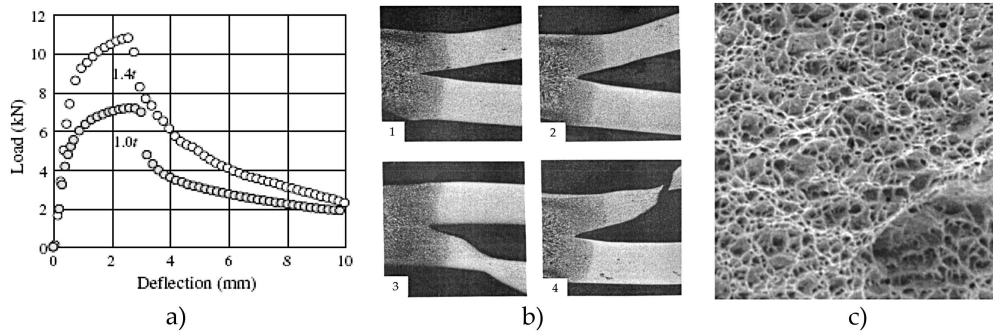


Figure 1.24: Tensile shear test: a) Load-deflection curves according to [LEE 05a], b) Pull-Out in the base material according to [ZUN 97] and c) ductile fracture surface according to [CHA 03a].

[WIL 79] affirm that interfacial failure should not be associated to brittle failure, even if brittle failure is often observed in the notch root because of martensite with high carbon content and opening mode. They observed ductile fracture surfaces in the case of ferritic steel spot weld testing. Moreover, Pouranvari [POU 07], Tao [TAO 08] and Dancette and al. [DAN 11a] also observe sheared ductile fracture surfaces after tensile shear tests and interfacial failure (figure 1.25).

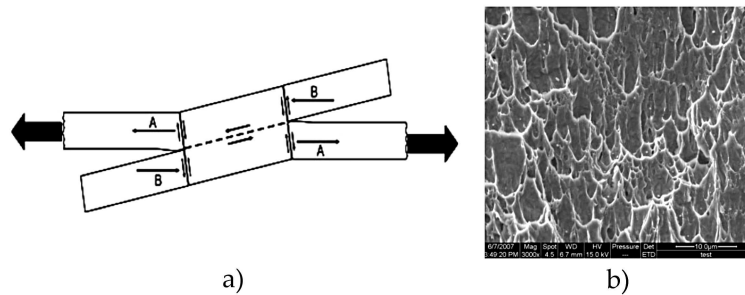


Figure 1.25: Interfacial failure during TSS test: a) Schematic stress dispersion in the spot weld according to [POU 07], b) Pull-Out in the base material according to [TAO 08].

Nevertheless, there is a transition mode between the two previous failure modes: partial interfacial failure (PIF). It occurs in particular for AHSS (dual phase steel (DP) or TRIP) during cross tension tests. However, as observed by Khan and al. [KHA 08], PIF could also occur during tensile shear tests. Dancette and al. [DAN 11a] characterized the damage sequence of AHSS spot welds in cross tension, and observed PIF on DP980 spot welds (figure 1.26.a). They identified two main mechanisms in the nugget: (i) ductile shear around the weld from the notch tip and (ii) semi-brittle fracture in the weld nugget, starting at the faying surface. Nait-Oultit and al. [NAI 08] mentioned two potential mechanisms to explain the crack deviation of PIF:

- micro segregation effect around the weld and in the columnar grains of the fusion zone,
- microstructural barriers in the fine grain zone around nugget due to high grain boundaries density.

For ten years, many study focuses on the tensile shear test of AHSS like Choi and

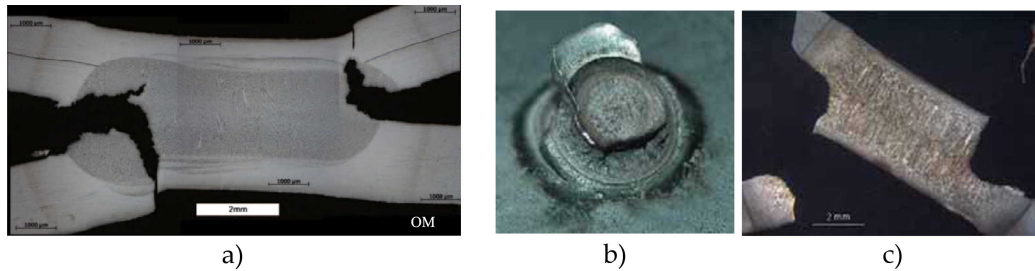


Figure 1.26: Partial Interfacial failure: a) micrograph of DP980 spot welds in cross tension according to Dancette and al. [DAN 11a], b) macroscopic visual aspect and c) micrograph of final failure occurred both in the weld nugget and the base metal (M800GI 2.0 mm) according to Bouzekri and al. [BOU 10].

al. [CHO 10], Bouzekri and al. [BOU 10], Jong and al. [JON 11], Pouranvari and al. [POU 11] [POU 12], Dancette and al. [DAN 12], Abadi and al. [ABA 14], Spena and al. [RUS 15] and Wang and al. [WAN 16].

The transition between button pull out failure and full interfacial failure mode of DP weld joints was studied a lot. Abadi and al. [ABA 14] observed that the higher the DP steel grade is, the larger the nugget diameter should be to obtain button pull out mode. Pouranvari and al. [POU 12] showed that increasing the fusion zone size allows to obtain pull out failure mode on DP980. Dancette and al. [DAN 12] and Spena and al. [RUS 15] observed that tensile shear strengths of spot welds increase with the welding current until expulsion occurs and reduce strengths.

However, for Peterson [PET 02] and Bouzekri and al. [BOU 10], the failure mode has no particular effect on the failure strength, even if the energy absorbed is clearly lower in the case of interfacial failure mode. Sun and al. [SUN 06] [SUN 08] observed the same phenomenon in cross tension, but spot welds that failed in button pull out mode showed a performance 10% higher than in interfacial failure during tensile shear tests.

Indeed, the welding of AHSS is sensitive to the base material chemical composition and strength. The higher the strength of the base material and the more highly alloyed the chemical composition, the higher the scattering in the transition between BPO and FIF. A large carbon content induces tempering in the sub critical HAZ and then softening of weld joint. Other elements like sulphur induces segregation in the nugget and its border. These phenomena conduct to a complex mix of failure modes such as partial interfacial failure or partial dome failure.

### 1.2.2.2 Improvement of fracture behaviour

In the automotive industry, interfacial failures are usually considered as brittle and low strength. Some authors focused on improving the failure modes of spot weld by modifying the process or using pre- and post-treatment on spot welds. Peterson [PET 96] [PET 02], Cretteur and al. [CRE 02], Chuko and al. [CHU 02], Mimer and al. [MIM 04], Liao and al. [LIA 10] and Chabok and al. [CHA 17] worked on metallurgical Post-Weld Heat Treatment (PWHT) to improve weld joints performance or promote button pull out failure mode.

Mimer and al. [MIM 04] includes an in-process martensite tempering to reduce weld hardness and prevent interfacial failure. Chuko and al. [CHU 02] defined a post weld tempering incorporated to the welding cycle to improve behaviour of C-Mn resistance spot welds. Using lower currents and longer (30-35 cycles) tempering times provides the most robust tempering response to reduce hardness. Liao and al. [LIA 10] characterized the microstructures in the fusion zone of DP600 dual phase steel after resistance spot welding with tempering-pulse technology using optical microscopy, SEM and TEM.

Cretteur and al. [CRE 02] proposed a complete optimized welding process including pre and post-heating parameters. With this optimised cycle, the interface between both sheets and the heat affected zone (HAZ) are free of cracks and no brittle fractures are observed on TRIP700 spot welds. Chabok and al. [CHA 17] observed the effect of a double pulse welding on the microstructure of DP1000 spot welds. They improved the cross tension strength by 30% and the absorbed energy.

Peterson [PET 02] focused on the dilution in fusion zone by adding a thin low alloyed steel sheet at the interface, eliminating the interfacial failure but modifying the weld strength.

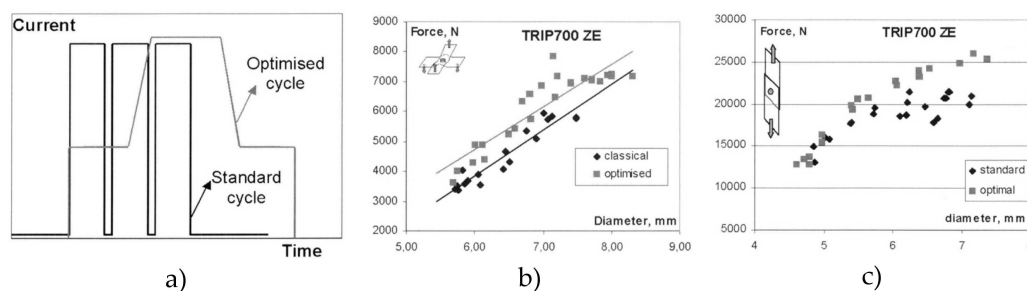


Figure 1.27: Improvement of weldability of TRIP steels by use of in-situ pre and post-heat treatments according to Cretteur and al. [CRE 02]: a) optimised welding cycle comparison with standard welding cycle, b) CTS improvement and c) TSS improvement.

Some authors used shorter time heat treatments to desegregate the weld like Sawanishi and al. [SAW 14] and Van der Aa and al. [AA 15]. Sawanishi and al. [SAW 14] improved the strength of DP980 spot welds and changed the fracture mode from partial interfacial to button pull out. The joints were then observed in situ during tear tests and the pulsed current was effective in improving the ductility of the nuggets. Then EPMA of the nugget demonstrated that the segregation of phosphorus was prevented in the joint welded with the pulsed current. Van der Aa and al. [AA 15] also studied DP980 spot weld assemblies. They proposed a method to predict phase transformations and elemental segregation during resistance spot welding. Firstly, they identified Phosphorus segregation as the most problematic factor for weld strength. Thanks to FE model, a double pulse weld leads to significant improvement of behaviour and strength during cross tension test, compared to spot welds made with standard single pulse.

### 1.2.3 Mechanical behaviour of heterogeneous AHSS spot welds

In the vehicle weight reducing policy, carmakers optimize the car body using many steel grades. This is why many authors are interested in the dissimilar welding of these grades.

Heterogeneous welding induces particularities of the spot weld in two aspects: the first is the nugget geometry which is no longer symmetric depending on the heterogeneity degree, and the second is in particular in the metallurgy of the nugget due to dilution.

Many authors observed the positive effect of dilution in the nugget like, Hernandez and al. [HER 08], Biro and al. [BIR 12] and Zhang and al. [ZHA 14]. Hernandez and al. [HER 08] compared the homogeneous welding configurations of DP600 and DP780 to their heterogeneous one. For similar nugget diameter, a pull out failure mode was generally observed in dissimilar welds with DP600 paired to other AHSS compared to an interfacial failure mode for DP600 welded to itself. They also observed that the transition weld diameter was lower for dissimilar configuration. Biro and al. [BIR 12] observed the same positive effect during the cross tension test on DP980 and TRIP800 spot welds. They stated that thermal effect and notch root location could explain a part of the positive deviation but the main reason is geometrical (mechanical).

Moreover, some authors showed that the positive effect mainly comes from the nugget preferentially shifting into one of the two sheets. This shifting could come from two reasons:

- the steel sheets grade are close but their thicknesses are very different,
- the sheet thicknesses are the same but chemical compositions of steels are highly different (thermal conductivity).

Hernandez and al. [HER 08], Marashi and al. [MAR 10], Pouranvari and al. [POU 10a], Huin and al. [HUI 16] and Yuan and al. [YUA 17] highlighted this sheet thickness influence on spot welds strength in particular during tensile shear tests. Marashi and al. [MAR 10] and Pouranvari and al. [POU 10a] observed that final solidification line moves from sheet/sheet interface to the geometrical centre of the total thickness of the joint with increasing welding time (figure 1.28.a). This reduces the tendency of a dissimilar thickness spot weld to fail in the interfacial failure mode during tensile shear test increasing the TSS. One factor often mentioned to influence the tensile shear strength of dissimilar spot welds is the Ultimate Tensile Strength (UTS) of the thinnest sheet base metal according to Marashi and al. [MAR 10].

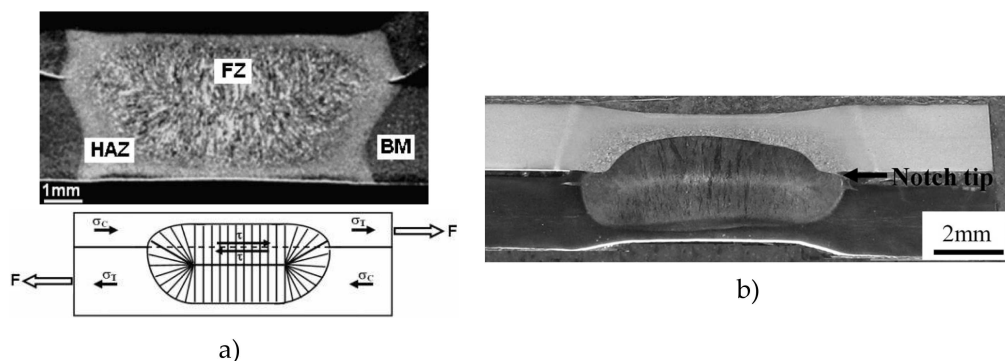


Figure 1.28: Micrographs and sketch of nugget shifting because of: a) sheet thicknesses according to Marashi and al. [MAR 10] and b) steel grades heterogeneity (high difference of thermal conductivities) according to Wei and al. [WEI 16].

Yuan and al. [YUA 17] focused on heterogeneous welding of DP600 steel with a low

carbon ferritic steel with dissimilar thicknesses. Due to the two factors previously enumerated, they showed that no interfacial failure occurred except for low intensity current where dome failure occurred. Failure is shifted to pull out failure in the low carbon ferritic steel. Choi and al. [CHO 11], Liu and al. [LIU 16] also highlighted the nugget shifting in the case of heterogeneous welding. Russo Spena and al. [RUS 16] observed that spot welding of TWIP and Q&P steels promotes the occurrence of an asymmetrical weld nugget with a greater dilution of TWIP steel because of its lower melting temperature and thermal conductivity. Welded samples tend to exhibit higher shear tension strength but failed in dome failure mode for a low welding current.

Wei and al. [WEI 16] focused on the heterogeneous welding of DP1000 steel with TWIP980 steel (high Mn) and observed the hardness and microstructure of the nugget depends on the dilution conducting to a full austenite nugget microstructure in the case of TWIP homogeneous welding and TWIP/DP heterogeneous welding, and to a full martensite in the case of DP homogeneous welding. The decreasing Mn content in the nugget decreases the stability of the austenite conducting to more stacking faults and twins in the case of DP/TWIP welding than TWIP/TWIP, during deformation process. The high content of alloying element could reduce the tensile shear strengths.

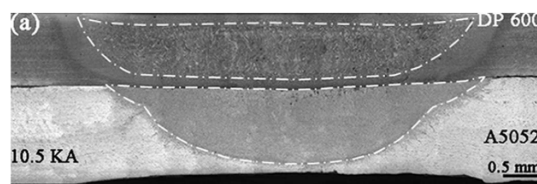


Figure 1.29: Micrograph of A5052 aluminium alloy and DP600 steel spot weld cross section according to Chen and al. [CHE 16].

Chen and al. [CHE 16] observed the ultimate nugget shifting proceeding to the highly heterogeneous welding of A5052 aluminium alloy and DP600 steel. In this case, there was no melting on the two metals, each having its own nugget (figure 1.29). Intermetallic layers formed during the welding process and constitute the weak point of spot welds showing cleavage fracture morphology.

## 1.3 Modelling of spot welded assemblies mechanical behaviour

### 1.3.1 Analytical models

The spot weld failure mode evolution could be described by analytical models involving simple mechanical description. These models are presented in this section for the two loading modes: cross tension and tensile shear.

#### 1.3.1.1 Cross tension model

When button pull out failure mode occurs, the failure strength could be estimated assuming a stress distribution around the spot weld and integrating it on the button lateral surface. During cross tension, the most simple hypothesis consists in assuming a uniform stress distribution (figure 1.30.a). Considering the failure mechanism of button pull out



mode, the cross tension strength could be related to the shear stress ( $\tau$ ). This description was adopted by many authors: Smith [SMI 80], Sakuma and al. [SAK 03], Chao [CHA 03b] [CHA 03a], Kuo and al. [KUO 04] and Sun and al. [SUN 06]. They established direct relations between the cross tension strength and the lateral surface of button ( $A_f$ ):

$$CTS_{BP} = A_f \cdot \tau \quad (1.4)$$

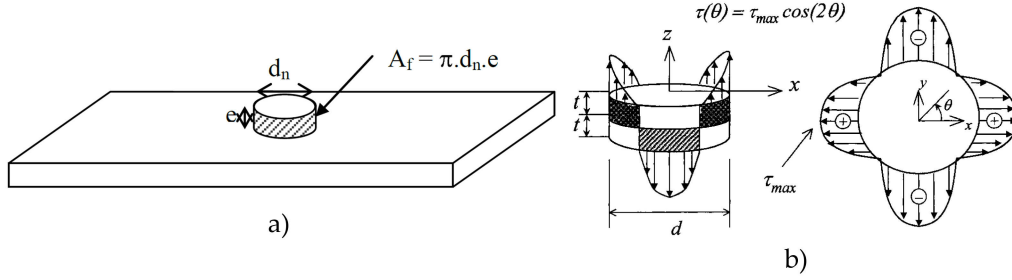


Figure 1.30: Button pull out failure mode: a) Schematic of failure surface  $A_f$  according to Dancette [DAN 09] and b) Stress distribution around button according to Chao [CHA 03b].

The analytical expression could differ following the authors:

- Chao [CHA 03b] [CHA 03a] described  $\tau$  with an angle dependence as shown in figure 1.30.b,
- Sun and al. [SUN 06] used the yield strength (YS) of the HAZ.
- Sakuma and al. [SAK 03] used the base material UTS and an adjusting constant.

However, when full interfacial failure mode occurs, two kind of approaches are used. The first one consists in expressing the strength as a function of the failed surface (with a diameter  $d_n$ ) and steel strength as the button pull out models previously exposed (figure 1.31). Kuo and al. [KUO 04] and Sun and al. [SUN 06] focused on this approach introducing YS ( $Rel_{FZ}$ ) or UTS as critical parameters obtaining this equation for Sun and al. [SUN 06]:

$$CTS_{FIF} = \pi \cdot \left(\frac{d_n}{2}\right)^2 \cdot Rel_{FZ} \quad (1.5)$$

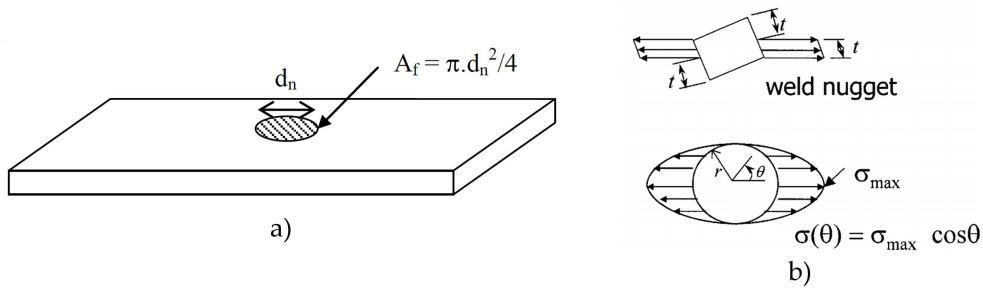


Figure 1.31: Full interfacial failure mode: a) Schematic of failure surface  $A_f$  according to Dancette [DAN 09] and b) Stress distribution around button according to Chao [CHA 03a].



The second approach introduces the linear elastic fracture mechanic to estimate the brutal crack initiation from the notch root. Smith [SMI 80] and Chao [CHA 03b] estimate the mode I stress intensity factor ( $K_{Ic}$ ) in the notch root of spot weld from Tada and al. [TAD 85] formulation (figure 1.32). They expressed the cross tension strength when interfacial failure occurred by:

$$CTS_{FIF} = 1.25 \cdot K_{Ic} \cdot \left(\frac{d_n}{2}\right)^{5/2} \quad (1.6)$$

where  $K_{Ic}$  is the mode I stress intensity factor to the fusion zone toughness. All authors agreed to link the cross tension strength of spot weld to the nugget diameter. Using the strength formulations for the two failure modes, Chao [CHA 03b] defined a critical nugget diameter describing the failure mode transition (figure 1.32.b).

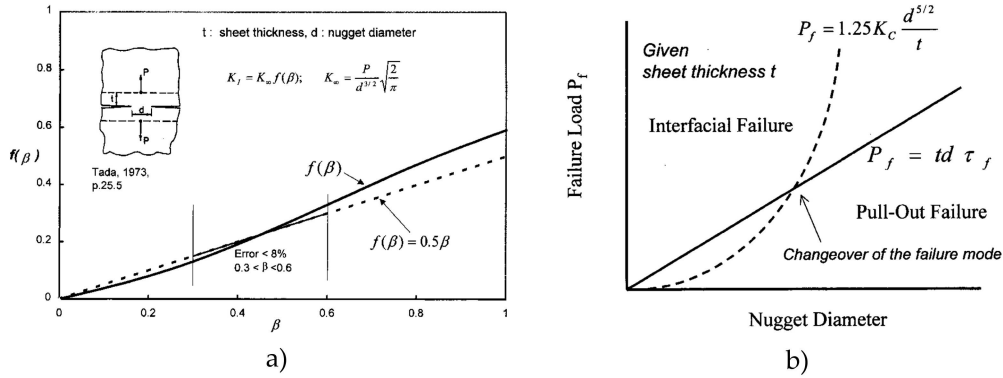


Figure 1.32: a) Mode I stress intensity factor in a spot weld notch root and b) critical nugget diameter for failure mode transition according to Chao [CHA 03a].

### 1.3.1.2 Tensile shear model

The model developed for cross tension tests are reproduced for tensile shear tests to estimate the spot weld strength. As before, an approach based on the failed surface for the button pull out failure mode was assumed by Sakuma and al [SAK 03], Chao [CHA 03a], Kuo and al. [KUO 04] and Pouranvari and al. [POU 07] conducting to the following expression:

$$TSS_{BP} = \alpha \cdot e \cdot d_n \cdot R_{BM} \quad (1.7)$$

where  $e$  and  $d_n$  are respectively sheet thickness and nugget diameter,  $R_{BM}$  is the UTS of the base material and  $\alpha$  is an adjusting parameter.

Similarly, for interfacial failure, Sakuma and al. [SAK 03], Kuo and al. [KUO 04] and Satonaka and al. [SAT 04] expressed the tensile shear strength as:

$$TSS_{IF} = \gamma \cdot \pi \cdot \left(\frac{d_n}{2}\right)^2 \cdot R_{FZ} \quad (1.8)$$

where  $d_n$  is the nugget diameter,  $R_{FZ}$  is the UTS of the fusion zone and  $\gamma$  is a adjusting parameter.

Sevim and al. [SEV 06] chose the linear elastic mechanic approach using this time the mode II stress intensity factor because of the loading mode.

Since the applied load on the spot weld is not that easy to identify during cross tension and tensile shear tests, some authors were interested on the spot weld behaviour under mixed lads. Chao [CHA 03a], Lin and al. [LIN 02] [LIN 03] and Langrand and al. [LAN 04] focused on the relation between the stress state and failure criterion.

### 1.3.2 Finite element models

As the automotive industry uses more and more alloyed steel with high strength (AHSS), analytical models are not sufficient any more to describe spot weld behaviour. Furthermore, heterogeneous welding complexifies the analytical approach because of the different HAZ created. To better describe the mechanical behaviour of spot weld, some authors decided to use a Finite Element (FE) modelling approach. Fine spot weld behaviour models were built in order to understand the mechanisms and to provide criterion for developing a simplified model to predict the failure behaviour of spot weld in body in white structures (essentially for crash application modelling).

#### 1.3.2.1 Homogeneous spot weld modelling

Deng and al. [DEN 00], Abid and al. [ADI 04], Xu and al. [XU 14] and Nielsen and al. [NIE 15] studied the stress distribution in the spot weld using FE modelling with 3D elements. They mainly focused on the tensile shear test of spot welds, even if Deng and al. [DEN 00] also studied spot weld behaviour during peel test. During peel test, Deng and al. [DEN 00] stated that applying an elastic loading leads to a linear distribution of the S11 stress (normal stress to the interface between nugget and base material at the notch root) in the sheet thickness where neutral fibre is the symmetry. They observed that the bending stress state is dominant in the notch root zone and the nugget centre is stress free.

Indeed, during the tensile shear test, Deng and al. [DEN 00], Abid and al. [ADI 04], Xu and al. [XU 14] and Nielsen and al. [NIE 15] observed the S11 stress presents a singularity at the notch root and its distribution in the sheet thickness suggests a combined bending and tension stress state (figure 1.33). Deng and al. [DEN 00] also observed that S13 (shear component favouring the interface shearing) becomes predominant when the nugget diameter decreases. Xu and al. [XU 14] identified four preferential angles where yielding could initiate. They also stated that stress distribution along nugget could be useful for determining the stress intensity factor (SIF).

The notch root of spot weld is inherently a zone containing stress singularities. It plays the main role during static tests in the crack initiation. Some authors decided to characterize these singularities using the stress intensity factor (SIF) firstly introduced by Pook [POO 75] [POO 79]. Supported by FE modelling, Zhang and al. [ZHA 99], Bouafia and al. [BOU 09] and Sadasue and al. [SAD 16] studied the evolution of SIF in the three modes (I, II and III). They observed the mode I is dominant in cross tension whereas the

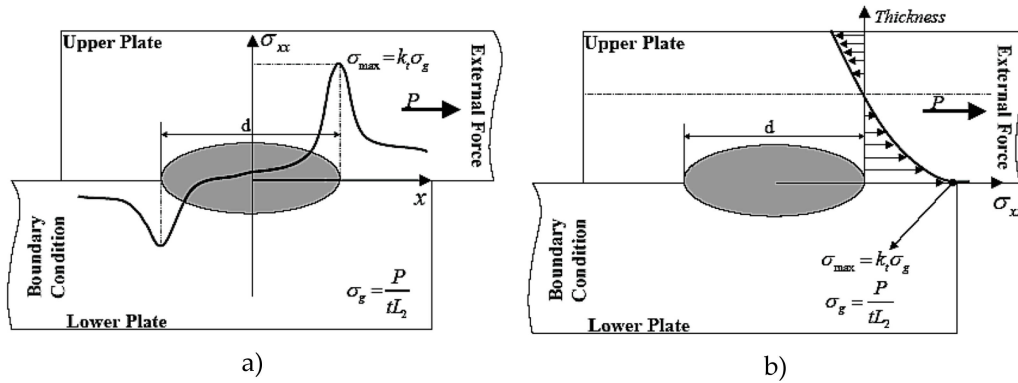


Figure 1.33: Stress distribution during tensile shear test according to Abid and al. [ADI 04]: a) S11 stress singularity at the notch root and b) S11 stress distribution in the sheet thickness.

mode II is dominant in tensile shear.

#### a. Heat Affected Zones (HAZ) discretization

Beyond the elastic plastic behaviour of spot weld assembly (stress distribution in the weld), many authors interested to the complete numerical prediction of spot weld strength under different loading. Radakovic and al. [RAD 08] used a very simple approach consisting in modelling the whole spot weld like a homogeneous part with properties based on a experimental test on base material. This approach is only efficient if button pull out mode is studied, but not for other spot weld behaviours. Yang and al. [YAN 08] used a fine discretization of the heat affected zones based on a hardness map performed on the spot weld cross section (figure 1.34.a). Elastic plastic constitutive laws of the different zones were established based on a standard convention table, the hardness can approximately be converted into the tensile strength. Dancette and al. [DAN 11b] and Mahelle and al. [MAH 07] showed that the HAZ constitutive laws could be obtained by thermal mechanical simulation process using Gleeble machine to reproduce the welding thermal cycle on standard tensile samples.

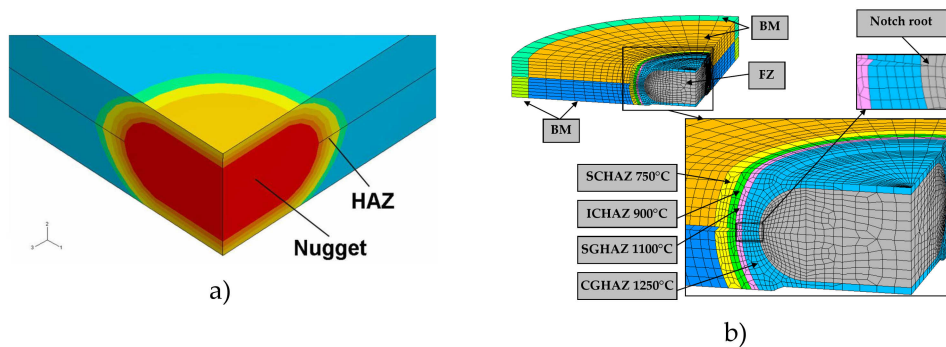


Figure 1.34: Discretization in many zones of the spot weld: a) according to Yang and al. [YAN 08] and b) according to Mahelle and al. [MAH 07].

#### b. Failure strain criterion

To complete their model, Yang and al. [YAN 08] introduced a failure strain criterion to describe the cross tension strength when button pull out mode occurs. Dancette and al. [DAN 12] also introduced a failure strain for each zone of their model, but corrected the ductile damage failure criterion with a damage evolution based on the measurement of effective plastic displacement at fracture of tensile test samples. Song and al. [SON 11] proposed a failure criterion based on the axial and shear loads applied on the spot weld with a calibrating factor  $\beta$  which is different depending on the steel grade. This failure criterion provides a relatively good description of the failure load in the case of button pull out failure.

Chung and al. [CHU 16] used a failure strain criterion but introduced the triaxiality dependence. Numerical inverse method on tensile tests was used to calibrate the constitutive laws of the different zones as well as the failure criteria. A Stress-triaxiality dependent effective fracture strain was proposed depending on the toughness of each zone (ductile or brittle). There was a reasonable degree of agreement between the experimental results and the simulations for the failure modes and strengths of weld joints of the three steel grades tested.

### **c. Void volume fraction failure criterion**

These simple failure criteria provide good correlation of the load-displacement response in the case of button pull out failure, however, in AHSS spot welding, interfacial failures occur and need to be predicted. Many authors understood that the critical point of spot weld modelling is the stress triaxiality consideration in the ductile damage criterion because of singularities in the notch root. Borhana and al. [BOR 12] and Kosnan and al. [KOS 14] used a Rice and Tracey description [RIC 69] for their different zone constitutive laws. The law parameters are identified on the base material and extended to HAZ and fusion zone based on scaling of hardness. They obtained a good agreement on the load-displacement curve when spot weld failed in button pull out mode (in tensile shear for Bohrana and in cross tension for Kosnan). Kong and al. [KON 08] used a Gurson [GUR 77] model taking the existence of voids into account indirectly through their average diameter value to better describe the plastic flow of low carbon steel during tensile shear test. The Gurson ductile damage model parameters were identified by inverse method of tensile test on the base material. Lamouroux and al. [LAM 07] also used a Gurson ductile damage model but introduced the evolution of Tvergaard and Needleman [TVE 84] to better describe damage evolution of the steel (GTN-model). Using an inverse method for parameter identification, Lamouroux and al. [LAM 07] obtained a good agreement of load-displacement curves during tensile shear, lap shear and coach peel tests on several configurations with different thicknesses. However, no comparison between experiments and simulation on the failure modes is presented.

Some authors were interested in predicting the failure mode transition from interfacial failure to button pull out when the nugget diameter increases. Sommer [SOM 10] introduced three damage criteria in parallel to described the DP600 spot weld behaviour during tensile shear tests. The spot weld zone constitutive laws were adapted with a Gologanu Leblond Devaux (GLD) model [GOL 97] (improvement of Gurson model for non spherical void) and the combined fracture criteria of Thomason and Embury and critical shear stress. The main advantage of this model is the Embury description of the shear at the inter-

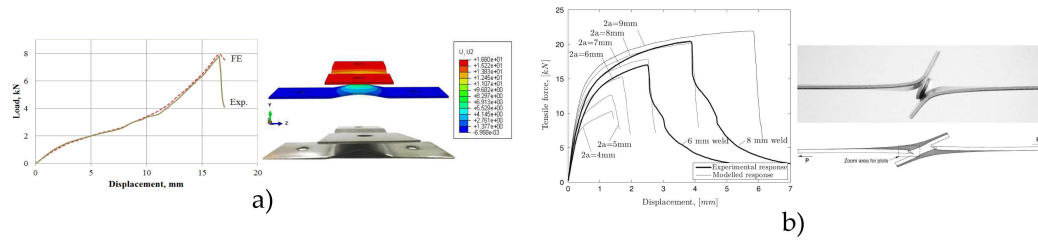


Figure 1.35: Comparison between experiments and simulation of load-displacement response and failure mode: a) cross tension according to Kosnan and al. [KOS 14] and b) tensile shear according to Nielsen [NIE 08].

face and the GLD-model which allows to describe interfacial failure. However, the model cannot describe partial interfacial failure. Nielsen [NIE 08] [NIE 10] also expanded the GTN-model to the GLD-model and concluded the GLD-model gives later drop in the load carrying capacity, which is due to a dependency on the void shape for the void growth rate.

#### d. Cohesive zones implementation

The mechanisms of interfacial failure of AHSS spot weld in cross tension are mainly brittle, usually presenting cleavage. Some authors chose to introduce cohesive zone behaviour to better describe these mechanisms (generally used to define interface under the three crack propagation modes (modes I, II and III)). The behaviour is usually described by a traction-separation law where the area under the curve corresponds to the interface toughness (figure 1.36.a).

Cavalli and al. [CAV 05] were the first to use the cohesive element approach in a mechanical FE modelling of aluminium spot weld behaviour. They identified mode I cohesive parameters on coach peel test failing in interfacial failure mode whereas mode II and III cohesive parameters were identified thanks to spot weld failing in the interfacial mode during tensile shear test. Then, cohesive parameters are validated on peel test.

Dancette [DAN 09] [DAN 12] also used cohesive zone to predict the interfacial failure of TRIP780 steel spot welds during cross tension. The model allows to capture the competition between semi-brittle fracture at the interface and ductile failure by button pull out at the weld boundary (figures 1.36.b and 1.36.c). The cohesive elements calibration was done by inverse method on spot weld load-displacement response.

Dang [DAN 15] also introduced cohesive elements at the sheets interface to predict interfacial failures.

Lacroix and al. [LAC 15] developed an in-situ methodology using the wedge test to observe the crack propagation in the nugget when interfacial failure occurs. Their FE model allows to estimate relevant values for the fracture energy and the fracture stress (fusion zone toughness) even if the maximum load of spot weld is overestimated.

#### 1.3.2.2 Heterogeneous spot weld modelling

Heterogeneous spot weld modelling is not common, only a few authors studied the subject in the past years. The main reason comes from the difficulties induced by the heterogeneity in the composition and mechanical properties. First, the nugget shifting involves very

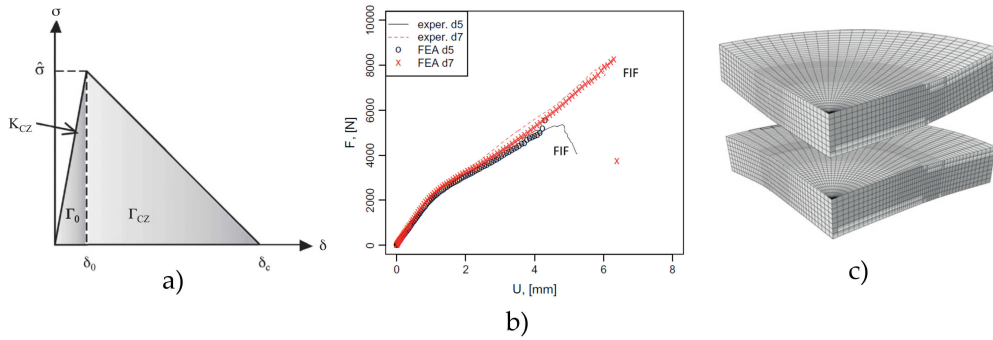


Figure 1.36: Cohesive zones in spot weld modelling according to Dancette and al. [DAN 12]: a) Bilinear mode I cohesive zone model at the faying surface, b) load-displacement curves and c) failure type for the homogeneous 1.5 mm weld assembly.

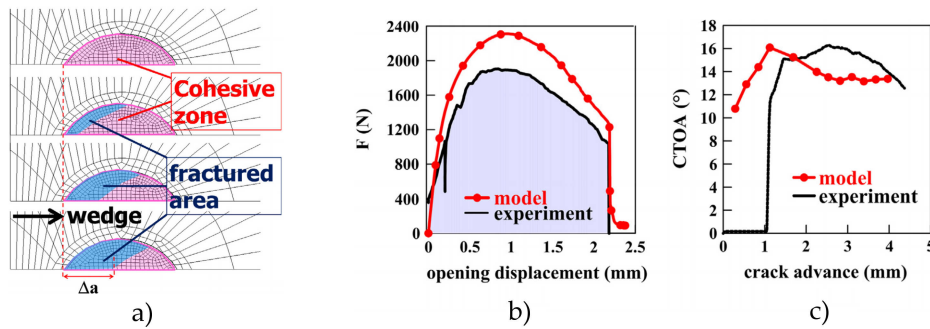


Figure 1.37: Model of crack propagation in DP600GI spot weld according to Lacroix and al. [LAC 15]: a) Crack front and fractured area at different stages of the wedge indentation, b) comparison of experimental results and simulation, load (F) and crack advance vs. wedge displacement, c) load (F) and crack opening angle (CTOA) vs. crack advance.

particular geometries for HAZ and fusion zone which need to be finely described in order to well predict the spot weld behaviour. Secondly, the fusion zone being a mixture of the two different steel sheets, its constitutive law is not easy to establish. The resultant behaviour of the nugget is significantly different from the two base materials. The fusion zone size and its particular equiaxed solidification makes the identification of its behaviour by direct testing difficult. Moreover, additional zones (for the two steel sheets) need to be mechanically characterized, which represents a larger amount of work.

Long and al. [LON 16] studied the welding of 1.5 mm DP600 steel with a 1.2 mm low carbon steel and the tensile shear response of the spot weld. The material properties of base metals are measured thanks to tensile tests. The strength properties of the weld nugget and of the different heat affect zones are estimated by extrapolation of the hardness values compared to the base material. The peak load and failure mode of weld joint depend on the resistance force generated by the failure zone. No failure criterion was introduced, and failure zone was considered as the necking zone. Finally, the model is in good agreement with the experimental elastic plastic response of the spot weld (figure 1.38).

Burget and Sommer [BUR 13] modelled the spot weld assembly of a 1.0 mm 22MnB5

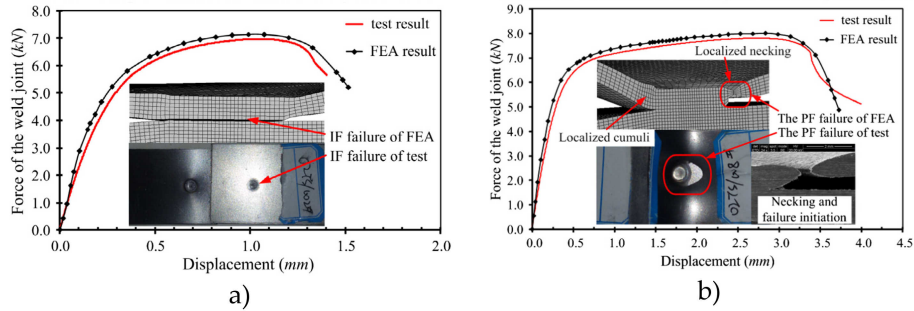


Figure 1.38: Model of DP600 steel and low carbon steel heterogeneous spot weld under tensile shear load according to Long and al. [LON 16], comparative result of load versus displacement and failure mode: a) interfacial failure, b) button pull out failure.

press hardened steel (1500 MPa) with a 1.5 mm micro alloyed high strength low-alloyed steel (HC340LAD, 415 MPa). They used an inverse method on three particular test specimens (smooth and notched tensile and double notched shear) to calibrate Gologanu material models and adjust a Thomason-Brown-Embury failure criterion for the different material zones of the weld. The spot weld discretization and the different mechanical tests modelled are presented in figure 1.39.

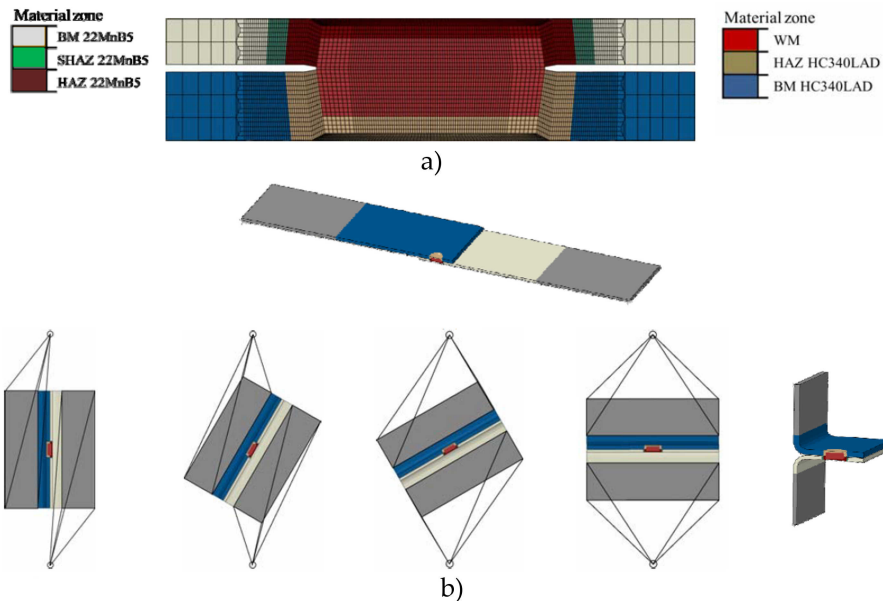


Figure 1.39: Model of 22MnB5 press hardened steel and micro alloyed high strength low-alloy steel heterogeneous spot weld according to Burget and Sommer [BUR 13]: a) Zone discretization and mesh, b) various loading modes applied.

The model is well predicting the spot weld load response in all the loading modes (figure 1.39.b) except in coach peel test. Focusing on the tensile shear test, the failure load is very well predicted but not the failure mode. When failure initiated in the coarse grain HAZ from the notch root in the experiments, failure initiated in the soft tempered zone of the 22MnB5 in the model. More generally, when Burget and Sommer [BUR 13] model



predicts the failure mode well, a deviation on the failure load is observed and when the failure load corresponds to the experiments, failure mode is not totally well predicted.

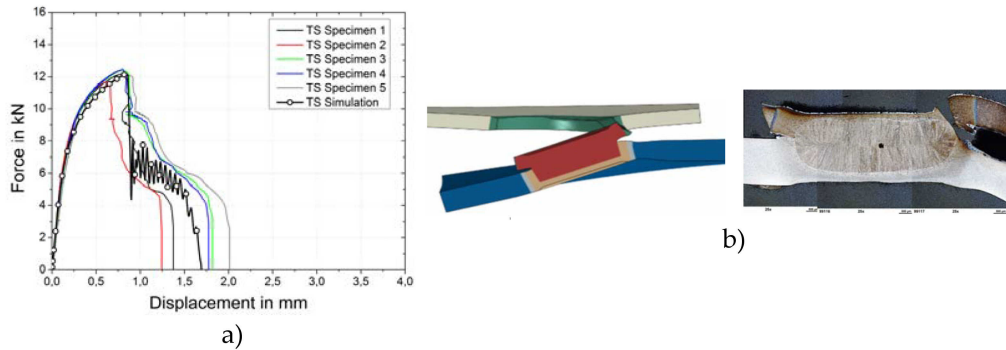


Figure 1.40: Model of 22MnB5 press hardened steel and micro alloyed high strength low-alloy steel heterogeneous spot weld under tensile shear loading according to Burget and Sommer [BUR 13]: a) experimental and simulated load-displacement curves comparison, b) experimental and simulated failure mode comparison.

Noh and al. [NOH 17] used exactly the same methodology than Chung and al. [CHU 16] on two heterogeneous spot weld assemblies:

- 1.6 mm dual phase DP980 steel welded to 1.2 mm TRIP980 steel,
- 1.2 mm GMW2 steel welded to 1.2 mm TRIP980 steel.

Experimental and simulation response of the tensile shear and U-shape tension tests were compared. For tensile shear tests on the two configurations, the spot weld load response in simulation is underestimated compared to the experimental one. However, in U-shape test, the spot weld load response is overestimated and does not really reproduce the elastic plastic behaviour of experimental spot welds (figures 1.41.a and 1.41.b). The failure modes seem to be well reproduced (figures 1.41.c and 1.41.d). Moreover, no interfacial failure are proposed in this study.

## 1.4 Conclusion

Many studies on the AHSS spot weld mechanical behaviour have been carried out. The modelling of button pull out failure mode has been processed by characterizing the critical plastic strain or using a ductile damage model. The introduction of triaxiality stress seems to be necessary observing the complex stress distribution in the spot weld during the different tests. Some authors showed the importance of having a good description of shear behaviour of materials in their ductile damage criterion (triaxiality stress close to 0) because it is often dominant.

However, interfacial failure causes more problems because of its brittleness in opening mode tests (cross tension or peel tests). Analytically, two approaches were used, first consisting to estimate the spot weld strength by the failed surface and the fusion zone strength, and the second introduced crack initiation study using a calculation of the stress intensity factor (SIF) in opening mode (mode I) at the notch root. The second formulation is widely used in the literature to characterize the spot weld fatigue behaviour.



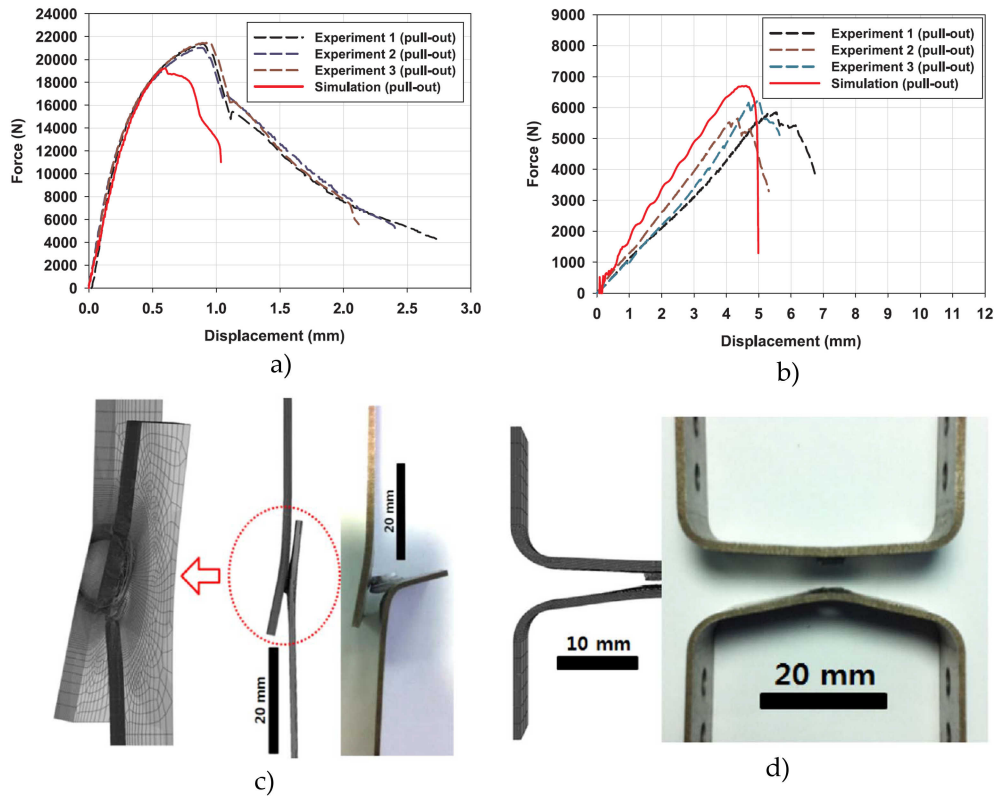


Figure 1.41: Comparison of experimental and simulated of the dissimilar DP980-TRIP980 button pull out failed spot welds according to Noh and al. [NOH 17]: a) failure strength under lap-shear test, b) failure strength under U-shape test, c) failure modes under lap-shear test and d) failure mode under U-shape test.

One more recent modelling approach consists in introducing a cohesive zone at the interface between the sheets to represent the brittle decohesion in the case of interfacial failure. However, few authors used this approach in the case of spot weld modelling, even if this cohesive zone can be used in all simulation types (elastic plastic, non linear, dynamic) and could be coupled to other failure criteria. The potential of this approach is very interesting because it could eventually predict partial failure modes, representing a crack bifurcation contrary to ductile damage models where initiation control the final failure mode.

## Chapter 2

# Experimental results of heterogeneous welding (Usibor1500/DP600)

Chapter 1 introduced the global heterogeneous welding problematic of Automotive High Strength Steels (AHSS). This second chapter focuses on the fine experimental characterization of heterogeneous welding of a martensitic steel (Usibor1500) with a ferrite-martensitic Dual Phase steel (DP600). Two welding processes widely used in the automotive industry are studied namely, resistance spot welding (RSW) and Arc welding. In this chapter, the experimental procedure will be developed and the material properties, weldability of assemblies, microstructure understanding, failure mechanisms related to the different failure modes and the influence of sheet thickness on the spot weld and its failure modes will be treated. Arc welding of Usibor1500 steels will also be addressed.

### Contents

<b>2.1</b>	<b>Materials and welding configurations</b>	<b>40</b>
2.1.1	Materials	40
2.1.2	Welding configurations	41
<b>2.2</b>	<b>Spot weldability</b>	<b>42</b>
<b>2.3</b>	<b>Failure modes</b>	<b>46</b>
2.3.1	Cross tension tests	47
2.3.2	Tensile shear tests	50
<b>2.4</b>	<b>Failure strength</b>	<b>56</b>
2.4.1	Cross tension strength	56
2.4.2	Tensile shear strength	58
<b>2.5</b>	<b>Discussion</b>	<b>60</b>
2.5.1	Liquid metal splash influence on cross tension performance	60
2.5.2	Positive deviation of cross tension failure load with dissimilar thickness	61
2.5.3	Dissimilar thickness effect in tensile shear	63
<b>2.6</b>	<b>Arc welding</b>	<b>63</b>
2.6.1	Configurations	64

2.6.2	Microstructures . . . . .	64
2.6.3	Failure Modes . . . . .	66
2.6.4	Failure strengths . . . . .	67
<b>2.7</b>	<b>Conclusion . . . . .</b>	<b>67</b>

---

## 2.1 Materials and welding configurations

### 2.1.1 Materials

In this chapter, the study focuses on the assembly of the AHSS Usibor1500 with the Dual Phase DP600 in a cold rolled state. The first one, Usibor1500, is used for security and structural parts of body in white (BIW), like door and B-pillar reinforcements. Its mechanical strength is very high (1500 MPa) which allows for a lightening of vehicle structure of 30 % to 50 % compared to conventional cold forming grades while maintaining an important crash performance. Usibor1500 is a hot-stamped steel (22MnB5) which allows to obtain complex geometries exhibiting perfect mechanical properties homogeneity. After heat treatment, the steel is 100 % martensitic (figure 2.1.a) and its tensile strength is around 1500 MPa with a maximal elongation of 6 % (figure 2.2). Usibor1500 is coated with a 25  $\mu\text{m}$  thick Al-Si coating after quenching.

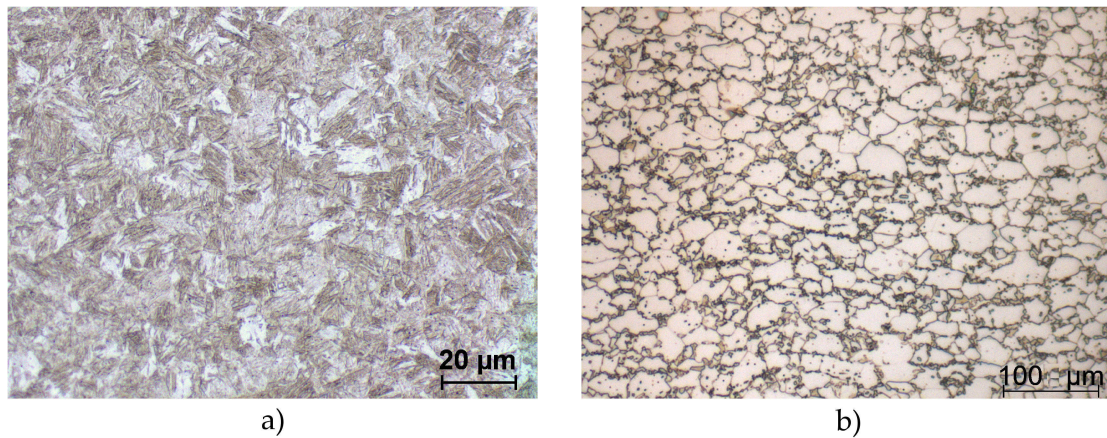


Figure 2.1: Optical view of a) Usibor1500 fully martensitic microstructure and b) DP600 microstructure (ferrite is white phase and martensite is dark phase).

The Dual Phase (DP) steels exhibit a good compromise between strength and drawability. The DP microstructure is composed of two phases: a soft ferritic matrix very ductile, strengthened with a variable quantity of hard phase (often martensite). The association of the two phases provides a very high ductility (so manufacturability), but also good mechanical properties which results in a good fatigue strength and a high energy absorption capability. Thanks to their mechanical properties, DP steels are proper candidates to structural and security parts of BIW. In this study, we will focus on the Dual Phase steel DP600, with an Ultimate Tensile Strength (UTS) of 600 MPa and an elongation around 20 % (figure 2.2). To obtain these mechanical properties, the DP600 microstructure con-

tains 10 % of martensite localized at the ferrite grain boundaries (figure 2.1.b). DP600 is coated with pure zinc (10  $\mu\text{m}$  thick hot dip galvanized GI coating).

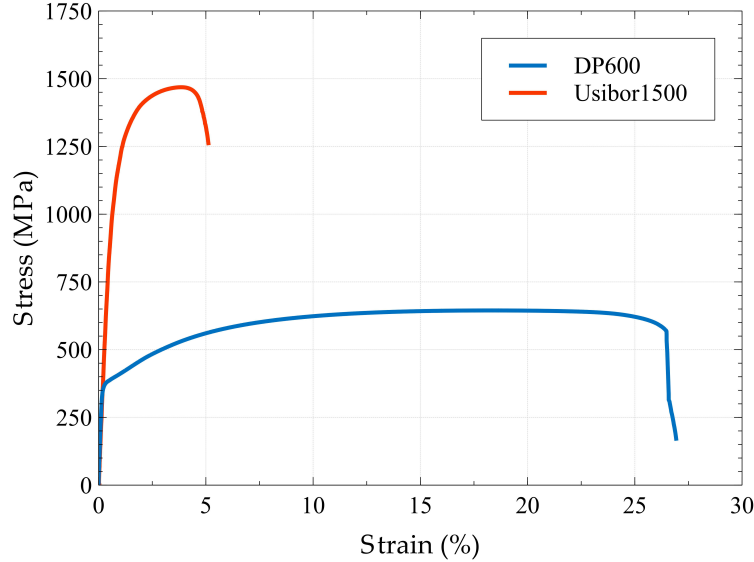


Figure 2.2: Mechanical properties of DP600 and Usibor1500 steel grades (Uniaxial ISO tensile test).

The chemical compositions of base materials are given in table 2.1. Carbon content in the DP600 is around 0.087 wt% whereas it is 0.220 wt% in the Usibor1500. G3Si is the material used for the filler wire during the arc welding process. As detailed below, DP600 and Usibor1500 are available with two sheet thicknesses in this study: 1.2 mm and 2.0 mm.

Steel grade (x 0.001 wt%)	C	Mn	B	Si	N	P	Cr	Cu	Al
DP600 1.2 mm	88	1870	-	150	4	13	97	25	21
DP600 2.0 mm	85	1885	-	241	5	14	210	12	32
G3Si (filler wire)	75	1460	-	547	6	11	182	-	26
Usibor1500 1.2 mm	221	1184	3	256	42	12	187	12	32
Usibor1500 2.0 mm	218	1149	3	266	-	12	189	-	35

Table 2.1: Chemical composition of steel grades (x 0.001 wt%).

### 2.1.2 Welding configurations

In the study, different thicknesses for each steel grade will be used. The thickness range goes from 1.2 mm to 2.0 mm, which are usual thicknesses found in the BIW. To study the influence of thickness on the resistance spot welding of AHSS in terms of microstructures and resultant mechanical properties, four configurations with varying thicknesses are welded. In the first two configurations, the sheet thickness is the same for Usibor1500 and DP600 (1.2 mm or 2.0 mm), these configurations will be called similar thickness configurations. The two last configurations are dissimilar in thickness. The first one corresponds

to the welding of 2.0 mm Usibor1500 with 1.2 mm DP600, whereas it is the opposite in the second one. These configurations are illustrated on the figure 2.3.

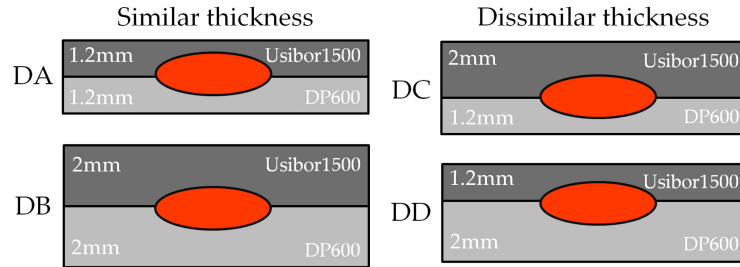


Figure 2.3: Spot welding configurations.

For arc welding, 1.5 mm and 2.0 mm Usibor1500 steel sheets are used, and heterogeneity comes from the filler wire used during process. A G3Si wire, with a chemical composition close to the DP600 one, is used to weld two overlapped Usibor1500 steel sheets with different thicknesses (figure 2.4).

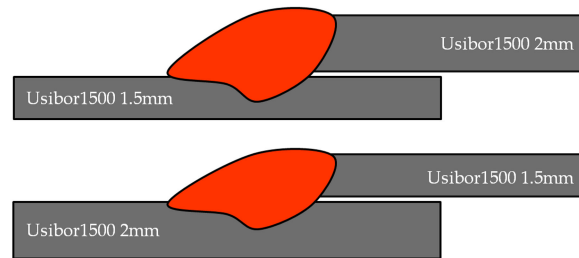


Figure 2.4: Arc welding configurations.

## 2.2 Spot weldability

In this part, the spot weldability of the different configurations will be discussed as well as the influence of the process on microstructure, nugget formation and hardness of the different heat affected zones (HAZ). For each configuration, the welding range is investigated using the ISO 18278-2 (2004) standard. The welding parameters directly depend on the steel sheet thicknesses and particularly on the thinnest one. The main welding parameters are collected in table 2.2. Welding time is expressed in periods (p) depending of the current frequency (50Hz in Europe).

Welding parameters	Electrode diameter	Pulse Number	Welding time	Holding time	Electrode force
DA	6 mm	1	17p	17p	400 daN
DB	8 mm	4	12p	25p	500 daN
DC	6 mm	1	17p	17p	400 daN
DD	6 mm	1	17p	17p	400 daN

Table 2.2: Welding parameters,  $p=0.02$  s.

Using the parameters of each configuration, the welding range is investigated by changing the welding intensity according to two conditions:

- Minimal welding intensity ( $I_{min}$ ) is given when a weld nugget diameter of 4mm is obtained;
- Maximal welding intensity ( $I_{max}$ ) is obtained when three samples can be welded at the same intensity without splash (expulsion of molten metal) (if one of the three is splashing during the process, intensity should be reduced until obtaining three spot welds without splash).

Using this methodology, the welding ranges obtained with a SCHLATTER Selecta P2 (AC mode) machine for the four configurations are shown in figure 2.5. The welding ranges are at least 2 kA large, which corresponds to a good weldability of the two steel grades.

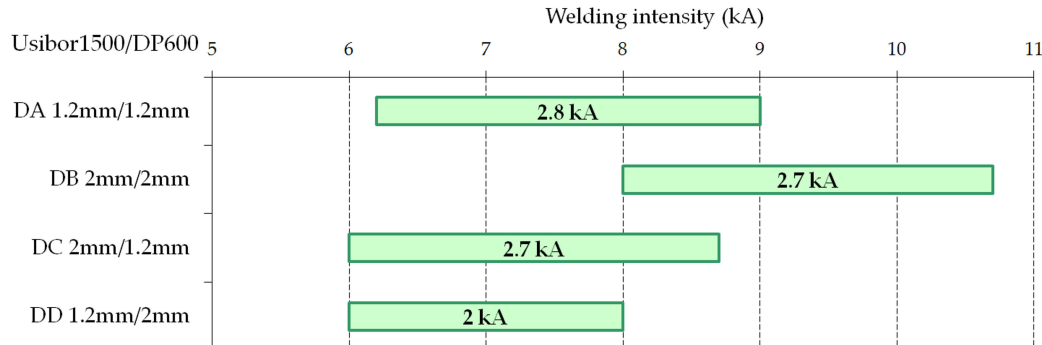


Figure 2.5: Spot welding intensity range of the four welded configurations.

The welding ranges of the four configurations are used to define three intensity values per configuration:

- Lower end intensity (close to  $I_{min}$ )
- Middle intensity (chosen in the middle of  $[I_{min}, I_{max}]$ )
- Higher end intensity (close to  $I_{max}$ )

The three intensities are used to weld mechanical tests samples. The reason for selecting different intensities along the range is that the weld diameter depends on the energy provided by Joule effect. For each configuration and intensity, seven samples are welded, one for the microstructural observations, three for the cross tension strength tests (CTS) and three for the tensile shear strength tests (TSS). The micrographic sample is cut perpendicular to the weld, polished and chemically etched to reveal the different zones



of the spot weld (Base material BM, heat affected zone HAZ, fusion zone FZ).

Using the polished samples, micrographic observations and micro hardness tests were carried out to characterize the heat affected zones and the fusion zone. Samples were cut at the middle section of the nugget with a tabletop cut-off machine, polished and chemically etched. The samples are polished to the micron step by step obtaining mirror and chemical etched by two chemical reagents, Bechet-Beaujard (Picric acid) and Nital 3 % (Nitric acid). Bechet-Beaujard permits to reveal the former austenite grain boundaries which allows to easily observe the nugget (figure 2.6.a). Nital is widely used in the steel industry to reveal microstructure, ferrite grains and martensitic structures in particular (figure 2.6.b). Microscopic observations were performed using a Zeiss Imager A1m device. During all experiments (from welding to observations), Usibor1500 was taken as the upper sheet.

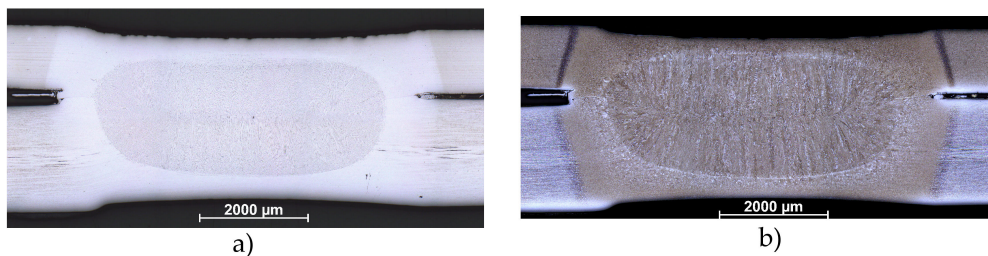


Figure 2.6: Chemical etching of a spot weld with a) Bechet-Beaujard reagent and b) Nital 3 % reagent.

The micrographic views of dedicated samples allow to compare the nugget size when the intensity changes. Figure 2.7 shows the Usibor1500-DP600 spot welds cross sections for two thickness configurations (DB, homogeneous and DD, heterogeneous) and the three positions in the welding range (lower end, middle and upper end). One can observe the increase in nugget size with increasing welding current intensity regardless of the configuration.

Micro-hardness tests were carried out on metallographic samples with a EMCOTEST M1C010 device with a 500 g Vickers setting (Hv0.5). All profile lines began with Usibor1500 base metal zone, through the fusion zone and ended within the DP600 base metal (figure 2.8.c and 2.8.d). Observing simultaneously the micrographic view and the hardness profile, some particular zones can be interpreted. Micro hardness profiles are presented in figure 2.8.a and 2.8.b for two configurations. The resistance spot welding process has direct consequences on local microstructures and hardness in the two steel grades. The DP600 ferritic martensitic steel shows a Heat Affected Zone (HAZ) almost two times harder than the base metal. This is a well-known consequence of the local thermal cycle exceeding the complete austenitization temperature  $A_{c3}$  and the subsequent fast cooling rate giving rise to an almost fully martensitic microstructure. The situation is different on the Usibor1500 side, where the base metal is already mainly martensitic with a high hardness. The local thermal cycle induces first some martensite tempering (hardness drop) where the peak temperature did not exceed about 700°C during the process. A higher peak temperature (above  $A_{c3}$ , closer to the weld nugget) produces some fresh martensite as in the DP600 HAZ, but with a higher hardness due to the higher carbon content of Usibor.

Note that for the sake of simplicity in this presentation, the global “HAZ” label is given

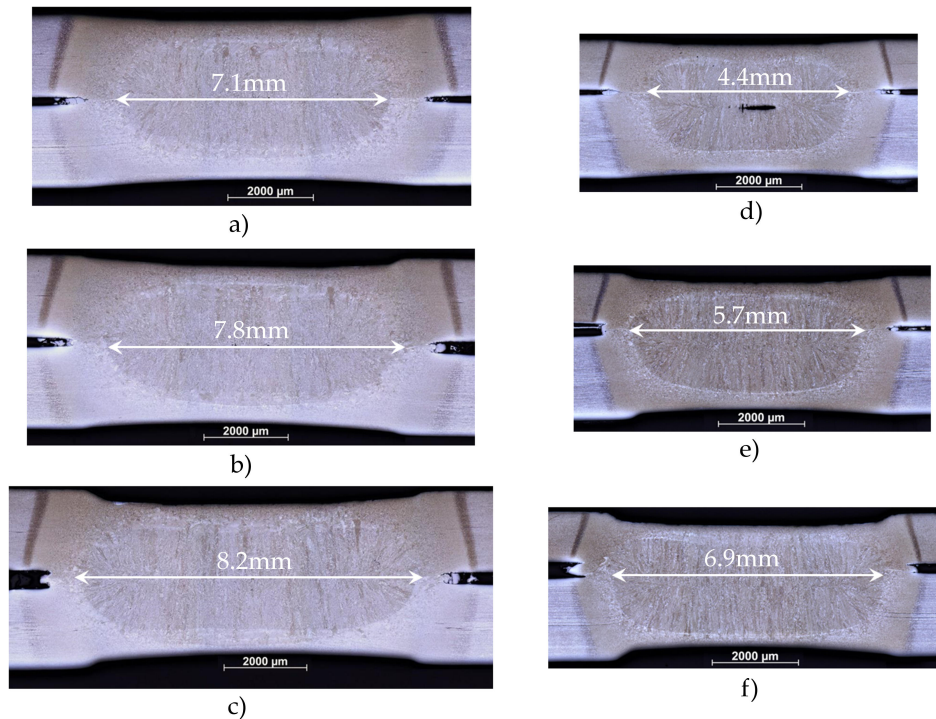


Figure 2.7: Spot weld metallographic cross sections for DB and DD configurations at the three positions in the welding range (Usibor1500 is always the upper sheet): a) DB lower end, b) DB middle position, c) DB upper end, d) DD lower end, e) DD middle position; and f) DD upper end.

only to the zones where the peak temperature exceeded  $A_{c3}$  in the solid state, even if metallurgical transformations may have occurred below (e.g., martensite tempering). The weld nuggets present intermediate hardness levels due to the homogenization of carbon content between DP600 and Usibor1500 and to the high cooling rate giving birth to very hard martensite. Based on the preceding and according to literature, six different hardness zones can be highlighted in these profiles:

- Usibor1500 base metal,
- Usibor1500 tempered zone,
- Usibor1500 HAZ,
- Fusion zone,
- DP600 HAZ,
- DP600 base metal.

It is important to note that the weld nugget chemical composition depends on the thickness ratio between Usibor1500 and DP600. Focusing on carbon content in the two types of steels and considering a simple rule of mixture, a thin Usibor1500 sheet on top of a thick DP600 one (DD configuration) will produce a fusion zone with a lower average carbon content than in the homogeneous thickness configurations (DA or DB). Consequently, the maximum carbon content in the fusion zone will be obtained in the DC configuration (thick Usibor1500 sheet with a thin DP one). These tendencies are verified by average hardness



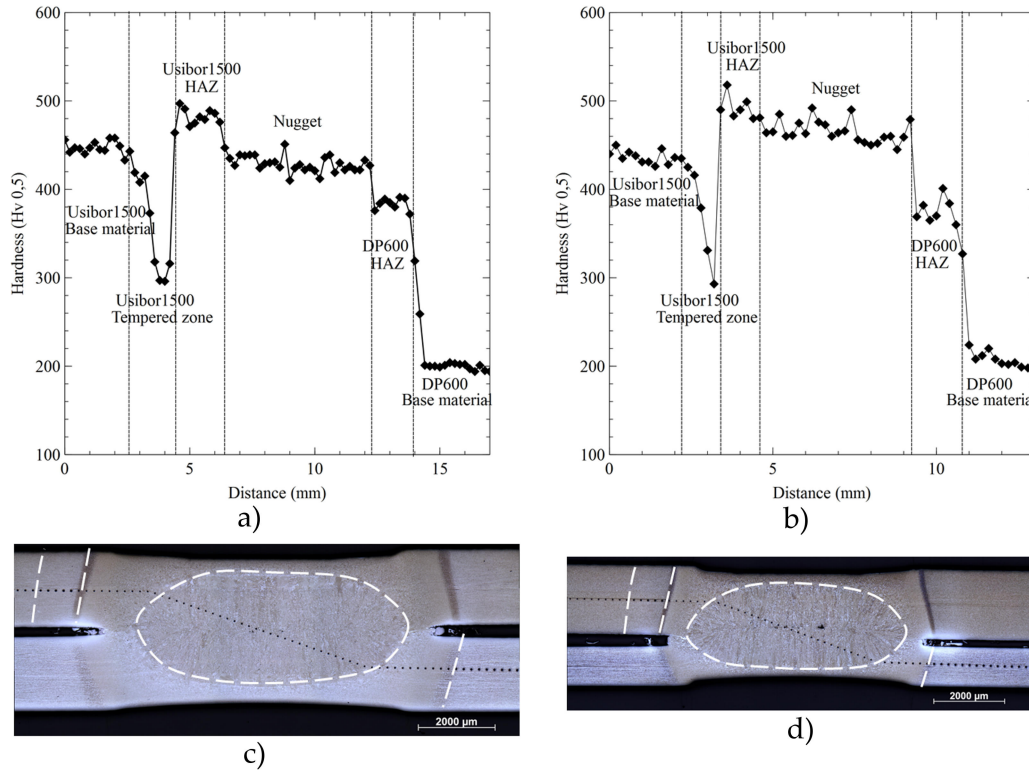


Figure 2.8: Spot weld hardness profiles for DB (Usibor1500 2.0 mm-DP600 2.0 mm) and DC (Usibor1500 2.0 mm-DP600 1.2 mm) configurations: a) DB hardness profile, b) DC hardness profile, c) DB metallographic cross-section and d) DC metallographic cross-section.

measurement of the weld nugget for the four configurations: weld nugget hardness is about 420 Hv in DA and DB configurations, 470 Hv in DC and 419 Hv in DD configurations. This is in accordance with the facts that the fusion zone is mainly martensitic and that martensite hardness is strongly dependent on carbon content.

## 2.3 Failure modes

The steel sheets were cut into 125x38 mm coupons along the transverse direction and resistance spot welded following ISO 18278-2 standard. Mechanical tests were carried out on Zwick tensile machine with a 100 kN load cell at a crosshead speed of 15 mm/min. Special hydraulic jaw assemblies were used in cross tension and tensile shear, according to the standards (respectively ISO-14272 and ISO-14273). All the samples are disposed with Usibor1500 as upper sheet in the tensile machine. Then displacement is imposed until spot weld failure. Two important characteristics of spot weld fracture are usually extracted and recorded after such destructive tests: failure load and failure mode. While the former is explicitly defined by the maximum load reached during the test, the latter refers to a specific classification and measurement procedure described in the following. Mild steel spot welds usually fail by Button Pull-Out (BPO) or Full Interfacial Failure (FIF). AHSS usually present additional failure modes: Partial Interfacial Failure (PIF)

but also the so-called Total (or Partial) Dome Failure, where the fracture path follows the FZ-HAZ interface (figure 2.9).

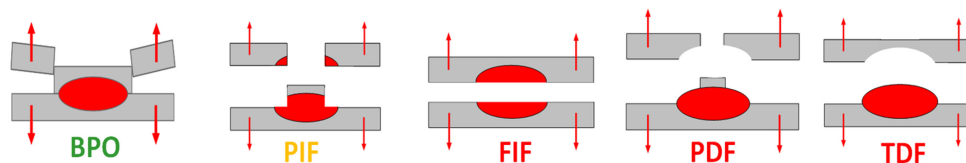


Figure 2.9: Spot weld failure modes: Button Pull-Out (BPO), Partial Interfacial Failure (PIF), Full Interfacial Failure (FIF), Partial Dome Failure (PDF), and Total Dome Failure (TDF).

Failure modes are investigated with the naked eyes first. If a button was formed, its diameter is measured using a vernier calliper along two directions (minimal and maximal diameter). Moreover, in all cases but BPO, the weld nugget size is investigated using an eye magnifier to allow measuring the weld diameter.

### 2.3.1 Cross tension tests

#### 2.3.1.1 Cross tension tests macroscopic investigations

Failure modes obtained after cross tension tests are gathered in table 2.3 for the four configurations, with an indication on the failure side (if 'Usibor1500 Failure' is specified, a button is remaining on DP600 steel sheet and a hole in the Usibor1500 one).

Configurations	Low Intensity Range	Middle Intensity Range	High Intensity Range
DA: Usibor 1.2 mm/DP600 1.2 mm	Usibor Failure (PIF)	Usibor Failure (BPO)	Usibor Failure (BPO + PDF)
DB: Usibor 2.0 mm/DP600 2.0 mm	Usibor Failure (PIF)	Usibor Failure (PIF)	Usibor Failure (BPO)
DC: Usibor 2.0 mm/DP600 1.2 mm	DP600 Failure (PIF)	DP600 Failure (BPO)	Usibor Failure (BPO + PDF)
DD: Usibor 1.2 mm/DP600 2.0 mm	Usibor Failure (BPO)	Usibor Failure (BPO)	Usibor Failure (BPO + PDF)

Table 2.3: Cross tension failure modes.

A majority of Button Pull-Out (BPO) and Partial Interfacial Failure (PIF) occurred. Failure occurred in the Coarse Grain HAZ (CGHAZ) of Usibor1500 for BPO and in the weld nugget for PIF, except for the DC configuration (2.0 mm Usibor-1.2 mm DP600) where failure was on the DP600 side for low and middle intensity ranges. Failure never occurred in the tempered zone of Usibor1500 in spite of hardness fall in this zone. A global trend of PIF to BPO failure mode transition from low to high welding current can be noticed, as often observed with increasing weld diameters. The observed failure modes are presented in figure 2.10 in more details.

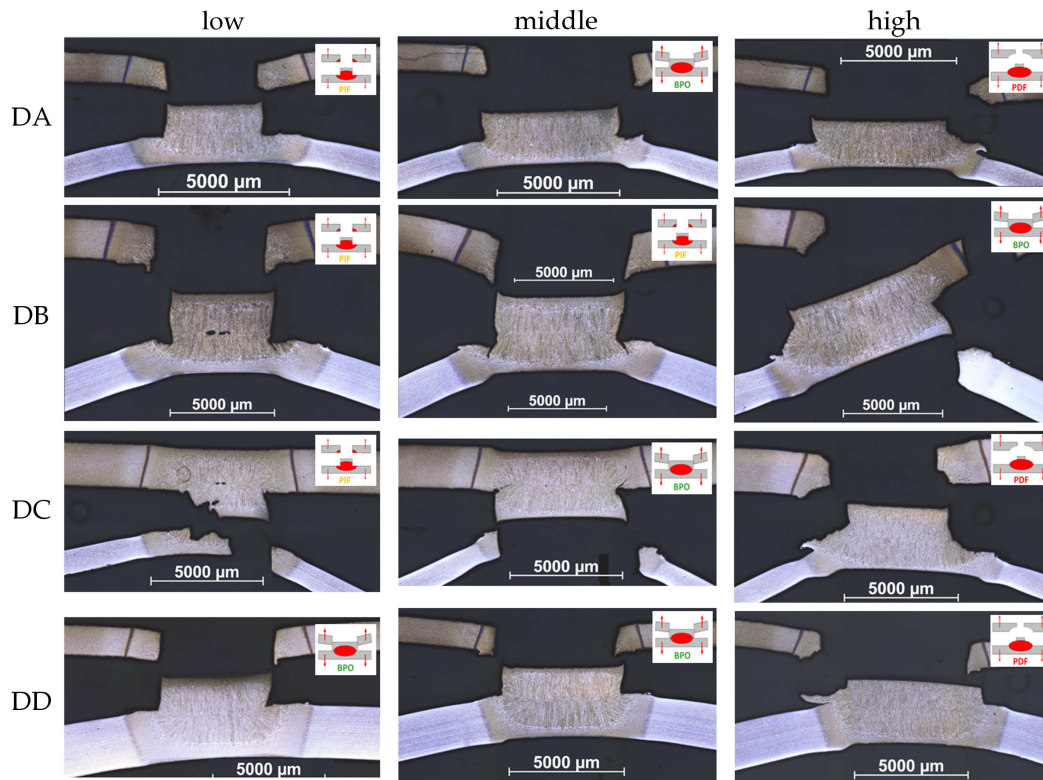


Figure 2.10: Spot weld cross tension failure modes for the four configurations (DA, DB, DC and DD) for the three welding intensities.

The macroscopic visual aspect of the broken welds corresponding to encountered failure modes are presented in figure 2.11.

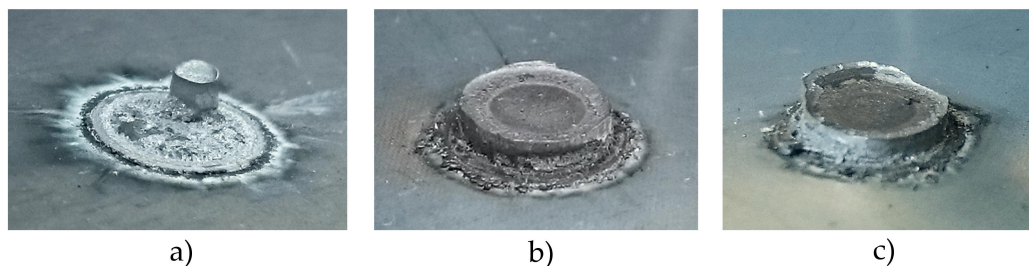


Figure 2.11: Main failure modes encountered during Cross Tension tests (macroscopic visual aspect): a) PIF, b) BPO, and c) BPO + PDF.

A remarkable feature is the initiation of a Partial Dome Failure at the upper end of the welding range in parallel to BPO. In fact, initiation of expulsion produces a particular geometry at the notch tip, where a small amount of liquid metal (splash) could escape from the nugget and promotes Partial Dome Failure. The latter occurs usually at an angle of about 30° to the faying surface. This is illustrated in more details in figure 2.12, where the initial dome crack eventually forks up into a button. This phenomenon seems to drive the failure zone transition from the DP600 side to the Usibor1500 in the DC configuration

close to the upper end of the welding range.

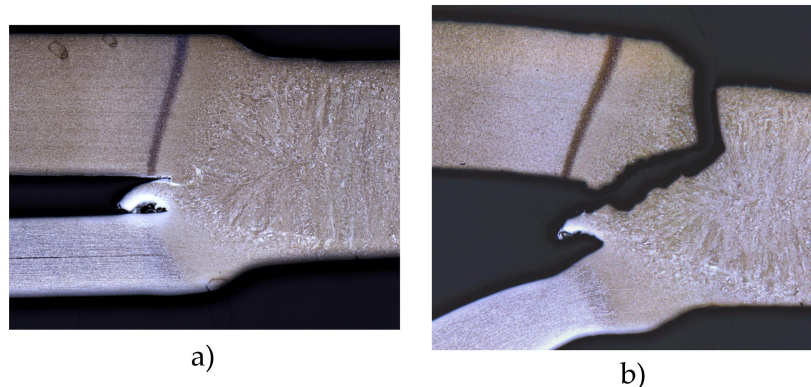


Figure 2.12: Beginning of expulsion in the DC configuration at the upper end of the welding range promoting partial dome failure: metallographic cross section before a) and after b) the cross tension test.

### 2.3.1.2 Cross tension tests fracture surfaces

Fracture surfaces of failed spot welds were then observed in a Scanning Electron Microscope (SEM) as presented in figure 2.13. In the case of Button Pull-Out (BPO), the lateral button surface was observed (Figure 2.13). Two types of fracture surfaces were identified in that case:

- A zone exhibiting small cavities due to debonding of the inclusions in the material (right zone).
- A zone exhibiting shear (left zone). The “pull-out” movement of the upper sheet in the final stage of fracture (vertical tangential motion of the fractured sheet with respect to the weld nugget) is indeed expected to produce such evidence of shearing, corresponding to the friction of upper sheet after failure.

When Partial/Full Interfacial Failure (PIF/FIF) is considered, the fracture surfaces exhibit brittleness. In figure 2.14, the investigations are focused on the interfacial failure zone, and two characteristic types of surface in the Interfacial Failure (IF) of spot welds were identified:

- A zone exhibiting cleavage, which is characteristic of a very fast crack propagation without deformation (left zone). This type of fracture is transgranular.
- Sometimes a zone with dendrites (right zone). During the welding process, the fusion zone is quenched, forming shrinkage at weld centre. When spot welds fail in Interfacial Failure mode, the shrinkage cavities allow to observe the dendrites of nugget solidification.

In the case of Partial Dome Failure (PDF), the partial dome is highlighted by the white dotted line area and the button by the white solid one in figure 2.16. As discussed above, the presence of a small weld metal splash promotes the partial dome. The latter was observed for an angular range of about  $30^\circ$  around the weld nugget in that particular case (figure 2.15).



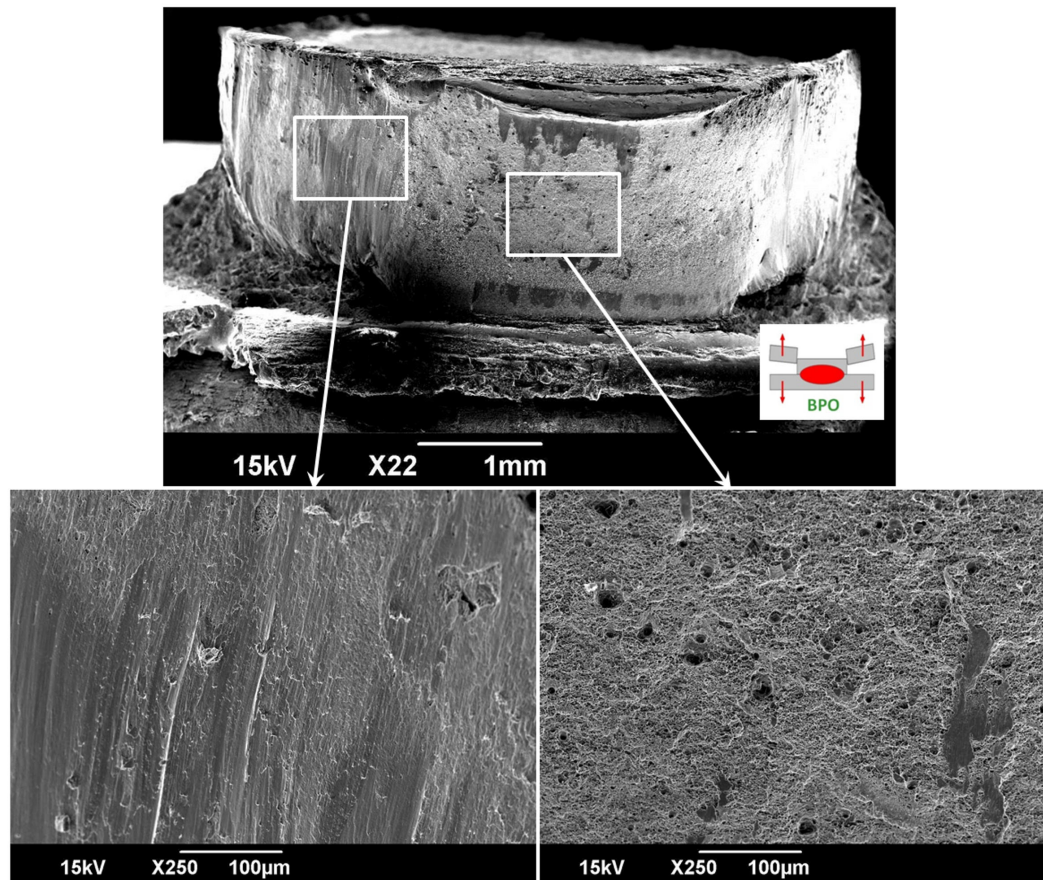


Figure 2.13: Scanning Electron Microscopy (SEM) fracture surfaces in cross tension of Button Pull-Out failure mode.

While the Button zone fracture surface in figure 2.16 is close to the one detailed in figure 2.13, the partial dome fracture surface presents some evidence of brittle failure, but not only. On the right zone of figure 2.16, some grains are observed which correspond to intergranular fracture (grain boundaries decohesion) in the coarse grain HAZ of Usibor1500.

## 2.3.2 Tensile shear tests

### 2.3.2.1 Tensile shear tests macroscopic investigations

The failure modes obtained in tensile shear in the four configurations are gathered in table 2.4 and illustrated in figure 2.17. Mainly Full Interfacial Failure (FIF, figures 2.17 and 2.18.a, low welding currents) and Button Pull-Out (BPO, figures 2.17 and 2.18.b, higher welding currents) are observed, as expected from the literature.

It is interesting to note that failure occurred in the Usibor1500 Coarse Grain HAZ most of the times, when not at the faying surface. The DC configuration (thick Usibor1500 sheet on top of a thin DP600 one) constitutes however an exception to that rule, with a failure occurrence rather on the DP600 side and a transition from Total Dome Failure (DP600-

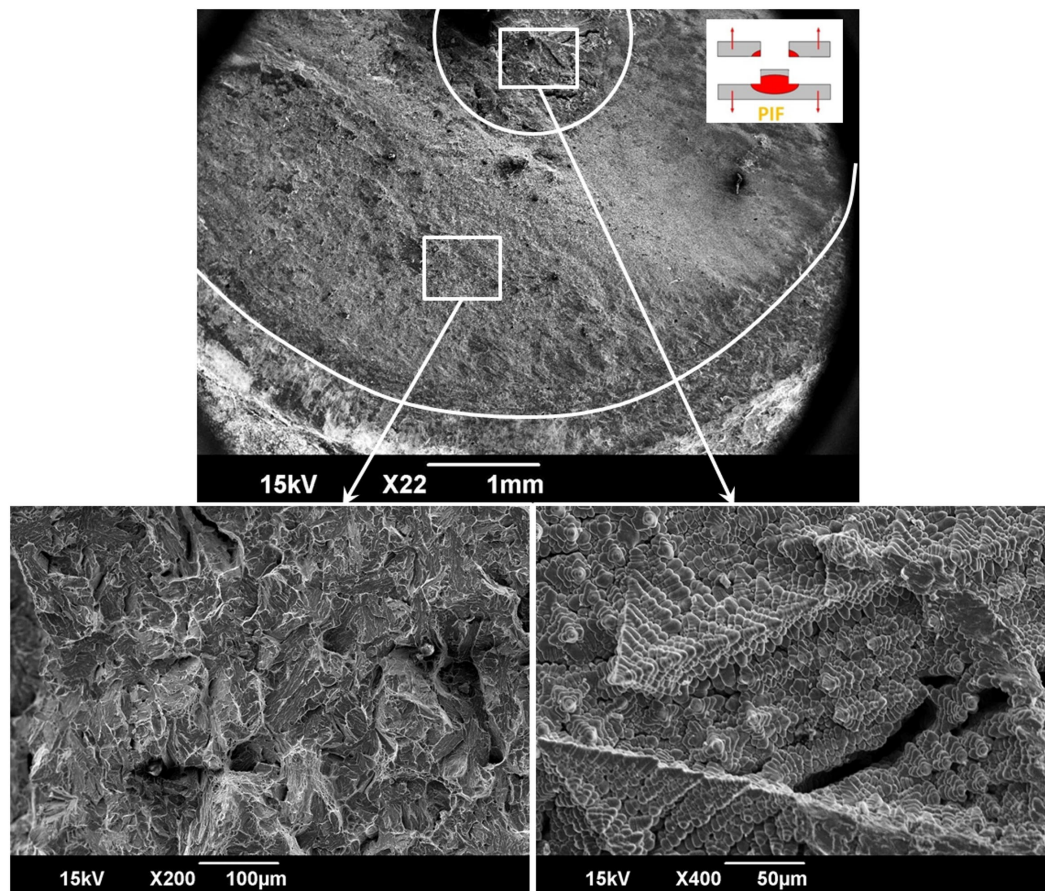


Figure 2.14: Scanning Electron Microscopy (SEM) fracture surfaces in cross tension of Interfacial failure mode.

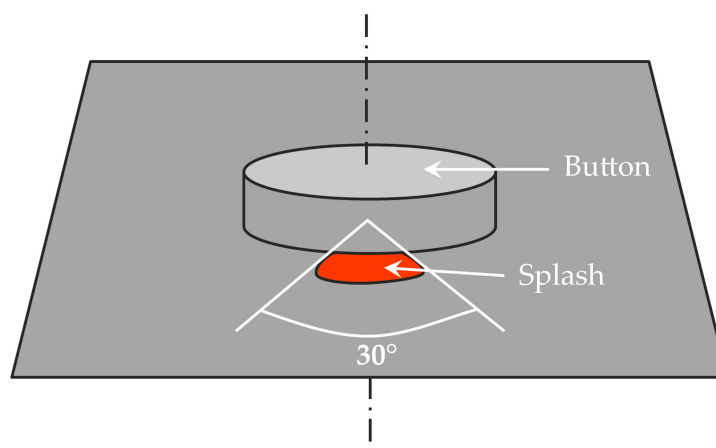


Figure 2.15: Splash angle along button periphery.

weld nugget interface, figures 2.17 and 2.18.c) to Button Pull-Out with increasing weld diameter.



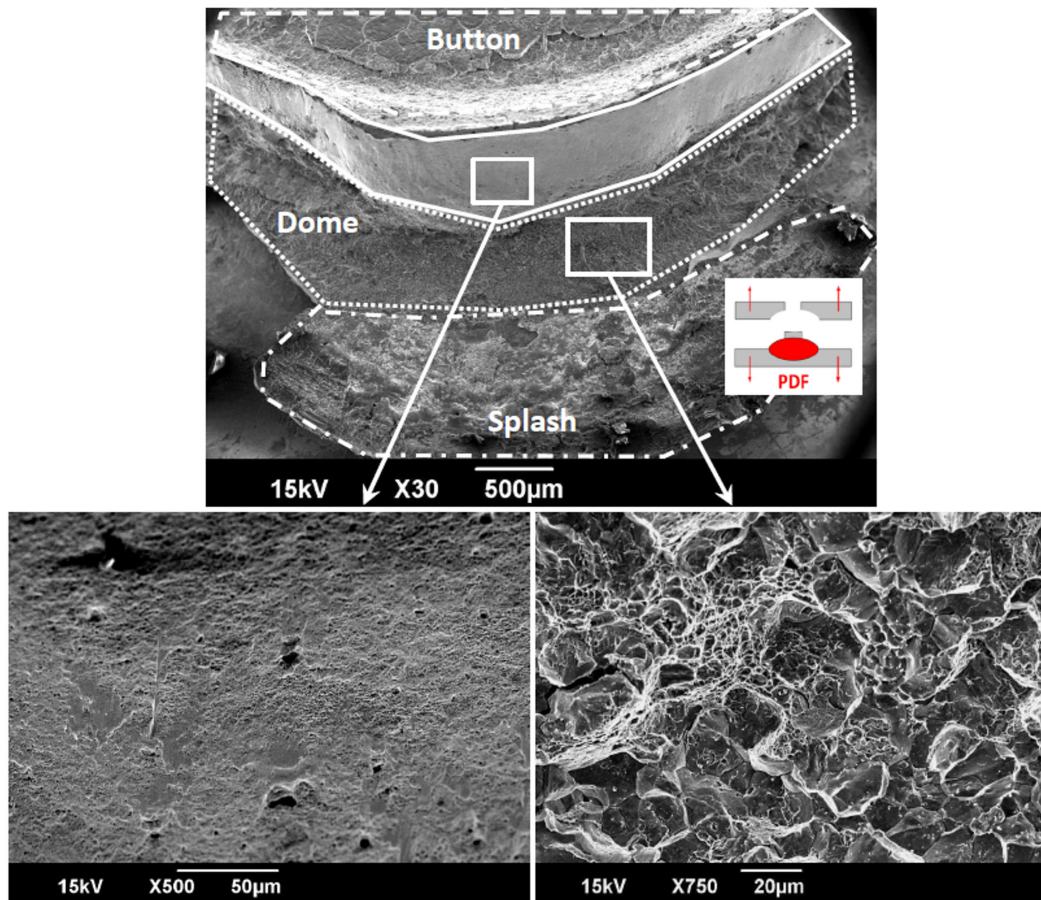


Figure 2.16: Scanning Electron Microscopy (SEM) fracture surfaces in cross tension of Partial Dome failure mode.

Configurations	Low Intensity Ranger	Middle Intensity Range	High Intensity Range
DA: Usibor 1.2 mm/DP600 1.2 mm	Usibor Failure (BPO)	Usibor Failure (BPO)	Usibor Failure (BPO)
DB: Usibor 2.0 mm/DP600 2.0 mm	FIF	Usibor Failure (BPO)	Usibor Failure (BPO)
DC: Usibor 2.0 mm/DP600 1.2 mm	DP600 Failure (TDF)	DP600 Failure (BPO + lateral PDF)	DP600 Failure (BPO)
DD: Usibor 1.2 mm/DP600 2.0 mm	FIF	FIF	Usibor Failure (BPO)

Table 2.4: Tensile shear failure modes.

The effect of the sheet thicknesses is observed by comparing DA and DB (homogeneous) configurations. A higher sheet thickness promotes Full Interfacial Failure (FIF) for small welds (low welding current). Concerning the DC configuration and the occurrence of TDF

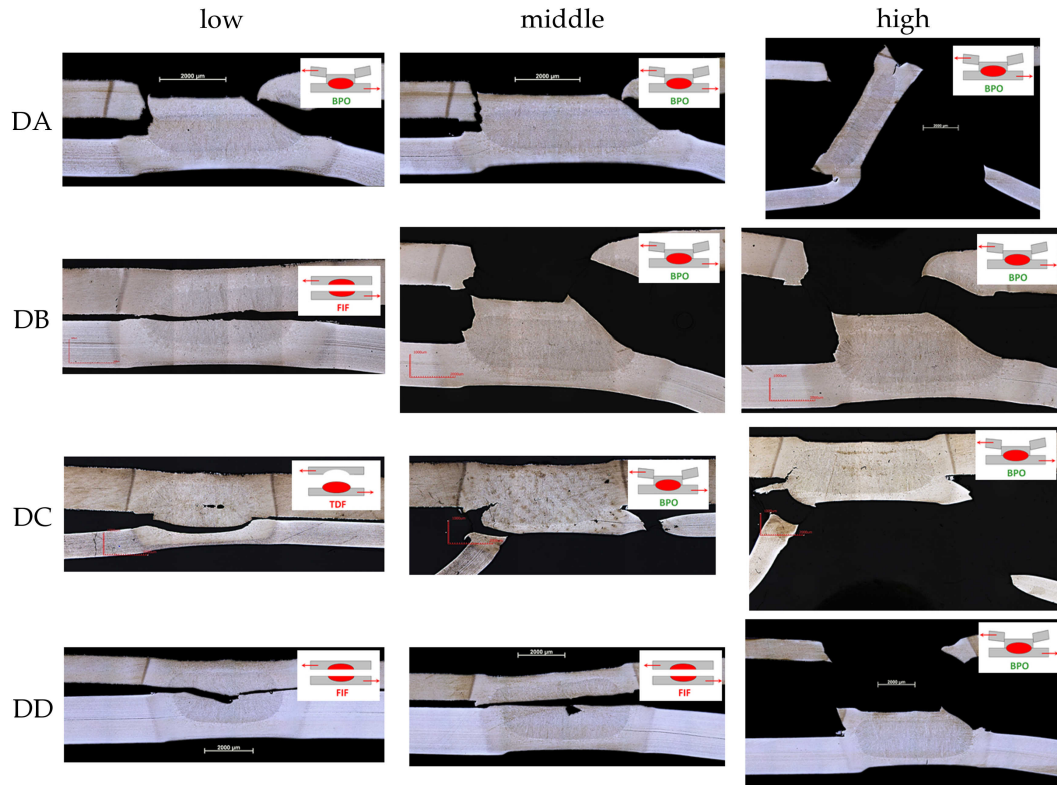


Figure 2.17: Spot weld tensile shear failure modes for the four configurations (DA, DB, DC and DD) and the three welding intensities.

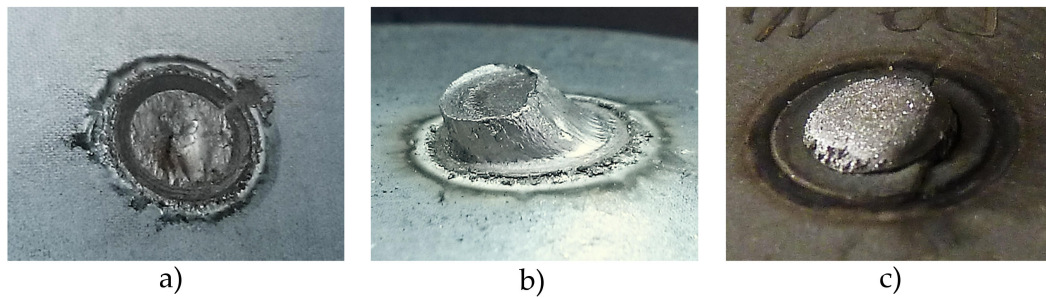


Figure 2.18: Main failure modes encountered during Tension Shear tests (macroscopic visual aspect): a) FIF, b) BPO and c) TDF.

instead of FIF for low welding current, a closer look at figure 2.17 shows that the faying surface between the notch tips is not far from being aligned with the DP600-weld nugget interface. This is geometrically favourable to the occurrence of Dome Failure.

### 2.3.2.2 Tensile shear tests fracture surfaces

SEM investigations of fractures surfaces for the three failure modes are shown in figures 2.19, 2.20 and 2.21.

The buttons obtained in tensile shear exhibit a particular aspect as shown in figure



2.18.b, where one side of the button is at close to  $45^\circ$  to the faying surface. The investigations of button lateral surfaces reveal a dimple structure which involves ductile failure in the base material HAZ. Moreover, the dimple structure is oriented in the loading direction and some shear is observed on the surfaces (figure 2.19).

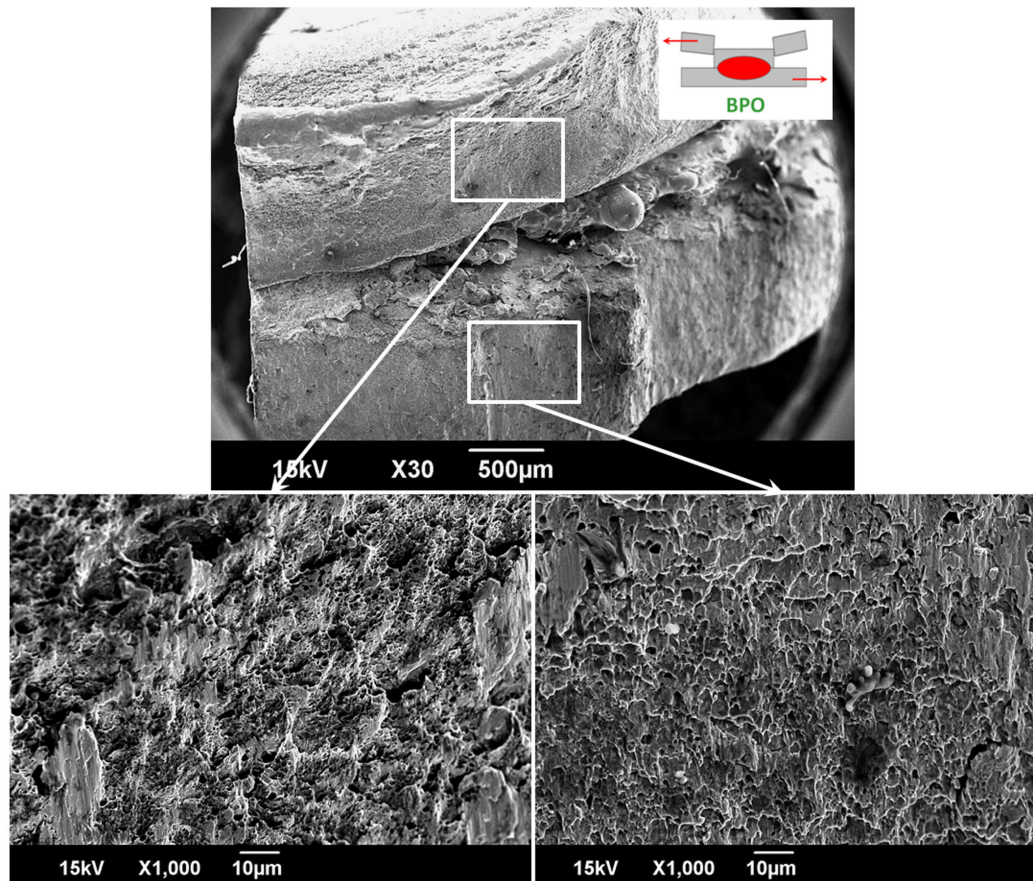


Figure 2.19: Scanning Electron Microscopy (SEM) fracture surfaces in tensile shear of Button Pull-Out failure mode.

The nugget zone of the Full Interfacial Failure mode presents a ductile aspect with sheared dimples too (figure 2.20). Note that a few cavities with apparent dendrites can also be seen close to the nugget centre in this case due to welding process (shrinkage in the fusion zone during solidification). Contrary to Partial Interfacial failure mode in the cross tension tests, in tensile shear case, the surfaces of Full Interfacial failure zone are ductile. The Interfacial failure modes do not correspond to the same failure mechanism between the two mechanical tests.

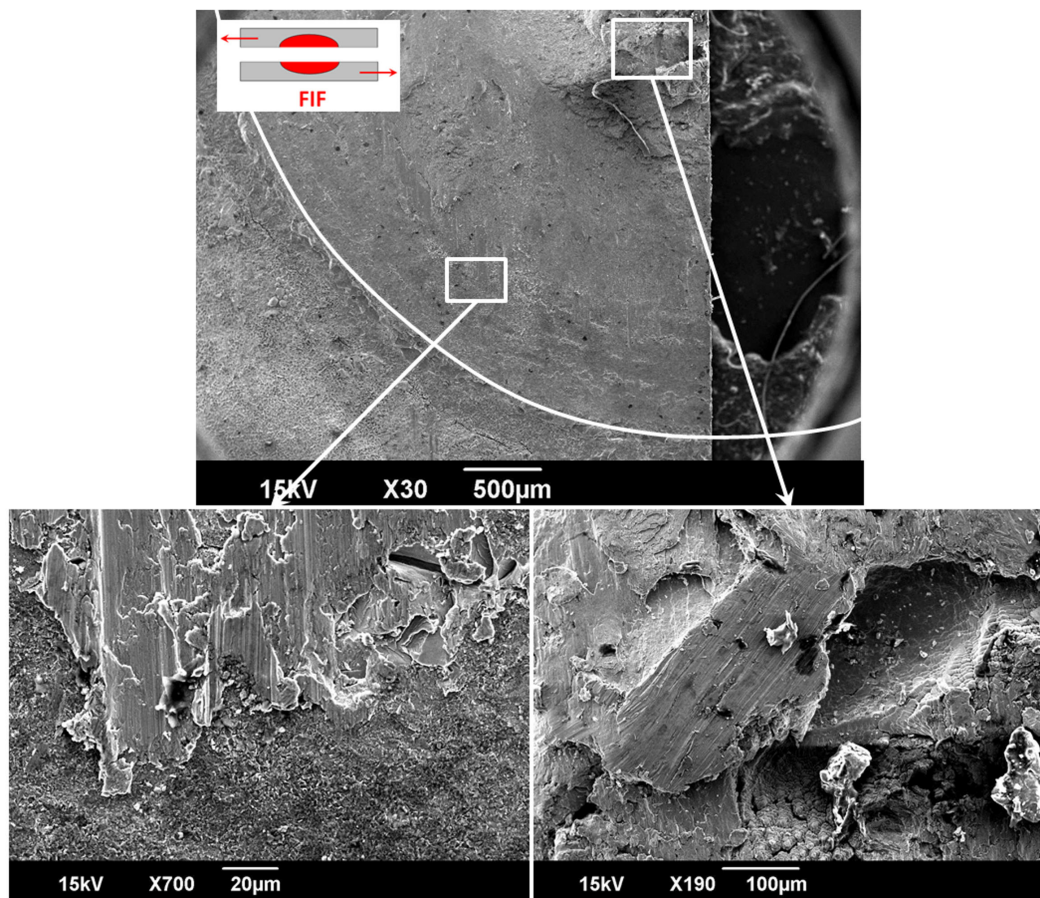


Figure 2.20: Scanning Electron Microscopy (SEM) fracture surfaces in cross tension of Full Interfacial Failure mode.

Dome fracture surfaces in figure 2.21 exhibit a transition from a mixed mode domain (intergranular cracks and dimples in the 200 µm layer close to the notch root) to a mainly ductile mechanism with elongated dimples along the dome. Another particularity is the molten coating during the process, which formed a bonding zone between the two steel sheets.

The detailed observation of the different failure modes provides understanding on failure mechanisms and sheet thickness influence. To complete the analysis, the failure strengths will now be discussed.



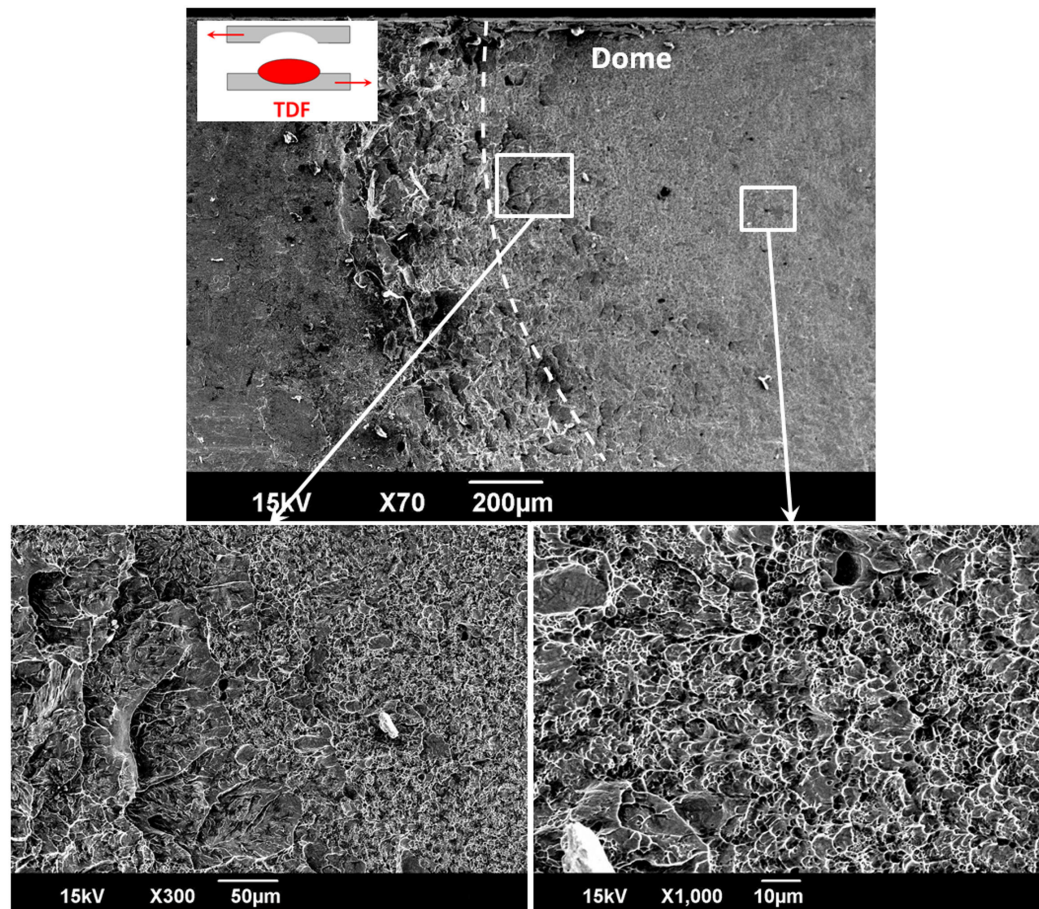


Figure 2.21: Scanning Electron Microscopy (SEM) fracture surfaces in cross tension of Total Dome Failure mode.

## 2.4 Failure strength

### 2.4.1 Cross tension strength

The failure loads of the four configurations of spot welds measured during the cross tension tests are given in table 2.5.

Configurations	Low Intensity Range	Middle Intensity Range	High Intensity Range
DA: Usibor 1.2 mm/DP600 1.2 mm	482 $\pm$ 26	566 $\pm$ 15	513 $\pm$ 20
DB: Usibor 2.0 mm/DP600 2.0 mm	1108 $\pm$ 88	1164 $\pm$ 120	1305 $\pm$ 114
DC: Usibor 2.0 mm/DP600 1.2 mm	633 $\pm$ 64	847 $\pm$ 77	837 $\pm$ 89
DD: Usibor 1.2 mm/DP600 2.0 mm	482 $\pm$ 11	600 $\pm$ 9	794 $\pm$ 94

Table 2.5: Cross tension failure loads (daN, average of three tests).

The fracture loads are plotted as a function of the measured weld diameters for the four studied configurations in figure 2.23. Four additional configuration results derived from internal ArcelorMittal Data are superimposed in figure 2.24 to compare homogeneous and heterogeneous welding. These configurations are:

- Heterogeneous welding of Usibor1500 1.5 mm with DP600 1.5 mm
- Homogeneous welding of DP600 1.0 mm
- Homogeneous welding of DP600 1.8 mm
- Homogeneous welding of Usibor1500 1.5 mm

A common parameter to evaluate the performance of a RSW assembly is the ratio  $\alpha$  (performance parameter) of the failure load normalized by the weld dimensions [BIR 12]:

$$\alpha = CTS/(d_w \times t) \quad (2.1)$$

where  $CTS$  is the cross tension failure load (daN),  $d_w$  is the weld nugget diameter and  $t$  is the sheet thickness. In the cases of dissimilar sheet thicknesses (DC and DD configurations),  $\alpha$  is calculated with the smallest sheet thickness in accordance with the ISO standard [ISO 04], as the welding process parameters are also driven by the thinnest sheet.

Figures 2.22 and 2.24 illustrate the increase in failure load with increasing sheet thickness in the homogeneous thickness configurations. This was indeed expected based on Chao [CHA 03b] or Pouranvari [POU 10b] studies for example. Note that this trend is verified for the homogeneous steel grade configurations, but also for the heterogeneous ones.

Based on the heterogeneous thickness configurations (DC and DD) in figure 2.23, it is interesting to note that the corresponding  $\alpha$  performance parameters (respectively, 99 daN/mm<sup>2</sup> and 92 daN/mm<sup>2</sup>) are almost as high as the best ones obtained in the case of DP600 homogeneous welding (94–101 daN/mm<sup>2</sup>, figure 2.24) and definitely better than the one of Usibor1500 homogeneous welding (69 daN/mm<sup>2</sup>). Similar positive effect of heterogeneous welding was already observed for example in Biro and al. [BIR 12]. Note that changing the homogeneous Usibor1500 1.5 mm configuration into a heterogeneous Usibor1500 1.5 mm/DP600 1.5 mm configuration, figure 2.24, also produces a slight increase

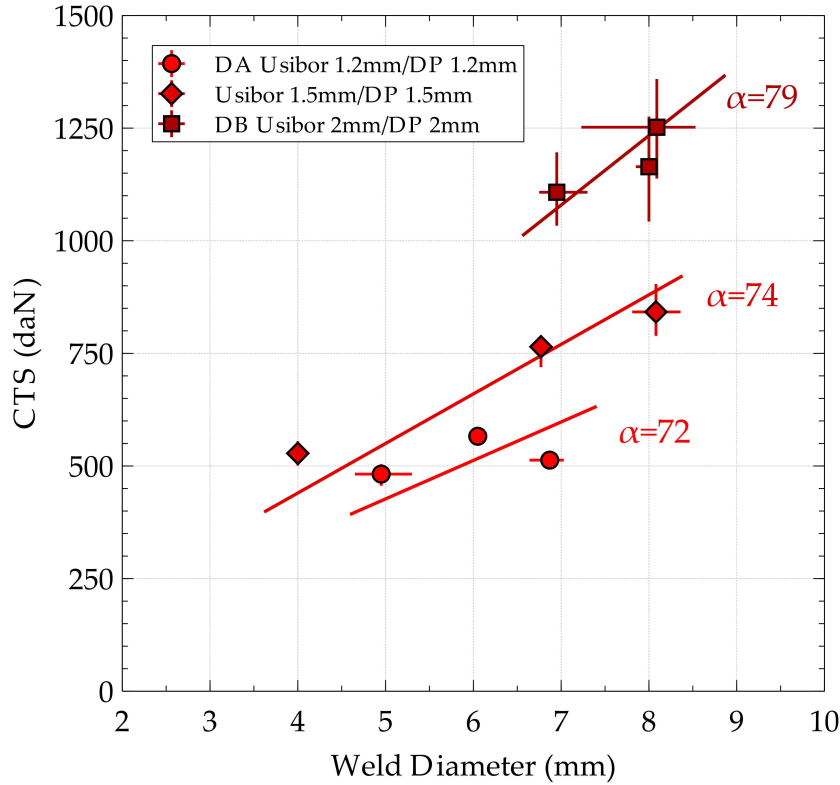


Figure 2.22: Cross tension failure load (CTS) as a function of weld diameter and welding assembly: Usibor1500 and DP600 heterogeneous welding configurations with similar thickness.  $\alpha$  in  $\text{daN}/\text{mm}^2$ .

in  $\alpha$  performance parameter (from  $69 \text{ daN}/\text{mm}^2$  to  $74 \text{ daN}/\text{mm}^2$ ). In other words, DP600 improved the spot weld performance of Usibor1500.

Partial Dome Failures (PDF) were observed for three of the four configurations (DA, DC and DD) for the high welding current intensity. Observing these particular points, it appears that the corresponding loads are under the spot weld performance curves ( $\alpha$  slope). This indicates that the occurrence of limited expulsion tends to reduce the weld performance for a given weld diameter. Thus, better understanding the subsequent dome failure mechanism remains an important challenge as it affects the failure load significantly.

#### 2.4.2 Tensile shear strength

Spot weld failure loads in tensile shear are presented in table 2.6 for the different configurations and plotted in figure 2.25 as a function of the weld diameter.

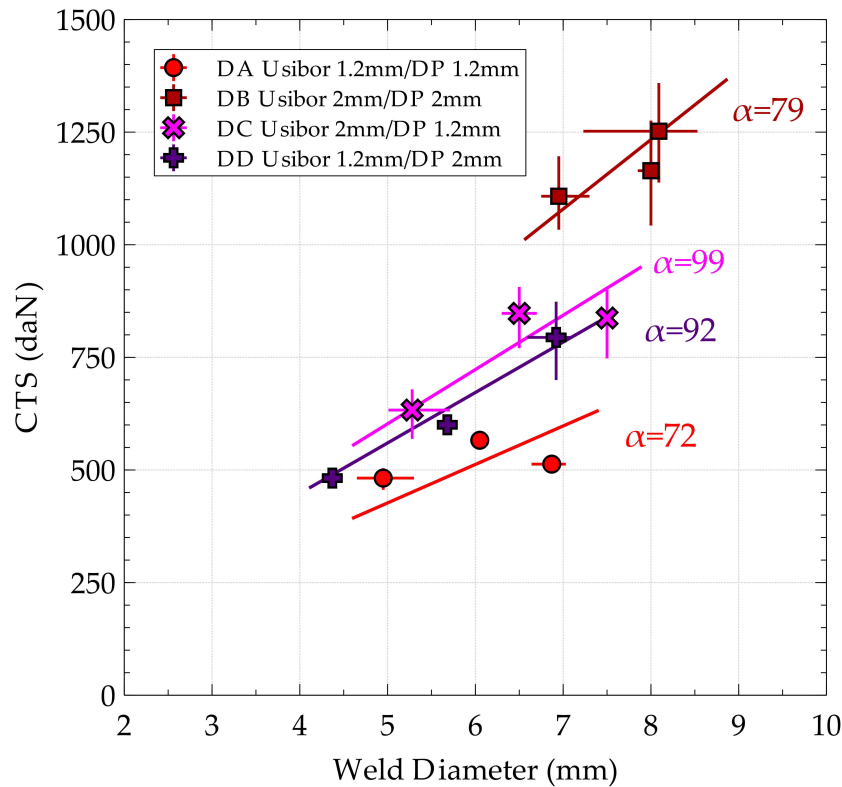


Figure 2.23: Cross tension failure load (CTS) as a function of weld diameter and welding assembly: Usibor1500 and DP600 heterogeneous welding configurations.  $\alpha$  in  $\text{daN}/\text{mm}^2$ .

Configurations	Low Intensity Ranger	Middle Intensity Range	High Intensity Range
DA: Usibor 1.2 mm/DP600 1.2 mm	$1287 \pm 55$	$1411 \pm 81$	$1539 \pm 5$
DB: Usibor 2.0 mm/DP600 2.0 mm	$2595 \pm 76$	$2989 \pm 31$	$3313 \pm 77$
DC: Usibor 2.0 mm/DP600 1.2 mm	$1387 \pm 64$	$1585 \pm 12$	$1750 \pm 5$
DD: Usibor 1.2 mm/DP600 2.0 mm	$1255 \pm 91$	$1879 \pm 31$	$2000 \pm 3$

Table 2.6: Tensile shear failure loads (daN, average of three tests).

For a given 9mm weld diameter, the DB failure load is more than twice higher than in the DA case. As opposed to the cross tension case where the heterogeneous DC configuration presented a higher strength than the DD one, the DD configuration performs better in tensile shear. Moreover, DA and DC configurations present almost the same levels of failure loads. In other words, increasing the Usibor1500 sheet thickness from 1.2 mm to 2.0 mm did not affect the failure load (but shifted failure on the DP side), while thickening rather the DP600 sheet (DD configuration) produced a significant increase in failure load.

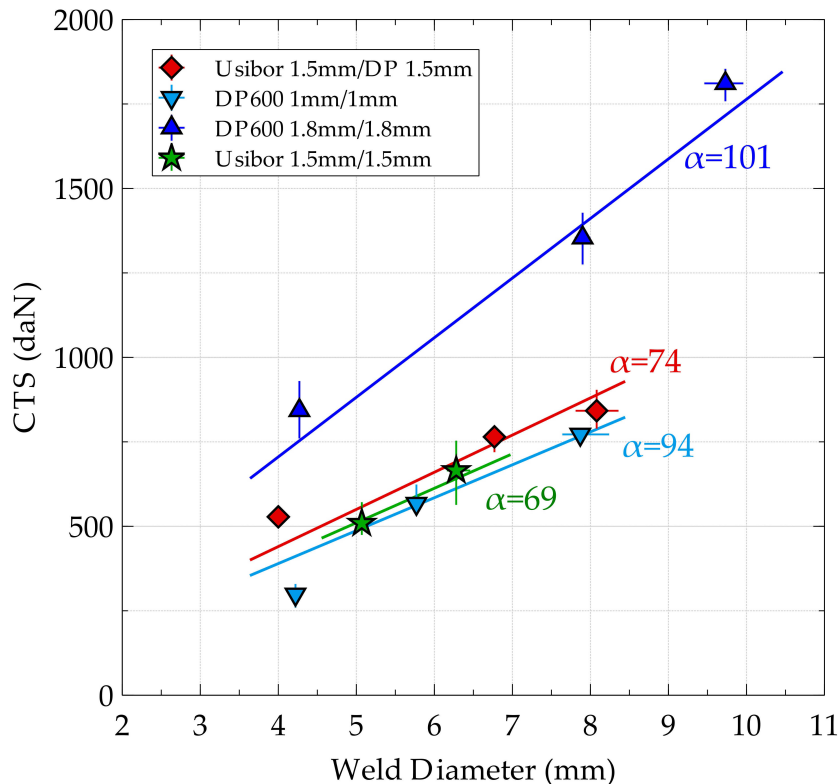


Figure 2.24: Cross tension failure load (CTS) as a function of weld diameter and welding assembly: Usibor1500 and DP600 homogeneous welding configurations compared with the dissimilar 1.5 mm Usibor1500/1.5 mm DP600.  $\alpha$  in  $\text{daN}/\text{mm}^2$ .

## 2.5 Discussion

### 2.5.1 Liquid metal splash influence on cross tension performance

In the experimental procedure, a prior characterization of the welding range was done according to the ISO 18278-2 standard of RSW. This allowed identifying a maximum welding current before the appearance of significant splash, for each configuration. Metallographic inspection, as in figure 2.7.c and 2.7.f, illustrates, however, that such upper end definition of the welding range does not prevent limited weld metal splash at the notch tip. This may be due to a slightly inhomogeneous distribution of the electrode force around the spot weld. Cross tension failure modes and strengths sections (2.3.1 and 2.4.1) illustrated that this promoted the occurrence of (partial) dome failure in cross tension and was correlated with a decrease in failure load, in spite of a higher weld diameter.

Figure 2.26 highlights the example of the DA configuration at the upper end of the welding range. It illustrates that considering the plug diameter instead of the full weld diameter helps retrieving an almost linear correlation between the failure load in cross tension and the diameter, as often observed in the literature [POU 07] and [CHA 03b]. This is as if the metal splash acted as an easily opening pre-crack reducing the apparent diameter of the weld. However, this decrease in failure load is not observed in tensile shear, where the tangential loading mode of the faying surface makes it less sensitive to

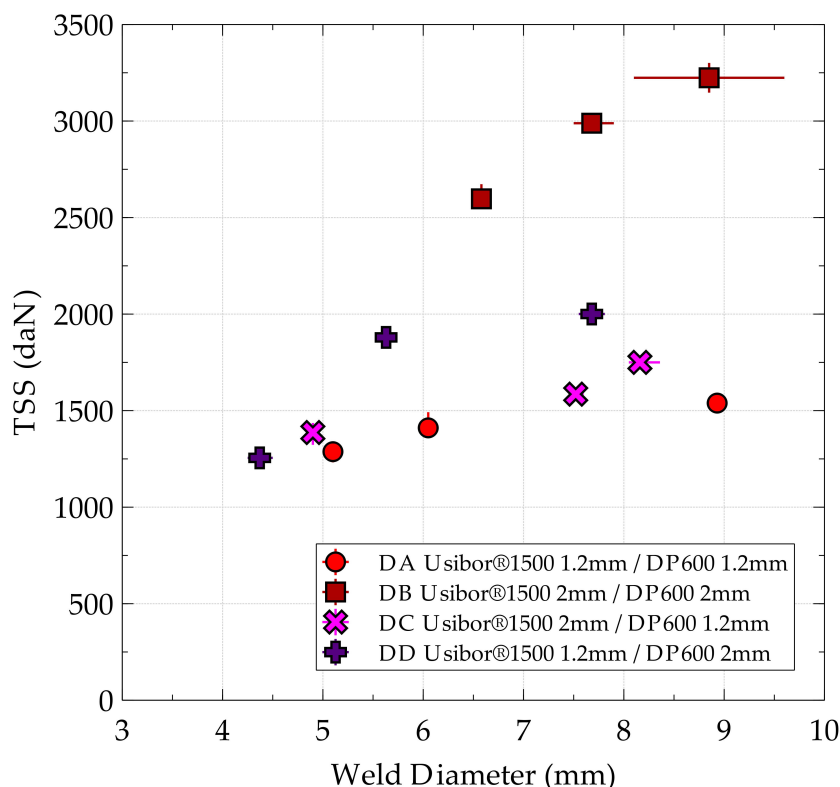


Figure 2.25: Tensile shear failure load (TSS) as a function of weld diameter and welding assembly.

such irregularities of the notch tip.

### 2.5.2 Positive deviation of cross tension failure load with dissimilar thickness

Cross tension failure modes and strengths in sections 2.3.1 and 2.4.1 illustrated above the positive effect of dissimilar thickness welding on the cross tension performance parameter  $\alpha$ , that can be seen as the failure load normalized by the sheet thickness and the weld diameter. Dissimilar thickness configurations (DC and DD) present indeed higher  $\alpha$  than the three iso-thickness configurations (DA, DB and 1.5 mm/1.5 mm). Such effect is also seen in the experimental results of Biro et al. [BIR 12], concerning mostly a DP980 steel in that case. Several phenomena can be proposed to contribute to the positive deviation.

Firstly, chemical dilution in the weld nugget affects hardenability and hardness in the case of dissimilar welding with different steel grades. This was clearly observed in section 2.2 where the weld nugget hardness strongly differs from the Usibor1500 and DP600 HAZ. It is itself significantly affected by the thickness ratio of the two sheets influencing the final composition of the weld nugget and its hardness (470 Hv for DC, 419 Hv for DD).

Secondly, increasing the sheet thickness is likely to reduce the cooling rates during the process, as shown by Kim [KIM 15] or Eshraghi [ESH 14], and consequently the types of microstructures obtained in the weld nugget and HAZ, as detailed in Dancette et al.



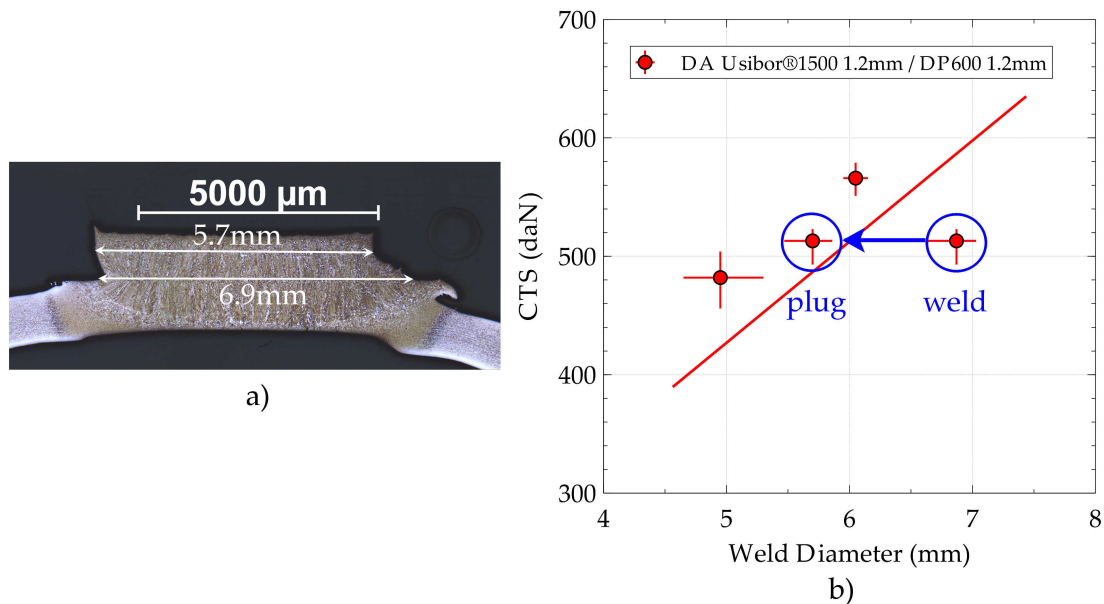


Figure 2.26: DA configuration spot weld: a) Metallographic cross-section at the upper end of the welding range after cross tension, highlighting two possible values of diameter (plug or weld). b) DA failure loads as a function of diameter, with a possible horizontal shift of the upper end spot welds when considering the effective plug diameter instead of the full weld diameter.

[DAN 11b]. In the present study, increasing the sheet thickness from 1.2 mm (DA configuration) to 2.0 mm (DB configuration) produces a slight decrease of average weld nugget hardness from 429 Hv to 413 Hv. However, the link from microstructure and hardness to damage behaviour and the resulting failure mode and failure load of spot welds remains very complex. As an example, the harder (and potentially more brittle) DC weld nugget is in fact presenting a slightly higher  $\alpha$  performance parameter in cross tension than the softer DD one (99 daN/mm<sup>2</sup> vs. 92 daN/mm<sup>2</sup> respectively).

Beyond microstructure types and hardnesses, simple geometrical considerations are also likely to affect the weld behaviour. First, the position of the notch tip with respect to the weld nugget height is affected by dissimilar thickness welding as illustrated in figure 2.27, where the nugget centre tends to shift towards the thicker sheet (DP600). Assuming that the former solidification plane presents a low toughness (orange zone) and since it is no more aligned with the notch tips in dissimilar thickness configurations, this may contribute to the better performance of the latter in cross tension, as also suggested in Biro et al. [BIR 12]. Indeed, the crack propagation along the arrow becomes less feasible when the nugget shift increases (figure 2.27). Another possible effect may arise from the notch tip radius and orientation with respect to weld nugget-HAZ interface, which is affected by dissimilar thickness welding and may have consequences on the initiation of crack propagation from the notch tip.

These different chemical, microstructural and geometrical features of heterogeneous spot welds are strongly interrelated and make it difficult to observe experimentally unambiguous trends in spot welds mechanical behaviour with a given parameter. One per-

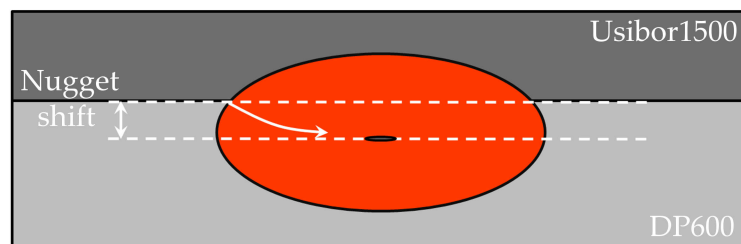


Figure 2.27: Nugget shift schema.

spective here is the development of finite element models (e.g., Dancette et al. [DAN 12] and [DAN 09]) that allow investigating separately the influence of the numerous influencing parameters, from the local constitutive behaviour to geometrical effects and their consequences on stress concentration or varying boundary conditions.

### 2.5.3 Dissimilar thickness effect in tensile shear

Contrary to cross tension, there is no global obvious and significant positive effect of dissimilar thickness on the tensile shear failure load with respect to the homogeneous configurations. However, all welds present a strong dependence of the failure load to the weld diameter and sheet thickness. These results are consistent with the conclusions of Marashi [MAR 10] and Pouranvari [POU 10a] who observed that nugget diameter and the weld fusion penetration are the two main controlling factors of Tensile Shear strength for a given sheet configuration.

One factor often mentioned to influence the tensile shear strength of dissimilar spot welds is the Ultimate Tensile Strength (UTS) of the thinnest sheet base metal [MAR 10]. The present study confirms that: for a given weld diameter, DD welds (thin Usibor1500 sheet) present a higher failure load than DC welds (thin DP600 sheet), despite the fact that final fracture is not taking place in the base metal. Consequently, one way to increase the tensile shear failure load of dissimilar spot welds consists in increasing the thickness of the lower grade sheet. This is illustrated by the comparison of DA (iso-thickness, 1.2 mm) and DD configurations (thick 2.0 mm DP600 sheet on a thin 1.2 mm Usibor1500 one): DD welds present a higher failure load than the corresponding DA welds at the same weld diameter. A consequence of the DD configuration is the lower weld rotation during loading due to lower bending deformation in this configuration.

## 2.6 Arc welding

In this part, the heterogeneous welding of Usibor1500 is studied. The sheets are welded in a overlap configuration (figure 2.4), which implies an upper and a lower sheet. The heterogeneity comes from two factors:

- The used filler wire (G3Si close to DP600 chemical composition to obtain heterogeneous welding),
- The thickness heterogeneity, because the two welded sheets have dissimilar thicknesses.

### 2.6.1 Configurations

The two welded configurations are:

- DA: 2.0 mm Usibor1500 as upper sheet and 1.5 mm Usibor1500 as lower one,
- DB: 1.5 mm Usibor1500 as upper sheet and 2.0 mm Usibor1500 as lower one.

Industrial requirements are numerous, for example the fusion zone penetration or the angle between the sheet and the seam, which are key parameters that must be controlled for the weld to be approved. For each configuration (with variation of grade or thickness), optimal welding parameters are found and collected in table 2.7.

Current type	Gas	Wire	Torch angle	Filler speed	Welding speed	Intensity	Voltage
Standard	8 % CO <sub>2</sub> + 92 % Ar	G3Si Ø1 mm	25°/10°	4.3 m/min	500 mm/min	115 A	18.5 V

Table 2.7: Arc welding parameters

For this design, only one type of tensile test is commonly carried out, a tensile test that is often related to the TSS test of spot welds. About five samples are tested for each configuration. One sample corresponds to a weld length of 30 mm, slice from larger weld. Fracture modes are observed for each sample and the strength is measured too. The five commonly encountered failure modes are collected in figure 2.28.

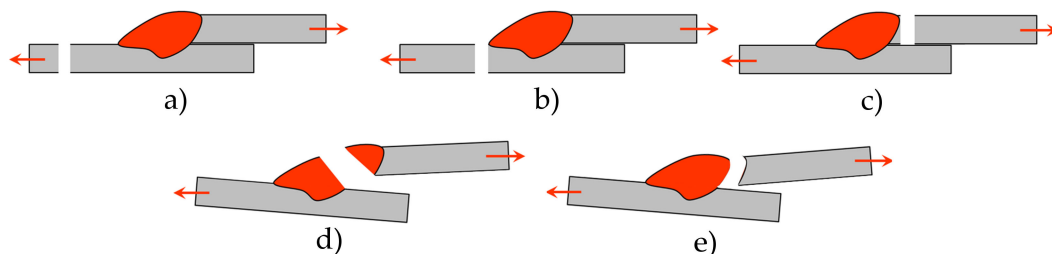


Figure 2.28: Arc weld failure modes: a) Base material failure, b) and c) HAZ failure, d) Molten zone failure and e) Border zone failure

The investigation methodology is the same as for spot welding. One sample is cut at the cross section of arc weld, polished and chemical by etched (with nitric acid) to reveal the different zones of the arc weld (Base material BM, heat affected zone HAZ, fusion zone FZ). The five other welded samples are tested in the tensile machine. Fracture modes are observed for each sample, and the failure strength is measured.

### 2.6.2 Microstructures

In this part, the microstructure of arc welds are investigated. The micrographic views of the two arc weld configurations allow to compare the fusion zone geometry in the two configurations, in particular on the weld height and width. In the DA case, because the

thicker sheet is located on the top of assembly, the fusion zone width is smaller than in the DB case where the molten metal dilution is more complicated on a thicker sheet. This result is confirmed by the high dilution observed in the DB case, where the distance between the CGHAZ and the notch root is higher than in the DA case.

Another remarkable geometrical parameter is the fusion zone penetration in the lower sheet. Once again, the sheet thickness influence on dilution is observed, where the fusion zone reaches the middle thickness in the thinner sheet (DB) but superficially penetrates the thicker sheet.

Some coating is concentrated under the fusion zone on the lower sheet and in the notch root. Temperatures reached during the welding process implies the melting of Al-Si coating which migrates and accumulates in the hottest zone (white phase in the notch root zone on figure 2.29.c and 2.29.d).

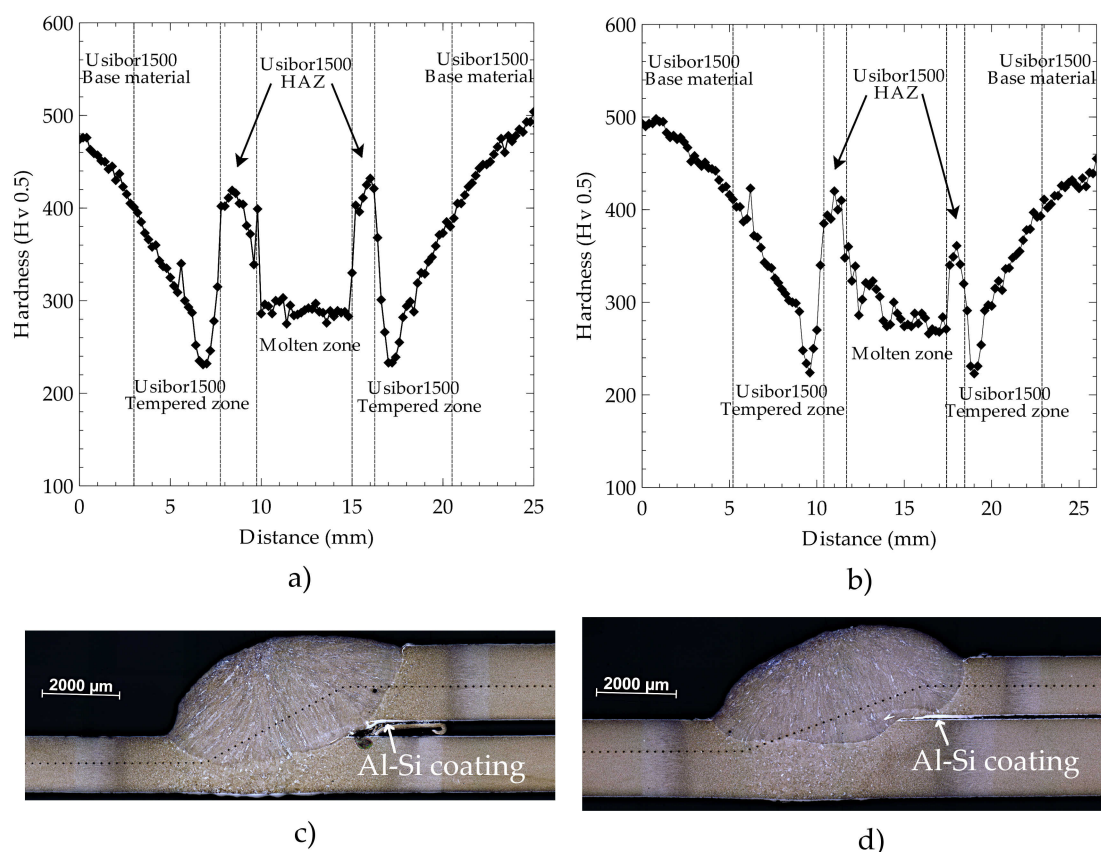


Figure 2.29: Arc weld hardness profiles for DA (Usibor1500 2.0 mm-Usibor1500 1.5 mm) and DB (Usibor1500 1.5 mm-Usibor1500 2.0 mm) configurations: a) DA hardness profile, b) DB hardness profile, c) DA metallographic cross-section and d) DB metallographic cross-section.

Concerning the microstructures, the consequences of the arc welding process are similar to that of the spot welding one. Usibor1500 has a heat affected zone (HAZ) which has two parts, the tempered martensite zone and the hard HAZ. The first one is the zone which

endorses a tempering of the Usibor1500 martensite, decreasing its hardness (hardness drop in figure 2.29.a and 2.29.b). The second HAZ is the hard one, which underwent temperature above  $A_{c3}$ , and is fully martensitic with austenite grain coarsening close to the fusion zone.

The tempered zone reaches hardness values around 230 Hv, which is clearly less than for spot welding (300 Hv in the tempered zone). This comes from the cooling rate that is lower in the arc welding and the self-tempering of weld pool during the linear welding process. The cooling rate also affects the tempered zone size, resulting in larger tempered zones for arc welds than for spot welds.

The cooling rate affects the hardness of hard Usibor1500 HAZ (undergone temperature above  $A_{c3}$ ). In arc welds, this zone presents only 400 Hv, whereas its hardness reached 500 Hv in spot welds. Such decrease could also be explained by the microstructure morphology: during arc welding, the lath close to the interface could grow more easily than in the coarse grain zone of the resistance spot welds (RSW). Moreover, no self-tempering (RSW case) results into very hard and brittle martensite phase.

Molten zone hardness is around 280 Hv, due to the important amount of G3Si brought during process. This hardness value gives a approximation of the dilution ratio between G3Si and Usibor1500 during the welding process.

Based on the preceding and according to literature, four different hardness zones can be highlighted in these profiles:

- Usibor1500 base metal,
- Usibor1500 tempered zone,
- Usibor1500 HAZ,
- Fusion zone.

### 2.6.3 Failure Modes

The weld assemblies were cut into 30 mm width sample along the welding direction. Mechanical tests were carried out on Zwick tensile machine with a 100 kN load cell at a crosshead speed of 15 mm/min. Special hydraulic jaw assemblies were used, according to the standards. Jaws of the tensile machine are shifted to take the sheets positioning into account. This test is occurring till the arc weld fails.

Two important characteristics of arc weld fracture are usually extracted and recorded after such destructive tests: failure load and failure mode. While the former is explicitly defined by the maximum load reached during the test, the latter refers to a specific classification (figure 2.28). The obtained failure modes are gathered in figure 2.30.

In the two configurations failure occurs in the thinnest sheet side, but failure is not located in the same zone. For the configuration DA with the thinnest sheet downside, the failure occurs in the tempered martensite zone. A large deformation with necking could be observed in figure 2.30.a.

For DB configuration (thinnest sheet on upside), failure occurs in the fusion zone. This failure seems to initiate close to the notch root. In an other hand, large deformation is observed in the tempered zone of the thinnest sheet, which induces a tight competition between the two failure modes.

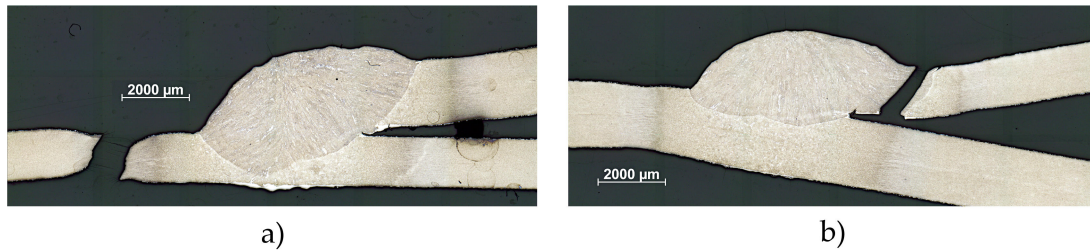


Figure 2.30: Arc weld failure modes: a) DA configuration (thicker upside) and b) DB configuration (thicker downside).

#### 2.6.4 Failure strengths

The failure strengths of the two arc welds configurations are collected in the table 2.8:

Configuration	Strengths	Standard deviation $\pm$
DA Usibor1500 2.0 mm as upper sheet	816	9
DB Usibor1500 1.5 mm as upper sheet	836	16

Table 2.8: Arc welding failure strengths (MPa, average of five tests).

The strengths of the two configurations are almost the same. These results support the hypothesis of close competition between the failure modes. Globally, the second configuration (with the thinner sheet upside) shows better strengths results. It could be explained by the assembly stiffness. When the thicker Usibor1500 sheet is upside, the weld bead is larger and a little harder and thus increases the arc weld stiffness. During tensile test, the rotation and notch root opening are delayed compared to the other configuration. This involves high stress concentration in the thinner (and downside) sheet, which failed earlier in the weakest zone (Tempered martensite zone of thinner sheet). In the other configuration, the weld bead is a little softer and more elongated. This geometry promotes the arc weld rotation during the test and notch root opening. It allows a better stress repartition in the tempered martensite zone of the thinnest sheet.

## 2.7 Conclusion

In this section, weldability of two widely used steels in industry (Usibor1500 and DP600) was studied. A fine microstructural characterization was executed on base materials and spot welds and their weldability was studied. Four configurations of thicknesses were welded to highlight the geometry influence and failure mechanisms.

Then, failure modes and strengths of the four Usibor1500/DP600 assemblies (thicknesses varying) for three intensities along the welding range were observed. Failure modes were firstly highlighted by macroscopic investigations and then by scanning electron mi-

croscopy in order to identify ductile or brittle fracture surfaces. Failure strengths were compared between the four configurations and homogeneous data of same steel grades.

Then, several aspects were discussed, in particular the influence of liquid metal splash on cross tension failure strengths when intensity is close to upper end of the welding range. Moreover, a positive deviation of weld assemblies strength was highlighted in the case of dissimilar thickness spot welds, in particular thanks to dilution in the fusion zone. However, during tensile shear tests, no positive effect of the dissimilar thickness was observed.

## Chapter 3

# Experimental results of highly heterogeneous welding (Duplex/DP600)

Chapter 2 presented the characterization of the mechanical behaviour of heterogeneous weld assemblies for two Automotive High Strength Steels (AHSS) widespread in automotive industry (DP600 and Usibor1500). This chapter focuses on the fine experimental characterization of highly dissimilar welding of a third generation steel (Duplex) with the same common DP600 steel as above. Similarly, resistance spot welding (RSW) and Arc welding will be studied. The same experimental procedure as in chapter 2 will be followed, from the material properties, to the failure mechanisms of the different welds, depending on the configuration.

### Contents

<b>3.1</b>	<b>Materials and welding configurations</b>	<b>70</b>
3.1.1	Materials	70
3.1.2	Duplex steelmaking	70
3.1.3	Microstructures	74
3.1.4	Welding configurations	75
<b>3.2</b>	<b>Spot weldability</b>	<b>76</b>
3.2.1	Welding range	76
3.2.2	Heat affected zone microstructures	78
<b>3.3</b>	<b>Failure modes</b>	<b>85</b>
3.3.1	Cross tension tests	86
3.3.2	Tensile shear tests	92
<b>3.4</b>	<b>Failure strengths</b>	<b>96</b>
3.4.1	Cross tension strengths	96
3.4.2	Tensile shear strengths	98
<b>3.5</b>	<b>Discussion</b>	<b>100</b>
3.5.1	Aluminum effect on performance	100
3.5.2	Ferrite layer formation	101



<b>3.6 Arc welding</b>	<b>106</b>
3.6.1 Configurations	106
3.6.2 Microstructures	107
3.6.3 Mechanical tests	110
<b>3.7 Conclusion</b>	<b>111</b>

---

## 3.1 Materials and welding configurations

### 3.1.1 Materials

In this chapter, the study focuses on the assembly of the third generation AHSS Duplex with the Dual Phase DP600.

Duplex steel, is a new concept aiming at reducing the car weight. Duplex concept consists in obtaining ferritic-austenitic steels with low density (thanks to of high aluminium and manganese content, see table 3.1). Duplex aims at replacing DP600 in the automotive industry thanks to their high UTS ( $\approx 800$  MPa) and high elongation ( $\sim 30\%$ ). It is assumed that the weight saving could be greater than 10%. Due to the high amount of aluminium and manganese, Duplex welding is a significant challenge.

Steel grade (x 0.001wt%)	C	Mn	Si	N	Al
DP600 1	88	1870	150	4	21
DP600 2	104	1550	169	4	29
G3Si (filler wire)	75	1460	547	6	26
Duplex 4Al	200	7920	300	4	4070
Duplex 8Al	200	7600	270	3	7840

Table 3.1: Chemical composition of steel grades (x 0.001wt%)

### 3.1.2 Duplex steelmaking

Duplex steels are breakthrough products under development at ArcelorMittal. The manufacture of studied samples is done by Vacuum Induction Melting casting (VIM). This process induces small base material volumes. The initial aim for the studied Duplex steels was 8wt% of manganese and 4wt% or 8 wt% for the aluminium content. In this way, the aluminium effect on microstructure and welding could be studied. Lastly, after casting, the chemical composition of obtained materials are collected in table 3.1. The final chemical compositions are consistent with the stated objectives. Small ingots ( $135 \times 95 \times 30$  mm<sup>3</sup>) were obtained at the end of casting. This is the initial state as received in this project. In order to weld these Duplex steels, ingots had to be turned into steel sheets.

The first process to transform the ingots into sheets is the hot rolling. This step allows to reduce thickness from 30 mm to 2.7 mm, obtaining a hot rolled steel. Hot rolling is a milling process involving high temperature rolling (typically at a temperature over 900 °C), above the steel recrystallization temperature. Thus the steel can be shaped and formed

easily, and can be produced in much larger sizes. Because of the important thickness reduction, the hot rolling process is done in several steps. All the parameters are wisely chosen to obtain a fine microstructure. These parameters (holding temperature, end rolling temperature, cooling rate and winding temperature) directly influence the microstructure of the obtained steel sheets. They are collected in table 3.2.

Thickness reduction	Heating time and temperature	Passes	End of rolling temperature	Cooling rate	Winding temperature and cooling rate
30 mm to 2.7 mm	30 min and 1250 °C	7	900 °C	30 °C/s	550 °C at 30 °C/h

Table 3.2: Hot rolling parameters

After hot rolling, the microstructure of the two Duplex grades was checked, observing cross sections with optical microscopy and performing hardness tests. The microstructure of the two hot rolled Duplex steels are presented in figure 3.1 (chemical etching: KLEMM II and Nital 1%).

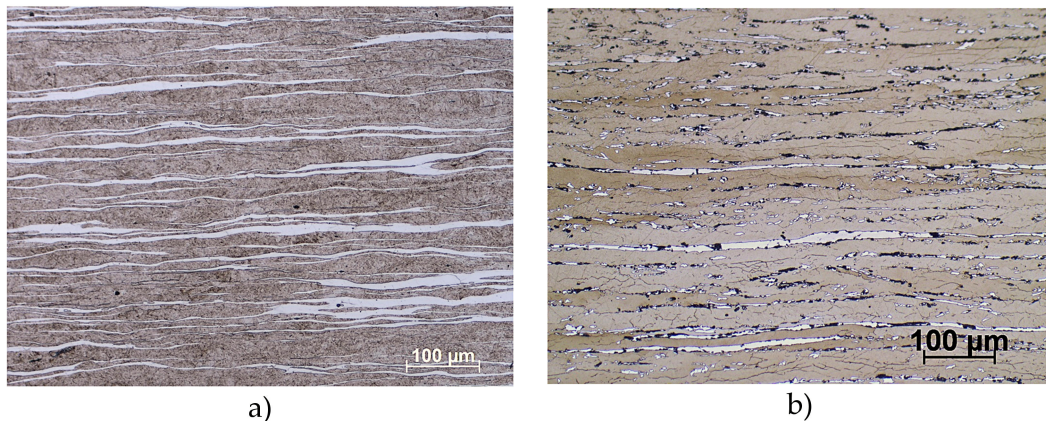


Figure 3.1: Hot rolled steel microstructures: a) Duplex 4Al and b) Duplex 8Al.

The rolling direction is visible on the two micrographs (horizontal). Duplex 4Al is formed of two constituents, the ferrite (white areas) and a compound of fine lamella of ferrite and austenite (dark areas on figure 3.1.b). The volume fraction of ferrite is about 40%, even if white areas on the micrography are only 15%.

Duplex 8Al contains three phases, a ferrite matrix oriented in the rolling direction (darker phase), austenite at ferrite grain boundaries (white phase), and kappa phase in the austenite grains (black phase). The volume fraction of ferrite is about 80% and the austenite + kappa about 20%. The kappa phase (ordered  $Fe_yAlC_x$ ) appeared because of a too low cooling rate during hot rolling [SCH 05] [PAR 84], but is not harmful.

Hardness tests on the two grades lead respectively to 400 Hv and 280 Hv for Duplex 4Al and 8Al, which is consistent with ferrite volume fraction (ferrite phase is softer than austenite phase).

The obtained sheet thicknesses after hot rolling are too important for Resistance Spot Welding (RSW). An additional step is needed: cold rolling. Because of high hardness values (in particular for Duplex 4Al) and of significant kappa phase content (in the Duplex 8Al), an experimental procedure was set up to evaluate the cold rolling ability of the two Duplex steels. After many trials, practical heat treatment temperatures for the two steel grades were identified: 650 °C for 4Al and 850 °C for 8Al. The cold rolling process success turned out to be impossible without heat treatments (left sample in figure 3.2.a and 3.2.b). Duplex 4Al was too hard for rolling mill, and Duplex 8Al fully delaminated after a few passes. The different treatments listed were tested, on Duplex 4Al:

- 4Al-1: no treatment
- 4Al-2: 650 °C for 20 minutes
- 4Al-3: 650 °C for 30 minutes

And on Duplex 8Al:

- 8Al-1: no treatment
- 8Al-2: 850 °C for 5 minutes
- 8Al-3: 850 °C for 15 minutes

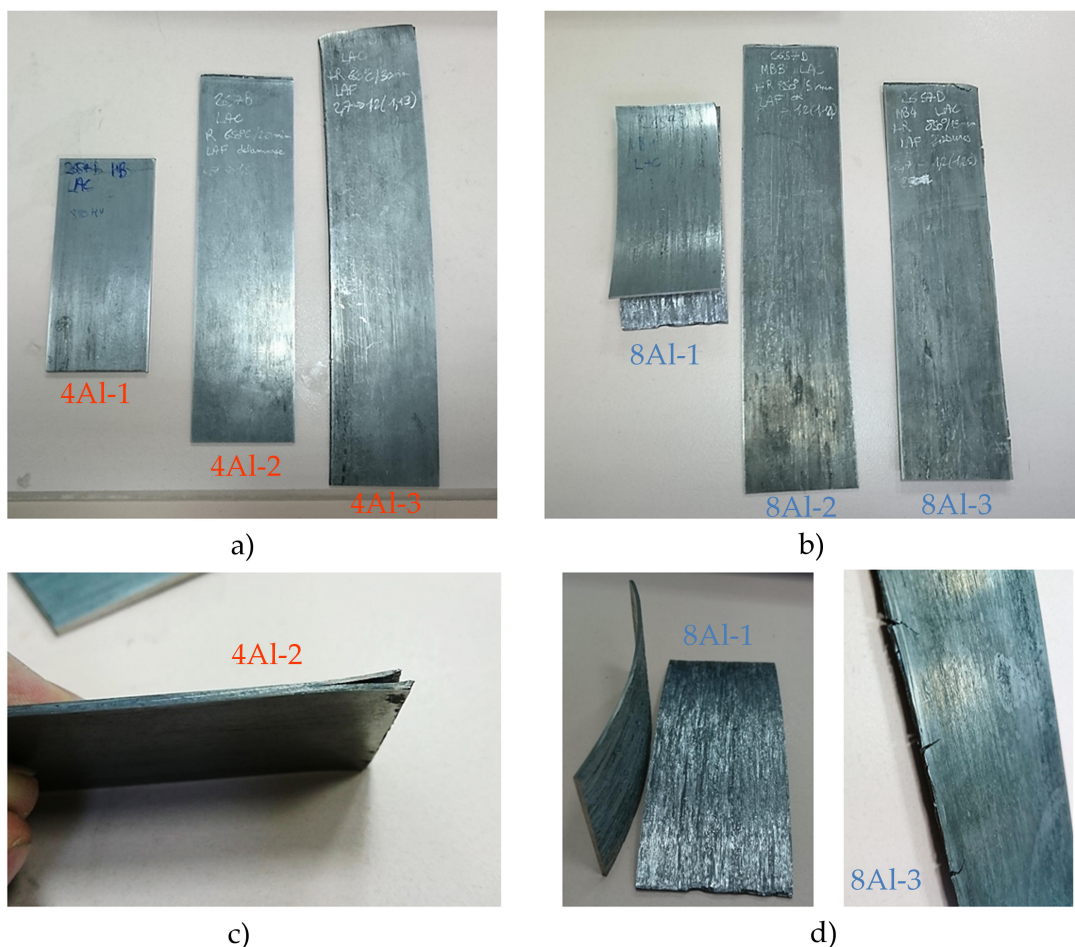


Figure 3.2: Cold rolling tests a) Duplex 4Al, b) Duplex 8Al, c) delamination of Duplex 4Al and d) delamination and cracking of Duplex 8Al.

For Duplex 4Al, 20 minutes of treatment were not enough, and delamination appeared at the sheet extremities before obtaining the final 1.2 mm thickness, whereas 30 minutes seem sufficient to obtain a softer material and a perfect sheet of 1.2 mm without cold rolling defects (figure 3.2.a and 3.2.c).

For Duplex 8Al, 15 minutes of treatment was inappropriate because of the occurrence of cracks at the sheet edges and on the surface (3.2.d), whereas the sheet treated for 5 minutes presented no defects. The 5 minutes treatment allows partial ferrite recrystallization and stress relaxation.

Finally, 650 °C for 30 minutes (Duplex 4Al) and 850 °C for 5 minutes (Duplex 8Al) heat treatments were chosen. These treatments are not optimal but allow a safe compromise for base materials cold rolling.

The microstructures of the two Duplex grades are the same before and after cold rolling (figure 3.3). The phase fractions are similar and the microstructure looks crushed in the transverse direction. The hardness clearly increased for the two grades because of strain hardening from 280 Hv (after HT 650 °C 30 minutes) to 400 Hv for the Duplex 4Al and from 270 Hv to 360 Hv for the Duplex 8Al.

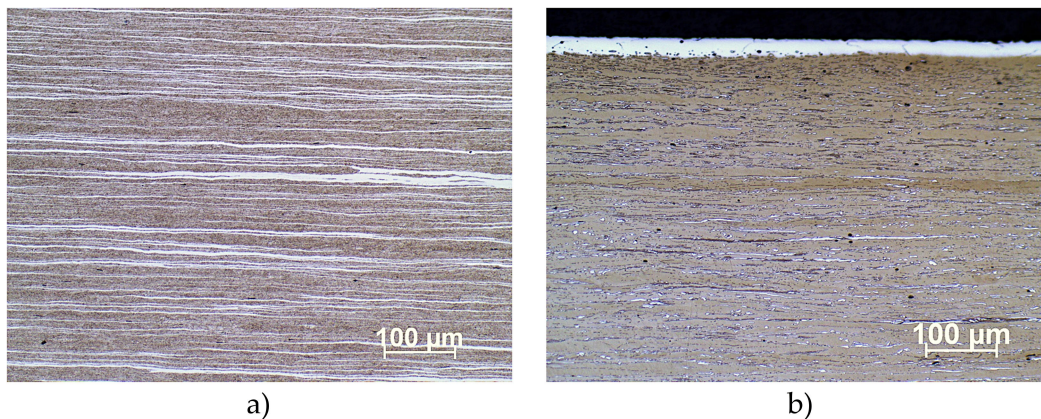


Figure 3.3: Cold rolled steel microstructures: a) Duplex 4Al and b) Duplex 8Al.

After cold rolling, an annealing is always carried out to release the stress and dislocations in the sheets. However, to obtain the best final product mechanical properties, the annealing was done at 850 °C for 136 seconds. The treatment was realized under controlled atmosphere (argon gas).

Mechanical tests (ISO tensile tests) were done on the two Duplex grades, before and after annealing. The mechanical behaviour of Duplex 4Al and 8Al before and after annealing is shown in figure 3.4.

By comparison with DP600, Duplex steels show higher Ultimate Tensile Strengths (UTS) and almost the same elongation properties, in particular for the Duplex 4Al. Using a Duplex 4Al steel instead of DP600 steel could allow the Carmakers to decrease the sheet thickness, and in this way reduce the CO<sub>2</sub> emissions. It is important to note that the initial density of Duplex steels is lower than DP600's one.

The main characteristics (A% and UTS) of the two Duplex base materials are collected in table 3.3.



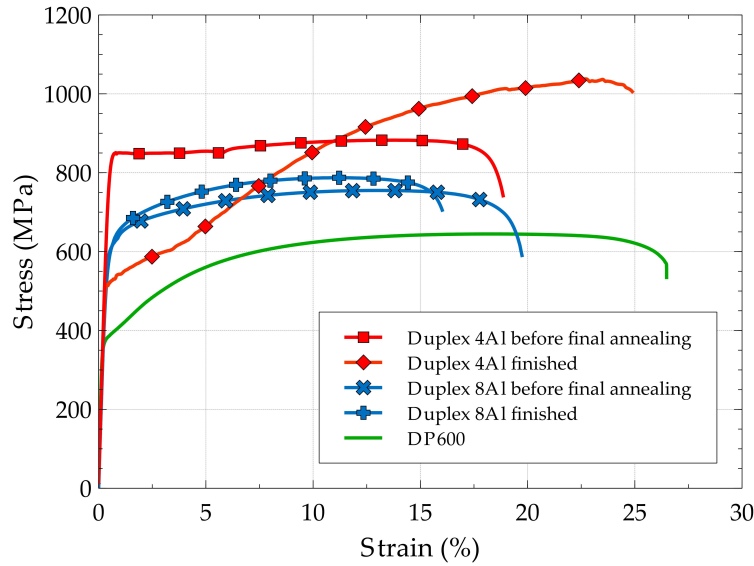


Figure 3.4: Mechanical properties of Duplex steel grades before and after homogenizing annealing (Uniaxial ISO tensile test).

Steel grade	Elongation at rupture A% (%)	Ultimate Tensile Strength UTS (MPa)
Duplex 4Al	24.9	1045
Duplex 8Al	16.0	787

Table 3.3: Mechanical properties of Duplex steel grades in the final state (Uniaxial ISO tensile test).

The discussions about the final mechanical properties obtained is out of the scope of this PhD but it is worth noting that this work constitutes one of the first attempts to optimize the process for these grades.

### 3.1.3 Microstructures

In this section, the Duplex and DP600 microstructures are finely characterized by Confocal Laser Scanning Microscopy (CLSM) and Scanning Electron Microscopy (SEM). For confocal microscopy, KLEMM II etching reagent was used to observe the microstructure. For SEM observation, Villela and Nital 1% etching reagents were used to reveal the microstructure of steels, because KLEMM II is an electron barrier. The observed microstructures are shown in figures 3.5 and 3.6.

DP600 base material is made of martensite islands in a ferritic matrix (localized at the ferrite grain boundaries) (figure 3.5.a and 3.5.b). The confocal microscopy allows to estimate the ferrite grain size in the microstructure: around 10  $\mu\text{m}$ . The SEM observation shows the martensite location (white phase), at the ferrite grain boundaries, and allows to estimate the martensite phase fraction (around 10%).

For the two Duplex steels (4Al and 8Al), a ferritic matrix is observed completed with

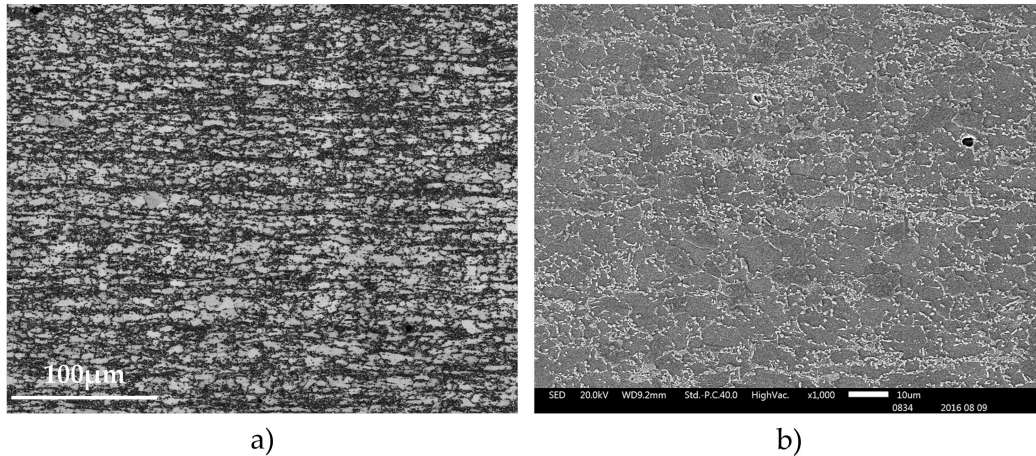


Figure 3.5: Microstructure of DP600 base material: a) confocal microscopy observation and b) SEM observation.

austenite with a varying phase content, and the rolling direction is observable in the microstructures (horizontal in figure 3.6).

Figure 3.6.a shows Duplex 4Al observed with confocal microscopy, where ferrite is the dark phase and austenite is the white one. The ferrite and austenite fractions are approximatively balanced (50% ferrite, 50% austenite). The microstructure is composed of two domains, one fully ferritic with large bands, and the second also exhibiting large bands but with interconnected ferrite and austenite phase inside, as in a pearlitic microstructure.

Figure 3.6.c shows Duplex 8Al microstructure, Ferrite is still the dark phase and is predominant with a phase fraction of about 90%. The banded microstructure is observed in the Duplex 8Al case too, with austenite at the ferrite grain boundaries. No kappa phase is observed in the austenite islands because the cooling rate was important enough to not form kappa.

### 3.1.4 Welding configurations

In this study, only one thickness for each steel grade will be used. The chosen thickness is 1.2 mm, which corresponds to a usual thickness for spot welded steels. Unlike in the previous chapter (Usibor1500/DP600 welding), the thickness influence will not be studied in this part because:

- of the small amount of Duplex base materials,
- this Duplex welding study will therefore focus on the metallurgical aspects.

Two configurations will be welded:

- Duplex 4Al (1.2 mm) with DP600 (1.2 mm),
- Duplex 8Al (1.2 mm) with DP600 (1.2 mm).

Because Duplex products are under development, these steels are not coated unlike DP600 (GI 10 µm). The welding of these two configurations will allow to measure the aluminium influence on the spot welding geometry, microstructure and mechanical performance.

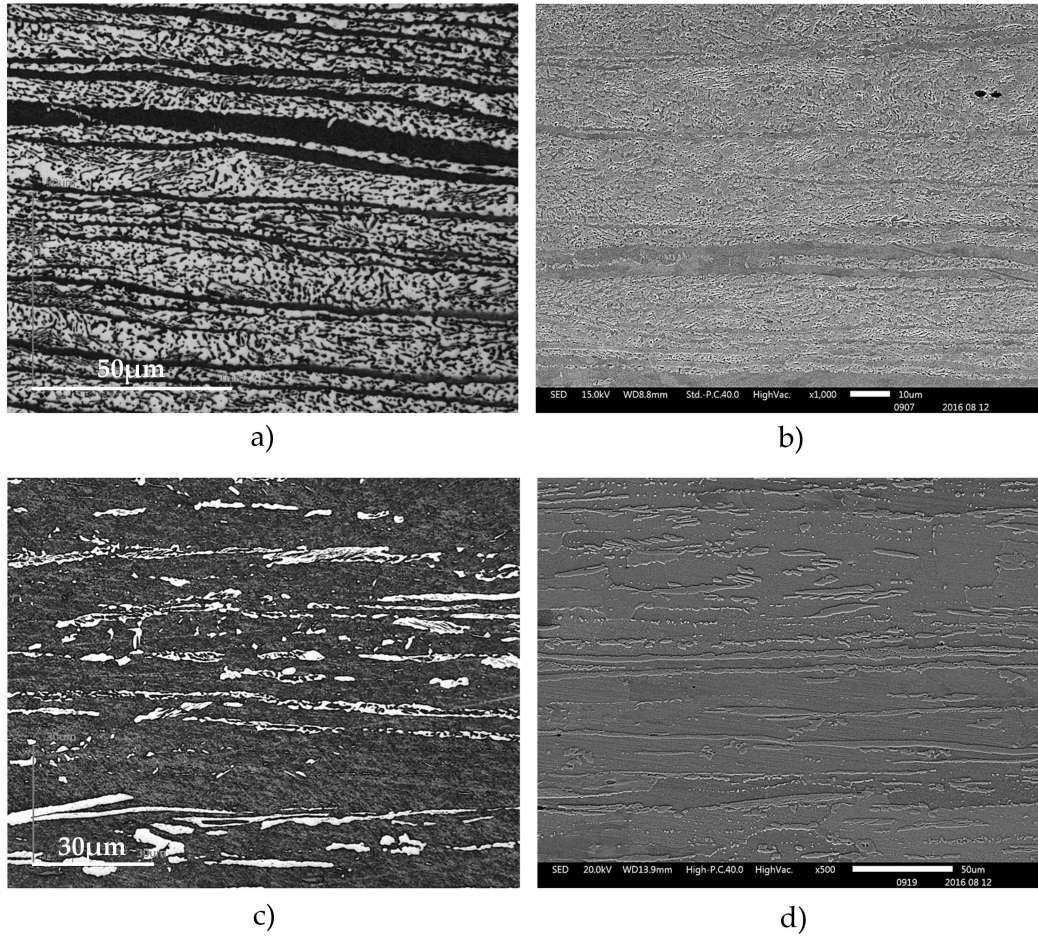


Figure 3.6: Microstructure of Duplex base materials: a) confocal microscopy observation of Duplex 4Al, b) SEM observation of Duplex 4Al, c) confocal microscopy observation of Duplex 8Al and d) SEM observation of Duplex 8Al.

## 3.2 Spot weldability

### 3.2.1 Welding range

In this part, the spot weldability of the two configurations will be discussed as well as the influence of process on microstructure, nugget formation and hardness of each heat affected zone (HAZ). For each configuration, the welding range is investigated using the ISO 18278-2 standard (2004). The main welding parameters are collected in table 3.4.

Electrode diameter	Pulse Number	Welding time	Holding time	Electrode force
6 mm	1	15 p	15 p	400 daN

Table 3.4: Welding parameters (Duplex is welded with DP600 in both cases),  $p=0.02$  s.

Using the same parameters for each configuration, the welding range is investigated by

changing the welding intensity according to two same conditions as in chapter 2 ( $I_{min}$  and  $I_{max}$ ).

Using this methodology, the welding ranges obtained with a SCHLATTER Selecta P2 machine for the two configurations are shown in figure 3.7. The welding ranges are around 1 kA large (0.8 kA for Duplex 4Al and 1.1 kA for Duplex 8Al).

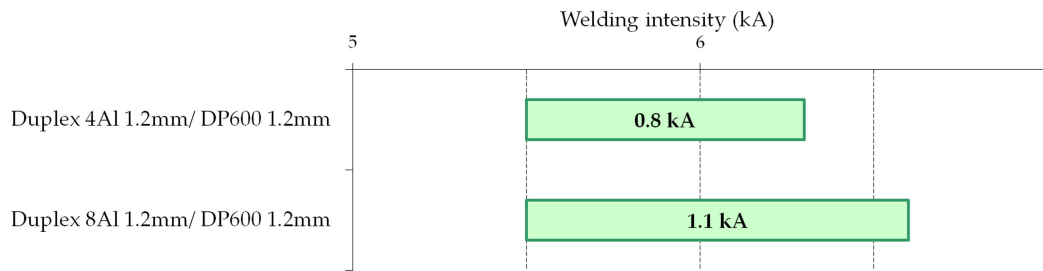


Figure 3.7: Spot welding intensity range of the two welded configurations.

As in chapter (chapter 2), the welding ranges of the two configurations are used to define three intensity values by configuration:

- Lower end intensity (close to  $I_{min}$ )
- Middle intensity (chosen in the middle of  $[I_{min}, I_{max}]$ )
- Higher end intensity (close to  $I_{max}$ )

These three intensities in each welding configuration are used to weld several test and observation samples.

For each configuration, and welding current, seven samples are welded, one for the microstructural observations and hardness tests, three for the cross tension tests (CTS) and three for the tensile shear tests (TSS). The micrographic sample is cut at the middle cross section of spot weld, polished and chemical etched (with Villela and Nital 1% reagents) to reveal the different zones of the spot weld (Base material BM, heat affected zone HAZ, fusion zone FZ and other particular zones). The six other welded samples are tested, three in CTS and three in TSS. Fracture modes are observed for each sample, and the failure strength is measured.

The micrographs of dedicated samples allow to compare the nugget size when the intensity changes. Figures 3.8 and 3.9 show the present Duplex 4Al/DP600 and Duplex 8Al/DP600 spot weld cross sections for the three positions in the welding range. One can observe the increase in nugget size with increasing welding current intensity regardless of the welded steels.

On the micrographic views, a white layer is observed between the fusion zone (nugget) and the DP600 HAZ. This zone will be investigated, like all the HAZ, in the next section.

All micro-hardness profile lines start in the Duplex base metal, cross the fusion zone and end within the DP600 base metal (figure 3.10.c and 3.10.d).

In figures 3.10.a and 3.10.c, for Duplex 4Al the hardness value of base material is 250 Hv, the fusion zone 430 Hv, and DP600 base material 200 Hv. DP600 HAZ hardness is 360 Hv as expected, but Duplex HAZ is difficult to characterize because of limited number of measurement points in this zone. In figure 3.10.b and 3.10.d), Duplex 8Al base material exhibits a hardness value of 260 Hv and the fusion zone hardness is 290 Hv.



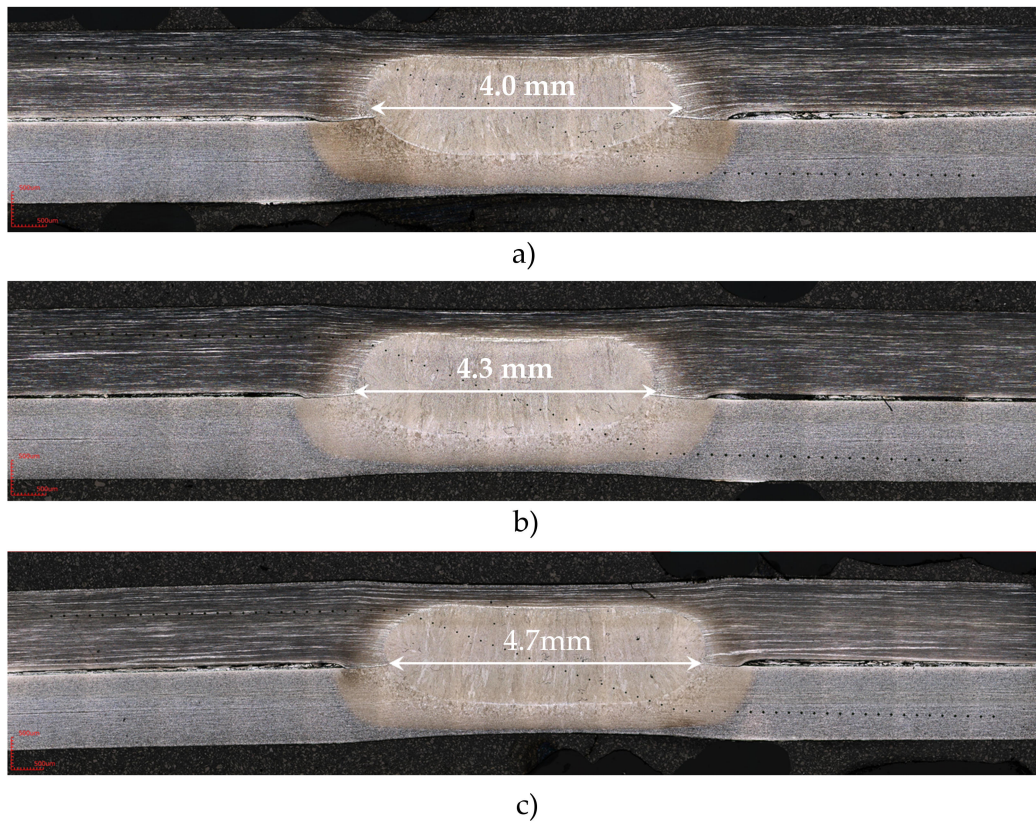


Figure 3.8: Spot weld metallographic cross sections of Duplex 4Al/DP600 spot welds at the three positions in the welding range (Duplex 4Al is always the upper sheet): a) lower end, b) middle position, c) upper end.

To better understand the HAZ microstructure and hardness, a finer investigation is carried out in the next section.

### 3.2.2 Heat affected zone microstructures

Heat Affected Zones (HAZ) of Duplex welds show some unusual features. Duplex products being under development, the welding process impact on microstructure is not really known. In this section, microstructures of HAZ will be observed and characterized.

#### 3.2.2.1 Microstructures observation (Laser and Electron Scanning)

First, the Duplex 4Al HAZ has been observed. This zone is located between the nugget (fusion zone) and the Duplex 4Al Base Material (BM). In figure 3.11, a focus on the Duplex 4Al HAZ is done. On the left, the molten nugget (fusion zone) is observed consisting of a mix of Duplex 4Al and DP600 cooled from melting temperature to 20 °C in a few seconds. On the right, the Duplex 4Al base material is observed with a microstructure oriented in the rolling direction composed of austenite and ferrite. Finally, between the two previous zones, grain coarsening is observed in the HAZ. In particular, nearly equiaxed ferrite grain

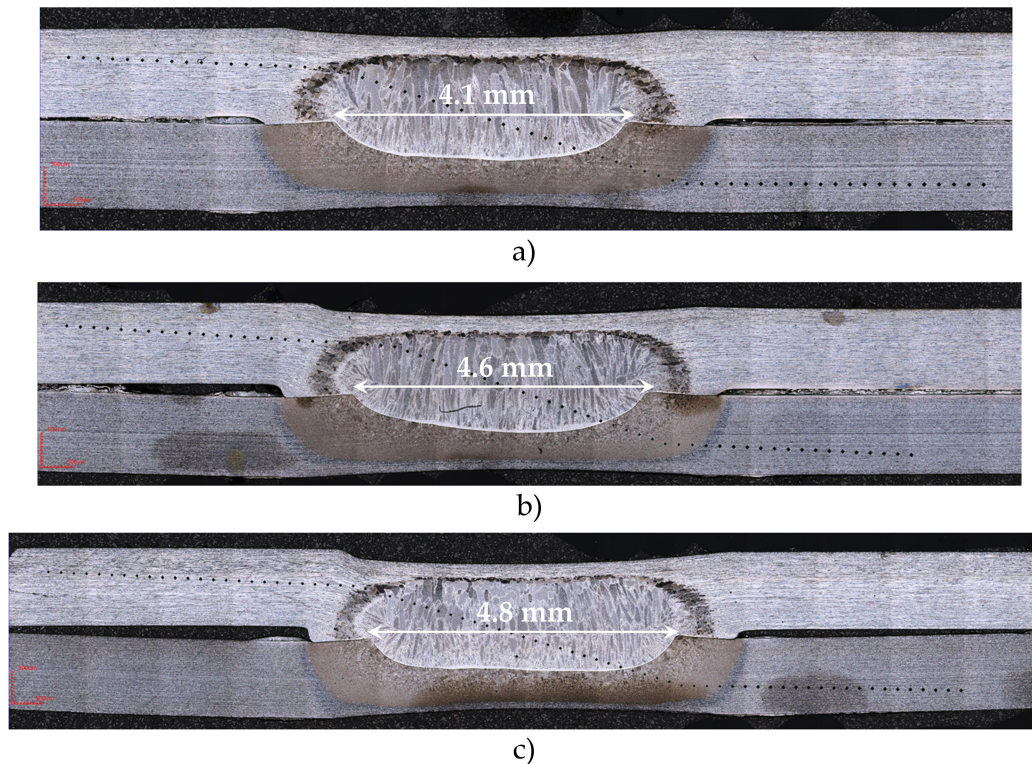


Figure 3.9: Spot weld metallographic cross sections of Duplex 8Al/DP600 spot welds at the three positions in the welding range (Duplex 8Al is always the upper sheet): a) lower end, b) middle position, c) upper end.

and some austenite at the grain boundaries can be seen.

Second, the Duplex 8Al HAZ is shown in figure 3.12. A coarsening of ferrite grain is observed when reaching the vicinity of the nugget but on a larger zone than for Duplex 4Al HAZ. Moreover, grain coarsening is clearly more important for the Duplex 8Al HAZ, with ferrite grains which could reach size greater than  $100\text{ }\mu\text{m}$ . Some austenite was also formed at the grain boundaries like in the Duplex 4Al HAZ, but the real particularity of Duplex 8Al HAZ is the formation of a acicular phase with 18R-type Long Period Stacking Ordered (LPSO) structure called "18R martensite" by Cheng and al. [CHE 03]. This phase is formed in the grain centre (fine acicular microstructure, figure 3.12.b and 3.12.c), and carbon depleted zone is observed between intergranular austenite and 18R martensite concentrated in the grain centre, in fact, ferrite is depleted in carbon. Some investigations showed that carbon content in the 18R martensite is precisely half the intergranular austenite one.

The fine observation of Duplex 8Al/DP600 spot welds microstructure revealed a particular microstructure at the interface between the DP600 HAZ and the nugget. First, the nugget contains oriented ferrite grains from solidification with austenite at the grain boundaries and some 18R martensite inside, but less than in the Duplex 8Al HAZ. This is attributed to dilution with DP600 (lower amount of carbon). Moreover, a ferrite layer is observed (figure 3.13) at the interface, on the nugget side, with no martensite 18R and no austenite, which is probably due to carbon depletion in this zone as shown by Babu



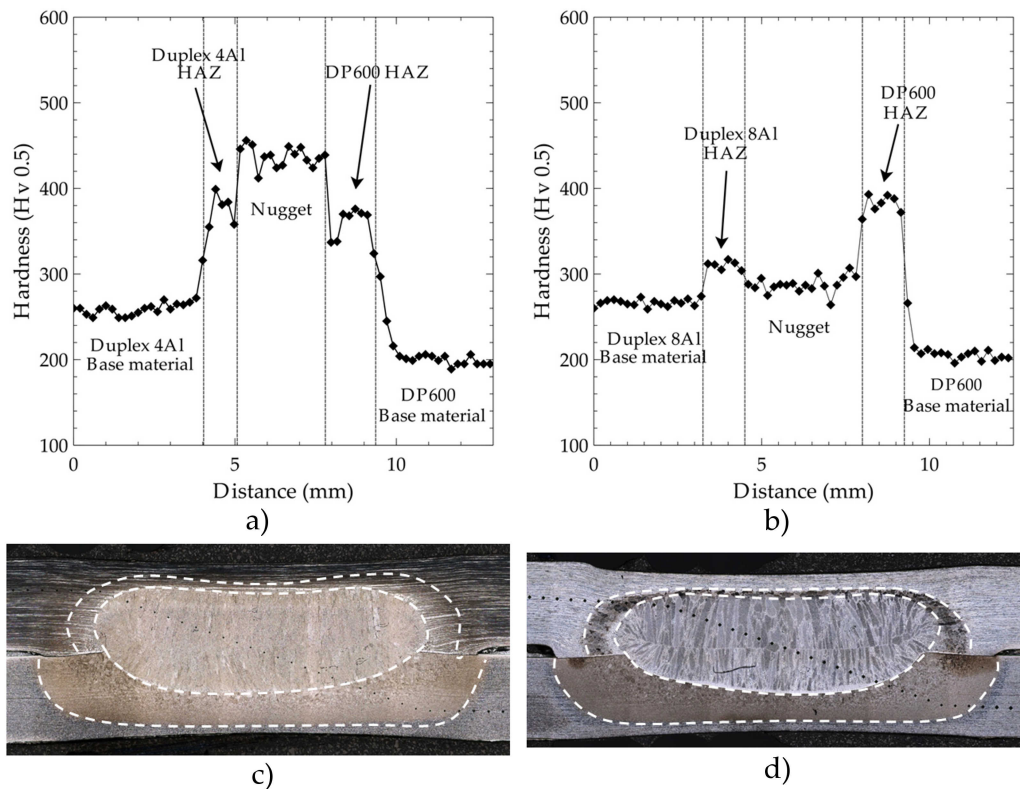


Figure 3.10: Spot weld hardness profiles for Duplex 4Al/DP600 and Duplex 8Al/DP600 configurations: a) Duplex 4Al hardness profile, b) Duplex 8Al hardness profile, c) Duplex 4Al metallographic cross-section and d) Duplex 8Al metallographic cross-section.

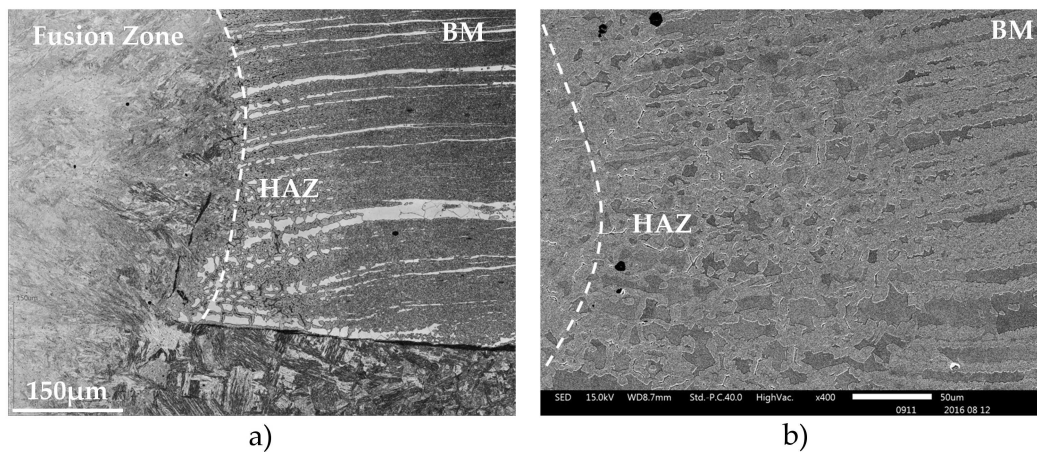


Figure 3.11: Microstructure of Duplex 4Al heat affected zone with scanning microscopy a) Laser (confocal) and b) Electron (SEM).

[BAB 02]. The thickness of this layer goes from 20 µm to 40 µm depending on the distance to the nugget centre. It is thin at the peripheral region (close to the notch root) and it increases when approaching to the central axis of the weld which is consistent with obser-

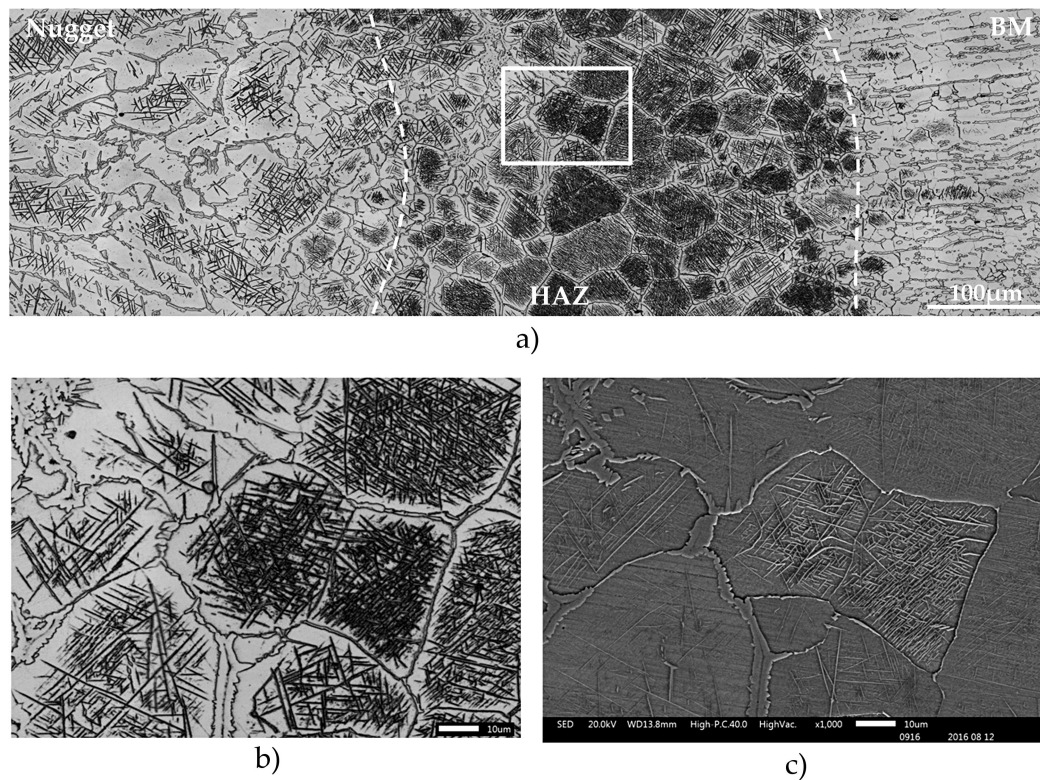


Figure 3.12: Microstructure of Duplex 8Al heat affected zone with scanning microscopy: a) Laser (confocal), b) Laser zoom on HAZ (confocal) and c) Electron zoom on HAZ (SEM).

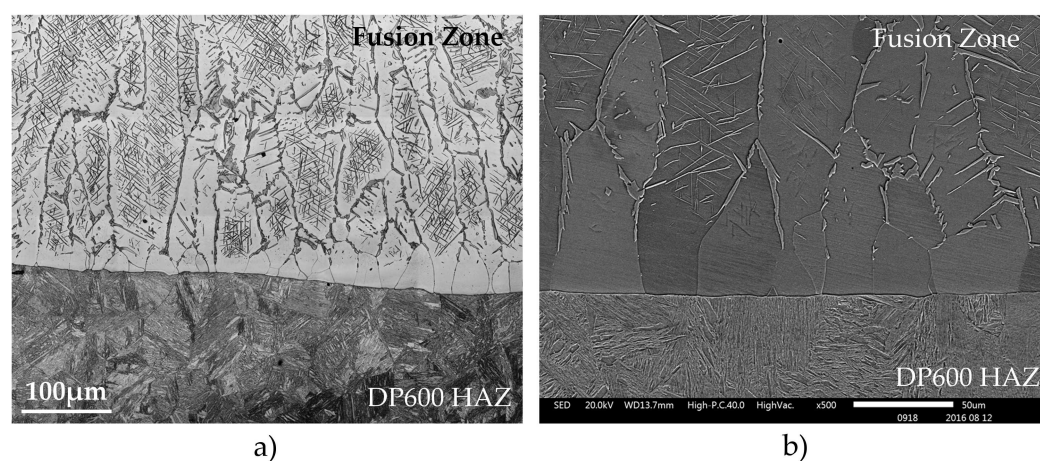


Figure 3.13: Microstructure of the Ferrite Layer with scanning microscopy of Duplex 8Al/DP600 spot weld: a) Laser (confocal) and b) Electron (SEM).

ventions by [QIU 09a] [QIU 09b] for another dissimilar spot welding system. Unfortunately, it seems to be a weak zone for the spot weld, which will be discussed later.

### 3.2.2.2 Hardness characterization

The micro-hardness tests done on spot welds didn't give any specific information on the HAZ and the ferrite layer because the step and the load were too large (200  $\mu\text{m}$  and 500 g Vickers setting). New finer hardness tests were carried out with a 100 g Vickers setting and a 50  $\mu\text{m}$  step. These tests were done through each HAZ (Duplex 4Al and Duplex 8Al) and the ferrite layer. These new hardness tests allow to better estimate the local properties of the different zones but an important dispersion is still observed, due to important microstructure variations. The tests results are collected in figure 3.14.

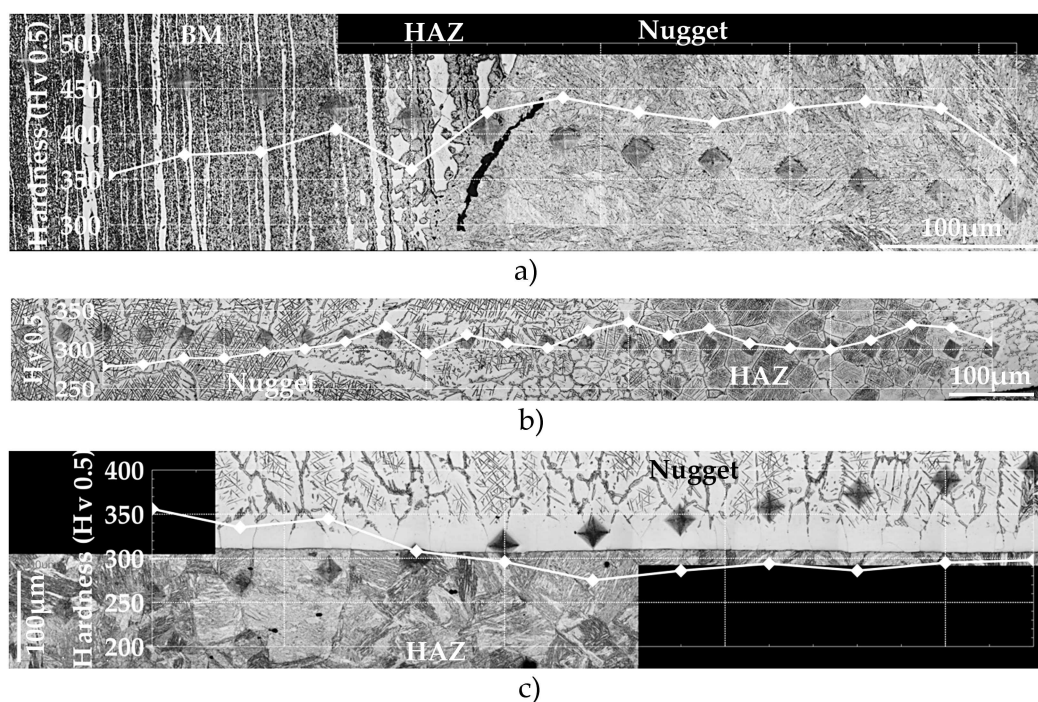


Figure 3.14: Hardness profile (Hv0.1 with 50  $\mu\text{m}$  indent spacing) of HAZ a) Duplex 4Al HAZ, b) Duplex 8Al HAZ and c) Interface between DP600 HAZ and Nugget (melted DP600 and Duplex 8Al) (ferrite layer).

In figure 3.14.a, the estimated hardness of Duplex 4Al HAZ is 370 Hv even if, close to the interface with the nugget, ferrite grains are coarsening which can induce some scattering of the hardness. For the Duplex 8Al HAZ (3.14.b), the hardness values oscillate between 300 Hv and 330 Hv depending on the measurement location, at the centre of ferrite grain or at the grain boundary (austenite-rich).

For the DP600 HAZ and ferrite layer in the nugget of welded Duplex 8Al and DP600 (3.14.c), the hardness values are difficult to evaluate because of the low layer thickness. However a trend is observed, the hardness value of the ferrite layer 275 Hv is lower than in the nugget 300 Hv and it constitutes the weak point of the assembly when the DP600 side is considered.



### 3.2.2.3 Electron Back-Scatter Diffraction (EBSD) analysis

In the Duplex 4Al and 8Al HAZ, ferrite grain coarsening is observed after welding of the Duplex steel with DP600 steel. This grain coarsening is more important when the temperature reached in this zone is close to the fusion temperature, so geometrically close to the nugget (fusion zone). It is critical to know if the coarsening affects the grain orientation, or if rolling direction affects recrystallized ferrite grain. EBSD analysis was carried out to observe the randomness of crystallographic orientation of these grains.

For the sample preparation, a mechanical polishing was done until  $1\mu\text{m}$  and Struers OPU ( $0.2\mu\text{m}$ ) was used for 10 minutes. The analysis was done with a FEG JEOL 7001F SEM equipped with an EBSD camera. The analysed zone is marked in figure 3.15.

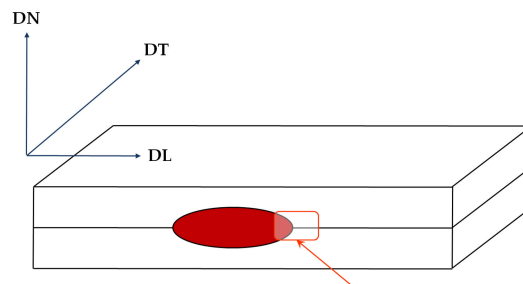


Figure 3.15: Analysed zone with EBSD.

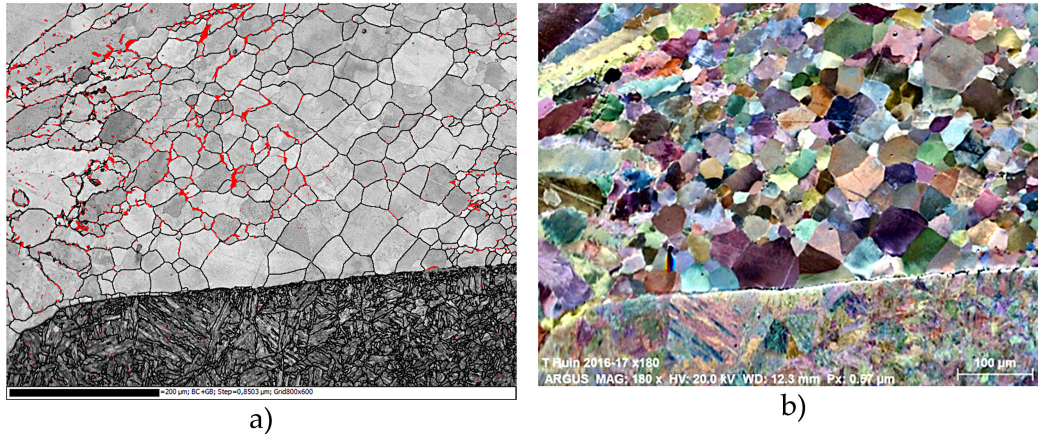


Figure 3.16: Microstructure of Duplex 8Al HAZ a) alpha Band contrast map, b) Forward-scattered Electron (FSD) image with pseudo backscatter colours.

The magnification of the first analysis was  $\times 180$ , with a resolution of  $0.85\mu\text{m}$  on a  $690\mu\text{m} \times 510\mu\text{m}$  area. In figure 3.16, just after the nugget interface, large equiaxed grains of ferrite may reach a diameter of almost  $100\mu\text{m}$ . Some inter granular austenite is observed at the ferrite grain boundaries (red zone in figure 3.16.a).

Concerning the ferrite grain crystallographic orientation, there is no particular preferred orientation (see figure 3.17). Orientations distribution looks random on the whole Duplex HAZ area whatever the represented axis (X,Y,Z), in the IPF colour code.

A more detailed analysis was done in the Duplex HAZ with a  $\times 1000$  magnification

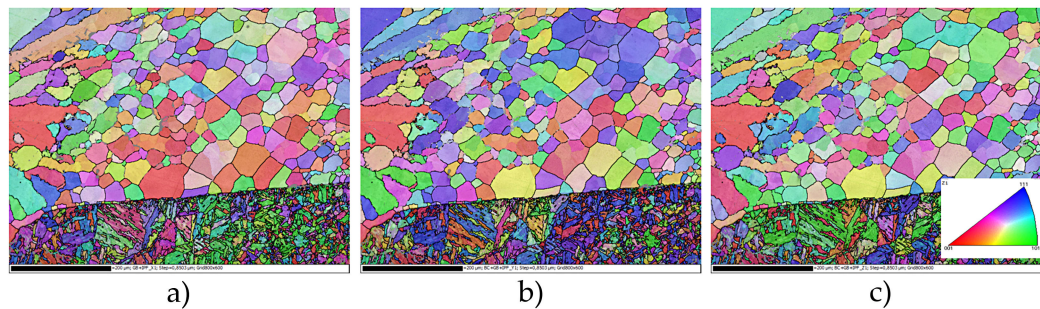


Figure 3.17: Inverse Pole Figures (IPF) of Duplex 8Al HAZ: a) along X axis, b) along Y axis and c) along Z axis.

(figure 3.18). The resolution is 61nm. This analysis confirmed the presence of inter granular austenite. 18R martensite began to appear in the ferrite grain but was too fine for this resolution. It seems that 18R martensite is clearly different from the intergranular austenite. Its particular rhombohedral cristal symmetry should be indexed during EBSD scan to verify if the needles could be captured.

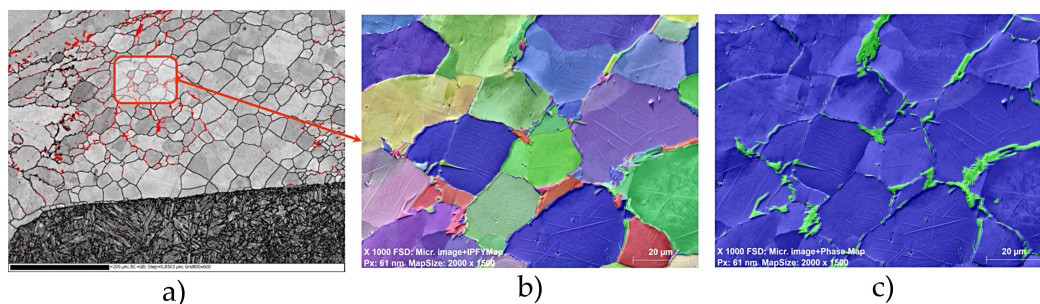


Figure 3.18: Zoom on Duplex 8Al HAZ a) observed zone, b) FSD image and IPF Y, c) FSD image and phase identification.

A detailed analysis was also done at the interface between DP600 HAZ and the nugget with a x600 magnification and a 170nm resolution (figure 3.19). This analysis confirmed the presence of inter granular austenite in the nugget, but not in the ferrite layer at the nugget periphery with DP600 HAZ. Moreover, it seems that a fine layer of austenite could form at the interface.

Moreover, it is important to notice that the ferrite layer is not a real ferrite layer which formed during the welding process but an extension of nugget ferrite grains with a carbon depletion (lack of 18R martensite).

### 3.2.2.4 Energy-Dispersive X-ray spectroscopy (EDX)

During micrographic analysis on the spot welds between Duplex (4Al or 8Al) and DP600, some artefacts were observed in the nugget. These artefacts correspond to fine dark particles of 250µm in length, in every spot weld (see figure 3.20). To determine the nature and chemical composition of these inclusions, EDX analysis focused on one of these inclusions.



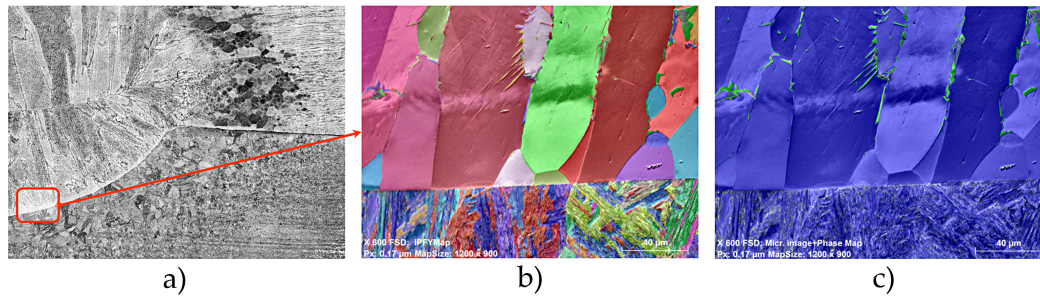


Figure 3.19: Zoom on the interface between DP600 HAZ and nugget of Duplex 8Al/DP600 spot weld: a) observed zone, b) FSD image and IPF Y and c) FSD image and phase identification.



Figure 3.20: Scanning laser observations of dark inclusions in the nugget of Duplex 4Al/DP600 spot welds.

In this analysis, an inclusion was isolated and an EDX map was realized. None of the most probable chemical elements (Iron (Fe), Manganese (Mn), Silicon (Si), Zinc (Zn)) was detected. Only aluminium (Al) and oxygen (O) were measured (figure 3.21). These inclusions seem to correspond to aluminium oxide: alumina. Alumina probably comes from sheet surfaces and was not diluted in the molten nugget because of its high melting temperature (2072 °C). This hypothesis is reinforced by the continuity of alumina at the notch root in figure 3.20. These alumina phases do not seem to affect the failure modes, but this will be investigated in the next sections.

### 3.3 Failure modes

The procedure is the same as in chapter 2. The Duplex sheet is in all cases on the upper side in the tensile machine. This test is occurring till the spot weld fails.

Failure modes are investigated with the naked eyes first. If a button (or dome) is formed, its diameter is measured using a vernier calliper along two perpendicular directions. Moreover, in all cases, the weld nugget size is investigated by micrography on cross



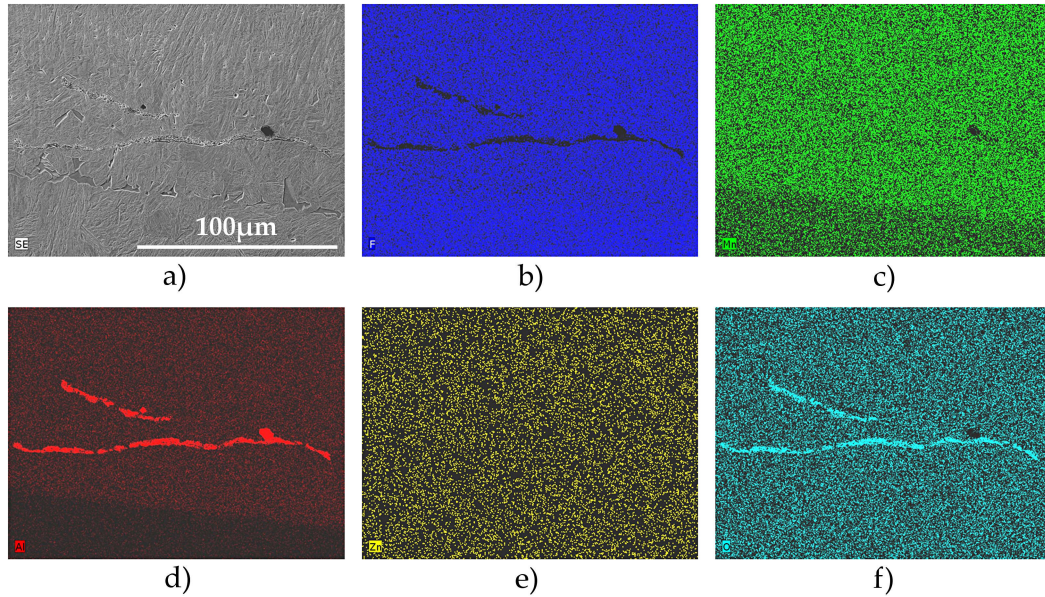


Figure 3.21: Dark inclusion in the nugget: a) SEM view, b) Fe distribution, c) Mn distribution, d) Al distribution, e) Zn distribution and f) O distribution.

sections.

### 3.3.1 Cross tension tests

As explained previously, nine CTS samples are welded for each configuration, three for low current, three for medium current and the three lasts for high current. The fracture modes obtained for the Duplex 4Al/DP600 assemblies are collected in table 3.5. They are highly scattered, with the example of the low domain intensity where the six samples present three different failure modes in the two sheets (table 3.5, first column).

In order to conclude on the failure modes, three additional CTS samples were welded for each intensities to obtain better statistics. By lack of base material, another DP600 steel was used, with a chemical composition very close to the first DP600 used (see DP600 2 in table 3.1). The failure modes are collected in table 3.5.

Configurations	Low Intensity	Middle Intensity	High Intensity
Sample 1	Duplex Failure (TDF)	Duplex Failure (PDF)	Duplex Failure (PDF)
Sample 2	Duplex or DP600 Failure (TDF)	DP600 Failure (TDF)	Duplex Failure (PDF)
Sample 3	DP600 Failure (TDF)	Duplex Failure (TDF)	Duplex Failure (PDF)
Sample 4	Duplex Failure (TDF)	DP600 Failure (TDF)	DP600 Failure (TDF)
Sample 5	Duplex Failure (TDF)	DP600 Failure (TDF)	Duplex Failure (PDF)
Sample 6	Duplex Failure (TDF)	Duplex and DP600 Failure (TDF)	Duplex Failure (PDF)

Table 3.5: Cross tension failure modes of Duplex 4Al 1.2 mm / DP600 1.2 mm spot welds (First three samples were welded with DP600 (1) and three others with DP600 (2)).

Thanks to these additional CTS samples, the fracture modes of Duplex 4Al spot welds were determined and are integrated in the table 3.6 with the Duplex 8Al/DP600 failure modes. The Dome fracture mode is the main one, even if some partial dome failures occurred. In the Duplex 8Al case, Total Dome Failure always occurs at the interface between nugget and DP600 HAZ.

Configurations	Low Intensity	Middle Intensity	High Intensity
Duplex 4Al 1.2 mm / DP600 1.2 mm	Duplex Failure (TDF)	Duplex or DP600 Failure (TDF)	Duplex Failure (PDF)
Duplex 8Al 1.2 mm / DP600 1.2 mm	DP600 Failure (TDF)	DP600 Failure (TDF)	DP600 Failure (TDF)

Table 3.6: Cross tension failure modes for the two types of configuration.

### 3.3.1.1 Cross tension tests macroscopic investigations

Failure mainly occurs in the CGHAZ on the Duplex side for the Duplex 4Al welding, contrary to the Duplex 8Al welding which presents a failure on the DP600 side (in the ferrite layer between nugget and CGHAZ of DP600). The observed failure modes are presented in figures 3.22 and 3.23 in more details.

In the Duplex 4Al case, some fracture initiations appeared in the interface between DP600 HAZ and the nugget (figure 3.22.b and 3.22.c). These cracks indicate that there is a competition between several failure modes. This competition generally occurred between the DP600 HAZ/Nugget interface and the Duplex HAZ (with initiation in the nugget) which explains the different fracture modes observed in table 3.5. Some failure in the Duplex 4Al steel sheets are also observed.

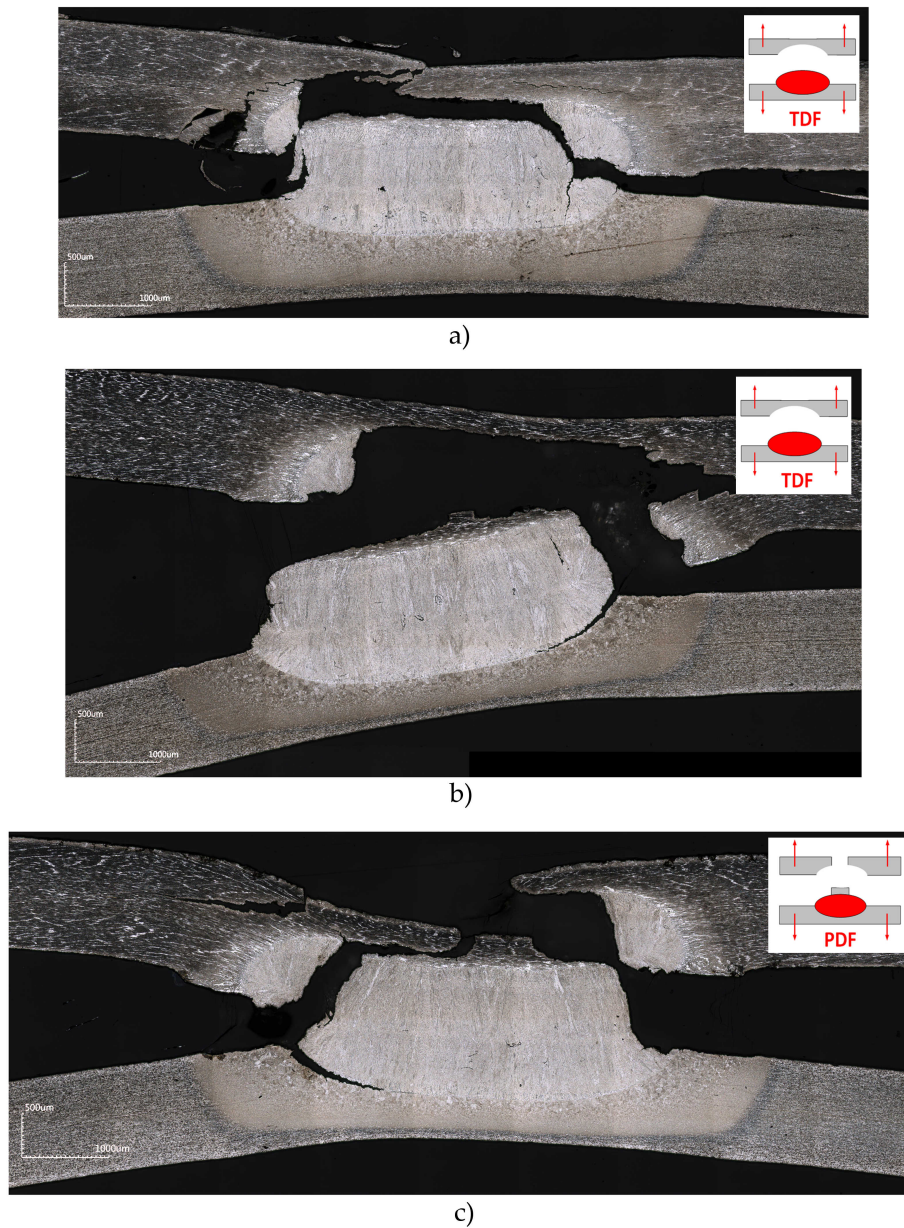


Figure 3.22: Spot weld cross tension failure modes of Duplex 4Al/DP600 spot welds for the three welding intensities: a) lower end, b) middle position, c) upper end.

In the Duplex 8Al case, no other initiation is observed. The failure mode is always in the ferrite layer at the DP600/nugget interface. This interface clearly corresponds to the spot weld weak point.

The macroscopic visual aspect of the broken welds corresponding to the encountered failure modes are presented in figures 3.24 and 3.25. Figure 3.24 represents the failure modes obtained for the three welding intensities for Duplex 4Al. Total Dome and Partial Dome are the dominant failure modes, but in this case, the shape of domes is not usual. Because failure initiate vertically in the nugget, the domes rather look like cubes. Crack



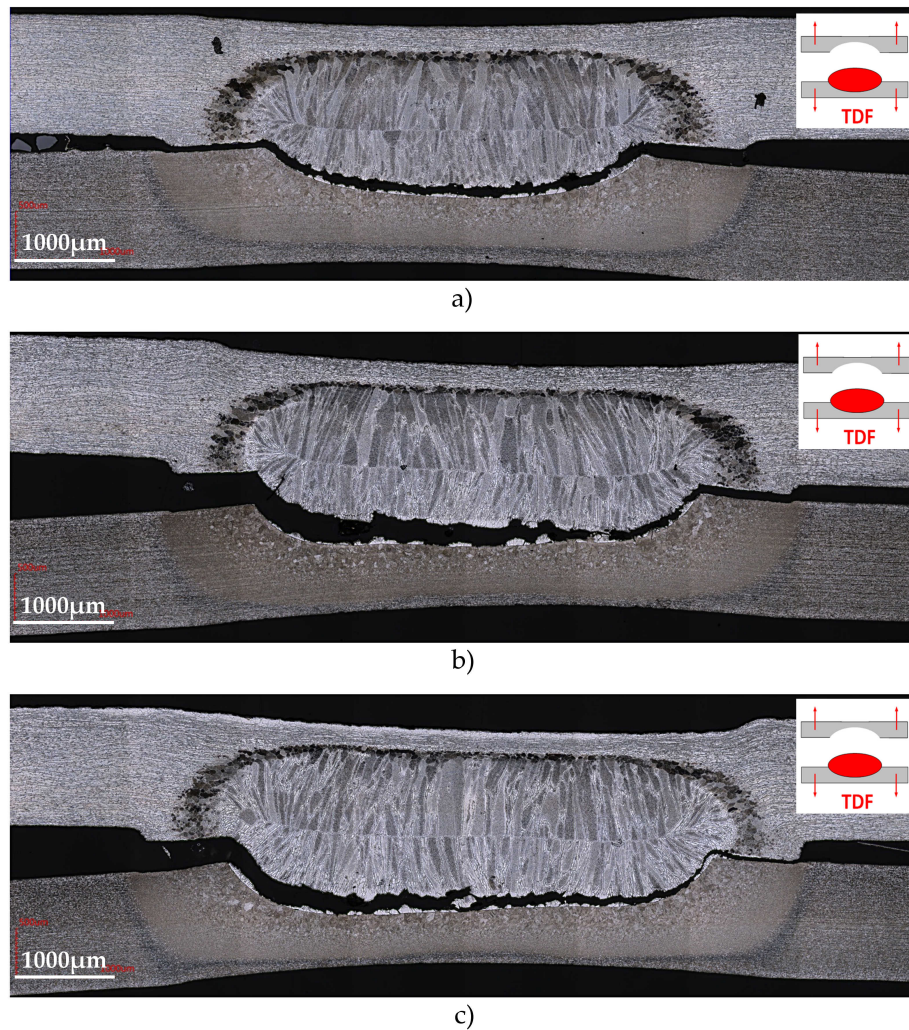


Figure 3.23: Spot weld Cross tension failure modes of Duplex 8Al/DP600 spot welds for the three welding intensities: a) lower end, b) middle position, c) upper end.

initiation at the interface between DP600 HAZ and nugget is also observable in figure 3.24.b (left part).

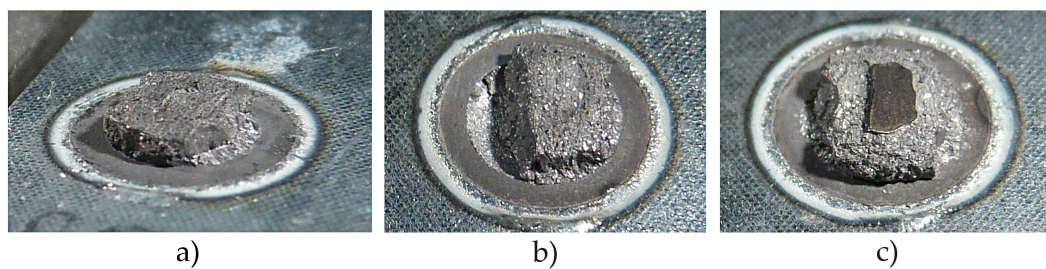


Figure 3.24: Failure modes encountered during Cross Tension tests on Duplex 4Al (macroscopic visual aspect): a) lower end, b) middle position, c) upper end.

The macroscopic visual aspect of Duplex 8Al spot welds is the same regardless the welding intensity. The perfect domes obtained are shown in figure 3.25 (with failure in the ferrite layer at the interface between DP600 HAZ and nugget).

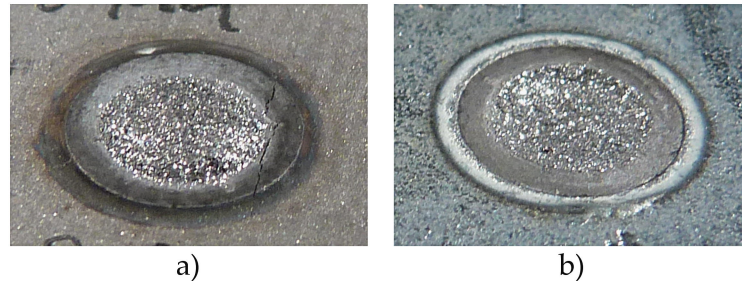


Figure 3.25: Failure mode encountered during Cross Tension tests on Duplex 8Al (macroscopic visual aspect): a) Duplex 8Al sheet, b) DP600 sheet.

### 3.3.1.2 Cross tension tests fracture surfaces

Fractures surfaces of failed spot welds were then observed in a Scanning Electron Microscope (SEM) as presented in figures 3.26, 3.27 and 3.28. In the case of Total and Partial Dome on the Duplex 4Al side, the lateral and top dome surfaces were observed (Figures 3.26 and 3.27).

As observed in the previous section, when Total Dome Failure is observed in Duplex 4Al welds, the failure almost starts in the middle of the nugget as a interfacial failure (see figure 3.22). Figure 3.26 is a set of SEM fractographs of Dome failed zones. Figure 3.26.a shows the Dome remaining on the DP600 sheet after failure, and the 3.26.b represents the hole left by the dome in the Duplex sheet. The other two fractographs 3.26.c and 3.26.d show brittle failures at the Dome periphery for 3.26.c and at a beginning of interfacial failure for 3.26.d. Intergranular failures are observed on the fractographs, but some cleavage is also observed on the fractograph at the top of the dome, which implies some transgranular failure in these zones.

In some cases (in particular for high intensities), a small button of Duplex steel stays on the Dome (figure 3.24.c). In fact, crack propagation stopped along the nugget and chose a favourite path through the Duplex HAZ until the upper sheet surface. This mixed mode is the Partial Dome Failure mode or PDF mode shown in figure 3.22. This mode represents the transition between TDF and BPO failure modes.

Figure 3.27 is a set of SEM fractographs of the failed Partial Dome zones. Figure 3.27.a shows the Partial Dome remaining on the DP600 sheet after failure, and the 3.27.b represents the correspond cross section of failure mode. Figure 3.27.c fractograph shows the same brittle intergranular surfaces of the Dome as in the previous case (TDF). By contrast, figure 3.27.d fractograph shows ductile shear failures at the Button periphery (lateral surface of Button) on the top of the Dome. The Dome presents in fact a square shape along the CTS sheet directions. Crack propagation from the notch root and through the nugget is always in the Duplex sheet direction in the CTS assembly. This square shape also appears on the partial button observed on the top of the Dome.

When Total Dome Failure occurs at the interface between DP600 HAZ and nugget



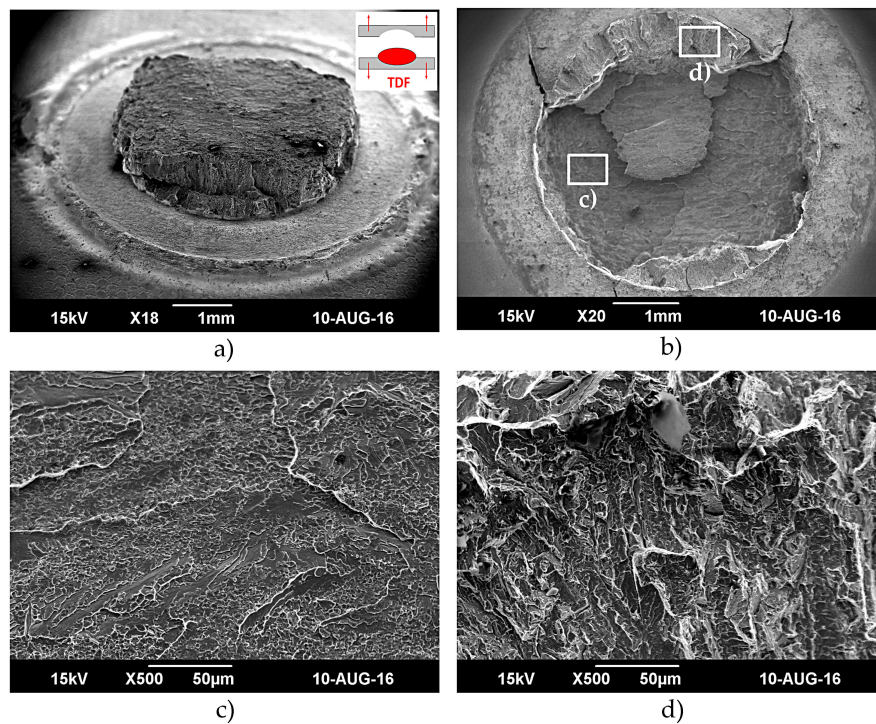


Figure 3.26: Duplex 4Al/DP600 spot weld Total Dome Failure (Duplex 4Al side) zones SEM fractographs.

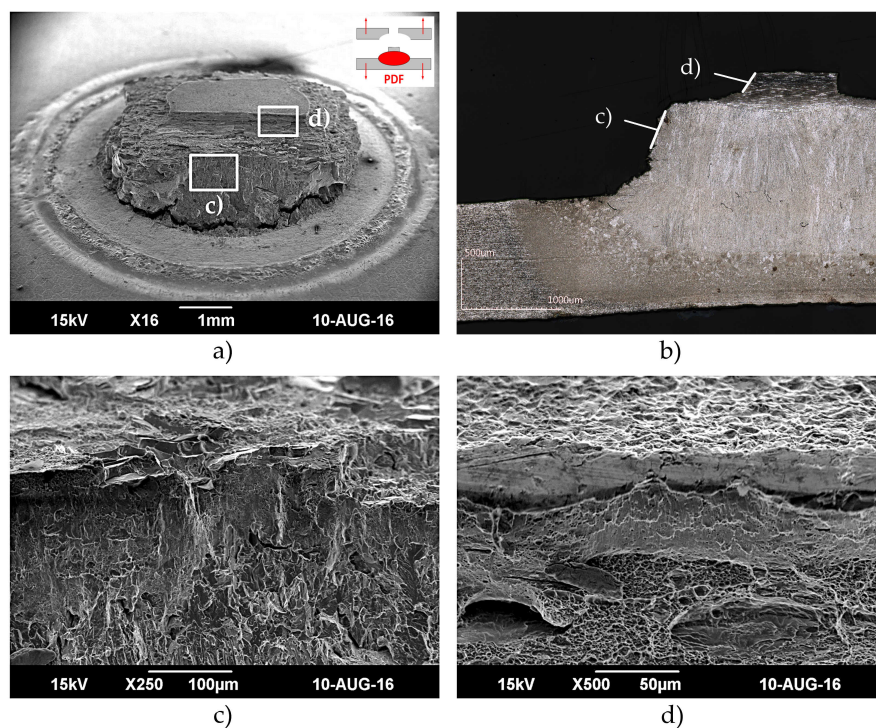


Figure 3.27: Duplex 4Al/DP600 spot weld Partial Dome Failure zones SEM fractographs.

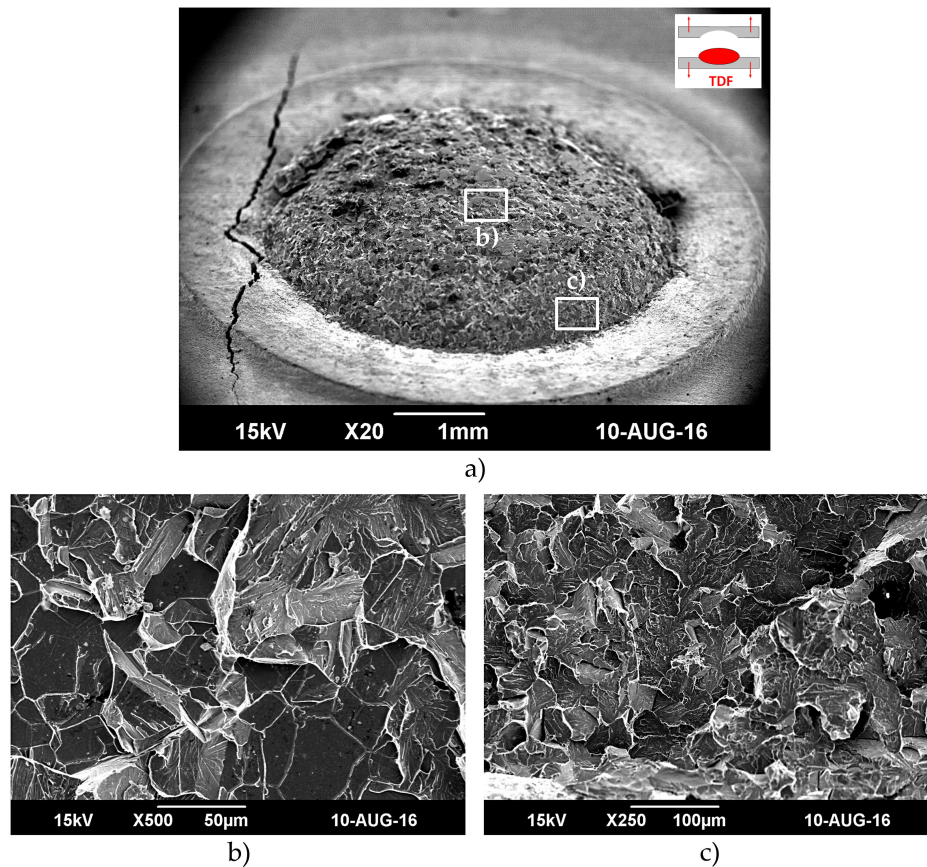


Figure 3.28: Duplex 8Al/DP600 spot weld Total Dome Failure (DP600 side) zones SEM fractographs.

(Duplex 8Al case in contrast with Duplex 4Al failure), it results into a perfectly round dome (figure 3.28.a). As one of the steels is much alloyed, the difference between resistivity and fusion temperature of steels induces a shift of the molten nugget position. This particular geometry combined to the interface microstructure provides Dome Failure. The crack shows a preferential path along the nugget boundary. Figure 3.28.a shows the Dome remaining on the Duplex sheet after failure. The other two fractographs 3.28.b and 3.28.c show brittle failures at the top of the Dome for 3.28.b and at the dome foot for 3.28.c. These fractographs show an intergranular brittle failure with grains between 10µm and 50µm. This observation permits to confirm that failure occurs in the nugget border, in the ferrite layer depleted in carbon as observed on the failed micrographs.

### 3.3.2 Tensile shear tests

#### 3.3.2.1 Tensile shear tests macroscopic investigations

As for the case of cross tension, fracture modes of Duplex 4Al spot welds in tensile shear are scattered but when at least two of the three fracture modes are the same for one welding intensity, this fracture mode becomes the more representative. Failures modes observed for each configuration are grouped in table 3.7. The main fracture mode is the



total Dome fracture, even if some partial dome failures occurred. Failure mainly occurs in the CGHAZ of the Duplex sheet for Duplex 4Al welds (figure 3.29), contrary to the Duplex 8Al welds presenting a failure on the DP600 side (in the ferrite layer between nugget and CGHAZ of DP600, figure 3.31) similarly to cross tension fracture modes.

It should be noted that for middle intensity welding of Duplex 4Al, either as cross tension or tensile shear tests, failure modes occur randomly in the Duplex sheet or in the DP600 sheet. This is confirmed by micrographic views of failed spot welds, on which a competition between the failure paths could be observed (cracks on the two sides).

Configurations	Low Intensity Range	Middle Intensity Range	High Intensity Range
Duplex 4Al 1.2 mm / DP600 1.2 mm	DP600 Failure (TDF)	Duplex or DP600 Failure (TDF)	Duplex Failure (PDF)
Duplex 8Al 1.2 mm / DP600 1.2 mm	DP600 Failure (TDF)	DP600 Failure (TDF)	DP600 Failure (TDF)

Table 3.7: Tensile shear failure modes.

Macrographic inspection of failed welds is presented in figure 3.29 for Duplex 4Al. For lower welding intensity, the TDF mode on the DP600 side is confirmed even if initiation in the Duplex 4Al side could also be observed on the left of the dome (figure 3.29.a). For middle and upper end intensities, the Dome on the Duplex side is observed with a particular cubic shape, as in the Cross Tension tests. Moreover, a sheared surface with an angle close to  $45^\circ$  is observed (figures 3.29.a and 3.29.b). This sheared surface is typical of the tensile shear tests.

During Tensile Shear tests on Duplex 8Al and DP600 welded assemblies, the failure occurred at the interface between the DP600 HAZ and the nugget as in Cross Tension tests. Whatever the mechanical test, the Duplex 8Al/DP600 spot welds fail in a Total Dome mode. In the case of Tensile Shear, a small part of the dome surface is sheared because of the friction of the dome on the DP600 sheet.

### 3.3.2.2 Tensile Shear tests fracture surfaces

SEM investigations of fracture surfaces for the three failure modes of Duplex 4Al spot welds are shown in figures 3.32, 3.33 and 3.34.

The first SEM investigations are focusing on the lower intensity case. Contrary to Cross Tension tests, during Tensile Shear tests of lower intensity the failure occurred at the interface between the DP600 HAZ and the nugget, like for Duplex 8Al welds. During tensile test, one sheet is pulled up and the other down. During and after failure, if the mode is a Dome or a Button, this Dome or Button will rub the other sheet and produce a sheared surface (figure 3.32.d).

Figure 3.32 is a set of SEM fractographs of the Total Dome zones which failed. Figure 3.32.a shows the Dome remaining on the Duplex sheet after failure, and 3.32.b represents the hole let by the Dome in the DP600 sheet. 3.32.c and 3.32.d fractographs respectively show brittle failures in the Dome zone and ductile shear failures where the Dome rubbed

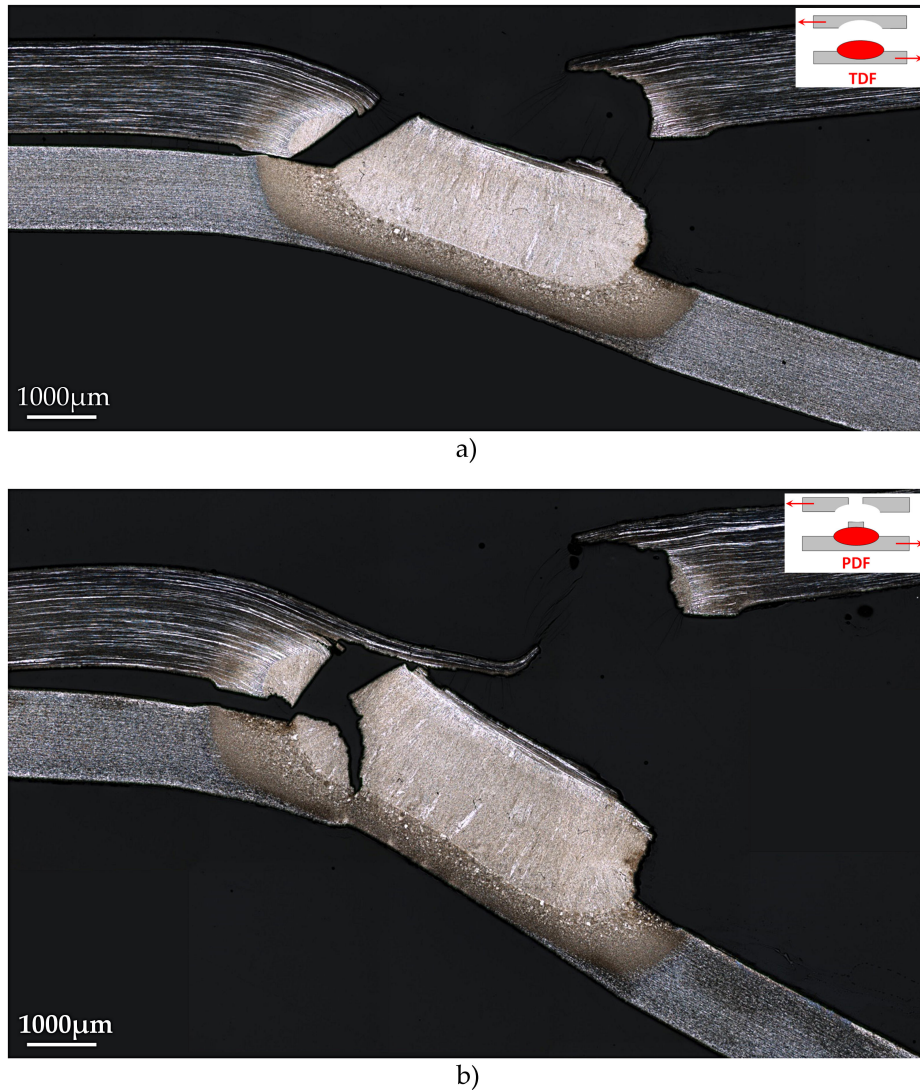


Figure 3.29: Spot weld Tensile Shear failure modes of Duplex 4Al/DP600 spot welds for middle and upper end welding intensities.

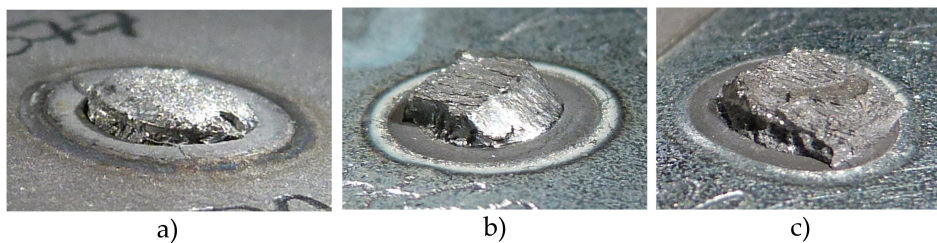


Figure 3.30: Failure modes encountered during Tensile Shear tests on Duplex 4Al (macroscopic visual aspect): a) lower end, b) middle position, c) upper end.

the DP600 sheet. The ductile shear failure exhibits oriented dimples whereas the brittle intergranular failure occurs in the ferrite layer at the nugget border on the DP600 side.



Figure 3.31: Spot weld Tensile Shear failure modes of Duplex 8Al/DP600 spot welds for middle end welding intensity.

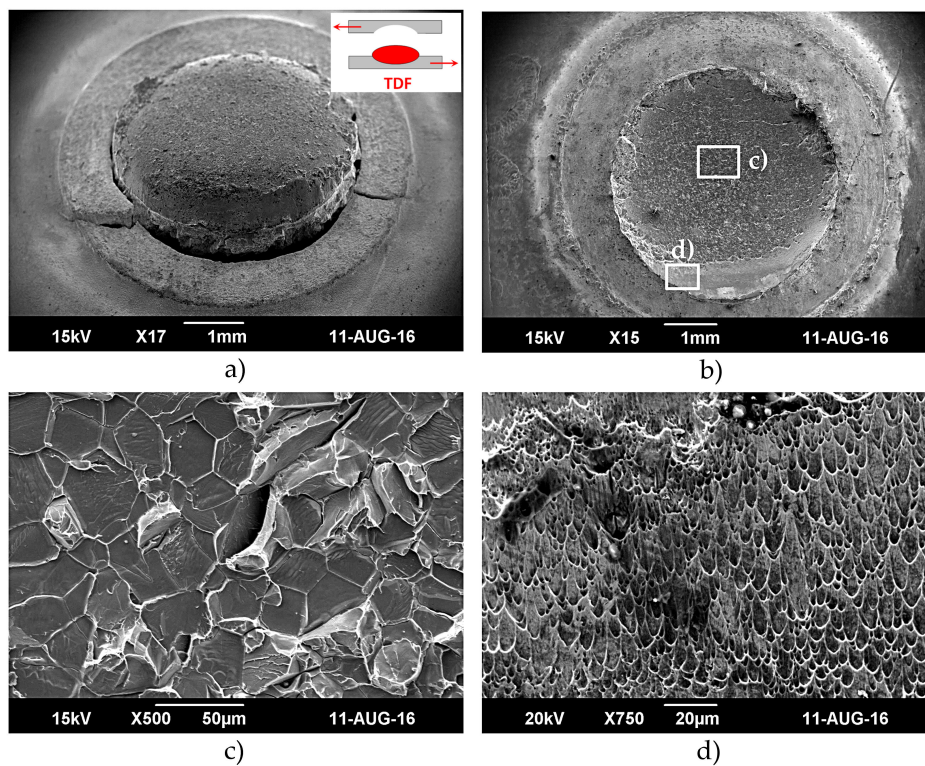


Figure 3.32: Duplex 4Al / DP600 spot weld Total Dome Failure (DP600 side) zones SEM fractographs.

It is important to notice the competition between the modes: in figure 3.32.a, crack initiation is observed in the Duplex 4Al HAZ under the dome. The strengths of these two zones seem to be very close to each other.

The second case is the middle intensity spot weld. The failure mode is similar to the previous one, but occurs in the Duplex sheet. Figure 3.33 is a set of SEM fractographs of the failed Total Dome zones. Figure 3.33.a shows the Dome remaining on the DP600 sheet after failure, and 3.33.b represents the hole left by the Dome in the Duplex sheet. 3.33.c and 3.33.d fractographs respectively show ductile shear failures where the Dome rubbed the Duplex sheet and brittle failures in the Dome zone. The ductile shear failure has



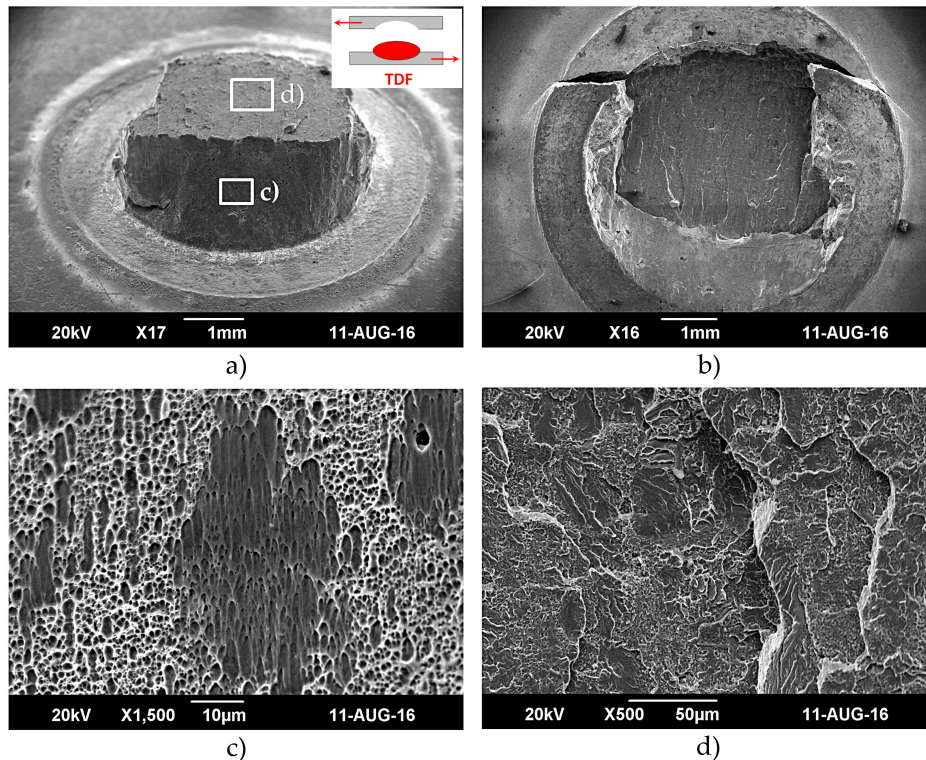


Figure 3.33: Duplex 4Al / DP600 spot weld Total Dome Failure (Duplex 4Al side) zones SEM fractographs.

oriented dimples whereas the brittle failure fractograph traduces an intergranular failure in the Duplex HAZ.

For the Duplex 8Al/DP600 spot welds, the failure modes are the same during cross tension and tensile shear tests (Total Dome Failure). Similarly, the fracture surfaces show the same characteristics after the two mechanical tests. Therefore, the fracture surfaces after tensile shear test present a brittle intergranular surface on the Dome. But, like after all tensile shear tests, a part of the surface is sheared during test.

## 3.4 Failure strengths

### 3.4.1 Cross tension strengths

Following the failure mode observations and the identification of the involved failure mechanisms, the analysis of spot weld strength will now be discussed. The failure loads of the two Duplex configurations of spot welds measured during the cross tension tests are given in table 3.8.

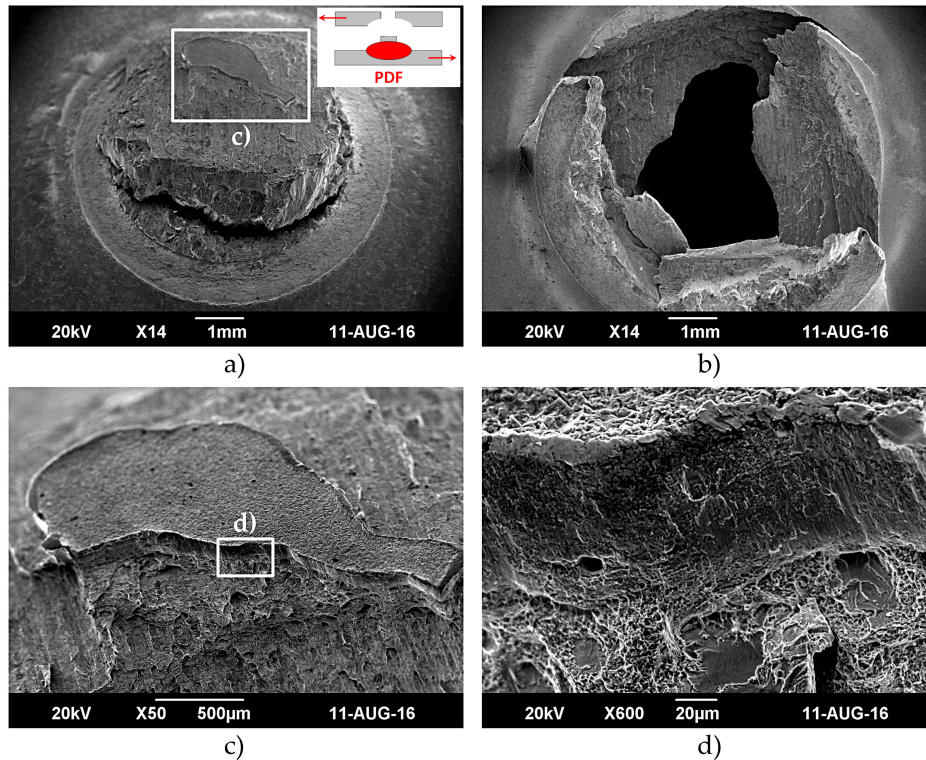


Figure 3.34: Duplex 4Al / DP600 spot weld Partial Dome Failure (Duplex 4Al side) zones SEM fractograph.

Configurations	Load (daN)		
	Low Intensity Range	Middle Intensity Range	High Intensity Range
Duplex 4Al 1.2 mm/DP600 1.2 mm	155 ±19	191 ±38	211 ±40
Duplex 8Al 1.2 mm/DP600 1.2 mm	91 ±10	106 ±5	120 ±2

Table 3.8: Cross tension failure loads (daN, average of six tests for Duplex 4Al and three for Duplex 8Al).

The above results are plotted as a function of the measured weld diameters in figure 3.35. Two additional configuration results derived from internal ArcelorMittal Data are superimposed in figure 3.35 to compare welds with different aluminium contents. These two additional configurations are:

- Heterogeneous welding of Duplex 6.2Al 1.2 mm with DP600 1.2 mm
- Heterogeneous welding of Duplex 6.7Al 1.2 mm with DP600 1.2 mm

The negative effect of aluminium content on the CTS performance is obvious. Duplex with 6.2 and 6.7 Al were welded previously (ArcelorMittal Internal Data) and respectively showed  $\alpha$  of 27 daN/mm<sup>2</sup> and 25 daN/mm<sup>2</sup> which is in the middle of the  $\alpha$  ramp for our two

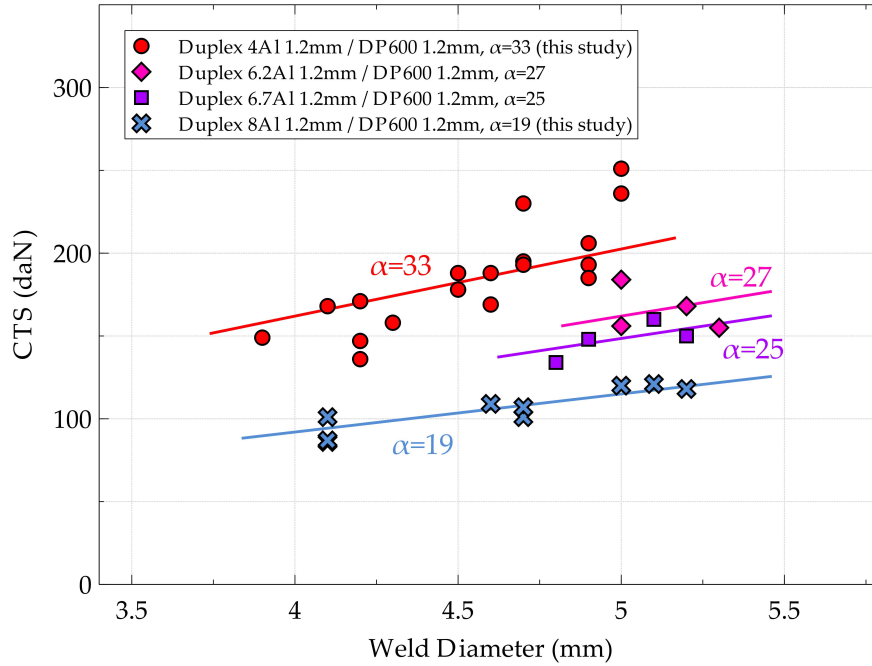


Figure 3.35: Cross tension failure load (CTS) as a function of weld diameter and welding assembly: Duplex (with different aluminium contents) and DP600 heterogeneous welding configurations.  $\alpha$  in  $\text{daN}/\text{mm}^2$ .

configurations welded in this project. The failure modes between the two configurations with Duplex with different aluminium content are remarkable: for the Duplex 4Al, failure mainly occurs in the Duplex HAZ, but for the 8Al, it occurs in the ferrite layer formed during the process between the molten nugget and the DP600 HAZ. The higher scattering observed for the Duplex 4Al is representative of the competitions between the different failure modes.

### 3.4.2 Tensile shear strengths

Spot weld failure loads in tensile shear are presented in table 3.9 for the different configurations and plotted in figure 3.36 as a function of the weld diameter.

Configurations	Load (daN)		
	Low Intensity Ranger	Middle Intensity Range	High Intensity Range
Duplex 4Al 1.2 mm/DP600 1.2 mm	645 $\pm$ 85	797 $\pm$ 10	1048 $\pm$ 125
Duplex 8Al 1.2 mm/DP600 1.2 mm	513 $\pm$ 62	594 $\pm$ 50	650 $\pm$ 27

Table 3.9: Tensile Shear failure loads (daN, average three samples).

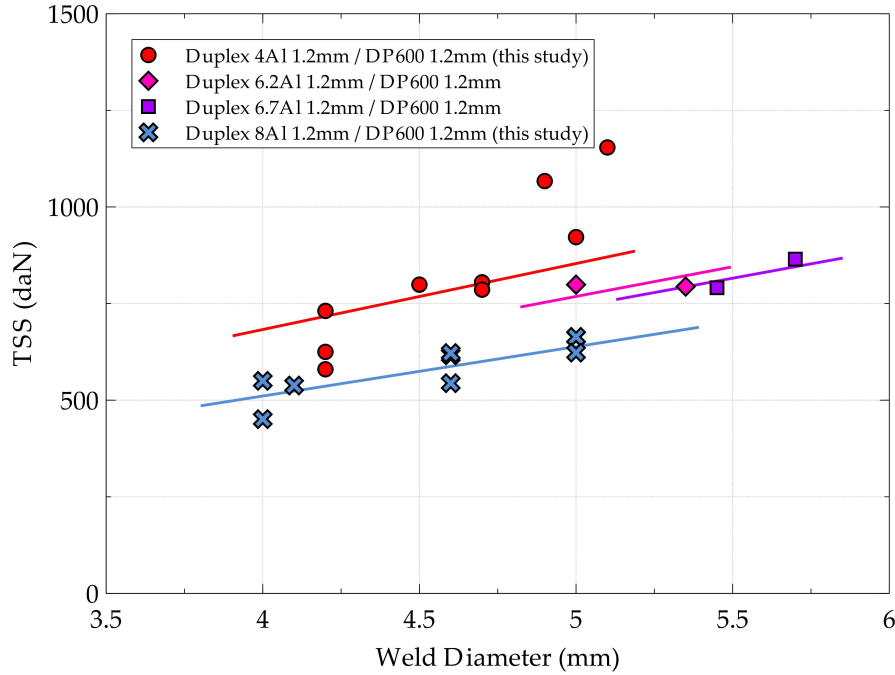


Figure 3.36: Tensile shear failure load (TSS) as a function of weld diameter and welding assembly.

As in the CTS tests case, the Tensile Shear Strengths decrease when aluminium content increases. In conclusion, the aluminium content has a negative effect on all the mechanical tests on spot welds (cross tension and tensile shear). The aluminium content can be related to the ferrite layer formation. It seems the higher the aluminium content the weaker (and larger) is the ferrite layer between the DP600 HAZ and nugget. Regardless of the loading configuration, the ferrite layer is the weakest zone in the Duplex spot welds.

TSS tends to follow a linear law ( $TSS = b \times d_w$ , where  $b$  is the configuration performance parameter and  $d_w$  the weld diameter) when the failure mode is Total Dome in the ferrite layer (DP600 side). But when the mode is transferred to the Duplex side (Duplex 4Al/DP600 for high welding current), an increase of the spot weld mechanical performance is observed.

In the Duplex 4Al/DP600 spot welds case, Tensile Shear Strengths (TSS) are highly dispersed (dispersion more or less 10% of average). The CTS were dispersed too. This dispersion comes from the various failure modes encountered during experimental tests. For one welding intensity, it was difficult to reproduce the failure modes between the different samples. This is the reason why dispersed strengths are obtained in the Duplex 4Al case whereas the Duplex 8Al dispersion is very low (figures 3.35 and 3.36).



## 3.5 Discussion

### 3.5.1 Aluminum effect on performance

As noted in the previous section, aluminium has a strong effect on spot welds performance. Usually, for low aluminium content in other high strength steels, the increase in aluminium content reduces the Cross Tension Strengths (CTS), but generally has a positive effect on the Tensile Shear Strengths (TSS). In this case however, aluminium content is so important that the welding metallurgy is fully modified compared to classical resistance spot welding.

Figures 3.37 and 3.38 allow to understand the negative effect of high aluminium contents on the spot weld performance. The CTS values are dramatically lower than usual AHSS CTS ( $\alpha$  generally greater than 70 daN/mm<sup>2</sup>). In figure 3.37, the CTS with Duplex steel is compared to the heterogeneous welding of Usibor1500/DP600 case with the lowest CTS performance of the four previous studied configurations (2). This comparison allows to highlight the really low values of Duplex CTS. For a 5 mm weld diameter, Usibor1500/DP600 spot welds fail with a strength of 500 daN while the strongest Duplex/DP600 configuration (Duplex with 4wt% of aluminium) hardly reaches 250 daN. The weakest configuration (Duplex with 8wt% of aluminium) shows even lower strength (100 daN).

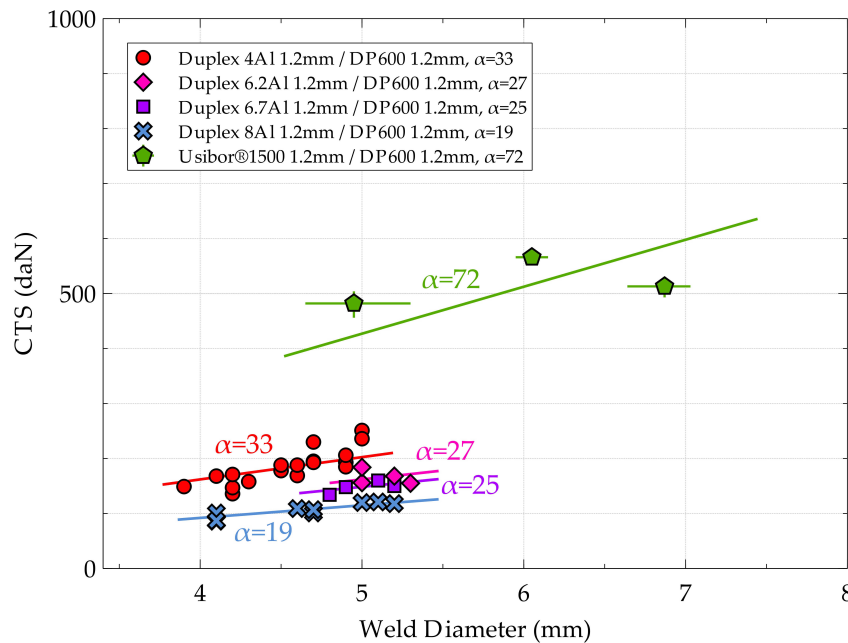


Figure 3.37: Cross tension failure load (CTS) as a function of weld diameter and welding assembly: Duplex (with different aluminium content) and DP600 heterogeneous welding configurations compared to the more unfavorable configuration of Usibor1500/DP600.  $\alpha$  in daN/mm<sup>2</sup>.

The tensile shear results of Duplex welds compared to the most unfavourable Usibor1500/DP600 configuration in tensile shear show also a lower performance as for cross tension. But when CTS of the Usibor1500/DP600 case were at least two times greater than the Duplex one, in tensile shear the difference between strengths is less important.

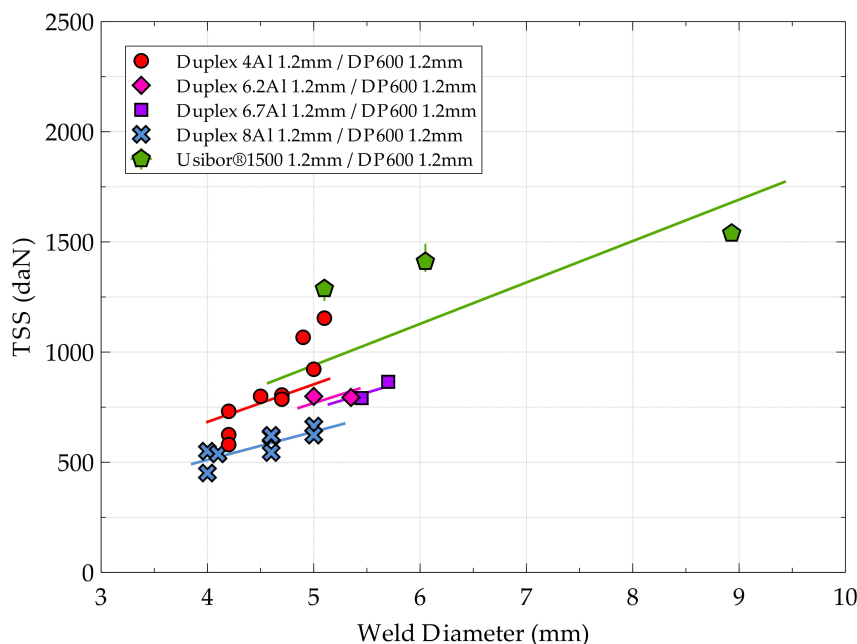


Figure 3.38: Tensile Shear failure load (TSS) as a function of weld diameter and welding assembly: Duplex (with different aluminium content) and DP600 heterogeneous welding configurations compared to the more unfavorable configuration of Usibor1500/DP600.

In fact, for 5 mm weld diameter, the Duplex 4Al/DP600 TSS is 1048 daN, on average, whereas Usibor1500/DP600 TSS is 1287 daN. There is only a small difference between TSS when Duplex 4Al spot welds fail in a hybrid Partial Dome Failure mode in the Duplex 4Al side. But when the failure occurs in the ferrite layer zone (Dome Failure between DP600 HAZ and nugget), TSS severely decreases as shown on figure 3.38.

In addition to a general negative effect on strength, the aluminium content (in large quantities) can relocate the failure zone by forming a weak ferrite zone at the interface between DP600 and the nugget. This generally precipitates the failure conducting to very low spot welds strengths. This phenomenon was observed by Qiu and al. [QIU 09a] for a steel/aluminium spot weld, where they explain that interfacial reaction layer can deteriorate the cross tension strength of the joint welded by resistance spot welding in the case that its thickness exceeds 1.5  $\mu\text{m}$ .

### 3.5.2 Ferrite layer formation

During heterogeneous welding process of Duplex (containing high aluminium content) with DP600, a ferrite layer is forming at the interface between DP600 HAZ and nugget (Fusion Zone) as observed in the two studied configurations 4Al and 8Al in figure 3.39.

The aluminium addition aims at reducing the steel density and at stabilizing the ferrite phase. When the liquid metal (molten DP600 and Duplex) interacts with the solid one (DP600 HAZ), physical phenomena such as wetting, diffusion of alloying elements, dissolution and formation of solid/liquid interface could occur. In addition, interfacial reactions leading to formation of intermetallic compounds could take place.

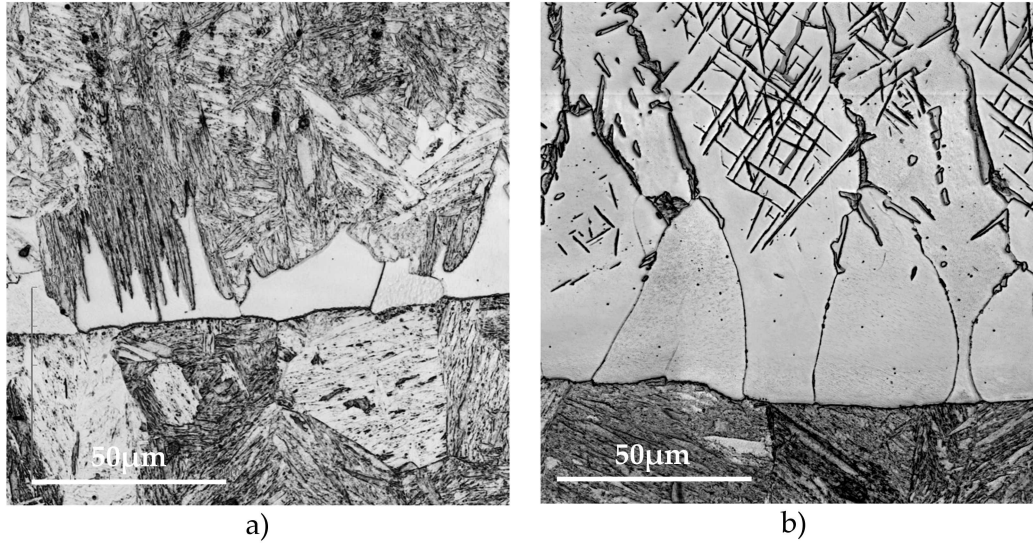


Figure 3.39: Ferrite layer (white phase) micrographic observations: a) Duplex 4Al/DP600, b) Duplex 8Al/DP600 (nugget is at top side and DP600 HAZ at the bottom side).

Since the steels to be welded have different chemical compositions, diffusion of alloying elements is expected during the joining process. Indeed, the resulting concentration gradient leads to the formation of a flux of alloying elements, which can act until the concentration gradient is reduced or eliminated.

The driving force for the diffusion of an element  $i$  depends on the concentration of the other alloying elements, because they modify its chemical potential. This phenomenon could lead to a up-hill diffusion process. [DAR 48] reported a very representative example of up-hill diffusion. He observed how C diffused from a steel of 0.32% carbon content to another having 0.58% carbon content as shown in figure 3.40. Indeed, the first steel had 3.8% Si, whereas the second one only 0.5%. Consequently, the difference of Si content between the two steel is the reason of up-hill diffusion. A high Si content decreased the affinity of phases available for C in the first steel.

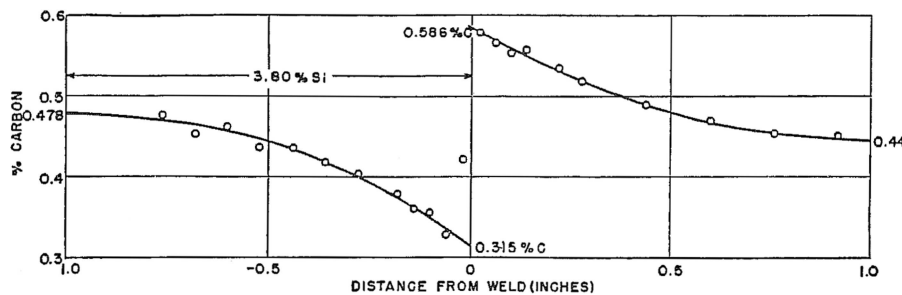


Figure 3.40: Concentration profile of C at the interface of 3.8 Si% steel/0.5 Si% steel

Moreover, the diffusion of alloying elements is mainly governed by temperature. According to the equation 3.1 which was confirmed for interstitial and substitutional systems, the diffusion coefficient is strongly dependent on the temperature  $T$ .

$$D = D_0 \times \exp(-Q/kT) \quad (3.1)$$

where  $D_0$  is the pre-exponential factor,  $Q$  is the activation enthalpy and  $k$  is the Boltzmann constant. It is important to notice that diffusion coefficients in liquid and solid metals are very different. In fact, diffusion rates of alloying elements in liquid steel are faster by several orders of magnitude than those in the solid at the same temperature.

In the Duplex case, just before the beginning of fusion zone solidification, the local carbon content (close to interface) decreases because of carbon diffusion in the solid DP600 HAZ. Formation of  $\delta$ -ferrite is observed at the interface periphery (3.39). It appeared that the larger the aluminium content, the larger was the ferrite layer. In fact, the larger the aluminium content, the larger the ferrite fraction and then the larger the carbon elements migration towards DP600 HAZ.

Some studies on simulated interface samples were undertaken at ArcelorMittal to observe the carbon diffusion around the ferrite layer. Such interfaces were simulated by melting Duplex (4Al and 8Al) on solid DP600 just under the fusion temperature of DP600 steel and quenching the assembly. The microstructure obtained after the interface simulation are very close to Duplex/DP600 spot weld microstructures (figure 3.41). It is important to note that in spot welding, the liquid is a mix of Duplex and DP600, the aluminium content is reduced by dilution with DP600, that is why the obtained microstructure are not exactly the same.

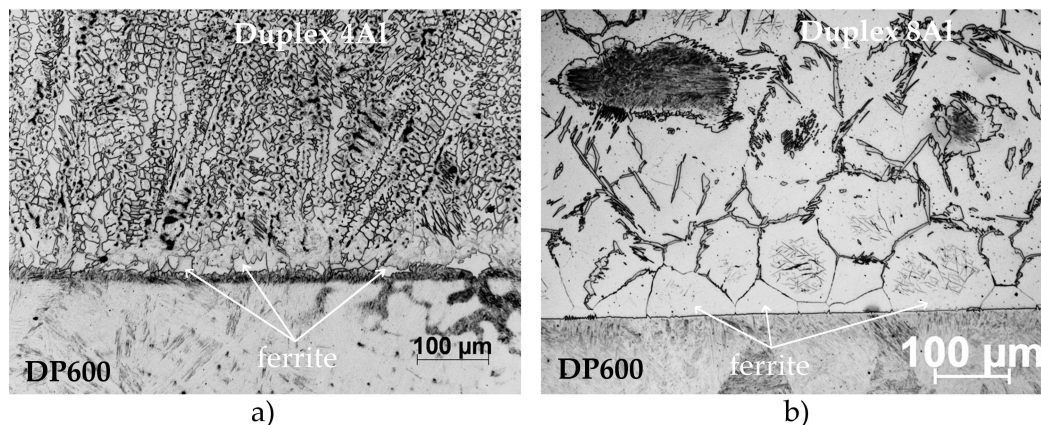


Figure 3.41: Simulated interfaces: a) Duplex 4Al/DP600 and b) Duplex 8Al/DP600.

To study the diffusion of chemical elements, Electron Probe Micro-Analysis (EPMA) was carried out at the interface between DP600 and Duplex. Also called Electron Micro-Probe Analysis (EMPA), this technique allows to measure quantitatively the composition of small areas on specimens. To characterize the ferrite layer formation, the carbon content is observed around the two interfaces (figures 3.42 and 3.43).

In the Duplex 4Al case, there is very limited carbon content in the ferrite grains at the interface between the two steel grades. Moreover, the ferrite layer formation induced a carbon diffusion towards the two steels around the layer. The carbon enrichment is particularly noticeable on the DP600 side, on a 50  $\mu\text{m}$  large layer along the interface. The

carbon content here is between 0.15wt% and 0.20wt% whereas far from the interface, carbon content is between 0.10wt% and 0.15wt%.

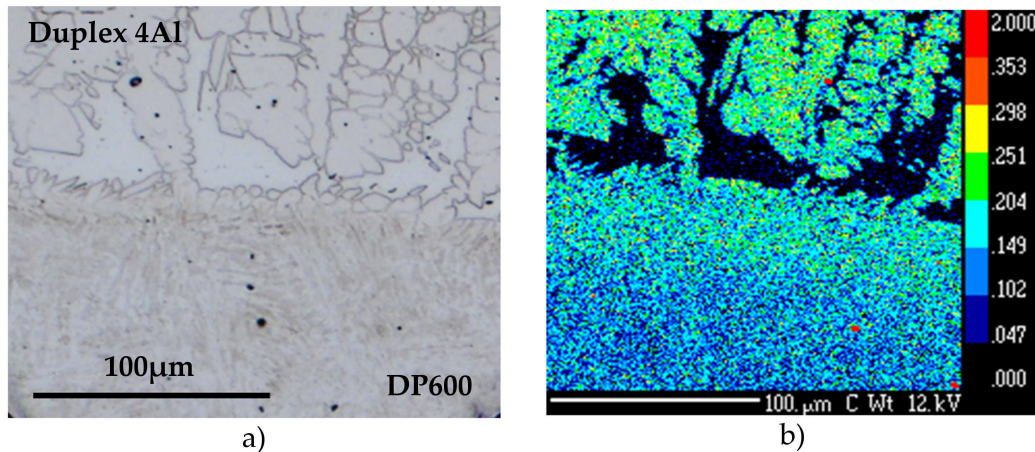


Figure 3.42: Interface of Duplex 4Al/DP600 assembly: a) micrographic view and b) C mapping (EPMA).

In the Duplex 8Al case, the carbon diffusion is even more obvious: on the DP600 side, the carbon content exceeds 0.30wt% very close to the interface. The enriched zone in the DP600 side is larger than for Duplex 4Al. Finally, when aluminium content is increased, the carbon diffusion is more important.

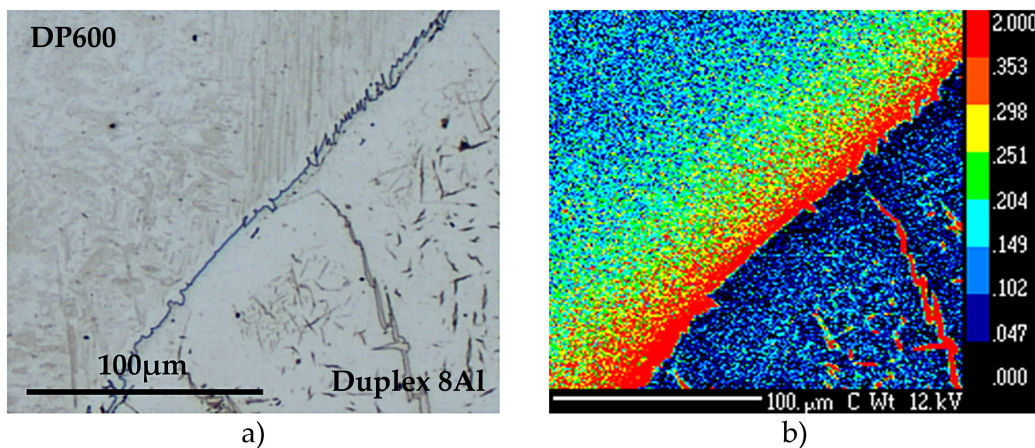


Figure 3.43: Interface of Duplex 8Al/DP600 assembly: a) micrographic view and b) C mapping (EPMA).

To better appreciate the carbon diffusion, one carbon content profile was extracted in the two cases (4Al and 8Al), presented in figure 3.44. The interface between DP600 and Duplex is represented by the vertical black line. The DP600 side is always on the left.

On the top graph (DP600/Duplex 4Al interface), a carbon content drop is observed just after the interface which correspond to the  $\delta$ -ferrite grain formation at the interface. In the DP600 steel close from the interface, on a 50  $\mu\text{m}$  layer, the carbon enrichment is remarkable (between 0.15wt% and 0.20wt%).



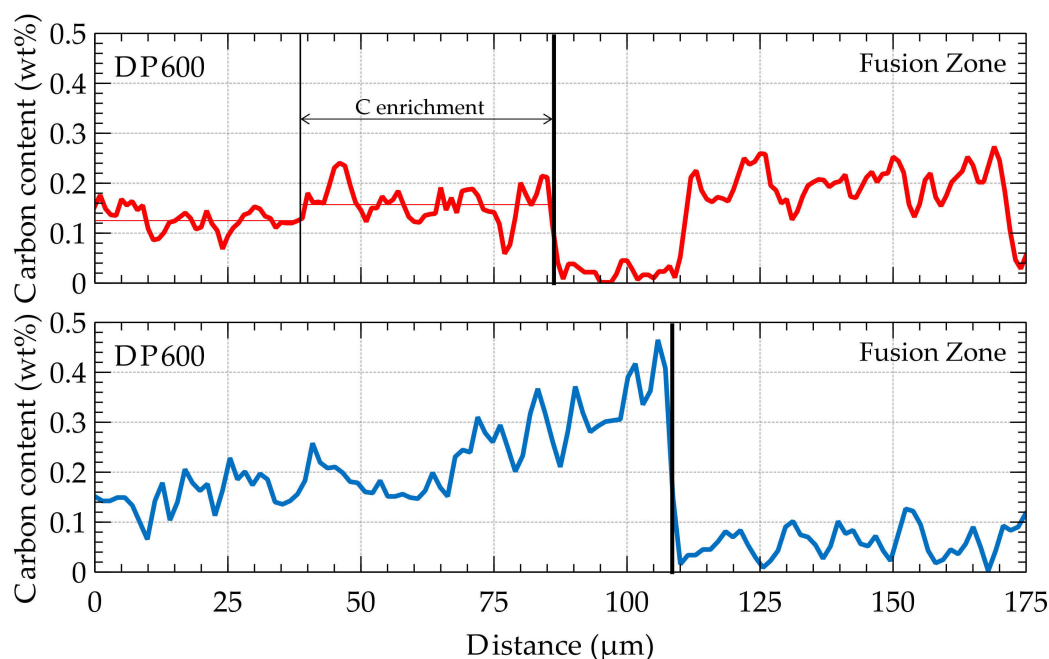


Figure 3.44: Concentration profile of C at the interfaces of Duplex 4Al/DP600 and Duplex 8Al/DP600 assemblies.

On the bottom graph (DP600/Duplex 8Al interface), the carbon drop is also observed from DP600 steel to Duplex 8Al. It could be essentially explained by the microstructure of the two steels, DP600 is martensitic (high carbon content) whereas Duplex is ferritic (low carbon). Because of ferritic microstructure and high initial carbon content of Duplex, all the carbon, initially found in the Duplex, diffused in the solid DP600 after solidification to a depth of 100  $\mu\text{m}$ , locally reaching carbon content over 0.4wt%.

Moreover, the carbon diffuses toward ferrite grain boundaries to form austenite or martensite, which conducts to an embrittlement of the ferrite layer. This phenomenon was observed by Million and al. [MIL 10] in austenite-ferrite dissimilar joint. The crack propagation at the interface between DP600 HAZ and nugget is shown in figure 3.45. The crack is not clearly following the interface but it is passing through the first grain of the ferrite layer. The crack propagation is essentially located at the ferrite grain boundaries, at the interface or in the nugget side. Indeed, the crack is following the ferrite layer, but has no preferred side (interface or nugget).

A zoom on the crack propagation is presented in figure 3.46. The figure allows to clearly see that the propagation is highly affected by the ferrite grain boundaries. Furthermore, the ferrite grains generally have a three-sided pyramid shape with the base either at the interface or on the nugget side (figure 3.39.b). Ferrite grains with their base at the interface tend to remain stuck to the interface during crack propagation which explains the particular crack propagation observed. But the top of grain could sometimes crack with a intragranular failure.

Moreover, a micrograph on failed spot welds allows to observe another fact about the crack propagation: the ferrite grains which remain stuck to the interface sometimes show a penetration of the interface. By contrast, the interfaces of the failed zone without stuck



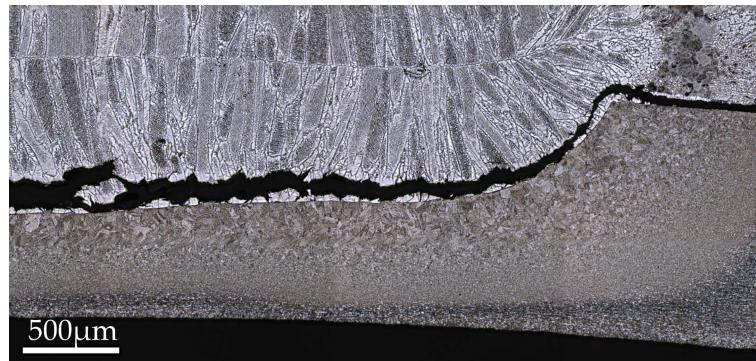


Figure 3.45: Failure propagation in the ferrite layer.

ferrite grain present a higher elevation as if the ferrite grain did not penetrate enough the interface to stay connected. Otherwise, when the ferrite grains well penetrates the DP600 HAZ, crack propagation tends to follow the ferrite grain boundaries enriched in residual austenite.

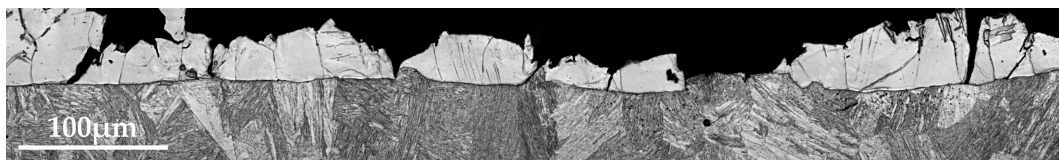


Figure 3.46: Zoom on the failure propagation in the ferrite layer.

To conclude, the carbon enrichment of the DP600 at interface was firstly thought to be responsible for the Duplex spot welds embrittlement. A better observation of the crack propagation allows to state that the interface is not the critical zone. Ferrite grain recrystallization combined to carbon diffusion in the grain boundaries, forming martensite or austenite, is assumed to play a more active role in Duplex spot welds performance at least in the cases considered here.

## 3.6 Arc welding

In this part, the heterogeneous welding of the two Duplex steels will be studied. The sheets are welded in a overlap configuration like in the previous chapter (figure 3.47). This involves that there is an upper and a lower sheet. The heterogeneity comes from the filler wire used (G3Si close to DP600 chemical composition to obtain heterogeneous welding)

### 3.6.1 Configurations

Since cold rolled Duplex steel sheets are too thin for arc welding, the welding tests were performed on hot rolled Duplex steel sheets before heat treatments. Thus, the two welded configurations are:

- 2.7 mm Duplex 4Al as upper and lower sheets (filler wire: G3Si)
- 2.7 mm Duplex 8Al as upper and lower sheets (filler wire: G3Si)

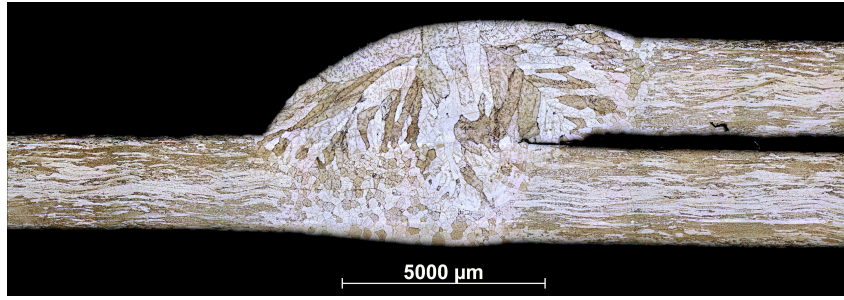


Figure 3.47: Overlap arc welding of hot rolled Duplex 8Al steel sheets using G3Si wire.

Optimal welding parameters are found and collected in table 3.10.

Current type	Gas	Wire	Torch angle	Filler speed	Welding speed	Intensity	Voltage
Standard	8% CO <sub>2</sub> + 92% Ar	G3Si Ø1 mm	25°/10°	4.3 m/min	500 mm/min	105 A	16.5 V

Table 3.10: Arc welding parameters

For this design, only one type of tensile test is commonly carried out, a tensile test which is close to tensile shear test for spot welds. Only two samples are tested for each configuration because the small quantity of material available. One sample corresponds to a weld length of 30 mm. Fracture modes are observed for each sample, and the strength is measured too. The five commonly encountered failure modes are collected in figure 2.28 of the chapter 2.

The investigation methodology is the same as previously introduced. One sample is cut at the cross section of arc weld, polished and chemical etched to reveal the different zones of the arc weld (Base material BM, heat affected zone HAZ, fusion zone FZ). The other two welded samples are mechanically tested. Fracture modes are observed for each sample, and the corresponding failure load is measured.

### 3.6.2 Microstructures

Hardness was measured on the cross section of Duplex arc welds. In figure 3.48, the profiles of heterogeneous welding of Duplex 4Al and Duplex 8Al are shown. The Duplex are welded by addition of G3Si wire, which induces the dilution of Duplex in the fusion zone.

In figure 3.48.a, Duplex 4Al base material presents a hardness around 375 Hv, whereas the quenched HAZ is around 450 Hv and the tempered HAZ is around 300 Hv. The lower hardness of the fusion zone compared to HAZ is due to the dilution with G3Si filler wire (425 Hv).

In figure 3.48.b, the Duplex 8Al base material has a hardness of 270 Hv. On average, Duplex 8Al HAZ and the fusion zone also have a hardness around 270 Hv, but the variations inside these zones are important ( $\pm 50$  Hv). Hardness seems to evolve following the microstructure, depending on the indented grain type.

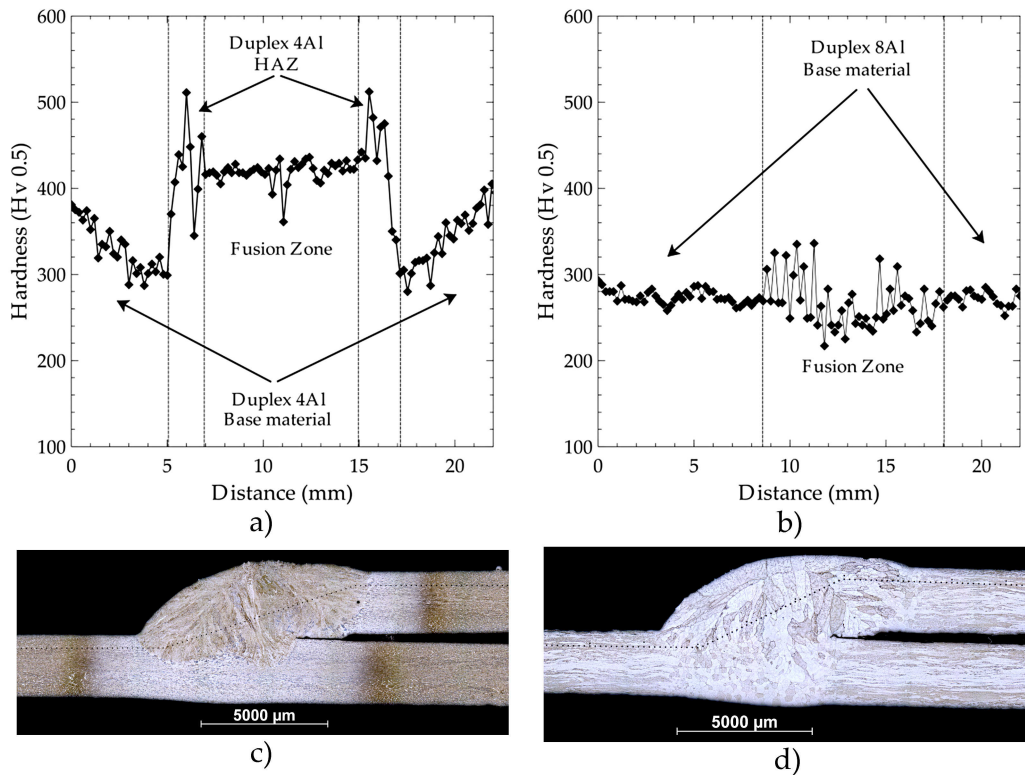


Figure 3.48: Arc weld hardness profiles for Duplex 4Al and Duplex 8Al configurations: a) Duplex 4Al hardness profile, b) Duplex 8Al hardness profile, c) Duplex 4Al metallographic cross-section and d) Duplex 8Al metallographic cross-section.

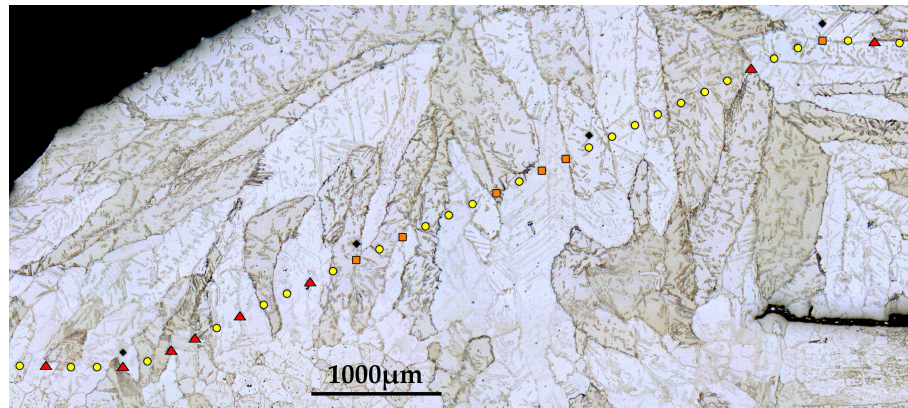


Figure 3.49: Hardness of Duplex 8Al arc welding in the Fusion Zone (red triangles correspond to the highest hardness values, orange squares to the intermediate hardness values and yellow circles to the lowest).

After fine observation of the Fusion Zone and hardness values (figure 3.49), there is no particular trend for hardness values, which seem almost random. Optical microscopy is not sufficient to conclude on the hardness values in the Fusion Zone.

A fine microstructure study of different zones has been realized using confocal mi-



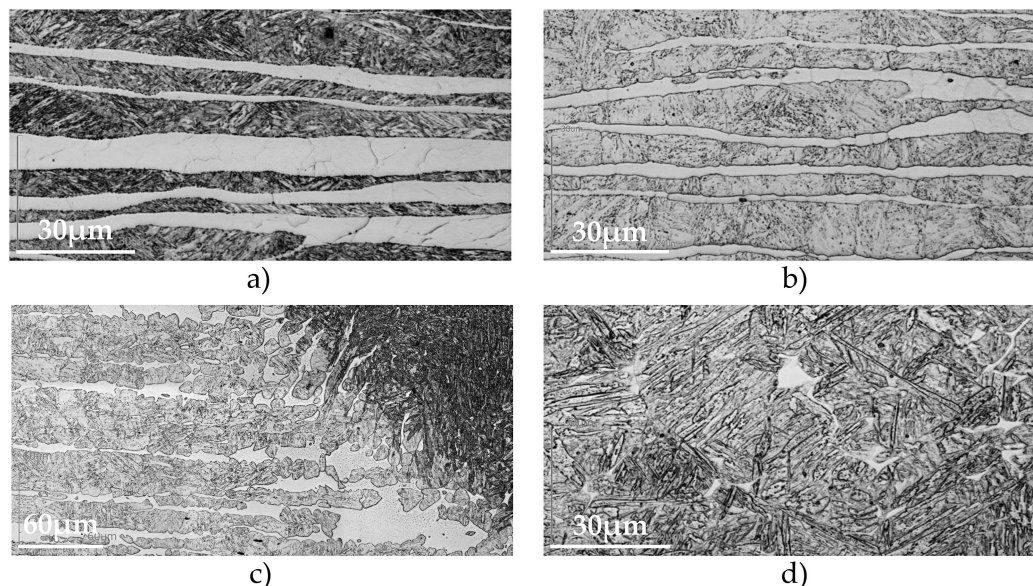


Figure 3.50: Duplex 4Al arc welding microstructures: a) base material, b) HAZ, c) interface HAZ/molten zone, d) molten zone (fusion zone).

croscopy analysis. In figure 3.50, the microstructures of the different specific zones of Duplex 4Al arc weld are observed. 3.50.a represents the base material microstructure with ferrite (white phase) and a compound of fine austenite + ferrite laths (dark phase). HAZ far from the interface is shown in 3.50.b, keeping the same appearance than base material, even if dark phase microstructure changes (laths growth). 3.50.c focuses at the interface between the Duplex HAZ and the fusion zone (of melted Duplex 4Al and G3Si), which presents a grain coarsening on a 100  $\mu\text{m}$  range area. Finally, 3.50.d represents the fusion zone microstructure, mainly martensitic with ferrite islet occasionally. The microstructures observed on arc welds are close to the spot welds microstructures even if thermal cycles are different during the process.

Figure 3.51 presents the microstructures of the different specific zones of Duplex 8Al arc weld. The base material microstructure with ferrite (white phase), austenite (dark phase) and kappa phase (small black zones in austenite grains) is shown in figure 3.51.a. This structure is due to a too low cooling rate during hot rolling process as shown by Wu and al. [WU 91]. HAZ under the fusion zone is shown in 3.51.b, the microstructure is different from the base material one, the ferrite grains recrystallized because of the heat treatment undergone during the welding process (round ferrite grain obtained with intergranular austenite). 3.51.c focused at the interface between the Duplex HAZ and the molten zone: a recrystallization of ferrite grain is observed close to the interface (on a 200  $\mu\text{m}$  range), with round ferrite grain and austenite at grain boundaries. Finally, 3.51.d represents the fusion zone microstructure, with large oriented ferrite grains (from 100  $\mu\text{m}$  to 1 mm) and some austenite inside the grains and at the grain boundaries. These grains come from the solidification mode during welding process. The microstructures observed on arc welds are rather close to the spot welds microstructures again, but no 18R martensite is observed in arc welds. Indeed, some ferrite grains from HAZ or fusion zone showed austenite laths inside the grain. Arc welding process thermal cycle are probably favourable to the carbon

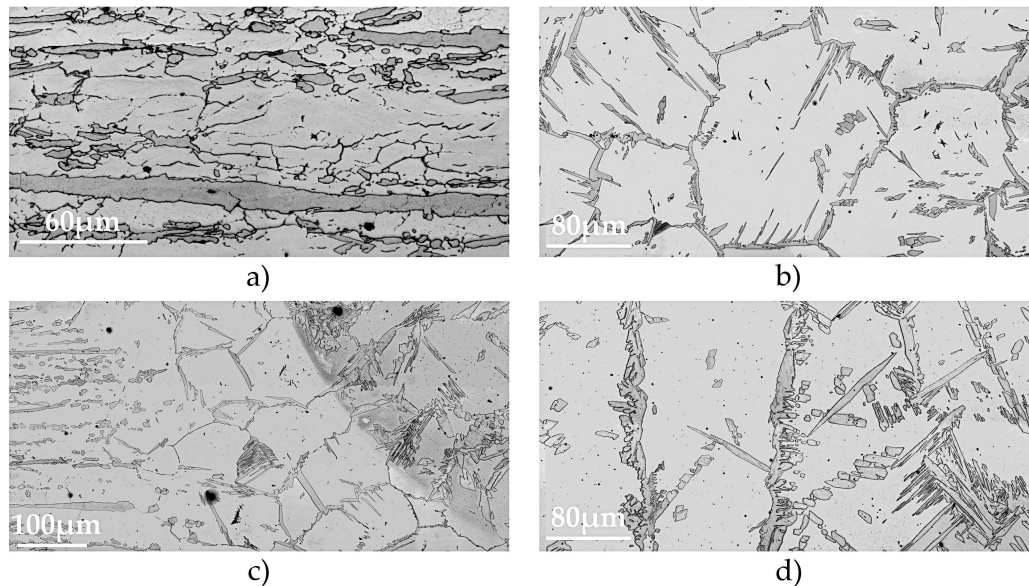


Figure 3.51: Duplex 8Al arc welding microstructures: a) base material, b) HAZ, c) interface HAZ/molten zone, d) molten zone (fusion zone).

diffusion towards grain boundaries which leads to the 18R martensite disappearance.

### 3.6.3 Mechanical tests

After performing the tensile mechanical tests, the observed failure modes are different for the two Duplex assemblies. In the case of Duplex 4Al arc welds, the failure occurs in the hard HAZ close to the interface (between fusion zone and HAZ) at the weld bead toe and propagating under the fusion zone (figure 3.52.a). In the Duplex 8Al case, failure occurs in the fusion zone, from the notch root, and propagating "vertically" along ferrite grains formed during solidification (figure 3.52.b).

Both failure modes are brittle. Concerning Duplex 4Al assembly, a brittle fractograph with a mix of intergranular and transgranular failures (characterized by cleavage on the lower part) is shown in figure 3.53.b. For Duplex 8Al assembly (figures 3.53.c and 3.53.d), the cleavage is omnipresent which involves a very brittle failure, as observed experimentally. The failure follows the microstructure in the Duplex 8Al case. Long grains are observed from the notch root until the weld bead surface and their size could reach the steel sheet thickness (several millimetres).

Failure strengths of arc welds are respectively 450 MPa and 260 MPa for Duplex 4Al and 8Al (figure 3.54). These strengths are very low compared to strengths of classical automotive steels with comparative UTS (800 MPa). Especially for Duplex 8Al arc welds, the microstructure orientation during solidification of weld pool induces an important weakness in the molten zone. To conclude, the negative effect of aluminium on performance is also observed for arc welded assemblies of Duplex. While failure occurs in the HAZ with a limited performance in the Duplex 4Al case, the Duplex 8Al clearly showed very bad performance with a failure in the fusion zone, which is generally not well accepted by the carmaking industry.

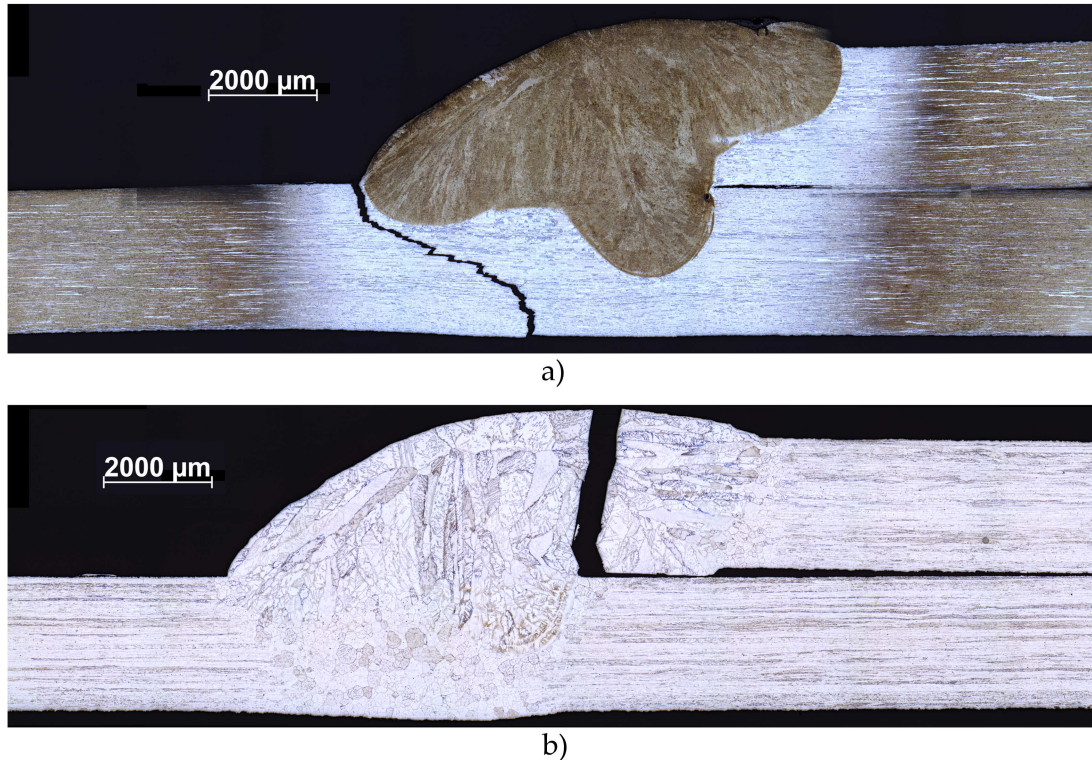


Figure 3.52: Failure modes of arc welds: a) Duplex 4Al and b) Duplex 8Al.

### 3.7 Conclusion

In this section, Duplex steels (4Al and 8Al) elaboration and characterization were presented. Their weldability with a widely used in industry steel grade (DP600) was studied. A fine microstructural characterization was executed on base materials and spot welds. The particularity of ferrite layer apparition at the DP600 HAZ and fusion zone interface was highlighted. Aluminium content influence on it thickness was also highlighted.

Moreover, failure modes of the two Duplex assemblies (Duplex 4Al/DP600 and Duplex 8Al/DP600) for three intensities along the welding range were observed. Failure strengths were measured and compared to highlight the aluminium content influence of spot weld loading bearing capacity. Then, higher is the aluminium content in Duplex steel, thicker is the ferrite layer, and lower are the cross tension and tensile shear strengths (because failure focused in the weak ferrite layer).

The spot and arc welds failure modes and strengths showed the importance of the fusion zone composition (corresponding to the dilution of steels) compared to thermal cycles undergone in weld zones. For this reason, an approach could be using of Schaeffler diagram as for stainless steel in order to ensure the weldability. this kind of approach is extensively studied in particular for high manganese content steels like Twinning Induced Plasticity (TWIP) steels.



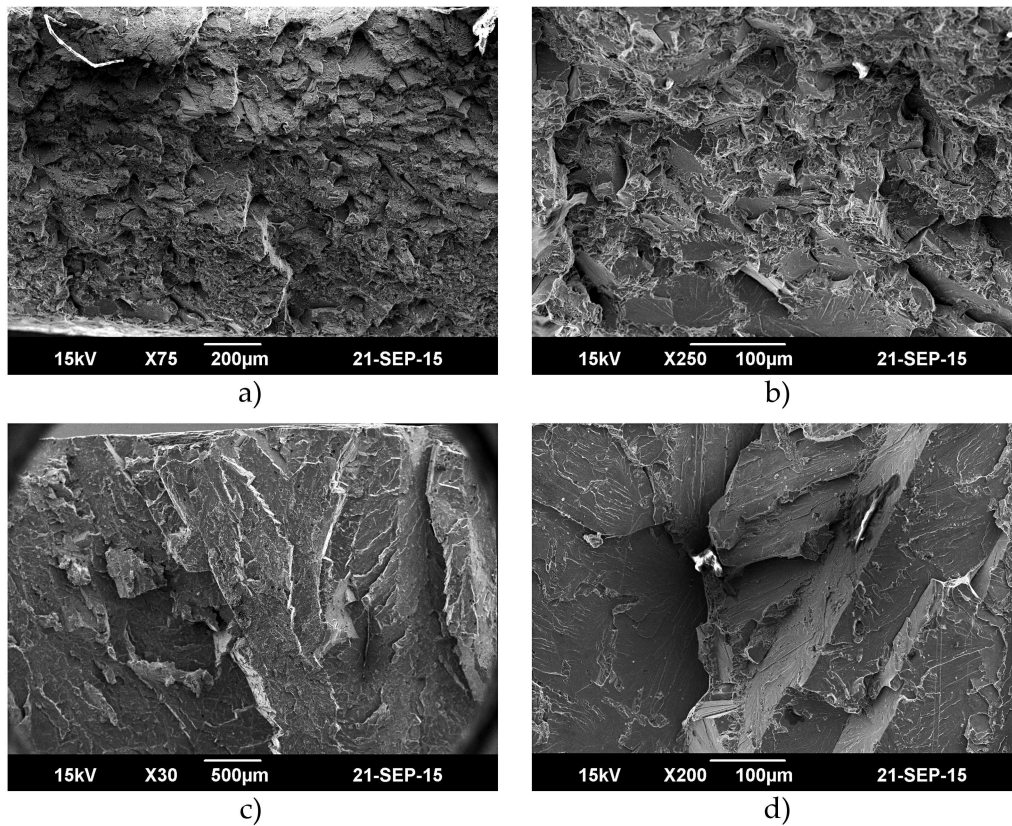


Figure 3.53: Fractography of failed surfaces: a) and b) on Duplex 4Al arc weld, c) and d) on Duplex 8Al arc weld.

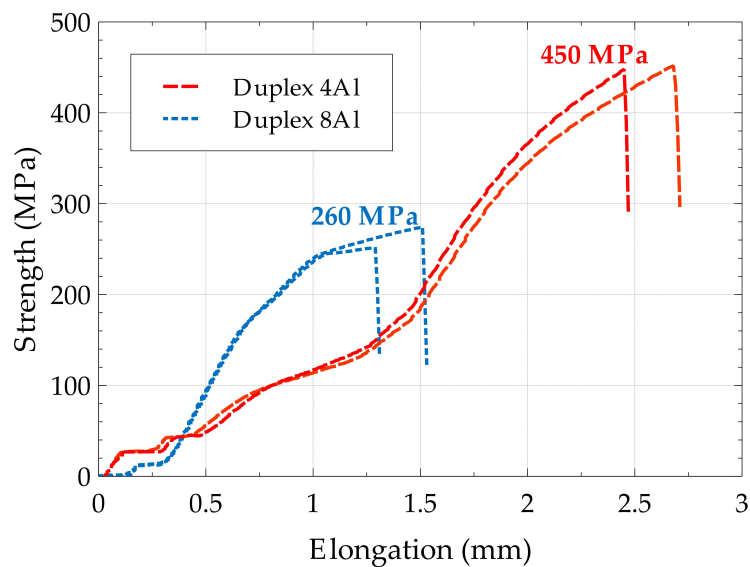


Figure 3.54: Tensile shear behaviour of Duplex 4Al and 8Al arc weld assemblies (Two samples for each configuration).

## Chapter 4

# Finite Element modelling of heterogeneous spot welds mechanical behaviour

Previous chapters focused on the experimental study of heterogeneous and very heterogeneous spot weld assemblies. Different failure mechanisms and failure modes were identified. In this section, a Finite Element modelling methodology for heterogeneous spot weld mechanical behaviour is established in order to predict the previous experimental results. First, the model details are explained, then the results are presented for the two heterogeneous spot weld assemblies.

### Contents

---

<b>4.1</b>	<b>FE modelling methodology . . . . .</b>	<b>113</b>
4.1.1	Spot weld zone discretization . . . . .	114
4.1.2	Elastic-plastic strain hardening law . . . . .	118
4.1.3	Ductile damage failure criterion . . . . .	121
4.1.4	Cohesive zones implementation . . . . .	126
<b>4.2</b>	<b>Heterogeneous welding model . . . . .</b>	<b>127</b>
4.2.1	Cross tension test results . . . . .	127
4.2.2	Tensile shear test results . . . . .	136
4.2.3	Discussion . . . . .	144
<b>4.3</b>	<b>Highly heterogeneous welding model . . . . .</b>	<b>145</b>
4.3.1	Cross tension test results . . . . .	145
4.3.2	Tensile shear test results . . . . .	146
4.3.3	Discussion . . . . .	148
<b>4.4</b>	<b>Conclusion . . . . .</b>	<b>148</b>

---

## 4.1 FE modelling methodology

In this section, the modelling methodology of spot weld assemblies is described. Several configurations are modelled:

- four Usibor1500/DP600 configurations with varying thicknesses as studied experimentally in chapter 2,
- one Duplex 8Al/DP600 configuration from experimental study of chapter 3.

Each of these configurations is furthermore considered at the lower end, middle and upper end of the welding range.

#### 4.1.1 Spot weld zone discretization

In his PhD thesis, Dancette [DAN 09] chose to cut the spot weld in three zones: Base Material (BM), sub-critical Heat Affected Zone (SCHAZ) with the mechanical behaviour of a 700 °C HAZ and fusion zone with the mechanical behaviour of a 1200 °C HAZ. Some comparisons were done with a twelve zones discretization and showed the simplified three zones model exhibits a good correlation with experiments in the case of homogeneous spot welding modelling. Consequently, in the case of heterogeneous welding, a simplified discretization of the weld zones should also well describe the spot weld behaviour.

In order to identify the important zones playing a role in the spot weld behaviour, micro hardness tests were performed on the weld joints. Weld zones presenting different hardness levels are taken into account in the discretization because their mechanical behaviours drastically change. The specific feature of heterogeneous welding is that the molten nugget is generally a mixture of the two base materials. In the case of very heterogeneous welding, chemical composition of the nugget will strongly differ from those of the two base materials. The resulting mechanical behaviour is then also likely to be significantly different.

In the case of Usibor1500/DP600 weld joints, the welding process has various effects on the two steels (Usibor1500 and DP600) because of their microstructures. Micro-hardness profiles on these spot welds allow to highlight six zones (figure 4.1), which are reproduced in the figure 4.2:

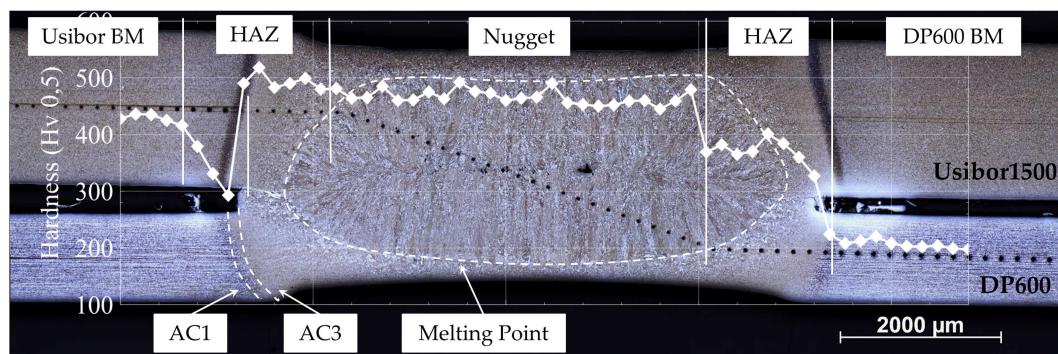


Figure 4.1: Micro-hardness profile on a Usibor1500/DP600 spot weld with the corresponding micrograph.

- Usibor1500 base material, not affected by welding process,
- Usibor1500 soft tempered zone, where a part of Usibor1500 steel martensite was tempered during the welding process,
- Usibor1500 HAZ, corresponding to the quenched HAZ,
- Fusion zone (nugget), quenched mixture of Usibor1500 and DP600 steels,
- DP600 HAZ, corresponding to the quenched HAZ of DP600 steel,

- DP600 base material, not affected by the welding process.

Furthermore, a cohesive zone is inserted at the former sheet interface (figure 4.2) to enable the prediction of potential brittle interfacial failure. The cohesive zone aspects will be described later in a dedicated section.

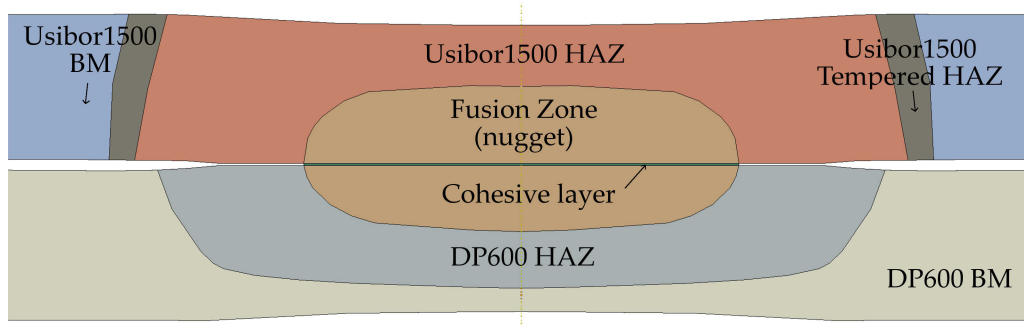


Figure 4.2: Minimal discretization for heterogeneous Usibor1500/DP600 spot weld behaviour.

In the case of Duplex 8Al/DP600 weld joints, heterogeneous welding induced the apparition of particular phases as explained in chapter 3. The typical hardness profile is shown in figure 4.3. On the DP600 side, the HAZ are the same as previously. However on the Duplex 8Al side, only one HAZ is observed because Duplex 8Al BM does not present martensite, inducing no tempering possibility in the HAZ. Moreover, the Duplex 8Al HAZ near the fusion zone has a hardness close to the base material even if the microstructure is completely recrystallized and martensite 18R is present in the grains. Because the Duplex 8Al HAZ seems to present a mechanical behaviour close to the base material one and since no mechanical test could be performed on this microstructure, the Duplex HAZ behaviour is chosen to be the same as the base material one in the model.

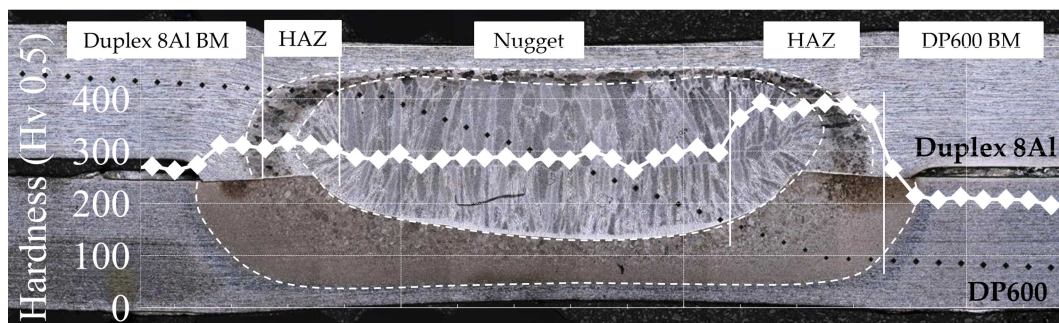


Figure 4.3: Micro-hardness profile on Duplex8Al/DP600 spot weld with the corresponding micrograph.

Following the former considerations, four zones with different mechanical behaviours need to be described (figure 4.4):

- Duplex 8Al base material and HAZ,
- Fusion zone (nugget), quenched mixture of Duplex 8Al and DP600 steels,
- DP600 HAZ, corresponding to the quenched HAZ of DP600 steel,
- DP600 base material, not affected by the welding process.



In order to allow interfacial failure, the same cohesive zone as in the Usibor1500/DP600 case is inserted at the faying surface. However, a new phase has to be considered: the ferrite layer at the interface between fusion zone and DP600 HAZ. As shown in chapter 3, all failures of Duplex8Al/DP600 spot welds took place along the ferrite layer, which was identified as brittle. To consider this particular brittle phase, a second cohesive zone was inserted at the DP600 HAZ/Fusion Zone interface (figure 4.4).

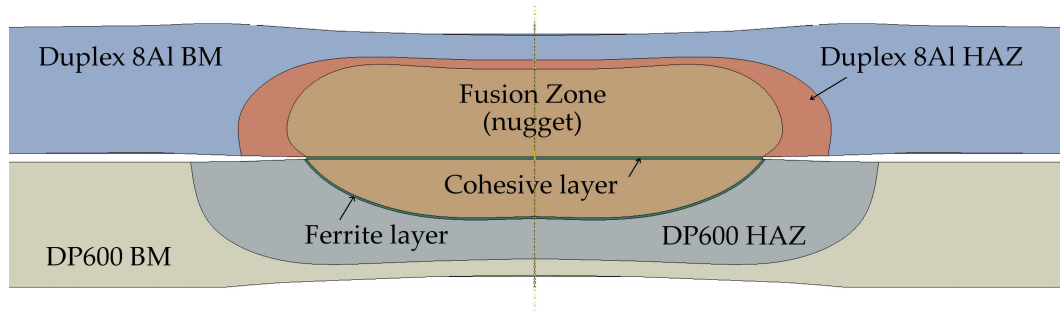


Figure 4.4: Minimal discretization for heterogeneous Duplex 8Al/DP600 spot weld behaviour.

The geometry of zones in the model is derived from the micrographs. Zones outlines are traced from etched micrograph cross sections to best represent the spot welds geometry (figures 4.2 and 4.4). Then, these sketches are circularly extruded around a vertical axis passing through nugget centre. The extrusion angle depends on the mechanical test modelled: in cross tension, the minimal symmetry allows to consider only a spot weld quarter whereas in tension shear half a spot weld has to be modelled (figure 4.5).

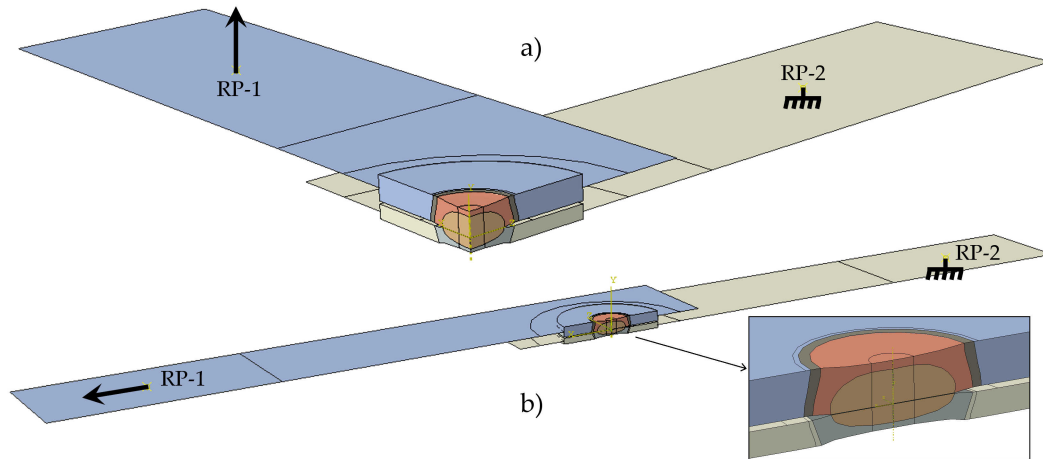


Figure 4.5: Minimal symmetry of heterogeneous spot weld mechanical tests with the loading conditions: a) spot weld quarter in cross section and b) half spot weld in tensile shear.

In order to reduce the number of elements, the steel sheets out of the spot weld zone are modelled with shell elements. This requires to use a particular coupling available in the Abaqus software, “Shell-to-Solid” coupling.

The boundary conditions are shown in figure 4.5. Displacement is imposed on the top



sheet (Usibor1500 or Duplex8Al following the case) on a reference point (RP-1), depending on the mechanical test: vertically for cross tension and in the sheet direction for tensile shear. DP600 sheet is blocked at the second reference point (RP-2). Reference points are coupled kinematically to all shell elements of the clamped zones during the test.

The Abaqus Explicit solver is used in order to observe model failure. The Explicit method is a true dynamic procedure originally developed to model high-speed impact events in which inertia plays a dominant role in the solution. Explicit solution method is valuable in solving quasi-static problems in particular when contact or failure problems are modelled. However, applying explicit dynamic procedure to quasi-static problems requires some special considerations. Since a static solution is, by definition, a long-time solution, it is often computationally impractical to analyse the simulation in its natural time scale, which would require an excessive number of small time increments. To obtain a valuable solution, events must be accelerated in some way. As the event is accelerated, the state of static equilibrium evolves into a state of dynamic equilibrium in which inertial forces may become dominant.

In the quasi-static spot weld mechanical problem, the goal is to model the test in the shortest time period in which inertial forces remain insignificant. In order to find this shortest time period, a modal study of the spot weld assembly should be done. This study allows to obtain the first natural frequency of the assembly, which leads to a corresponding critical period that should remain lower than the analysis time. In our case, depending on the spot welds, the first natural frequency is between 2000 Hz and 5200 Hz, which suggests to consider a time period over 0.0005 s. To be sure that no dynamic effect appears during simulation, a 0.01 s time period is taken for the following analyses.

However, to verify that there is no deviation during calculation, the Implicit solver was also used on the same models without failure criteria. If the Explicit response is following the Implicit one before the occurrence of significant damage, no dynamic effects are perturbing the response.

In order to optimize calculation time keeping an accurate description of spot weld mechanical behaviour, the chosen element size in the spot weld is 0.2 mm (figure 4.6). However, in the base material zones, 0.3 mm element size is taken to reduce the total number of elements. Abaqus C3D8R elements are used corresponding to an eight-node brick element with reduced integration and the ability to be used in Explicit simulations. This element type and mesh refinement was identified as a good compromise between computational cost and accuracy, which will be discussed in the next chapter 5.

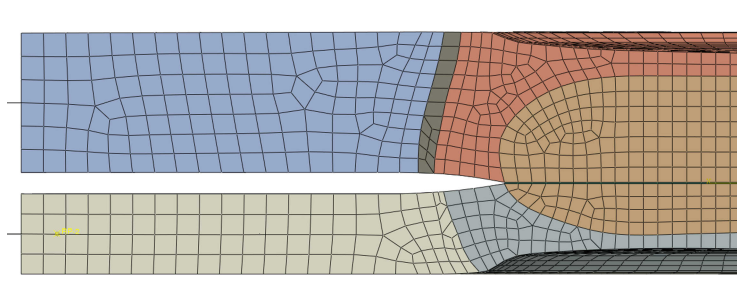


Figure 4.6: Mesh of a cross tension model.

The shell element type in the steel sheets outside of the 3D spot weld zone is S4R, a four-node shell element with reduced integration and five integration points along the thickness by default. The mesh size in the shell part is 1 mm to decrease the total number of elements in the model.

#### 4.1.2 Elastic-plastic strain hardening law

Spot weld zones being defined, their strain hardening laws have to be now characterized. Two independent methodologies could be used. The first one consists in simulating the thermal cycle undergone in each weld zone with a thermo-mechanical simulator (Gleeble 3500). As shown by Dancette and al. [DAN 11b], the HAZ microstructure could be reproduced and tensile tests could be performed hereafter in order to obtain the stress-strain curve of a zone. The second methodology consists in using empirical law of phase behaviours (martensite and tempered martensite behaviours in particular). Whatever the methodology, the tensile stress-strain curves were modelled by a Swift-Voce law [LEM 07], which allows to well describe the strain hardening of ferritic, martensitic and multiphase steels. The expression of the Swift-Voce law writes:

$$\sigma = (1 - \alpha) \cdot [K \cdot (\varepsilon_p + \varepsilon_0)^n] + \alpha \cdot [\sigma_{sat} - (\sigma_{sat} - \sigma_0) \cdot \exp(-m \cdot \varepsilon_p)] \quad (4.1)$$

where

$\varepsilon_p$  is the true plastic strain,

$\varepsilon_0$ ,  $K$  and  $n$  are the Swift law parameters,

$\sigma_0$ ,  $\sigma_{sat}$  and  $m$  are the Voce law parameters

and  $\alpha$  is a fitting parameter.

In the Gleeble simulator methodology, the Swift-Voce parameters for each zone are identified directly from the tensile curves using a dedicated program.

For the fusion zone, mechanical tests are more difficult to conduct for obtaining the constitutive behaviour. Indeed, thermo-mechanical simulator data is not available yet and requires a significant base material quantity. Moreover, in the case of heterogeneous welding, the nugget being a mixture of two steel grades, it is very difficult to reproduce the proper compound in order to perform mechanical tests. Allain and al. [ALL 12] and Arlazarov and al. [ARL 13] worked on the development of empirical constitutive laws for low alloyed martensitic steels and particularly on the manganese (Mn) effect on strength and strain hardening. This model is called Simplified Continuum Composite Approach (SCCA) for fresh and tempered martensite. It assumes that all composite elements of martensite undergo the same amount of strain.

To describe the stress-strain curve of fresh martensite as a large elastic-plastic transition the strain hardening can be expressed as the product of Young modulus ( $E$ ) by the fraction of elastic zones ( $1 - F$ ):

$$\frac{d\sigma}{d\varepsilon} = (1 - F) \cdot E \quad (4.2)$$

where  $\sigma$  and  $\varepsilon$  are respectively the macroscopic stress and strain of the material. The plastified zone fraction  $F$  is chosen as a probabilistic law:

$$F = 1 - \exp\left(-\left(\frac{\sigma - \sigma_{min}}{\sigma_0}\right)^p\right) \quad (4.3)$$

where  $\sigma_{min}$  is the minimum stress necessary to start plasticity,  $p$  and  $\sigma_0$  are the parameters that control the shape of  $F(\sigma)$  curve.

$\sigma_{min}$  and  $p$  can be taken as constants for all considered steels and the following values are found to be optimal:  $\sigma_{min} = 450$  MPa and  $p = 2.5$ . A linear dependence between  $\sigma_0$  and carbon equivalent  $C_{eq}$  is established in the form of the following equation:

$$\sigma_0 = 130 + 1997 \cdot C_{eq} \quad (4.4)$$

where  $C_{eq}$  is the parameter that considers the concomitant influence of C and Mn. It is proposed to take into account this synergy of C and Mn in the following way:

$$C_{eq} = C \cdot \left(1 + \frac{Mn}{K_{Mn}}\right) \quad (4.5)$$

where  $C$  and  $Mn$  represent initial C and Mn (wt%) contents, and  $K_{Mn}$  is the coefficient of the Mn influence, taken equal to 3.5. Finally, the parameters are given in table 4.1:

Physical parameters	Fitted parameters	Input data
$E$ (Young modulus)	$\sigma_{min} = 450$ MPa and $p = 2.5$	wt% of $C$ and $Mn$

Table 4.1: SCCA fresh martensite model parameters.

Similarly, a tempered martensite law was also developed. The Simplified Continuum Composite Approach (SCCA) is used to describe the behaviour law of tempered martensite too. It is considered that C in solid solution in tempered martensite decreases with temperature and time of tempering. Also it is supposed that the lath size of tempered martensite stays constant (150 nm) with tempering temperatures lower than 400 °C. At higher tempering temperatures the lath size increases with temperature and time of tempering. Strengthening due to the carbide precipitation is neglected. The plastified zone fraction  $F$  is the same as previously in equation 4.3 but  $\sigma_{min}$  formulation is now dependent on the lath size ( $\lambda$ ) as:

$$\sigma_{min} = \sigma_{0_F} + \frac{M \cdot \mu \cdot b}{\lambda} \quad (4.6)$$

where  $M$  average Taylor factor,  $\mu$  shear modulus and  $b$  Burgers vector are generic parameters and their value are respectively: 3, 80 000 MPa and  $2.5 \times 10^{-10}$  m. Considering  $\sigma_0$ , the linear dependence with  $C_{eq}$  still in solid solution is defined by equation 4.4 but  $C_{eq}$  is new given by:

$$C_{eq} = C_{ss} \cdot \left(1 + \frac{Mn}{K_{Mn}}\right) \quad (4.7)$$

where  $C_{eq}$  is the parameter that considers the concomitant influence of C and Mn,  $K_{Mn}$  is the coefficient of the Mn influence, taken equal to 3.5 and  $C_{ss}$  and  $Mn$  represent

C and Mn (wt%) in solid solution in tempered martensite contents.  $C_{ss}$  changes with temperature and time of tempering in the following way:

$$C_{ss} = C_{ini} - P \cdot T \cdot (K + \ln t) \quad (4.8)$$

where  $C_{ini}$  is the initial C (wt%),  $K$  and  $P$  are the fitting parameters ( $K = 20$  and  $P = 1.4 \times 10^{-5}$ ) and  $t$  the overaging time in seconds. Finally, the parameters are given in table 4.2:

Physical parameters	Fitted parameters	Input data
$E$ (Young modulus)	$\sigma_{min} = 450$ MPa, $p = 2.5$ , $K = 20$ and $P = 1.4 \times 10^{-5}$	$\lambda$ and wt% of $C$ and $Mn$

Table 4.2: SCCA tempered martensite model parameters.

A comparison between the two methodologies was initiated, on Usibor1500 quenched (figure 4.7.a) and tempered (figure 4.7.b) Heat Affected Zones. Figure 4.7 compares the constitutive law obtained with the two methodologies and the experimental behaviour. Obtained strain hardening law are satisfying whatever the methodology, however, using the SCCA is really more efficient because no base material nor experimental tests are needed.

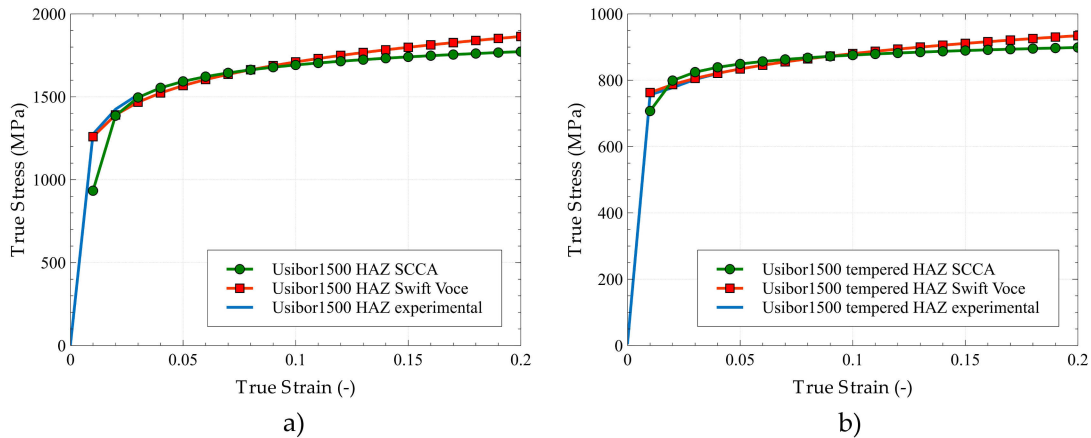


Figure 4.7: Comparison of elastic-plastic constitutive behaviours using the Gleeble + Swift-Voce and the SCCA methodologies: a) on the quenched Usibor1500 HAZ and b) on the tempered Usibor1500 HAZ.

Moreover, using SCCA laws presents the advantage to predict the constitutive law of the fusion zone by assuming an equivalent carbon of the mixture (area ratio). Consequently, the SCCA model is used to establish all elastic-plastic strain hardening law of the different zones for DP600 and Usibor1500 steels (figure 4.8).

It is important to notice that the Usibor1500 tempered zone behaviour is clearly weaker than the base material and HAZ ones. Chemical compositions of DP600 and Usibor1500 are rather close and their thermo-physical characteristics too. That is why welding process

produces an equal development of the nugget in the two sheets (no nugget shift). Consequently, the fusion zone constitutive behaviour can be considered as the average behaviour of the two HAZ.

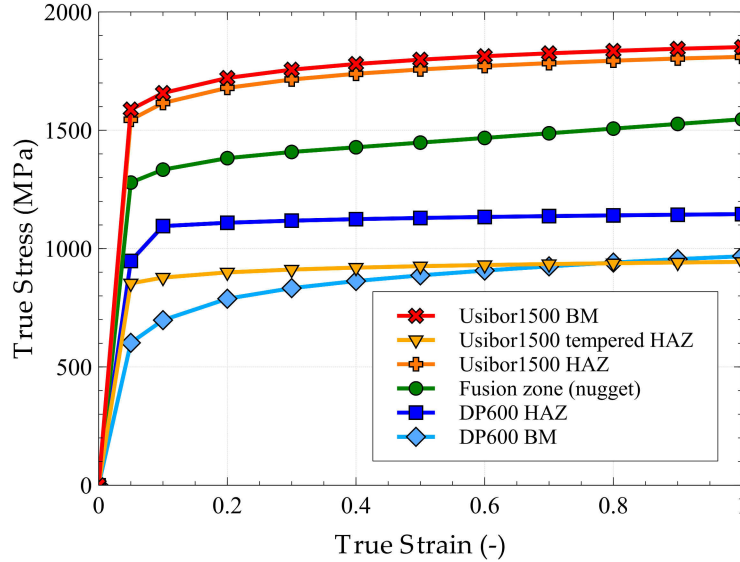


Figure 4.8: Elastic-plastic strain hardening law for each zones of a Usibor1500/DP600 spot weld (with same sheets thickness) established by SCCA model [ARL 13].

By contrast, this method cannot be used for Duplex steel HAZ because their manganese content is too high to enter in the model range. Thus, tensile tests were performed on Duplex steels, which allows to establish a Swift-Voce law for the base material. Concerning the fusion zone of Duplex 8Al/DP600 spot welds, a mixture law is used, based on the dilution ratio of each steel grade. The obtained elastic-plastic strain hardening law can be related to the hardness measures in the different zones. The increasing order of strengths of the elastic-plastic curves is the same as the increasing order of hardness in figures 4.1 and 4.3. This remains valid for both Usibor1500/DP600 and Duplex 8Al/DP600 welds.

In conclusion, the elastic-plastic strain hardening behaviour of the different zones of studied spot welds are now characterized. They are used in the following under the assumption of  $J_2$  (Von Mises) isotropic plasticity for the description of the yield locus in arbitrary complete stress states. However, damage and failure criteria are missing at this point in order to predict spot weld failure modes and load bearing capacities.

#### 4.1.3 Ductile damage failure criterion

Some authors used a Gurson-based ductile damage model in the spot weld mechanical behaviour simulation as presented in the section 1. These models can describe ductile damage in tension very well for steel, but not under shear loading. Moreover, the Gurson model is rather complex to set up: model parameters have to be fitted by an inverse method, modelling the tensile tests and identifying the parameters for each material. In the case of welding simulations, many zones need to be described, which turns out as a long and difficult identification work.



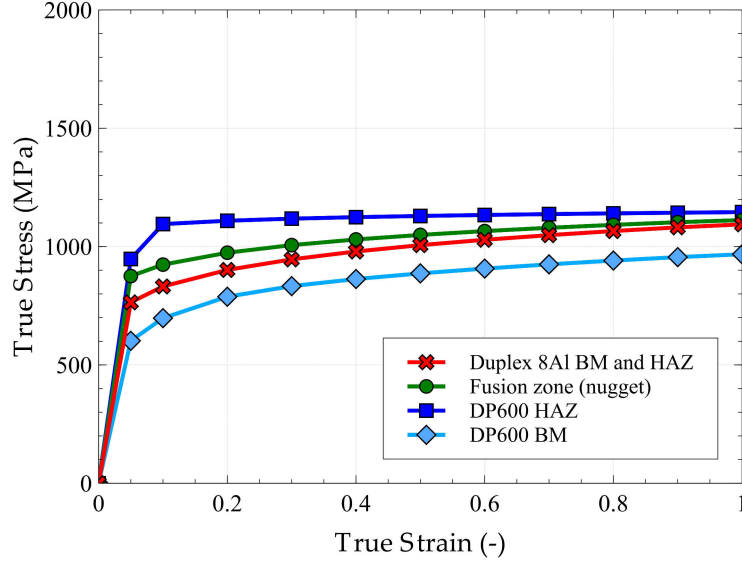


Figure 4.9: Elastic-plastic strain hardening law for each zones of a Duplex 8Al/DP600 spot weld (with same sheets thickness) established by SCCA model [ARL 13] for DP600 steel zones and by fitting Swift-Voce model on tensile test for Duplex 8Al steel zone.

In order to propose a simple and efficient simulation methodology, the failure criterion is decayed in a damage initiation and a damage evolution description.

Concerning the damage initiation, the proposed FE models are based on a failure strain initiation. In order to obtain a systematic damage initiation criterion, the Considere criterion [CON 85] was chosen because it is very simple to identify on the previously obtained stress-strain curves of each weld zone (figure 4.10). Considere criterion describes the beginning of plastic instability and is defined by the following equation:

$$\sigma^* = \frac{d\sigma}{d\varepsilon} \quad (4.9)$$

where  $\sigma^*$  is the stress at the beginning of necking. The corresponding strain ( $\varepsilon_0^{pl}$ ) is taken for onset of the damage initiation of the different zone. The identified damage initiation strains by the Considere criterion are collected in the tables 4.3 and 4.4 for the different zones .

Zones	Usibor1500 BM	Usibor1500 HAZ	Usibor1500 tempered	Fusion zone	DP600 HAZ	DP600 BM
$\varepsilon_0^{pl}$	0.070	0.071	0.050	0.064	0.051	0.160

Table 4.3: Identified damage initiation strain using Considere criterion for the different zones of a Usibor1500/DP600 spot weld.

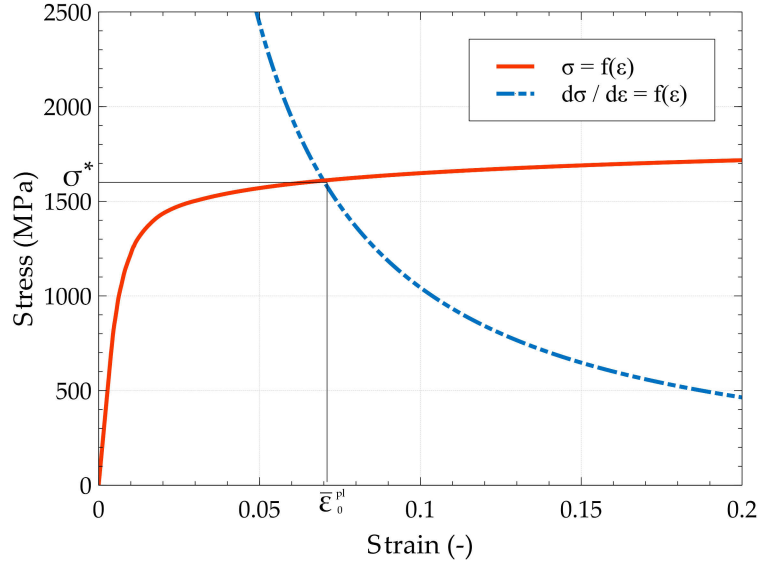


Figure 4.10: Considere criterion identification on Usibor1500 steel.

Zones	Duplex 8Al BM	Fusion zone	DP600 HAZ	DP600 BM
$\bar{\varepsilon}_0^{pl}$	0.114	0.076	0.051	0.160

Table 4.4: Identified damage initiation strain using Considere criterion for the different zones of a Duplex 8Al/DP600 spot weld.

However, as shown in the literature review, chapter 1, many authors highlighted the importance of taking stress triaxiality into account in the ductile damage criterion in order to reproduce the spot weld mechanical behaviour properly. Based on Chung and al. method [CHU 16], a stress triaxiality ( $t$ ) dependence is introduced for the damage initiation criterion of the different zones.

Along the whole stress triaxiality range, the damage initiation strain is defined by three functions of the stress triaxiality. The first one follows a first-order inverse function for the region beyond uniaxial tension mode ( $t \geq 0.33$ ) with a constant  $K$  as shown in the equation:

$$\bar{\varepsilon}_0^{pl} = \frac{K}{t} \quad \text{for } t \geq 0.33 \quad (4.10)$$

$K$  is calculated using the damage initiation strain  $\bar{\varepsilon}_0^{pl}$  at a stress triaxiality of 0.33 using Considere criterion.

Furthermore, a constant effective damage initiation strain, denoted by  $D$ , is assumed for the negative stress triaxiality region ( $t \leq 0$ ) as the half value of  $\bar{\varepsilon}_0^{pl}|_{t=0.33}$ :

$$\bar{\varepsilon}_0^{pl} = \frac{\bar{\varepsilon}_0^{pl}|_{t=0.33}}{2} = D \quad \text{for } t \leq 0 \quad (4.11)$$

In the transition zone ( $0 < t < 0.33$ ), a second-order polynomial function connecting the other two is assumed, and therefore, its expression is:

$$\bar{\varepsilon}_0^{pl} = 9 \cdot (\bar{\varepsilon}_0^{pl}|_{t=0.33} - \bar{\varepsilon}_0^{pl}|_{t=0}) \cdot t^2 + \bar{\varepsilon}_0^{pl}|_{t=0} = 9 \cdot \left( \frac{K}{0.33} - D \right) \cdot t^2 + D \quad \text{for } 0 < t < 0.33 \quad (4.12)$$

Consequently, there was only one constant, denoted by K, to obtain in this simplified fracture criterion.

This method allows to establish the damage initiation criterion for all the spot welds zones on the entire range of stress triaxiality. This criterion is represented in figure 4.11 for the base material of Usibor1500 steel.

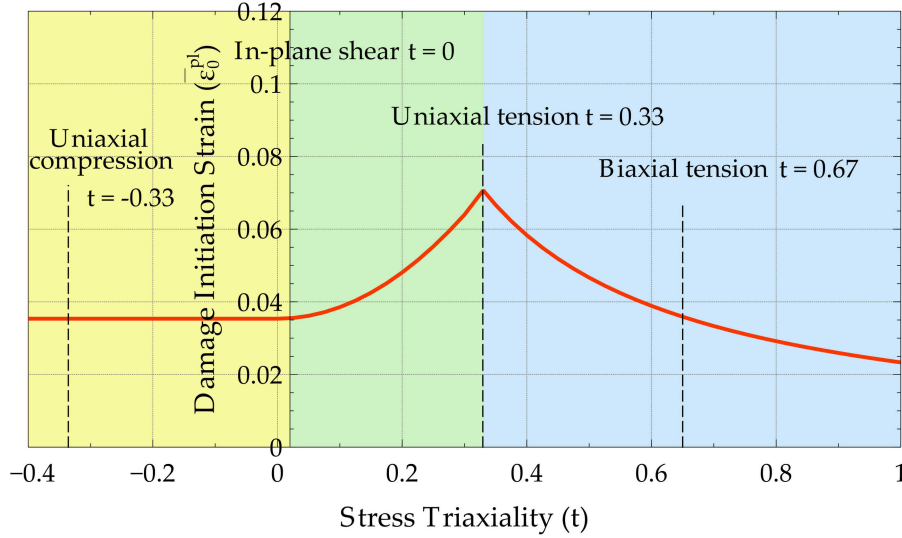


Figure 4.11: Stress triaxiality dependent effective damage initiation strain for damage initiation criterion of Usibor1500 base material.

Damage evolution is chosen as a linear evolution to simplify the ductile damage criterion. The FE element loss of stiffness after initiation takes place on a specific length different in each zone following their ductility. In figure 4.12.a,  $\sigma_{y0}$  and  $\bar{\varepsilon}_0^{pl}$  are the yield stress and equivalent plastic strain at the onset of damage, and  $\bar{\varepsilon}_f^{pl}$  is the equivalent plastic strain at failure, when the overall damage variable reaches the value  $D = 1$ . The overall damage variable,  $D$ , captures the combined effect of all active damage mechanisms and is computed in terms of potential individual damage variable,  $d_i$ . In this study, the only individual damage variables  $d_i$  is the linear damage evolution  $d$  (figure 4.12.b).

Indeed, the linear damage law and the material stiffness is degraded through the damage variable  $D$  as:

$$\sigma = (1 - D)\bar{\sigma} \quad (4.13)$$

$$D = \int_0^t \frac{\dot{\bar{u}}^{pl}}{\bar{u}_f^{pl}} dt \quad (4.14)$$

where  $\bar{\sigma}$  is the effective (undamaged) stress,  $\bar{u}_f^{pl}$  the effective plastic displacement at

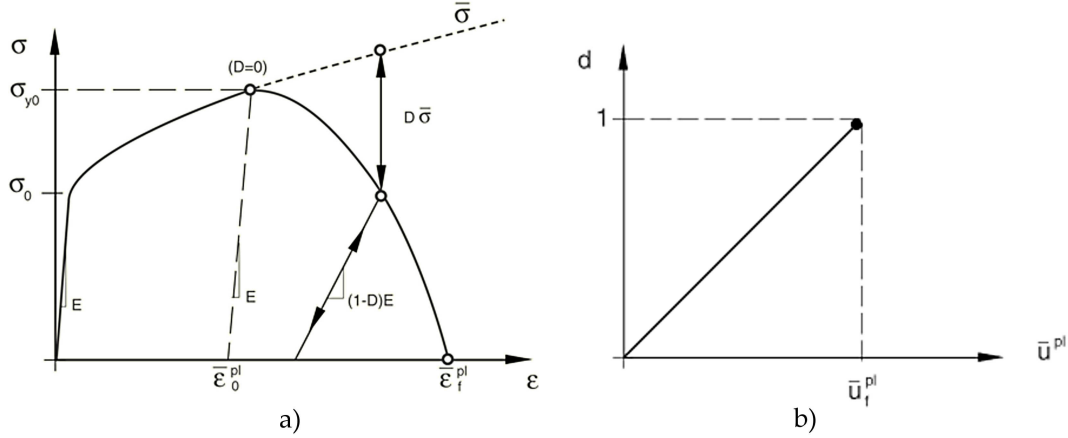


Figure 4.12: Damage evolution in Abaqus: a) stress-strain curve with progressive damage degradation and b) linear definition of damage evolution based on plastic displacement.

fracture,  $\dot{u}^{pl} = 0$  before damage initiation and  $\dot{u}^{pl} = \dot{\epsilon}^{pl} L$  during damage,  $L$  being a characteristic length of the finite element used.

Following the work of Hillerborg et al. [HIL 76], the effective plastic displacement  $\bar{u}^{pl}$  can be seen as the fracture work conjugate of the flow stress during damage. Its introduction in the definition of the damage variable  $D$  helps reducing the mesh dependency once damage is initiated, creating a stress-displacement response of an element instead of a stress-strain one.

The effective plastic displacement was identified for the different zones with the available tensile tests and extrapolated using the rule of mixture for the fusion zones. The effective plastic displacement  $\bar{u}_f^{pl}$  for a 0.2 mm mesh size are gathered in tables 4.5 and 4.6:

Zones	Usibor1500 BM	Usibor1500 HAZ	Usibor1500 tempered	Fusion zone	DP600 HAZ	DP600 BM
$\bar{u}_f^{pl}$ (mm)	0.03	0.02	0.2	0.1	0.1	0.2

Table 4.5: Identified effective plastic displacement at fracture for the different zones of a Usibor1500/DP600 spot weld.

Zones	Duplex 8Al BM	Fusion zone	DP600 HAZ	DP600 BM
$\bar{u}_f^{pl}$ (mm)	0.1	0.15	0.1	0.2

Table 4.6: Identified effective plastic displacement at fracture for the different zones of a Duplex 8Al/DP600 spot weld.

Observing the hardness values in each zone in figures 4.1 and 4.3, the predicted effective plastic displacements are consistent with the observed zone ductility. In figure 4.1, Usibor1500 tempered HAZ and DP600 have low hardness values compared to other zones. Accordingly, their softer behaviour allows for a larger effective plastic displacement

corresponding to a higher global ductility.

#### 4.1.4 Cohesive zones implementation

As shown in figures 4.13.b and 4.13.c, cohesive zones are integrated in the model at the sheets interface (between the two notch roots). In the Duplex 8Al/DP600 spot welding case, an additional cohesive zone is integrated at the interface between DP600 HAZ and the fusion zone in order to take the ferrite layer behaviour into account.

The theory of cohesive zone was briefly discussed in the literature review (chapter 1). The main advantage of this strategy is the inclusion of a progressive mechanical damage. The behaviour of cohesive zone is reflected in a linear elastic loading phase up to  $\sigma_{max}$ , the stress at damage initiation. Damage is represented by a decrease in stiffness from an initial opening displacement  $\delta_0$  until a critical one  $\delta_c$  of the interface where cohesive zone is broken. Making the hypothesis  $\delta_0$  should be as small as possible, cohesive zone is only defined by a stiffness  $K_{ZC}$ , a maximal stress  $\sigma_{max}$ . This corresponds to a toughness  $\Gamma$  of the cohesive zone, defined as the area under the curve after damage initiation (figure 4.13.a).

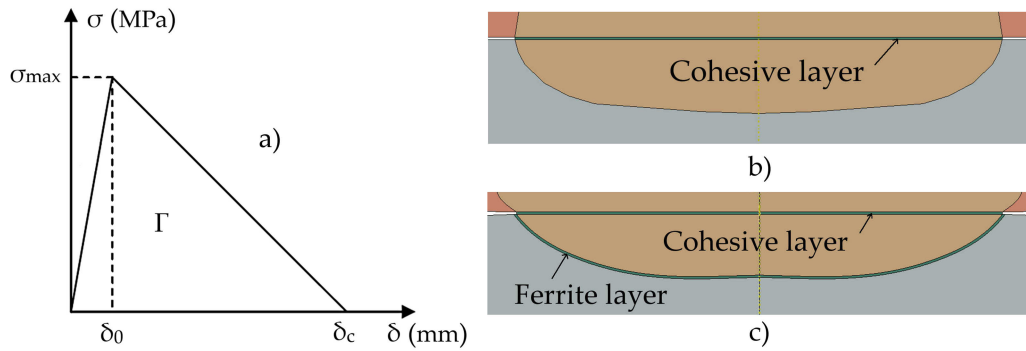


Figure 4.13: Cohesive zone implementation in spot weld FE models: a) Traction separation law of cohesive elements, b) cohesive zone at the sheets interface of Usibor1500/DP600 spot welds and c) cohesive zones at the sheets interface of Duplex 8Al/DP600 spot welds and at the DP600 HAZ and fusion zone interface.

In Abaqus software, cohesive elements are configured using the couple  $\sigma_{max}$  -  $\Gamma$  in the normal and two tangential directions corresponding to the three crack propagation modes (I, II and III). In the model, a 0.02 mm cohesive zone thickness is chosen, where the neighbouring elements are 0.2 mm in size.

A limited number of methods exist for cohesive parameters identification and are very complicated to set up on spot weld fusion zone. Lacroix and al. [LAC 15] developed a particular wedge test device to estimate the cohesive parameters of a spot weld in opening mode (mode I). It is however a complex experimental procedure.

An inverse identification procedure was used instead to identify the cohesive parameters. From cohesive parameters of Dancette and al. [DAN 12] and Lacroix and al. [LAC 15], for the two loading types (cross tension and tensile shear), two spot welds which failed in interfacial and in button pull-out modes were used to initiate the inverse procedure. Then the cohesive parameters were optimized in order to predict the failure



modes and strengths of these spot welds well enough under cross tension and tensile shear. Finally, the optimized cohesive parameter values were introduced in the other configurations to be validated.

The optimized cohesive parameters of the three cohesive zones are gathered in table 4.7:

Cohesive zones	$\sigma_{max}$ in MPa			$\Gamma$ in $\text{kJ m}^{-2}$		
	$\sigma_{max1}$	$\sigma_{max1}$	$\sigma_{max3}$	$\Gamma_1$	$\Gamma_2$	$\Gamma_3$
Usibor1500/DP600 fusion zone	3500	2300	2300	8	16	16
Duplex 8Al/DP600 fusion zone	2400	1600	1600	4	8	8
Duplex 8Al/DP600 ferrite layer	1200	1100	1100	3	1	1

Table 4.7: Identified parameter values of the three cohesive zones in the three directions (direction 1 is the stack direction, orthogonal to cohesive zone).  $\sigma_{max}$  in MPa and  $\Gamma$  in  $\text{kJ m}^{-2}$ .

## 4.2 Heterogeneous welding model

In this section, FE modelling results of heterogeneous Usibor1500/DP600 spot weld assemblies are presented. The load-displacement curves and failure modes of experimental and simulation cases under two loading types (cross tension and tensile shear) are compared.

FE modelling is applied on all Usibor1500/DP600 configurations introduced in chapter 2. As a reminder, these configurations are presented in figure 4.14.

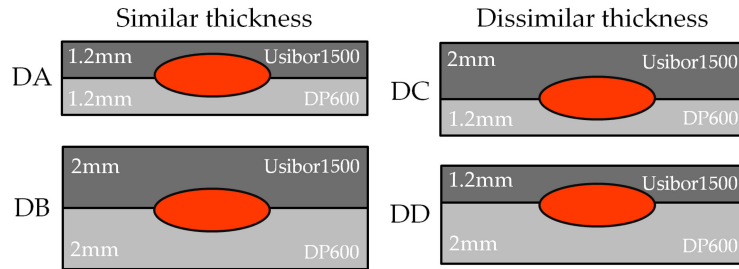


Figure 4.14: Usibor1500/DP600 spot welding configurations.

### 4.2.1 Cross tension test results

#### 4.2.1.1 Usibor1500 1.2mm/DP600 1.2mm spot welds (DA)

The results of Usibor1500 1.2 mm/DP600 1.2 mm spot welds (DA) in cross tension at lower end, middle and upper end intensities are respectively gathered in figures 4.15, 4.16 and 4.17.

The experimental failure modes (Button Pull Out with failure on the Usibor1500 side, hole in Usibor1500 sheet) are well reproduced by FE models. Moreover, the load-

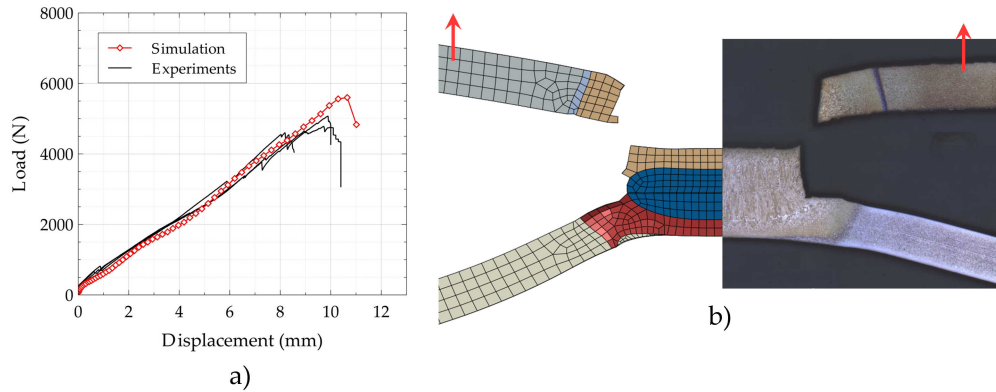


Figure 4.15: Comparison between experimental and simulation response in cross tension of Usibor1500 1.2 mm/DP600 1.2 mm spot weld (DA) at the lower end intensity: a) load-displacement curves and b) failure mode.

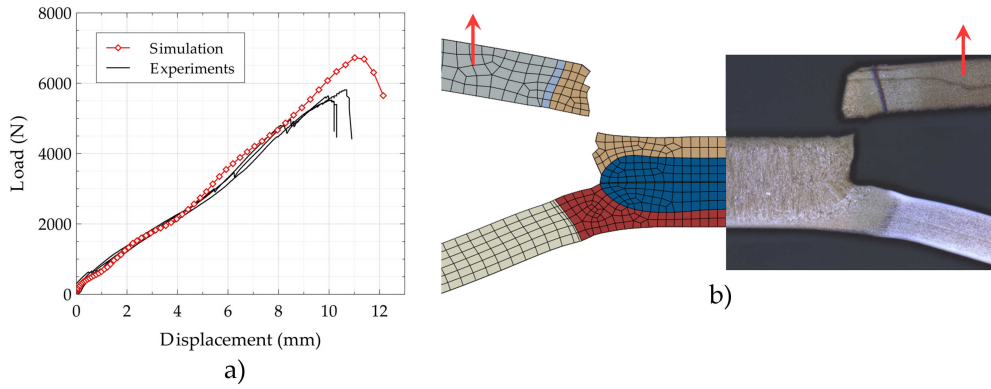


Figure 4.16: Comparison between experimental and simulation response in cross tension of Usibor1500 1.2 mm/DP600 1.2 mm spot weld (DA) at middle intensity: a) load-displacement curves and b) failure mode.

displacement curves are also well predicted even if the failure loads are always overestimated in the FE models.

It is important to notice that the decrease of maximum load between middle and upper end in experiments is reproduced by FE modelling.

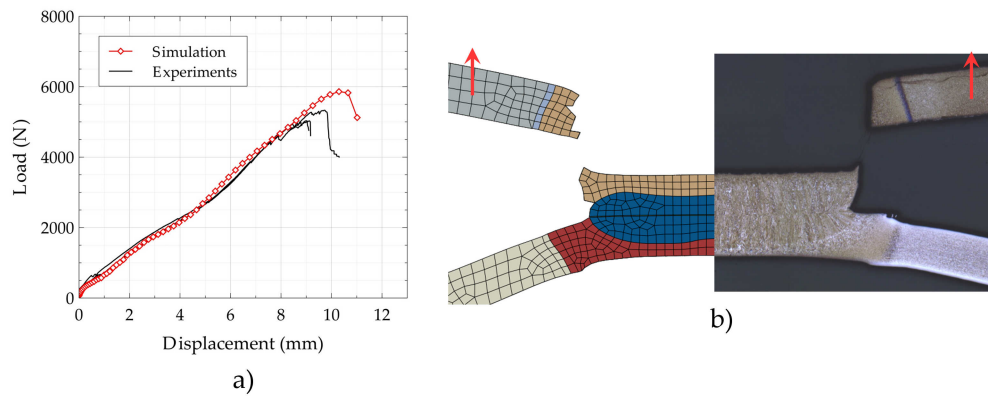


Figure 4.17: Comparison between experimental and simulation response in cross tension of Usibor1500 1.2 mm/DP600 1.2 mm spot weld (DA) at the upper end intensity: a) load-displacement curves and b) failure mode.

#### 4.2.1.2 Usibor1500 2mm/DP600 2mm spot welds (DB)

The results of Usibor1500 2 mm/DP600 2 mm spot welds (DB) in cross tension at lower end, middle and upper end intensities are respectively presented in figures 4.18, 4.19 and 4.20.

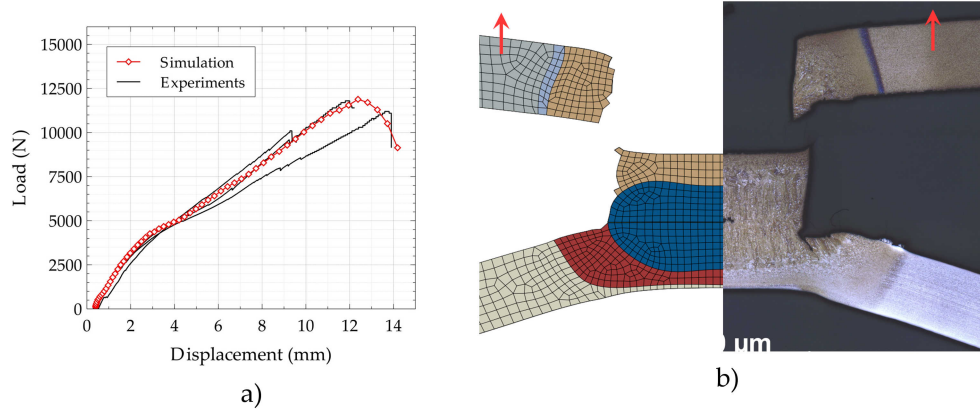


Figure 4.18: Comparison between experimental and simulation response in cross tension of Usibor1500 2 mm/DP600 2 mm spot weld (DB) at the lower end intensity: a) load-displacement curves and b) failure mode.

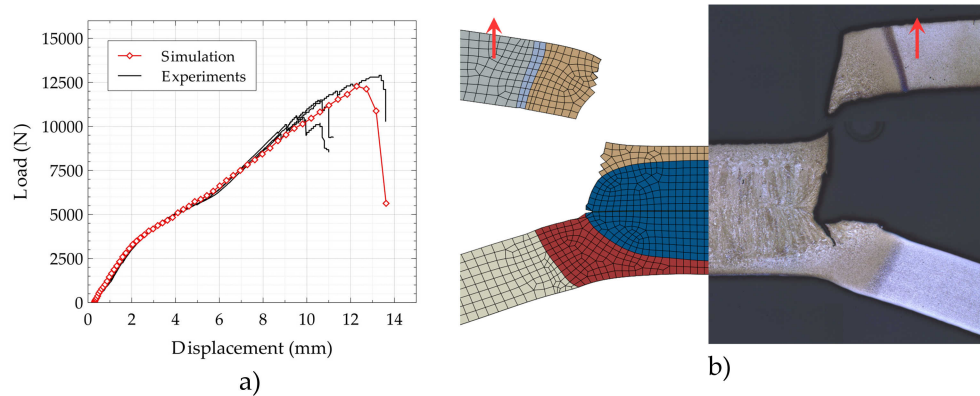


Figure 4.19: Comparison between experimental and simulation response in cross tension of Usibor1500 2 mm/DP600 2 mm spot weld (DB) at middle intensity: a) load-displacement curves and b) failure mode.

The experimental failure modes (Partial Interfacial Failure PIF and Button Pull Out BPO with failure in the Usibor1500 side, hole in Usibor1500 sheet) are rather well reproduced by FE models with the exception of the lower end intensity configuration, where the partial penetration of the crack at the interface is not predicted by the FE simulation.

However, load-displacement curves are well predicted in all configurations. Particularly, the evolution of the slope of the loading curves due to the elastic-plastic behaviour of the whole assembly is well reproduced.

In figure 4.21, the equivalent plastic strain is observed in the spot weld before and after the slope change. Figure 4.21.a shows the position in Load-Displacement curve of the two

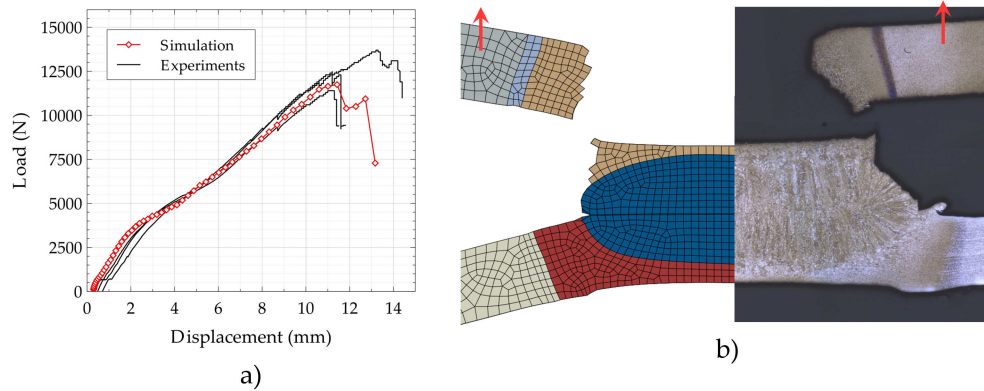


Figure 4.20: Comparison between experimental and simulation response in cross tension of Usibor1500 2mm/DP600 2mm spot weld (DB) at the upper end intensity: a) load-displacement curves and b) failure mode.

plastic strain states observed in figures 4.21.b and 4.21.c. The slope change is probably due to occurrence of plasticity in the notch root.

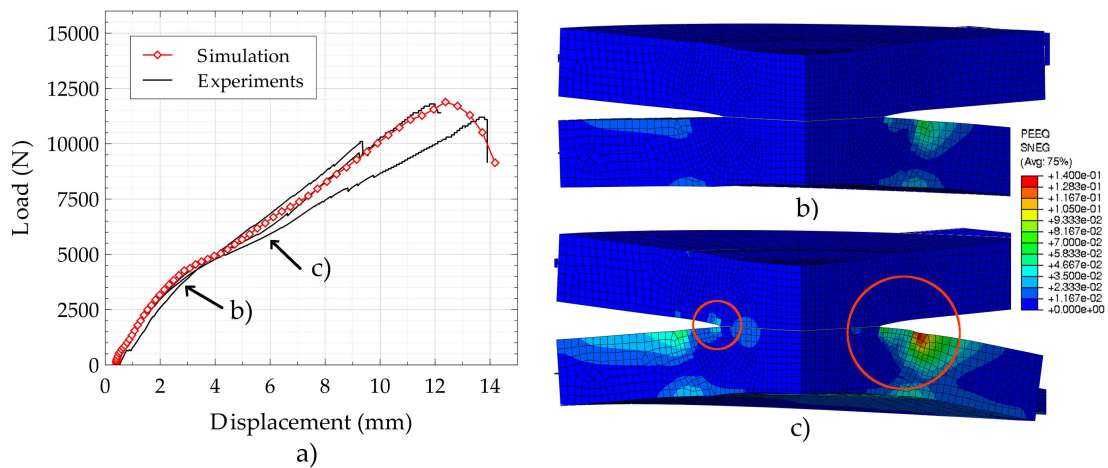


Figure 4.21: Comparison between experimental and simulation response in cross tension of Usibor1500 2mm/DP600 2mm spot weld (DB) at the upper end intensity: a) load-displacement curves and b) equivalent plastic strain before slope change and c) equivalent plastic strain after slope change.

#### 4.2.1.3 Usibor1500 2mm/DP600 1.2mm spot welds (DC)

The results of Usibor1500 2mm/DP600 1.2mm spot welds (DC) in cross tension at lower end, middle and upper end intensities are respectively presented in figures 4.22, 4.23 and 4.24.

The experimental failure modes (Button Pull Out BPO with failure on the DP600 side, hole in DP600 sheet) are globally well reproduced by FE models. Only the upper

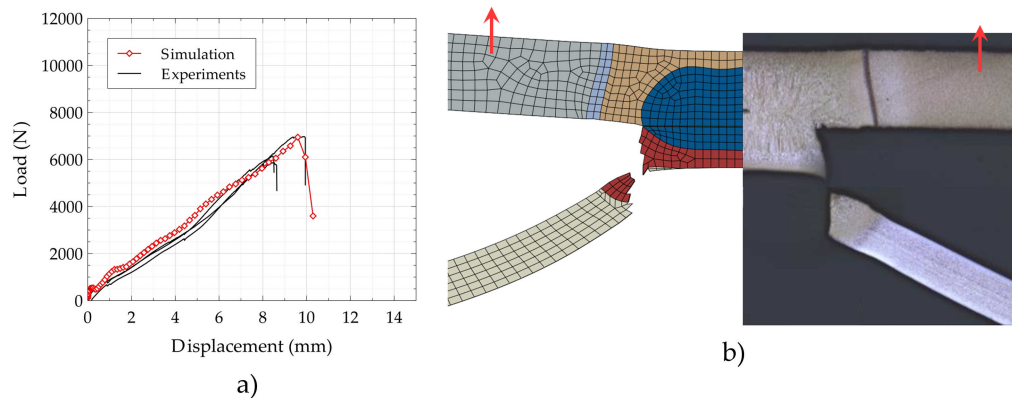


Figure 4.22: Comparison between experimental and simulation response in cross tension of Usibor1500 2 mm/DP600 1.2 mm spot weld (DC) at the lower end intensity: a) load-displacement curves and b) failure mode.

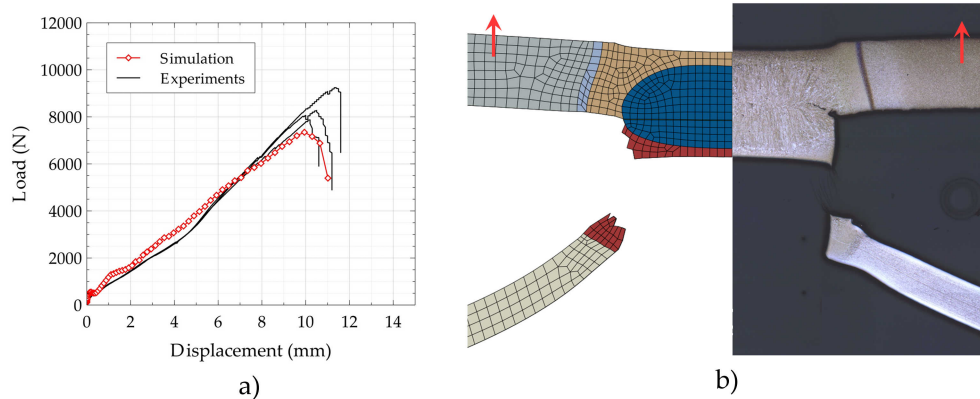


Figure 4.23: Comparison between experimental and simulation response in cross tension of Usibor1500 2 mm/DP600 1.2 mm spot weld (DC) at middle intensity: a) load-displacement curves and b) failure mode.

end intensity configuration FE simulation did not well reproduce the experimental failure because of the splash phenomenon explained in chapter 2 (expulsion of molten metal at the interface) and marked by a circle in figure 4.24. The presence of splash initiation prevents the crack propagation on the DP600 side and favours a Partial Dome Failure on the Usibor1500 side. Splash is very difficult to introduce in the model.

However, load-displacement curves as well as the evolution of the slope are well predicted in all configurations.



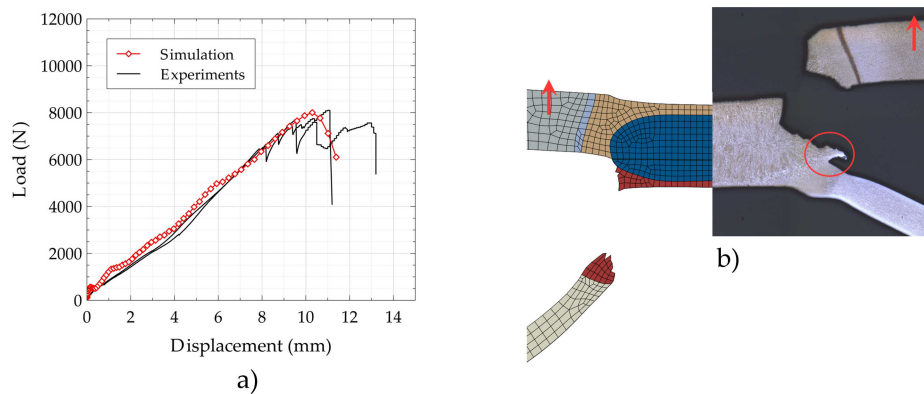


Figure 4.24: Comparison between experimental and simulation response in cross tension of Usibor1500 2 mm/DP600 1.2 mm spot weld (DC) at the upper end intensity: a) load-displacement curves and b) failure mode.

#### 4.2.1.4 Usibor1500 1.2mm/DP600 2mm spot welds (DD)

The results of Usibor1500 1.2 mm/DP600 2 mm spot welds (DD) in cross tension at lower end, middle and upper end intensities are respectively presented in figures 4.25, 4.26 and 4.27.

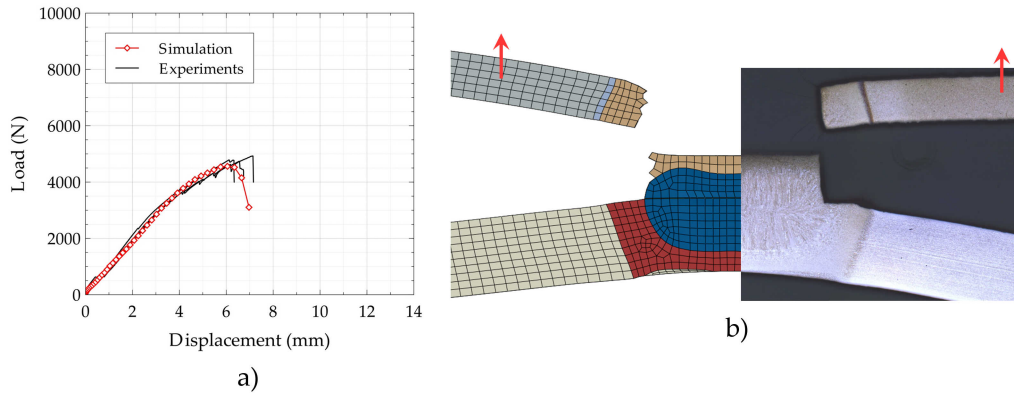


Figure 4.25: Comparison between experimental and simulation response in cross tension of Usibor1500 1.2 mm/DP600 2 mm spot weld (DD) at the lower end intensity: a) load-displacement curves and b) failure mode.

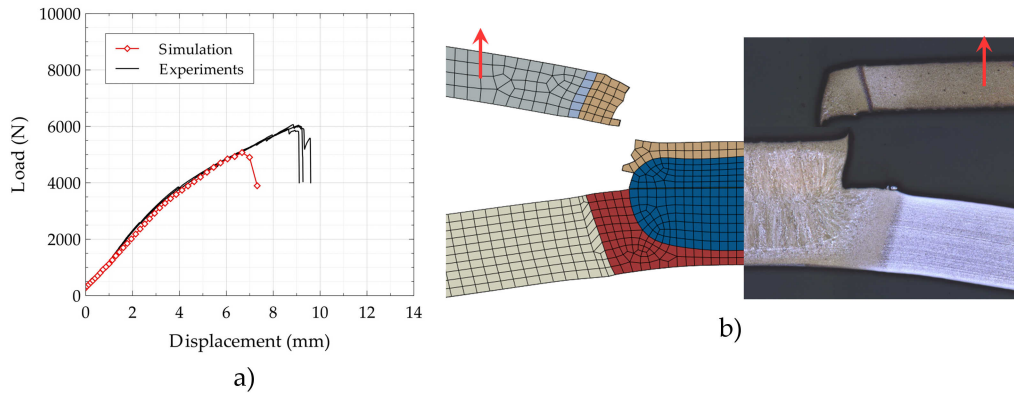


Figure 4.26: Comparison between experimental and simulation response in cross tension of Usibor1500 1.2 mm/DP600 2 mm spot weld (DD) at middle intensity: a) load-displacement curves and b) failure mode.

The experimental failure modes (Button Pull Out BPO with failure in the Usibor1500 side, hole in Usibor1500 sheet) are well reproduced by FE models for all configurations.

However, except at the lower end intensity, load-displacement curves are not very well reproduced. The beginning of the loading curves is ok, but simulations at the middle and upper end intensities underestimate the load bearing capacity of the assemblies, which is discussed below.

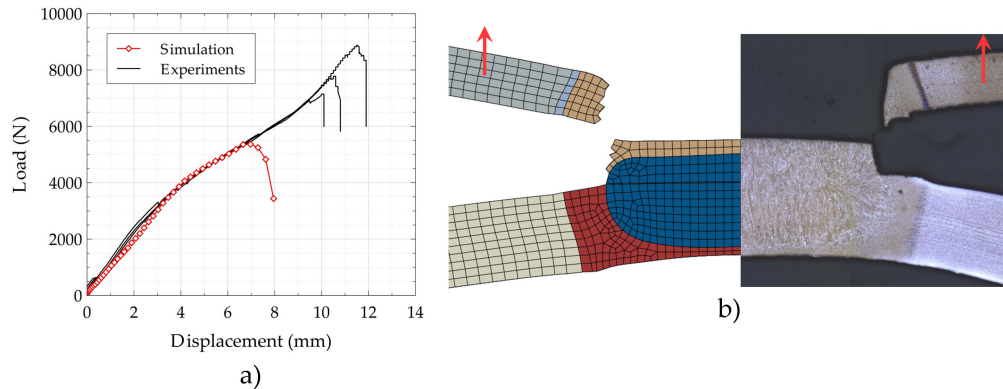


Figure 4.27: Comparison between experimental and simulation response in cross tension of Usibor1500 1.2 mm/DP600 2 mm spot weld (DD) at the upper end intensity: a) load-displacement curves and b) failure mode.

#### 4.2.1.5 Global assessment of the FE model in cross tension

Finally, FE modelling of Usibor1500/DP600 spot welds in cross tension shows good results in terms of load-displacement curves but also of failure mode prediction. As presented in table 4.8, the agreement between experimental and simulation failure modes is globally very good.

Configurations Usibor1500/DP600	Experimental failure mode	FE prediction
DA 1.2 mm/1.2 mm lower end	PIF (failure in Usibor1500 side)	✓(∼)
DA 1.2 mm/1.2 mm middle	BPO (failure in Usibor1500 side)	✓
DA 1.2 mm/1.2 mm upper end	PDF (failure in Usibor1500 side)	✓
DB 2 mm/2 mm lower end	PIF (failure in Usibor1500 side)	✓(∼)
DB 2 mm/2 mm middle	PIF (failure in Usibor1500 side)	✓(∼)
DB 2 mm/2 mm upper end	PDF (failure in Usibor1500 side)	✓(∼)
DC 2 mm/1.2 mm lower end	PIF (failure in DP600 side)	✓
DC 2 mm/1.2 mm middle	BPO (failure in DP600 side)	✓
DC 2 mm/1.2 mm upper end	PDF (failure in Usibor1500 side)	X
DD 1.2 mm/2 mm lower end	BPO (failure in Usibor1500 side)	✓
DD 1.2 mm/2 mm middle	BPO (failure in Usibor1500 side)	✓
DD 1.2 mm/2 mm upper end	PDF (failure in Usibor1500 side)	✓

Table 4.8: Experimental failure modes and their agreement with FE prediction for each Usibor1500/DP600 spot weld configuration in cross tension.

All failure modes are well predicted excepted for three cases. Two of them concern the upper end intensity configurations which present a small splash at the notch root (DB and DC upper end configurations). This splash modified the experimental failure mode, but

it was not modelled in the simulations since it is not uniformly present around the spot weld. Its influence is therefore not reproduced in the simulations. It could be introduced, but its geometry is complicated to reproduce with 2D cross sections.

Configurations Usibor1500/DP600	Experimental failure strength (average of three)	Predicted strength	Error in %
DA 1.2 mm/1.2 mm lower end	4820 N	5599 N	13.9
DA 1.2 mm/1.2 mm middle	5660 N	6725 N	15.8
DA 1.2 mm/1.2 mm upper end	5130 N	5859 N	12.4
DB 2 mm/2 mm lower end	11 080 N	11 886 N	0.7
DB 2 mm/2 mm middle	11 640 N	12 279 N	5.2
DB 2 mm/2 mm upper end	13 050 N	11 746 N	5.6
DC 2 mm/1.2 mm lower end	6330 N	6946 N	8.9
DC 2 mm/1.2 mm middle	8470 N	7346 N	13.2
DC 2 mm/1.2 mm upper end	8370 N	8004 N	4.4
DD 1.2 mm/2 mm lower end	4820 N	4559 N	5.4
DD 1.2 mm/2 mm middle	6000 N	5072 N	15.4
DD 1.2 mm/2 mm upper end	7940 N	5365 N	32.4

Table 4.9: Experimental failure strengths and their agreement with FE prediction for each Usibor1500/DP600 spot weld configuration in cross tension.

The last configuration not matching perfectly the experimental failure mode is the DB lower end configuration. Its experimental failure mode is Partial Interfacial Failure (PIF) but the simulation presents a BPO failure mode. Further adjustment of the cohesive zone parameters of the interfacial zone would probably allow to reproduce the partial crack penetration at the interface. However, the essential features of the failure in this configuration (side of the hole and load bearing capacity) are still captured.

However, in the DD configuration case, the strengths are not well predicted. In the model, failure occurred too early compared to experiments. It could come from the stress concentration in the notch root, because for a given displacement applied, the larger the nugget diameter, the higher the angle between Usibor1500 and DP600 sheets is. And the higher the angle, the higher the stress concentration in the notch root is. Moreover, it is important to notice that the scatter between experimental data is very important ( $\sim 15\%$ ) for the upper end intensity configuration.

## 4.2.2 Tensile shear test results

### 4.2.2.1 Usibor1500 1.2mm/DP600 1.2mm spot welds (DA)

The results of Usibor1500 1.2 mm/DP600 1.2 mm spot welds (DA) in tensile shear at lower end, middle and upper end intensities are respectively presented in figures 4.28, 4.29 and 4.30.

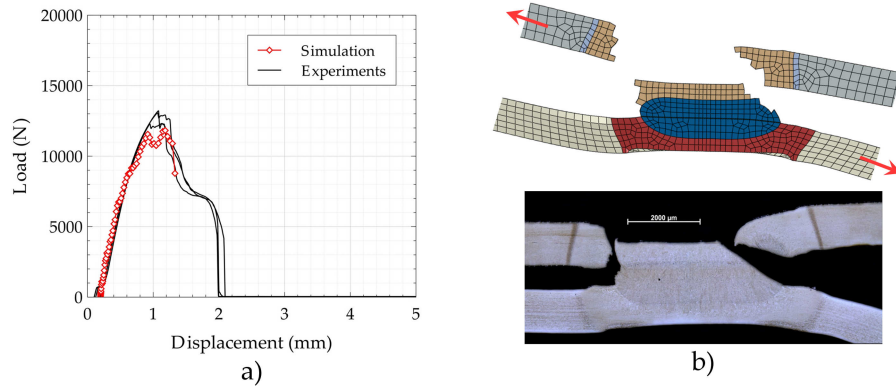


Figure 4.28: Comparison between experimental and simulation response in tensile shear of Usibor1500 1.2 mm/DP600 1.2 mm spot weld (DA) at the lower end intensity: a) load-displacement curves and b) failure mode.

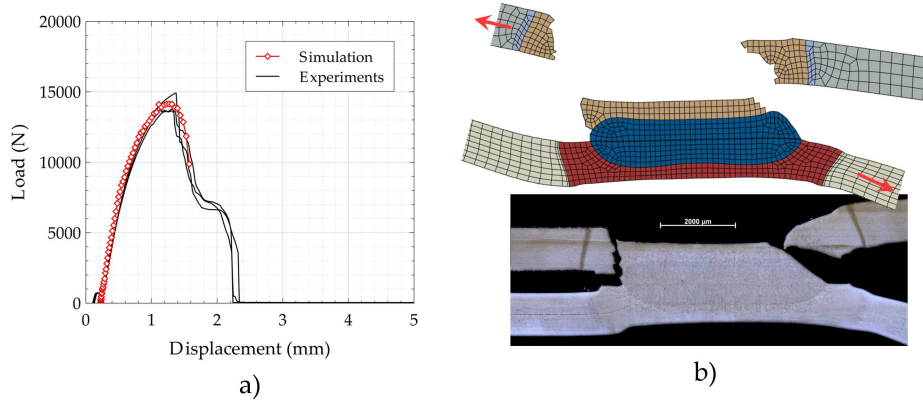


Figure 4.29: Comparison between experimental and simulation response in tensile shear of Usibor1500 1.2 mm/DP600 1.2 mm spot weld (DA) at middle intensity: a) load-displacement curves and b) failure mode.

The experimental failure modes (Button Pull Out with failure on the Usibor1500 side, hole in Usibor1500 sheet) are well reproduced by FE models. However, even if the failure zone (Usibor1500 HAZ) is well predicted in the lower end and middle configurations, failure in the tempered HAZ of Usibor1500 is not reproduced for upper end one.

The load-displacement curves are also well predicted except for upper end configuration where the failure in the CGHAZ of Usibor1500 leads to a slightly underestimated failure load.

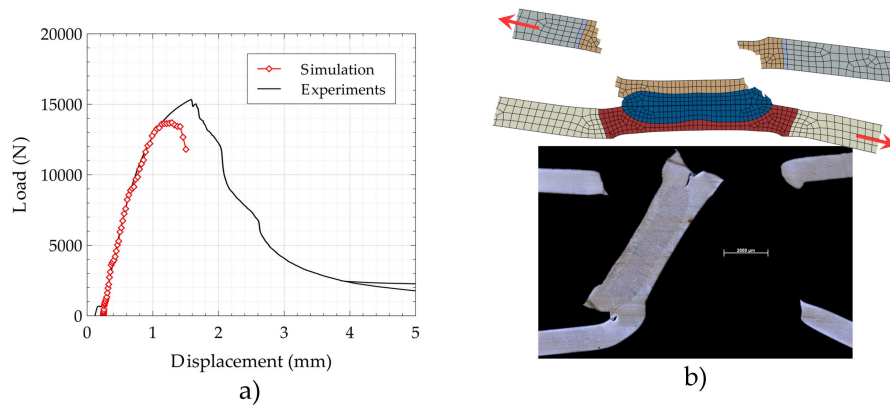


Figure 4.30: Comparison between experimental and simulation response in tensile shear of Usibor1500 1.2 mm/DP600 1.2 mm spot weld (DA) at the upper end intensity: a) load-displacement curves and b) failure mode.



#### 4.2.2.2 Usibor1500 2mm/DP600 2mm spot welds (DB)

The results of Usibor1500 2mm/DP600 2mm spot welds (DB) in tensile shear at lower end, middle and upper end intensities are respectively presented in figures 4.31, 4.32 and 4.33.

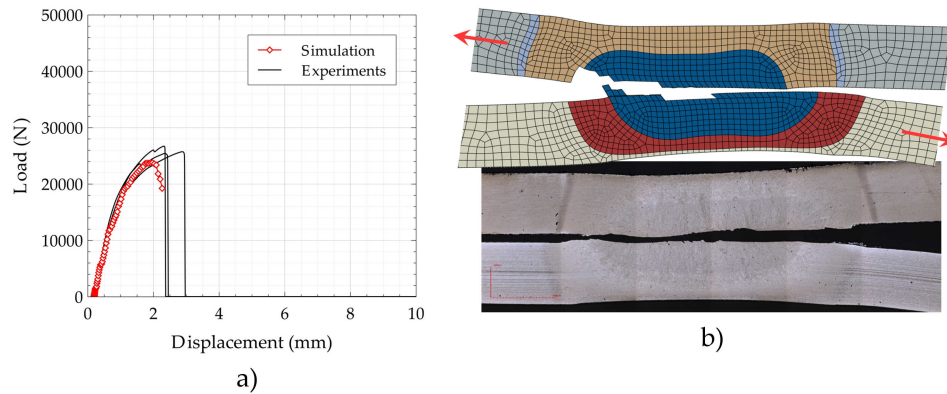


Figure 4.31: Comparison between experimental and simulation response in tensile shear of Usibor1500 2mm/DP600 2mm spot weld (DB) at the lower end intensity: a) load-displacement curves and b) failure mode.

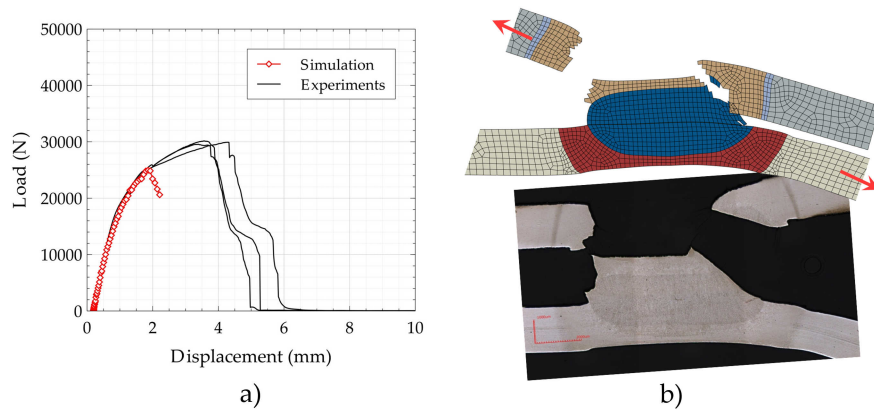


Figure 4.32: Comparison between experimental and simulation response in tensile shear of Usibor1500 2mm/DP600 2mm spot weld (DB) at middle intensity: a) load-displacement curves and b) failure mode.

The experimental failure modes (Full interfacial failure and Button Pull Out with failure in the Usibor1500 side, hole in Usibor1500 sheet) are well reproduced by FE models. The failure mode transition is well reproduced by FE model, which proves the robustness of the FE model. Contrary to analytical model, this FE model allows to predict the failure mode transition and to understand more precisely the mechanisms which change the failure mode.

However, the simulated load-displacement curves are drop down too early when BPO failures occurred in the Usibor1500 HAZ. The ductile damage criterion in this zone is probably underestimated.

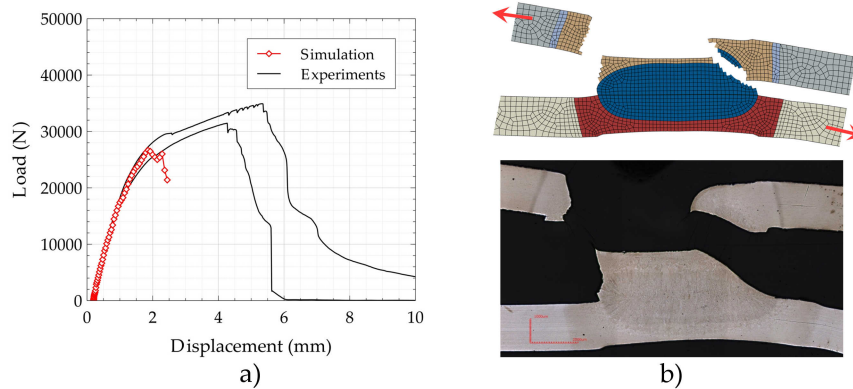


Figure 4.33: Comparison between experimental and simulation response in tensile shear of Usibor1500 2 mm/DP600 2 mm spot weld (DB) at the upper end intensity: a) load-displacement curves and b) failure mode.

#### 4.2.2.3 Usibor1500 2mm/DP600 1.2mm spot welds (DC)

The results of Usibor1500 2 mm/DP600 1.2 mm spot welds (DC) in tension shear at lower end, middle and upper end intensities are respectively presented in figures 4.34, 4.35 and 4.36.

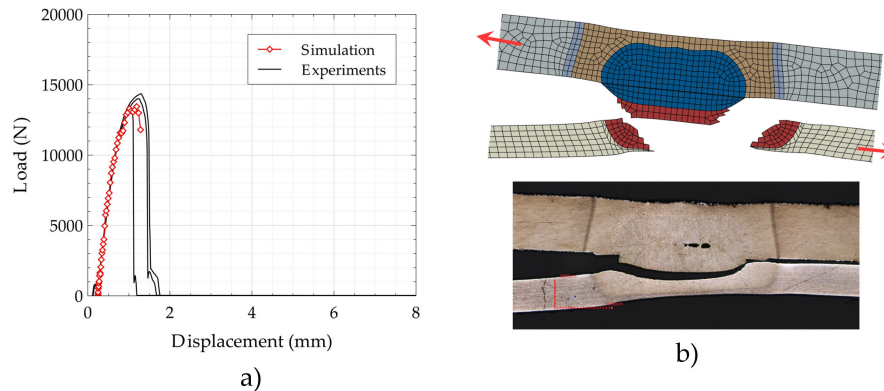


Figure 4.34: Comparison between experimental and simulation response in tensile shear of Usibor1500 2 mm/DP600 1.2 mm spot weld (DC) at the lower end intensity: a) load-displacement curves and b) failure mode.

The experimental failure modes (Total Dome Failure TDF and Button Pull Out BPO with failure in the DP600 side, hole in DP600 sheet) are well reproduced by FE models. The failure mode transition between lower end and middle configurations is also well captured by FE model. However, the simulation only predicts a Partial Dome at the lower end intensity as opposed to the experimental Total Dome.

The failure load levels are rather well predicted despite a tendency to anticipate again final failure in the middle and upper end configurations.

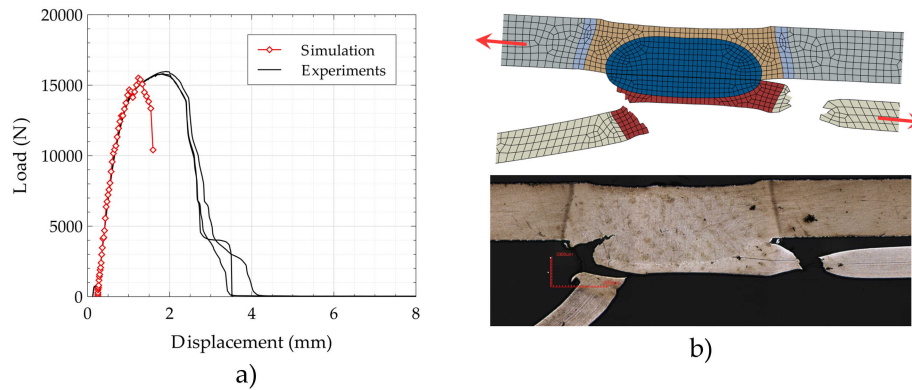


Figure 4.35: Comparison between experimental and simulation response in tensile shear of Usibor1500 2 mm/DP600 1.2 mm spot weld (DC) at middle intensity: a) load-displacement curves and b) failure mode.

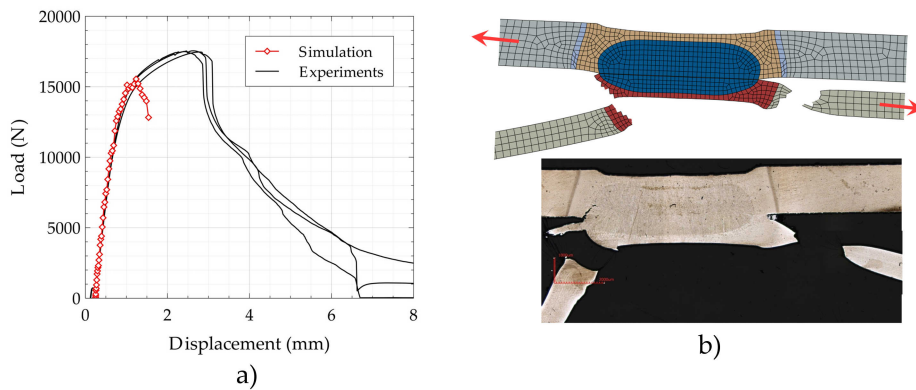


Figure 4.36: Comparison between experimental and simulation response in tensile shear of Usibor1500 2 mm/DP600 1.2 mm spot weld (DC) at the upper end intensity: a) load-displacement curves and b) failure mode.

#### 4.2.2.4 Usibor1500 1.2mm/DP600 2mm spot welds (DD)

The results of Usibor1500 1.2 mm/DP600 2 mm spot welds (DD) in tensile shear at lower end, middle and upper end intensities are respectively presented in figures 4.37, 4.38 and 4.39.

The experimental failure modes (Full interfacial failure and Button Pull Out with failure in the Usibor1500 side, hole in Usibor1500 sheet) are well reproduced by FE models. The failure mode transition (from FIF into BPO) between middle and upper end is once again well reproduced by FE model, which proves the model robustness.

Moreover, the load-displacement curves are well predicted whatever the failure mode or position in the welding range.

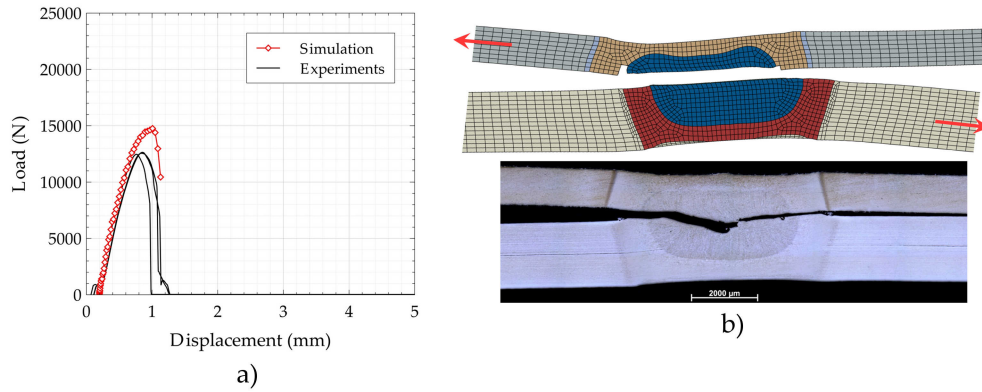


Figure 4.37: Comparison between experimental and simulation response in tensile shear of Usibor1500 1.2 mm/DP600 2 mm spot weld (DD) at the lower end intensity: a) load-displacement curves and b) failure mode.

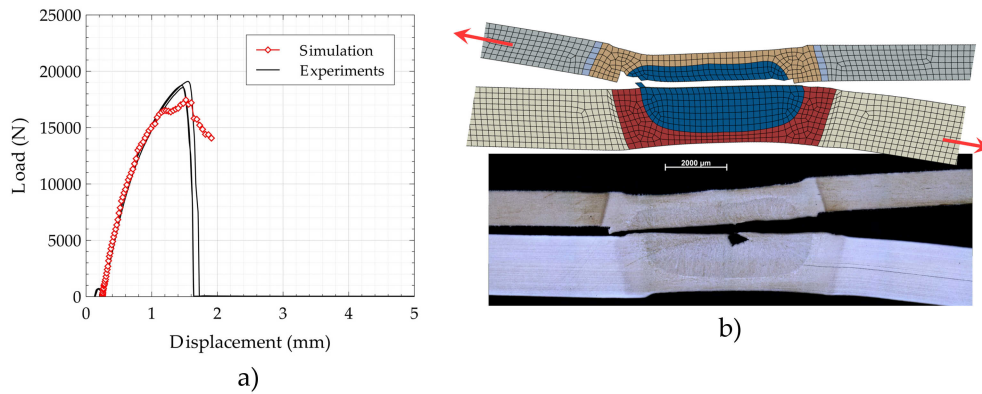


Figure 4.38: Comparison between experimental and simulation response in tensile shear of Usibor1500 1.2 mm/DP600 2 mm spot weld (DD) at middle intensity: a) load-displacement curves and b) failure mode.

#### 4.2.2.5 Global assessment of the FE model in tensile shear

Finally, FE modelling of Usibor1500/DP600 spot welds in tensile shear shows again good results in terms of load-displacement response but also of failure mode prediction. As gathered in table 4.10, the agreement between experimental and simulation failure modes is very accurate.

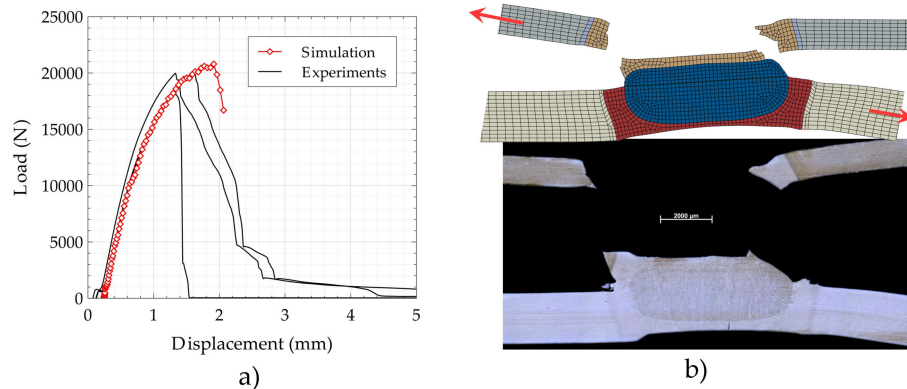


Figure 4.39: Comparison between experimental and simulation response in tensile shear of Usibor1500 1.2 mm/DP600 2 mm spot weld (DD) at the upper end intensity: a) load-displacement curves and b) failure mode.

Configurations Usibor1500/DP600	Experimental failure mode	FE prediction
DA 1.2 mm/1.2 mm lower end	BPO (failure in Usibor1500 side)	✓
DA 1.2 mm/1.2 mm middle	BPO (failure in Usibor1500 side)	✓
DA 1.2 mm/1.2 mm upper end	BPO (failure in Usibor1500 side)	✓(∼)
DB 2 mm/2 mm lower end	FIF	✓
DB 2 mm/2 mm middle	BPO (failure in Usibor1500 side)	✓
DB 2 mm/2 mm upper end	BPO (failure in Usibor1500 side)	✓
DC 2 mm/1.2 mm lower end	TDF (failure in DP600 side)	✓(∼)
DC 2 mm/1.2 mm middle	BPO (failure in DP600 side)	✓
DC 2 mm/1.2 mm upper end	BPO (failure in DP600 side)	✓
DD 1.2 mm/2 mm lower end	FIF	✓
DD 1.2 mm/2 mm middle	FIF	✓
DD 1.2 mm/2 mm upper end	BPO (failure in Usibor1500 side)	✓(∼)

Table 4.10: Experimental failure modes and their agreement with FE prediction for each Usibor1500/DP600 spot weld configuration in tensile shear.

All failure modes are well predicted excepted for three cases. Two of them concern the upper end intensity configurations DA and DD. In the FE model, failure in tempered HAZ of Usibor1500 does not occur unlike in experiments. Usibor1500 quenched HAZ ductile damage seems to be underestimated, which leads to a premature failure in this zone.

Configurations Usibor1500/DP600	Experimental failure strength (average of three)	Predicted strength	Error in %
DA 1.2 mm/1.2 mm lower end	12 870 N	11 819 N	8.2
DA 1.2 mm/1.2 mm middle	14 110 N	14 132 N	0.2
DA 1.2 mm/1.2 mm upper end	15 390 N	13 695 N	6.6
DB 2 mm/2 mm lower end	25 950 N	23 788 N	8.4
DB 2 mm/2 mm middle	29 890 N	24 950 N	16.5
DB 2 mm/2 mm upper end	33 130 N	26 657 N	19.5
DC 2 mm/1.2 mm lower end	13 870 N	13 448 N	3.0
DC 2 mm/1.2 mm middle	15 850 N	15 504 N	2.2
DC 2 mm/1.2 mm upper end	17 500 N	15 545 N	11.2
DD 1.2 mm/2 mm lower end	12 550 N	14 762 N	15.0
DD 1.2 mm/2 mm middle	18 790 N	17 455 N	7.1
DD 1.2 mm/2 mm upper end	20 000 N	20 796 N	6.9

Table 4.11: Experimental failure strengths and their agreement with FE prediction for each Usibor1500/DP600 spot weld configuration in tensile shear.

The last configuration which does not matches perfectly with experimental failure mode is the DC lower end configuration. Its experimental failure mode is Total Dome Failure but the simulation presents a Partial Dome Failure mode. This is probably due to the mesh size which is not refined enough in the FE models. However, obtaining a Partial Dome Failure is an important result and the predicted accuracy of the failure load prediction illustrates the close competition between Partial and Total Dome failure in this configuration.

### 4.2.3 Discussion

Despite a few discrepancies in the simulations, the present modelling methodology showed very accurate results on various heterogeneous Usibor1500/DP600 configurations, with varying sheet thicknesses, weld nugget size and loading types. This FE modelling methodology is validated for heterogeneous AHSS spot welds in cross tension and tensile shear.

Moreover, FE models allow to better observe the failure mechanisms of each failure modes and more particularly the stress triaxiality in the critical zone of crack initiation. For example, in the Button Pull Out failure mode case, stress triaxiality during crack initiation in cross tension is around 0.9 whereas it is only 0.6 in tensile shear in the first failed elements. FE model allows to estimate the stress triaxiality in the failed zone before failure, whereas it is impossible in a experimental way. It shows the importance to consider the stress triaxiality in the ductile damage criterion to provide a full predictive model for different loading types.

The difference between experimental and simulated load-displacement curves could be in part explicated by the linear damage evolution model used in the FE simulations. Damage evolution model could be improved by using a exponential evolution based on



experimental tensile tests. Indeed, the crack propagation could be more realistic and predicted failure load more accurate.

### 4.3 Highly heterogeneous welding model

In this section, FE modelling results of very heterogeneous Duplex 8Al/DP600 spot weld assemblies are presented. The load-displacement curves and failure modes of experimental and simulation cases under two loading types (cross tension and tensile shear) are compared.

FE modelling is applied on three welding intensities of Duplex 8Al/DP600 spot weld configurations introduced in chapter 3. Because the failure modes combination is too complex in the Duplex 4Al case, this case will not be modelled.

#### 4.3.1 Cross tension test results

The results of Duplex 8Al 1.2 mm/DP600 1.2 mm spot welds in cross tension at lower end, middle and upper end intensities are respectively presented in figures 4.40, 4.41 and 4.42. Middle intensity case was used to fit cohesive parameters.

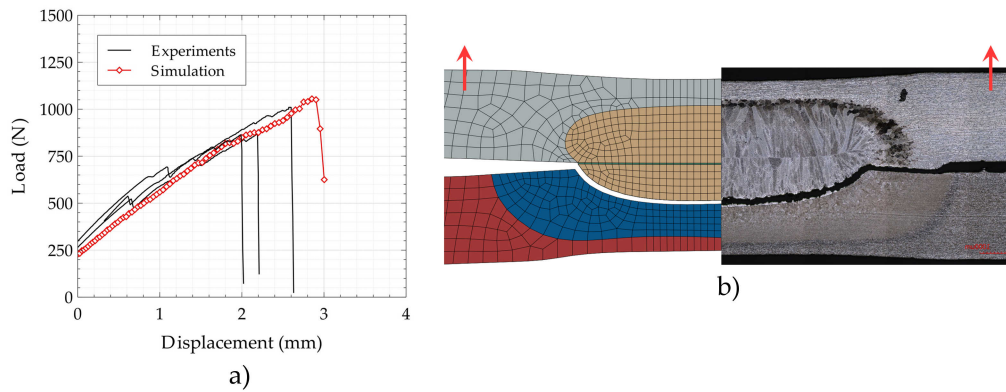


Figure 4.40: Comparison between experimental and simulation response in cross tension of Duplex 8Al 1.2 mm/DP600 1.2 mm spot weld at the lower end intensity: a) load-displacement curves and b) failure mode.

As expected, experimental failure modes (Total Dome Failure at the interface between DP600 HAZ and fusion zone) are well reproduced by FE models (table 4.12). Moreover, load-displacement curves are well predicted whatever the welding intensity.

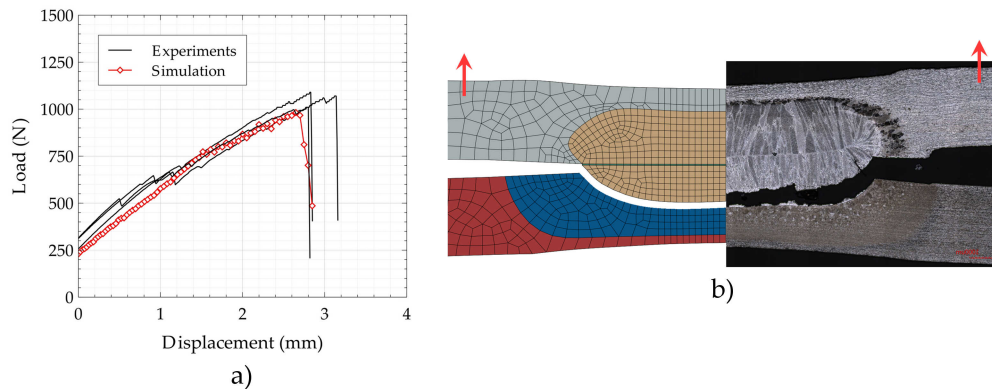


Figure 4.41: Comparison between experimental and simulation response in cross tension of Duplex 8Al 1.2 mm/DP600 1.2 mm spot weld at middle intensity: a) load-displacement curves and b) failure mode.

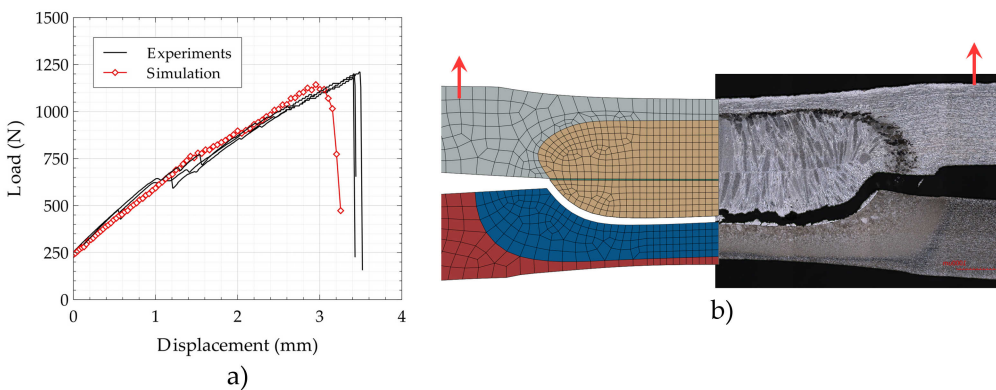


Figure 4.42: Comparison between experimental and simulation response in cross tension of Duplex 8Al 1.2 mm/DP600 1.2 mm spot weld at the upper end intensity: a) load-displacement curves and b) failure mode.

Configurations Duplex 8Al/DP600	Experimental failure mode	FE prediction
lower end intensity	TDF (failure in DP600 side)	✓
middle intensity	TDF (failure in DP600 side)	✓
upper end intensity	TDF (failure in DP600 side)	✓

Table 4.12: Experimental failure modes and their agreement with FE prediction for Duplex 8Al/DP600 spot weld configurations in cross tension.

### 4.3.2 Tensile shear test results

The results of Duplex 8Al 1.2 mm/DP600 1.2 mm spot welds in tensile shear at lower end, middle and upper end intensities are respectively presented in figures 4.43, 4.44 and 4.45.

As in the cross tension tests, experimental failure modes (Total Dome Failure at the

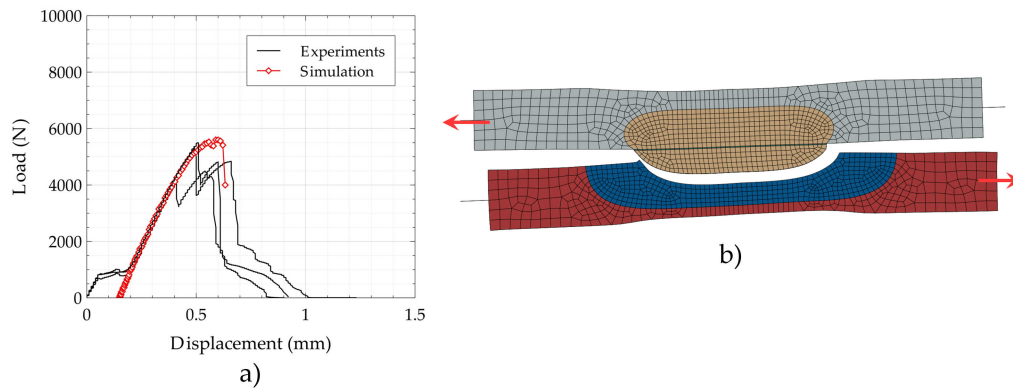


Figure 4.43: Comparison between experimental and simulation response in tensile shear of Duplex 8Al 1.2 mm/DP600 1.2 mm spot weld at the lower end intensity: a) load-displacement curves and b) failure mode.

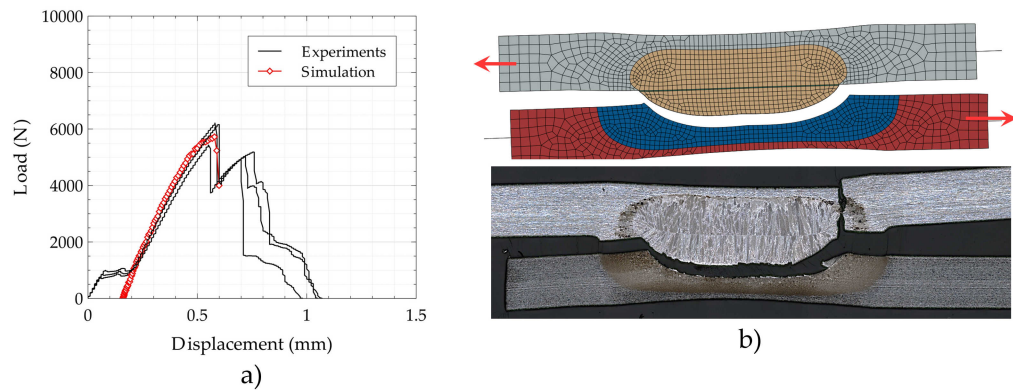


Figure 4.44: Comparison between experimental and simulation response in tensile shear of Duplex 8Al 1.2 mm/DP600 1.2 mm spot weld at middle intensity: a) load-displacement curves and b) failure mode.

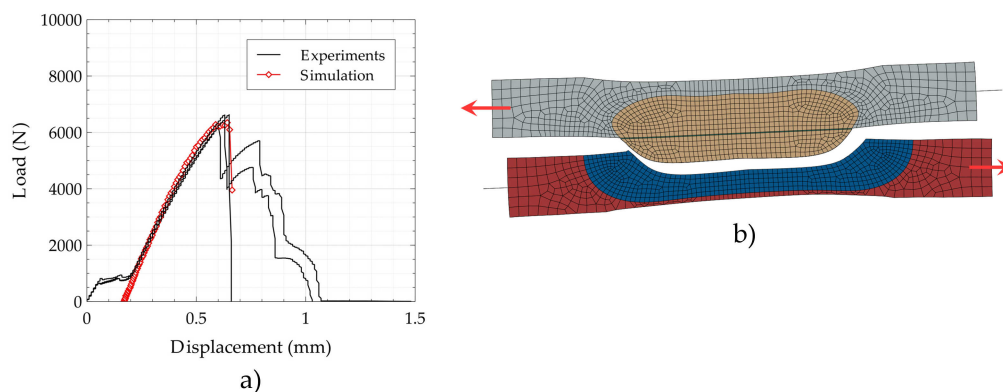


Figure 4.45: Comparison between experimental and simulation response in tensile shear of Duplex 8Al 1.2 mm/DP600 1.2 mm spot weld at the upper end intensity: a) load-displacement curves and b) failure mode.

interface between DP600 HAZ and fusion zone) are well reproduced by FE models in tensile shear tests (table 4.13). Moreover, load-displacement curves are well predicted again for the three welding intensities.

Configurations Duplex 8Al/DP600	Experimental failure mode	FE prediction
lower end intensity	TDF (failure in DP600 side)	✓
middle intensity	TDF (failure in DP600 side)	✓
upper end intensity	TDF (failure in DP600 side)	✓

Table 4.13: Experimental failure modes and their agreement with FE prediction for Duplex 8Al/DP600 spot weld configurations in tensile shear.

### 4.3.3 Discussion

Cohesive zone integration at the ferrite layer between DP600 HAZ and fusion zone is allowing to reproduce the Total Dome Failure (TDF) observed in the cross tension experiments. Moreover, FE models allow to observe crack propagation in the ferrite layer from the notch root to the dome peak in cross tension. In tensile shear, a decohesion of ferrite layer from right notch root (where load is applied on the lower DP600 sheet) is observed. Subsequently, when the first elements failed in tension (opening mode I), the remaining elements are sheared. As concluding remarks, this study allows to produce an estimate of the ferrite layer zone toughness ( $3 \text{ kJ m}^{-2}$ ) which is consistent with the  $\delta$ -ferrite experimentally observed. FE model is particularly well adapted in this case of highly heterogeneous welding.

## 4.4 Conclusion

In this section, a FE model for the prediction of the mechanical behaviour of AHSS resistance spot welds under two loading types, cross tension and tensile shear, was developed. This model is able to capture the competition between semi-brittle fracture at the interface and ductile failure by button pull out at the weld boundary and the partial and total dome failures. Ductile damage and fracture was considered in the different weld zones for this purpose, in addition to a cohesive zone at the faying surface and around the fusion zone when ferrite layer is observed at the fusion zone/HAZ interface.

Elastic-plastic strain hardening laws were identified using either: empirical model of the ferrite and martensite phases constitutive behaviour or a Swift-Voce model fitted on experimental tensile test performed on base material and simulated HAZ using Gleeble simulator, when available. This identification methodology and the chosen spot weld zones discretization are validated observing the good agreement of simulated load-displacement curves with the experimental ones.

Ductile damage criteria were introduced to predict the failure modes and loads of heterogeneous AHSS spot welds. Comparing the experimental and FE simulation results, the model shows a particular robustness with a good prediction in numerous cases with varying sheet thicknesses and loading configurations.

Cohesive zones were introduced at the steel sheets interface, but also at the fusion zone/HAZ interface when a new phase appeared (ferrite layer in Duplex 8Al/DP600 spot welds). Fusion zones cohesive parameters are consistent with those identified by Dancette and al. [DAN 12] and Lacroix and al. [LAC 15]. Concerning the ferrite layer zone, new cohesive parameters were identified. This allows to estimate the toughness of this thin ferrite layer on which no mechanical test can be easily performed.

Lastly, this model predicts well the failure modes and loads of AHSS spot welds, whatever the dissimilar grades or thicknesses of steel sheets. It allows to understand the failure initiation and propagation for the different failure modes.

The robustness of the FE model is verified by observing the transition of failure modes with different material parameters (in particular the sheet thickness) and process parameters (intensity). The FE model could be used as a tool to optimize the sheet thickness and process parameters of a configuration in order to obtain optimized welded assemblies, taking cautions about cohesive parameters.





## Chapter 5

# Finite Element model: limitation and potential

The previous chapter presented the FE modelling methodology and the results on some heterogeneous and very heterogeneous configurations. In this chapter, the limitations and the potential of the model will be investigated. Among limitations, mesh size and boundary condition influences will be in particular investigated. To highlight the model potential, two new configurations will be exposed.

### Contents

---

<b>5.1</b>	<b>FE model limitation . . . . .</b>	<b>151</b>
5.1.1	Solver influence . . . . .	151
5.1.2	Mesh size dependency . . . . .	154
5.1.3	Boundary conditions influence . . . . .	154
5.1.4	Mass scaling influence . . . . .	158
<b>5.2</b>	<b>FE model potential . . . . .</b>	<b>159</b>
5.2.1	Triple-sheet spot welded assembly modelling . . . . .	159
5.2.2	Arc welds FE modelling . . . . .	165
<b>5.3</b>	<b>Conclusion . . . . .</b>	<b>169</b>

---

## 5.1 FE model limitation

### 5.1.1 Solver influence

Cross tension and tensile shear tests conditions being quasi-static, it is natural to first consider an Implicit solver (Abaqus Standard) for spot weld mechanical test simulation. This solver allows to balance all the forces for each calculation increment. However, as soon as a failure criterion is introduced into the model, force balance becomes impossible, due to convergence issues. It is obvious that when the assembly fails in two parts, no equilibrium could be obtained.

By contrast, the Implicit solver has a great utility: it allows to validate the Explicit solver response before significant damage occurrence. Indeed, as there is no dynamic effects

in Implicit simulations, the quasi-static mechanical behaviour of spot welds is properly described. As explained in the chapter 4, the use of the dynamic Explicit solver requires some cautions in the model development to prevent the spot weld behaviour response to be perturbed by dynamic effects.

#### 5.1.1.1 Heterogeneous welding

In order to validate the Explicit solver response, the comparison with the Implicit one is done on several configurations. For the Usibor1500/DP600 spot weld case, two configurations were chosen:

- similar thicknesses Usibor1500 2 mm/DP600 2 mm at middle welding intensity,
- dissimilar thicknesses Usibor1500 1.2 mm/DP600 2 mm at middle welding intensity.

Comparison of Load-Displacement curves between Implicit and Explicit calculations of these two configurations in cross tension and tensile shear are shown in figures 5.1 and 5.2.

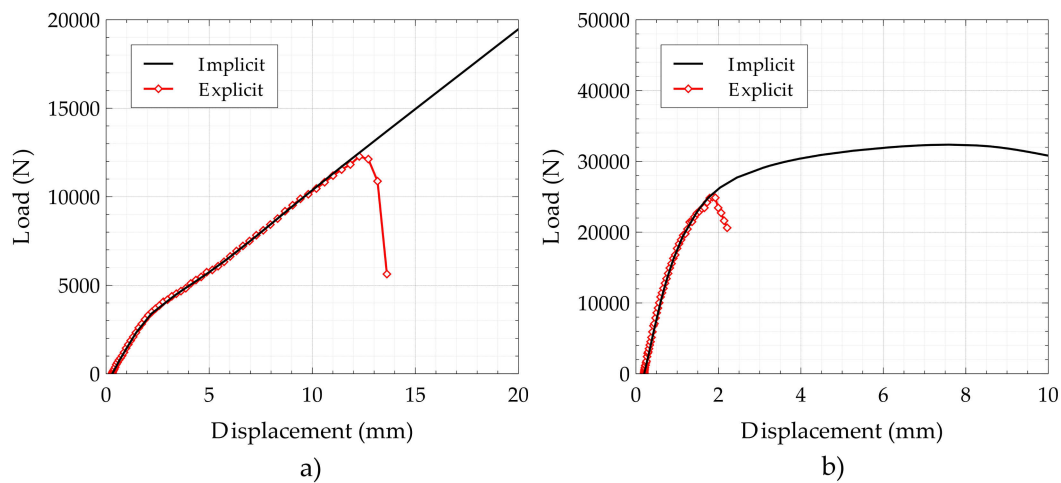


Figure 5.1: Implicit and Explicit solvers Load-Displacement response of Usibor1500 2 mm/DP600 2 mm configuration: a) in cross tension and b) in tensile shear.

Figures 5.1.a and 5.1.b presents the similar thickness configuration during cross tension (5.1.a) and tensile shear (5.1.b) tests. As expected, the response curves are totally overlaid up to the crack initiation in Explicit. Thus, Explicit response is validated and does not show disruptive dynamic effects due to the high velocity boundary condition.

Moreover, figures 5.2.a and 5.2.b presents the dissimilar thickness configuration during cross tension (5.2.a) and tensile shear (5.2.b) tests. In the same way, the Load-Displacement curves overlay is perfect up to crack initiation in Explicit. As the Explicit responses are evolving in the same way as the Implicit ones in many configurations, the present model construction with the Explicit solver as detailed in chapter 4 is considered as valid under quasi-static loading.

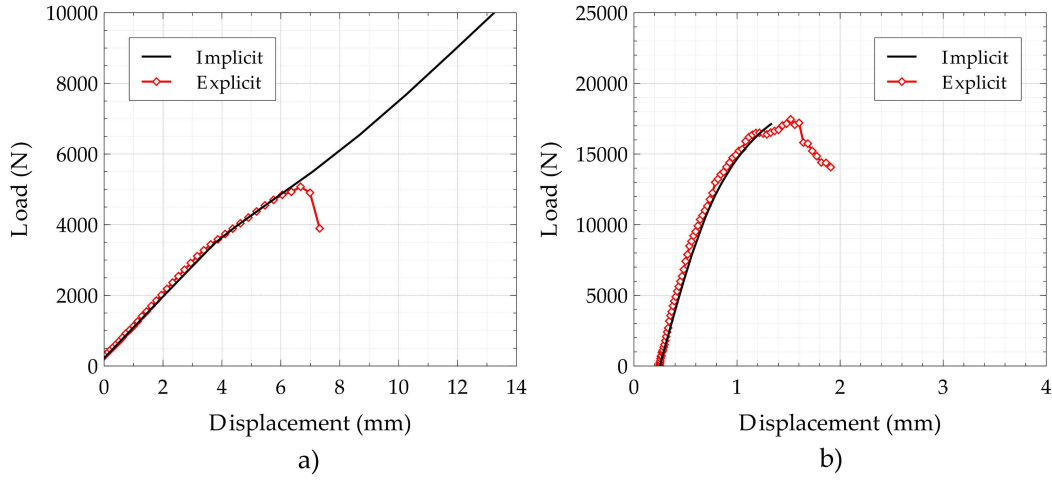


Figure 5.2: Implicit and Explicit solvers Load-Displacement response of Usibor1500 1.2 mm/DP600 2 mm configuration: a) in cross tension and b) in tensile shear.

#### 5.1.1.2 Very heterogeneous welding

In the following, the validity of the quasi-static Explicit model in the case of very heterogeneous welding (Duplex 8Al/DP600) is checked.

Figure 5.3 shows the Load-Displacement curves of Duplex 8Al 1.2 mm/DP600 2 mm at lower end intensity, in cross tension (5.3.a) and in tensile shear (5.3.b). As for the heterogeneous case previously detailed (Usibor1500/DP600), Explicit and Implicit solver responses are overlaid until crack initiation. In the Duplex 8Al/DP600 welding case, the curves separation occurred earlier because of the crack propagation in the ferrite layer. Indeed, crack initiation occurs at 60% of the maximal load and cohesive elements fail one by one until the last element at the top of the dome. Therefore a stiffness loss is observed in the Explicit response after crack initiation.

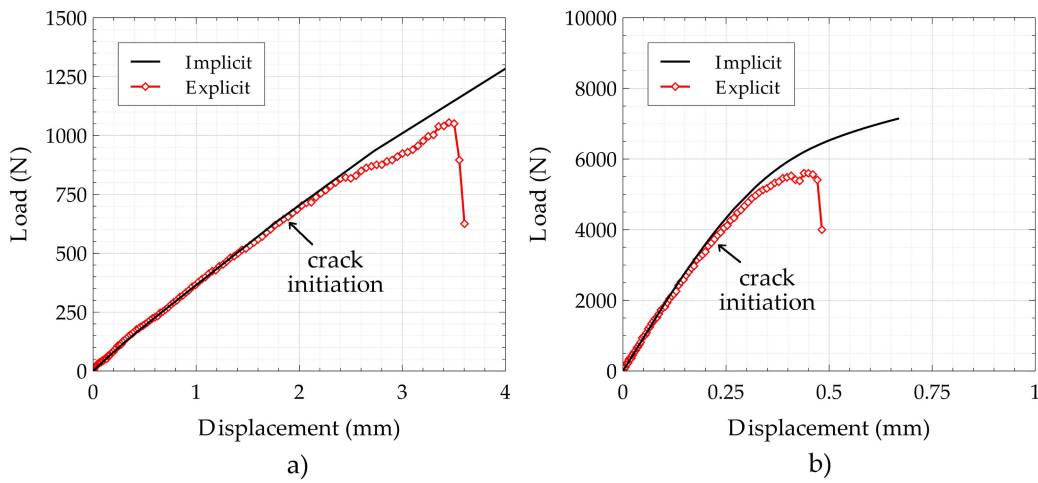


Figure 5.3: Implicit and Explicit solvers Load-Displacement response of Duplex 8Al 1.2 mm/DP600 1.2 mm configuration: a) in cross tension and b) in tensile shear.

In conclusion, no disruptive dynamic effects are identified in the very heterogeneous welding case too. Quasi-static Explicit models are validated in all configurations.

### 5.1.2 Mesh size dependency

Solid element type in the FE models is eight-node brick with reduced integration (C3D8R in Abaqus). These elements are generally adapted to cross tension and tensile shear tests implying bending and large deformation. In this section, convergence of FE model calculations is investigated with regard to the mesh size in the spot weld.

Mesh element size was chosen as 0.2 mm in order to have a good compromise between calculation time and accuracy. To evaluate the mesh size dependency, two additional mesh sizes were chosen and simulated with Explicit solver. In one case, the mesh has been refined with a size of 0.1 mm for base element and in the other case the mesh size has been increased to 0.3 mm for the base element (figure 5.4).

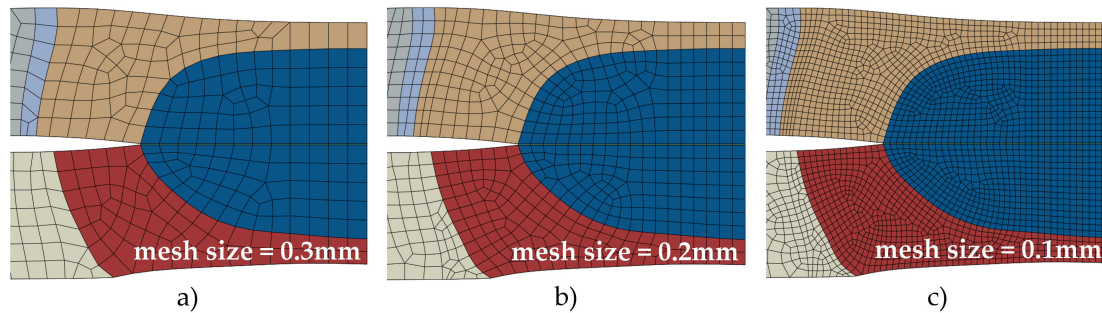


Figure 5.4: Usibor1500 2 mm/DP600 2 mm middle intensity configuration with different mesh size: a) coarse 0.3 mm b) intermediate 0.2 mm and c) fine 0.1 mm.

Then, FE simulations were run with the three mesh sizes and their Load-Displacement curves (and in particular the failure strength) and failure modes were compared. In figure 5.5.a, the three Load-Displacement responses are gathered and the global spot weld mechanical behaviour is preserved. Nevertheless, the failure strengths show difference. As expected, the following trend is observed: the smaller the mesh size, the earlier failure occurs. In figure 5.5.a, the fine mesh (0.1 mm) response presents a failure strength lower than other mesh sizes (9% lower).

Concerning failure modes, there is a Button Pull Out failure in the Usibor1500 HAZ in the three cases. However, a mesh design sensitivity could be observed, in particular at the nugget periphery. It seems that when the mesh is finer, the failure tends to follow more closely the nugget border.

### 5.1.3 Boundary conditions influence

In this section, the boundary conditions influence is studied. In fact, a displacement is imposed on the upper sheet with a particular velocity in the Explicit solver. This velocity is chosen to be lower than the critical velocity (derived from lower resonance frequency) to remain in the quasi-static hypotheses domain.

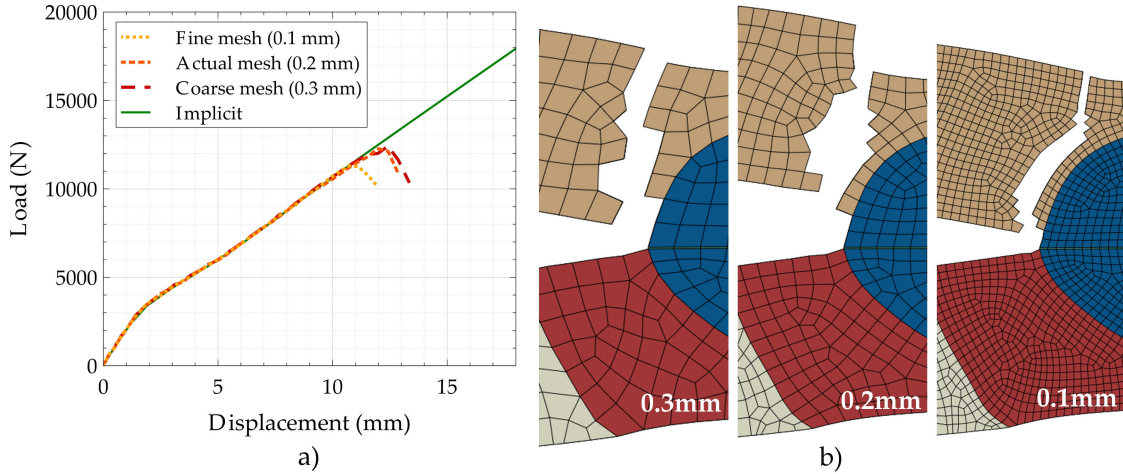


Figure 5.5: Usibor1500 2 mm/DP600 2 mm middle intensity configuration with three different mesh sizes: a) Comparison of Load-Displacement responses and b) Comparison of the failure modes.

### 5.1.3.1 Boundary condition velocity value

In Explicit solver, the increment time is function of the length of the smallest element in the model and of the element material density. As density is the same in the whole model, the increment time is defined by the properties of the smallest element, which is one of the cohesive elements because of the cohesive zone thickness.

For a given increment time, a way to accelerate the calculation, is to decrease the simulation time (testing time in the simulation), which results in increasing the testing velocity. However, increasing velocity encounters two limitations: velocity needs to be lower than the critical velocity identified by the modal analysis and the system kinetic energy has to remain a small fraction of system internal energy for quasi-static analyses.

In order to observe the velocity influence on the spot weld mechanical behaviour response, a FE model (Usibor1500 2 mm/DP600 2 mm middle intensity configuration) was solved with six different boundary conditions:  $2 \text{ m s}^{-1}$ ,  $5 \text{ m s}^{-1}$ ,  $10 \text{ m s}^{-1}$ ,  $20 \text{ m s}^{-1}$ ,  $30 \text{ m s}^{-1}$  and  $40 \text{ m s}^{-1}$ . Load-Displacement response curves of these six FE model with different boundary conditions are represented in figure 5.6. Moreover, Implicit solver response curve is also integrated in the figure in order to have a reference for the spot weld quasi-static mechanical behaviour.

For this configuration, the critical velocity is around  $80 \text{ m s}^{-1}$  (first natural frequency is around 2000 Hz). All velocity solved are under this critical value. However, in figure 5.6, it can be clearly seen that the simulations with the higher velocities do not reproduce the Implicit solver result. In fact, the higher the velocity, the higher the disruptive dynamic effects. In this case, when velocity is over  $10 \text{ m s}^{-1}$ , the Load-Displacement response of the model is modified by inertial effects.

Besides, a velocity of  $10 \text{ m s}^{-1}$  is a little too high to predict the failure strength well: even if the loading curve is well predicted, some oscillations are observable close to the failure strength region, which perturbate the predicted failure strength. This is due to the

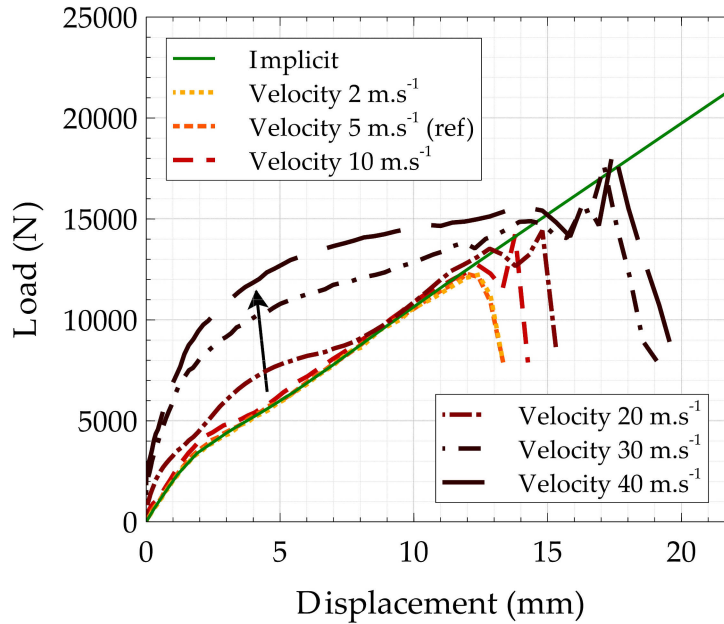


Figure 5.6: Usibor1500 2 mm/DP600 2 mm middle intensity configuration with six different velocities (2, 5 (ref), 10, 20, 30 and 40, in  $\text{m.s}^{-1}$ ).

high amount of released energy during fracture involving unexpected kinetic effects.

Another way to know if dynamic effects disturb FE model response is to compare Internal and Kinetic energy. Indeed, Kinetic energy has to remain a small fraction of the Internal energy along the simulation time. In figure 5.7.a, where the boundary velocity is  $5 \text{ m.s}^{-1}$  and the Load-Displacement curve did not show any variation compared to the Implicit response, the Kinetic energy is only a small fraction of the Internal energy over the whole test history (until fracture). Moreover, even after fracture, Kinetic energy value stays around 10% of Internal energy.

With the higher velocities and a behaviour already quite different from the Implicit response in figure 5.6, the Kinetic energy is a significant fraction of Internal one as shown in figure 5.7.b. Just before fracture, the Kinetic energy represents 50% of Internal one. Just after fracture, it almost reaches the Internal energy level.

These comparisons between Implicit and Explicit and between the Kinetic and Internal energies allow to identify the highest velocity to use in the FE models in order to optimize the computational time without modifying the simulated FE spot weld behaviour.

### 5.1.3.2 Amplitude form of applied velocity

Velocity influence was studied in previous section. However, there are many ways to apply velocity in the model. It is obvious that applying directly the maximum velocity value from the beginning of the simulation would generate huge dynamic issues. Therefore a progressive velocity is applied from 0 to its maximum value.

However, in order to minimize dynamic effects, two amplitude forms have been introduced in the FE models and their respective Load-Displacement responses were compared.



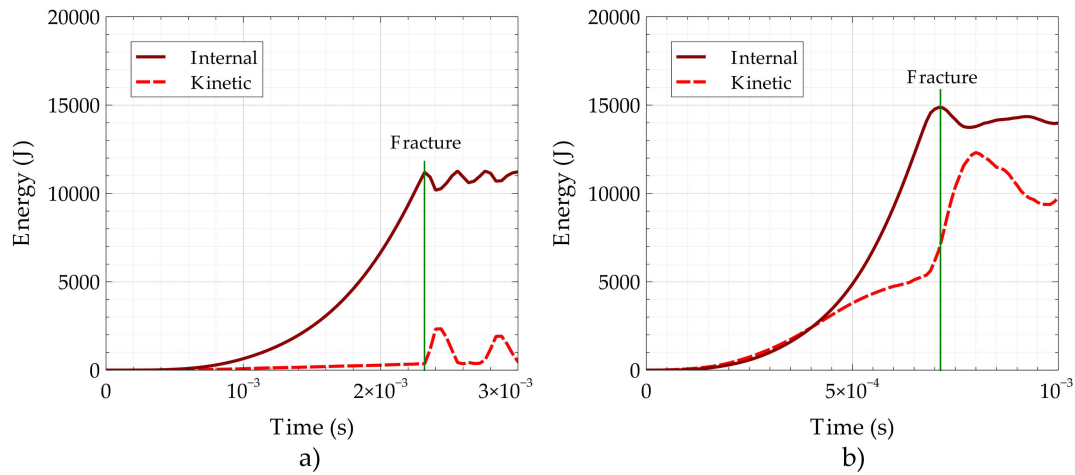


Figure 5.7: Internal and Kinetic energies comparison of Usibor1500 2 mm/DP600 2 mm middle intensity configuration with two different velocities: a)  $5 \text{ m s}^{-1}$  (ref) and b)  $30 \text{ m s}^{-1}$ .

First amplitude form is a simple ramp where velocity is null at simulation beginning and increases to its maximum value for final simulation time. Second amplitude form is the well known “smooth step” which allows to minimize dynamic effects (figure 5.8).

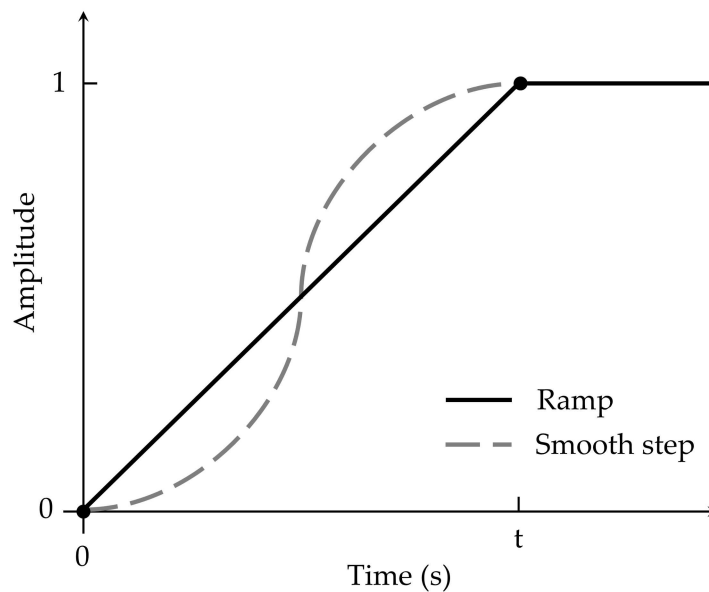


Figure 5.8: Amplitude forms to apply a progressive increase of velocity (ramp and smooth step).

After simulation of the two models, their Load-Displacement response curves were collected in figure 5.9 with the Implicit response as reference. The main result is that the failure strength is well predicted in the two cases and loading curves show a satisfying global stability.

Nevertheless, smooth step amplitude response shows some deviations from Implicit

solver curve. This can be explained by the amplitude form, which presents a maximum of acceleration (derivative of velocity, represented by curve gradient in figure 5.8). This maximum of acceleration induces side dynamic effects in the spot weld which are observable in the Load-Displacement response. However, that unexpected side effect are not sufficient to drastically modify global spot weld behaviour.

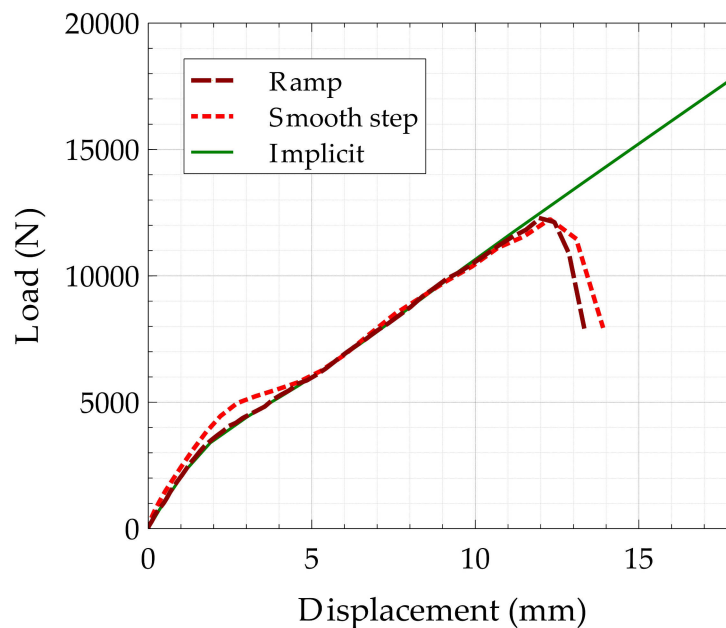


Figure 5.9: FE model Load-Displacement response curves for two different types of boundary condition amplitude (ramp and smooth step).

#### 5.1.4 Mass scaling influence

As previously explained, increment time is a function of the length of the smallest element in the model and of element density. In order to increase the increment time, the density could be increased with caution. A well known tip is the use of “Mass Scaling” factor, multiplying the mass (or density) of a carefully chosen zone by this factor. For a given simulation time, this method allows to increase the minimal increment time, and then optimise the computing time.

However, as presented previously, adding mass on elements could enhance dynamic side effects. To evaluate the optimal mass scaling factor, three models were computed with different mass scaling factor in the spot weld region (0, 10 and 100). Load-Displacement response curves of these models were compared in figure 5.10 with Implicit solver response as reference.

Only the Load-Displacement curve with a 100 mass scaling factor shows deviations due to dynamic side effects and leads finally to a poor prediction of the spot weld behaviour and failure strength. However, with a mass scaling factor of 10, the model shows good agreement with Implicit response and no mass scaling case. Moreover, using a mass scaling factor of 10 allows to divide the calculation time by approximately four.

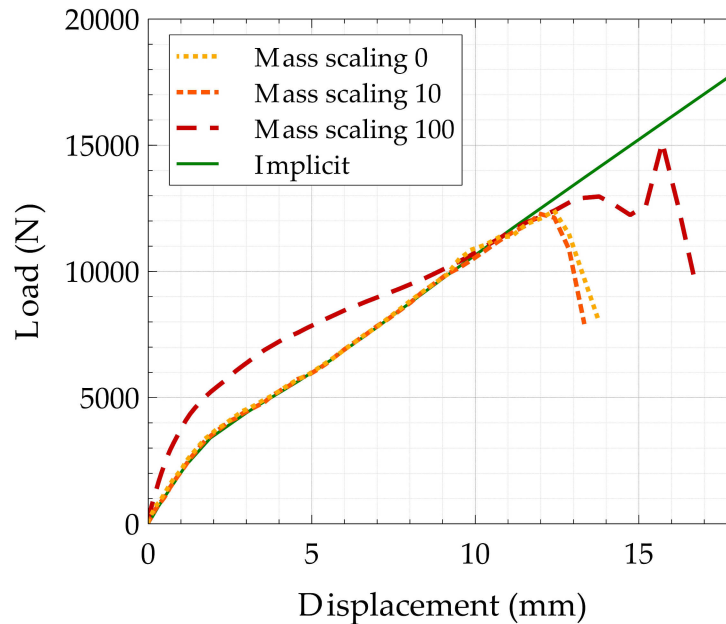


Figure 5.10: Usibor1500 2 mm/DP600 2 mm middle intensity configuration with three different mass scaling on elements (no mass scaling, mass scaling factor 10 and mass scaling factor 100).

## 5.2 FE model potential

In this section, FE model potential will be analysed by presenting two extensions. First, a spot weld configuration with three steel sheets will be simulated with the same FE method and in a second part, the FE modelling method will be applied to a new welding type assembly: arc welds.

### 5.2.1 Triple-sheet spot welded assembly modelling

Carmakers often have to join several steel sheets during body in white production. Indeed, beyond the classical double sheet spot welded assembly, the behaviour of triple-sheet spot weld assemblies is equally important. In this section, the FE model will be used to predict the failure strength and mode of a triple-sheet spot welded assembly.

#### 5.2.1.1 Materials and welding configurations

The configuration studied here is an assembly of three 1.5 mm thick sheets, two are made of Usibor2000 steel grade and the last one is a DP780 steel. As Usibor1500, Usibor2000 is a fully martensitic press hardened steel, but with a higher carbon content than Usibor1500, which allows to reach an Ultimate Tensile Strength (UTS) around 2000 MPa. DP780 steel belongs to the dual phase grade family. DP780 is ferritic martensitic steel with a UTS around 780 MPa. Their chemical composition is given in table 5.1:

Steel grade (x 0.001 wt%)	C	Mn	B	Si	Al
DP780 1.5 mm	156	1900	-	178	17
Usibor2000 1.5 mm	336	619	3	541	46

Table 5.1: Chemical composition of DP780 and Usibor2000 steel grades (x 0.001 wt%).

Welding configuration is an assembly of a DP780 steel sheet as middle sheet and Usibor2000 steel sheets as upper and lower sheets (figure 5.11). Indeed, even if the assembly is symmetric, during cross tension tests, the two lowest sheets have been clamped together (lower Usibor2000 and DP780 sheets) whereas upper Usibor2000 sheet is translated upward.

Welding parameters of this study are given by a carmaker and collected in the table 5.2:

Electrode diameter	Pulse Number	Welding time	Holding time	Electrode force
8 mm	1	28 p	15 p	500 daN

Table 5.2: Welding parameters for triple sheet Usibor2000/DP780 assembly,  $p=0.02$  s.

These parameters produce a significant spot welding intensity range from 4.0 kA to 7.0 kA. As in the previous study, three welding intensities are chosen in order to represent all the welding range. Lower end corresponds to 4.5 kA, middle to 5.8 kA and upper end to 7.0 kA.

One spot weld sample obtained for each of these three welding intensities was cut for a middle cross section and chemically etched to observe spot weld microstructure and fusion zone diameter (figure 5.11). As observed in previous study, molten zone diameter increases with welding intensity.

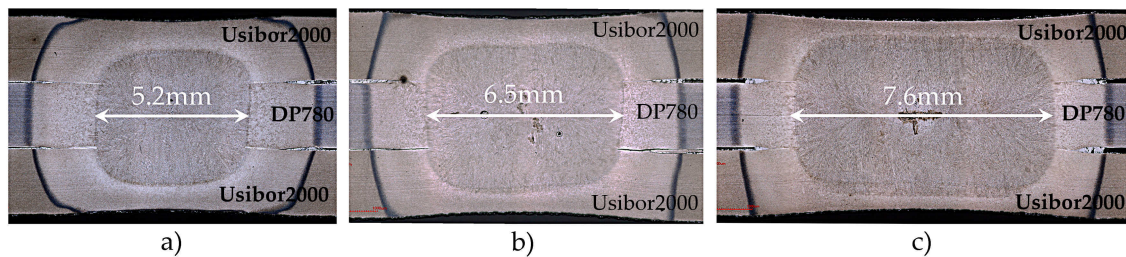


Figure 5.11: Usibor2000 1.5 mm/DP780 1.5 mm triple-sheet spot weld assembly cross section for three welding intensities: a) lower end 4.5 kA, b) middle 5.8 kA and c) upper end 7.0 kA.

Micro-hardness tests were carried out on metallographic samples. Profile line began in Usibor2000 base metal zone, through the fusion zone and ended within the middle DP780 base metal (figure 5.12.b). Observing simultaneously the micrographic view and the hardness profile, same particular zones as in Usibor1500/DP600 welds are observable.

However, as steel grades are higher (Usibor2000/DP780 UTS > Usibor1500/DP600 UTS), hardness are also higher.

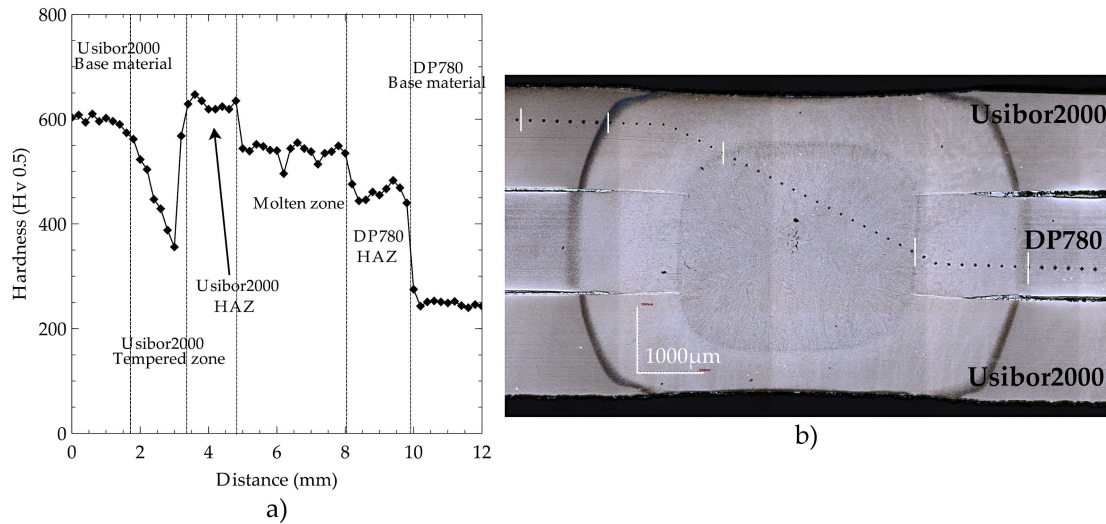


Figure 5.12: Usibor2000 1.5 mm/DP780 1.5 mm triple-sheet spot weld assembly micro-hardness tests on cross section for lower end intensity configuration: a) micro hardness profile and identified zones, b) corresponding cross section micrograph with hardness indents.

As expected, a tempered HAZ is observable in Usibor2000 sheet between base material and quenched HAZ.

### 5.2.1.2 FE model data setting

FE model is built with the methodology previously presented in chapter 4. The geometry of the zones and the discretization are based on the micrograph and micro hardness tests (figures 5.11 and 5.12). Indeed, the zone discretization is presented in figure 5.13:

Due to their different mechanical response, six zones need to be described:

- Usibor2000 base material, not affected by welding process,
- Usibor2000 soft tempered zone,
- Usibor2000 HAZ, corresponding to the quenched HAZ of Usibor2000 steel,
- Fusion zone (nugget), quenched mixture of Usibor2000 and DP780 steels,
- DP780 HAZ, corresponding to the quenched HAZ of DP780 steel,
- DP780 base material, not affected by welding process.

Moreover, as shown in figure 5.13, two types of cohesive layer are introduced in the FE model: the first one to predict brittle interfacial failures and the second one to predict brittle dome failures between Usibor2000 HAZ and the fusion zone. Cohesive zone layer thickness is 0.02 mm.

Constitutive laws of each zone were identified as in chapter 4 using the SCCA martensite model and tensile tests on based material. However, as Fusion Zone is a mixture of the

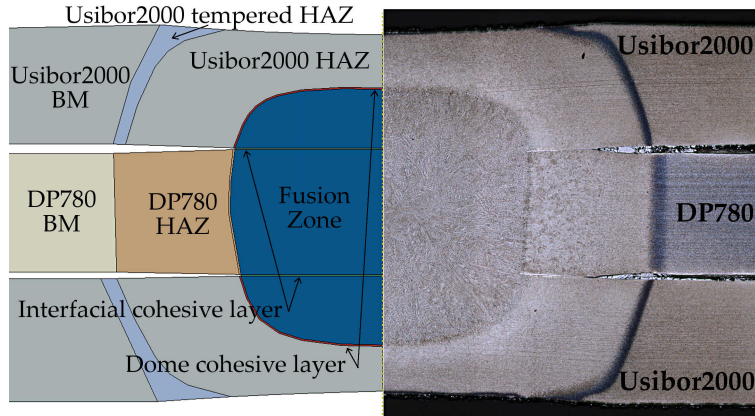


Figure 5.13: Discretization for dissimilar Usibor2000 1.5 mm/ DP780 1.5 mm triple-sheet spot weld FE model.

two steel grades, its constitutive law is established by mixing Usibor2000 HAZ and DP780 HAZ constitutive laws. This law is established by determining the average stress of the two zones for a given strain.

As Usibor2000 base material and HAZ show very close hardness values, a simplification is done by using the same constitutive law for the two zones. Then, the elastic-plastic strain hardening law used for the calculation are shown in figure 5.14.

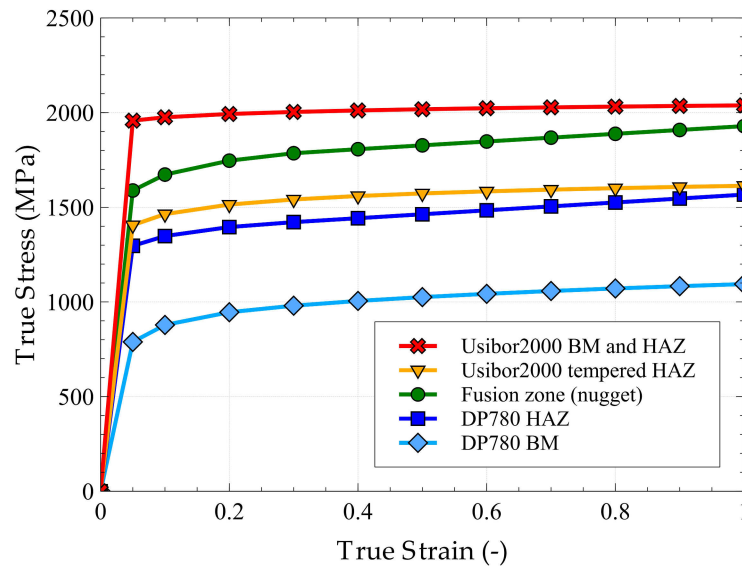


Figure 5.14: Elastic-plastic strain hardening law for each zones of Usibor2000 1.5 mm/DP780 1.5 mm triple-sheet spot weld established by SCCA model [ARL 13].

Concerning ductile damage parameters, the identification method is the same as in chapter 4, using the Considere strain as damage initiation and a corresponding effective plastic displacement as damage evolution. Damage initiation criteria were collected in table 5.3.



Zones	Usibor2000 BM and HAZ	Usibor2000 tempered HAZ	Fusion zone	DP780 HAZ	DP780 BM
$\bar{\varepsilon}_0^{pl}$	0.029	0.056	0.069	0.054	0.115
$\bar{u}_f^{pl}$ (mm)	0.02	0.15	0.06	0.1	0.2

Table 5.3: Identified damage initiation strain using Considere criterion criterion and effective plastic displacement at fracture for the different zones of a Usibor2000/DP780 spot weld.

Moreover, damage evolution description (effective plastic displacement) identified for each zone is given in table 5.3.

As before, cohesive zones' parameters are identified by inverse method on one configuration (middle intensity) then introduced in other models. The optimized cohesive parameters for the two different cohesive zones are gathered in the table 5.4:

Cohesive zones	$\sigma_{max}$ in MPa			$\Gamma$ in $\text{kJ m}^{-2}$		
	$\sigma_{max1}$	$\sigma_{max1}$	$\sigma_{max3}$	$\Gamma_1$	$\Gamma_2$	$\Gamma_3$
Usibor2000/DP780 fusion zone	3500	3500	3500	8	8	8
Usibor2000/DP780 dome layer	2800	2800	2800	4	1.5	1.5

Table 5.4: Identified parameter values of the three cohesive zones in the three directions (direction 1 is the stack direction, orthogonal to cohesive zone).  $\sigma_{max}$  in MPa and  $\Gamma$  in  $\text{kJ m}^{-2}$ .

Boundary conditions are chosen in order to reproduce the experimental quasi-static mechanical test (figure 5.15). A displacement is imposed on upper Usibor2000 steel sheet whereas the two lower sheets (DP780 and second Usibor2000 sheets) are clamped.

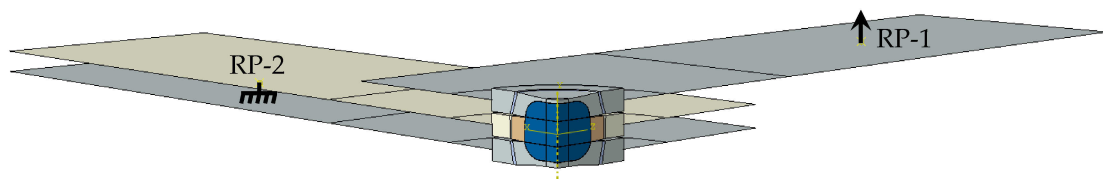


Figure 5.15: Minimal symmetry of Usibor2000/DP780 triple-sheet heterogeneous spot weld mechanical tests with the loading conditions: spot weld quarter in cross section.

0.2 mm mesh size is chosen to optimize computing time. Mesh is represented in figure 5.16 for the three welding intensity configurations.

### 5.2.1.3 Modelling results

The simulation results of Usibor2000 1.5 mm/DP780 1.5 mm triple-sheet spot welds in cross tension at lower, middle and upper end intensities are respectively shown in figures 5.17, 5.18 and 5.19.

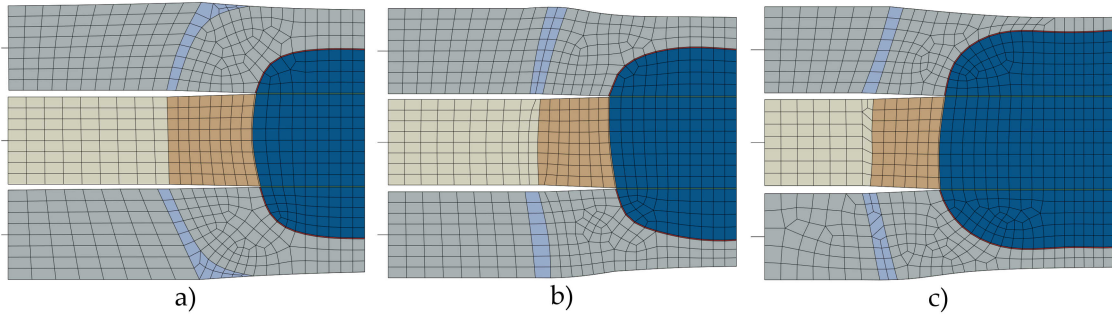


Figure 5.16: Mesh of Usibor2000/DP780 triple-sheet heterogeneous spot weld models in cross tension for three welding intensity configurations: a) lower end, b) middle and c) upper end.

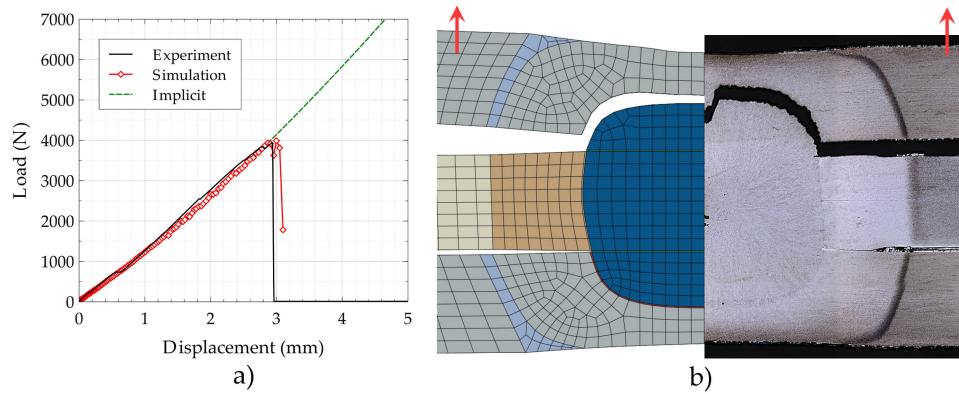


Figure 5.17: Comparison between experimental and simulation response in cross tension of Usibor2000 1.5 mm/DP780 1.5 mm triple-sheet spot weld at lower end intensity: a) load-displacement curves and b) failure mode.

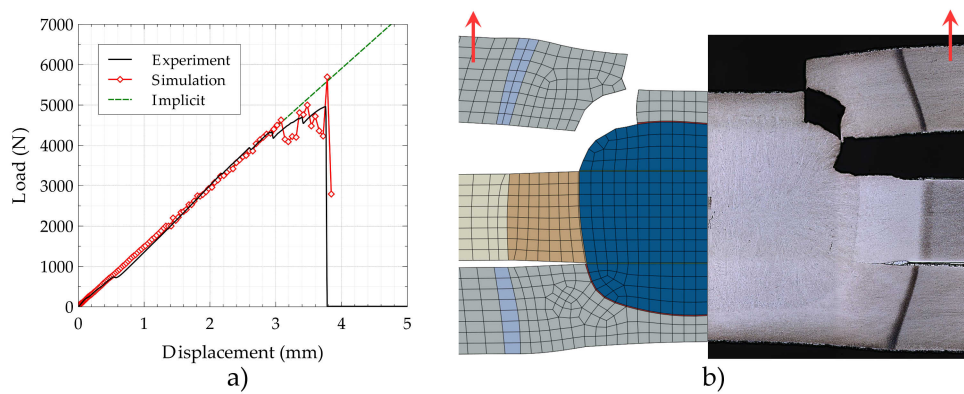


Figure 5.18: Comparison between experimental and simulation response in cross tension of Usibor2000 1.5 mm/DP780 1.5 mm triple-sheet spot weld at middle intensity: a) load-displacement curves and b) failure mode.

Experimental failure modes range from total dome failure (TDF) for lower end intensity

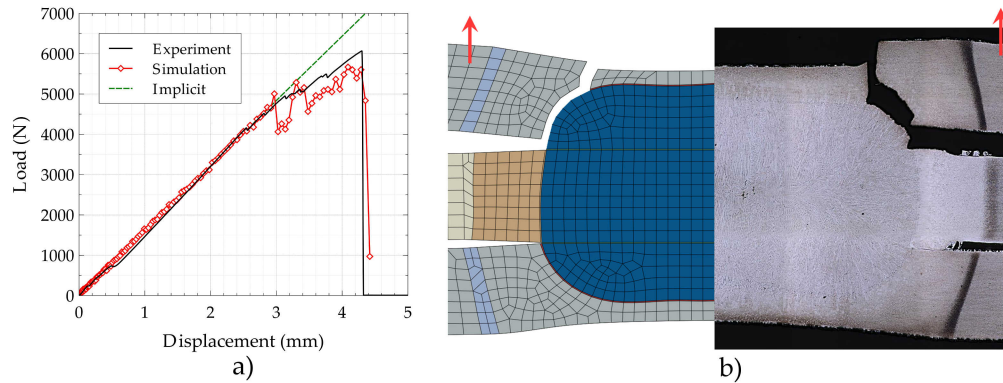


Figure 5.19: Comparison between experimental and simulation response in cross tension of Usibor2000 1.5 mm/DP780 1.5 mm triple-sheet spot weld at upper end intensity: a) load-displacement curves and b) failure mode.

to partial dome failure for middle and upper end intensities. The FE models predict the failure modes well in all three cases as shown in figures 5.17.b, 5.18.b and 5.19.b.

Moreover, load-displacement responses are well predicted in almost all configurations (figures 5.17.a, 5.18.a and 5.19.a). However, for the upper end configuration, the FE simulation response clearly underestimates experimental one even if relative error is less than 10% on the failure strength.

FE model response is very “noisy”. Load drops in the loading curves are related to progressive cohesive element deletion inducing dynamic oscillation.

A deviation from the Implicit model response is observed in figures 5.17.a, 5.18.a and 5.19.a. This deviation starts when the first dome cohesive elements failed in FE model or when the crack initiated at the notch root during experimental cross tension tests.

In conclusion, the present FE methodology allows to predict the failure modes and strengths rather well for triple-sheet spot weld assemblies.

## 5.2.2 Arc welds FE modelling

In this section, the two Usibor1500 arc welded assemblies presented in the chapter 2 are simulated. As a reminder, two steel sheets were used (1.5 mm and 2.0 mm). The welding configuration was overlap. Two configurations have been tested: one with the thicker sheet (2.0 mm) as the upper sheet and one as with the thicker sheet as the lower one.

### 5.2.2.1 FE model data setting

FE model is built with the same methodology than for spot weld assemblies in chapter 4. The zone geometry and discretization are based on the micrograph and micro hardness tests on arc weld section. Indeed, the zone discretization is presented in figure 5.21.

The particularity of the model is to have three different zones in the tempered HAZ of Usibor1500. This was introduced in the model in order to be more representative of the mechanical behaviour of this tempered zone which is much more spread (almost 10 mm long in arc welds whereas only 2 mm thick in spot welds in figure 5.20).

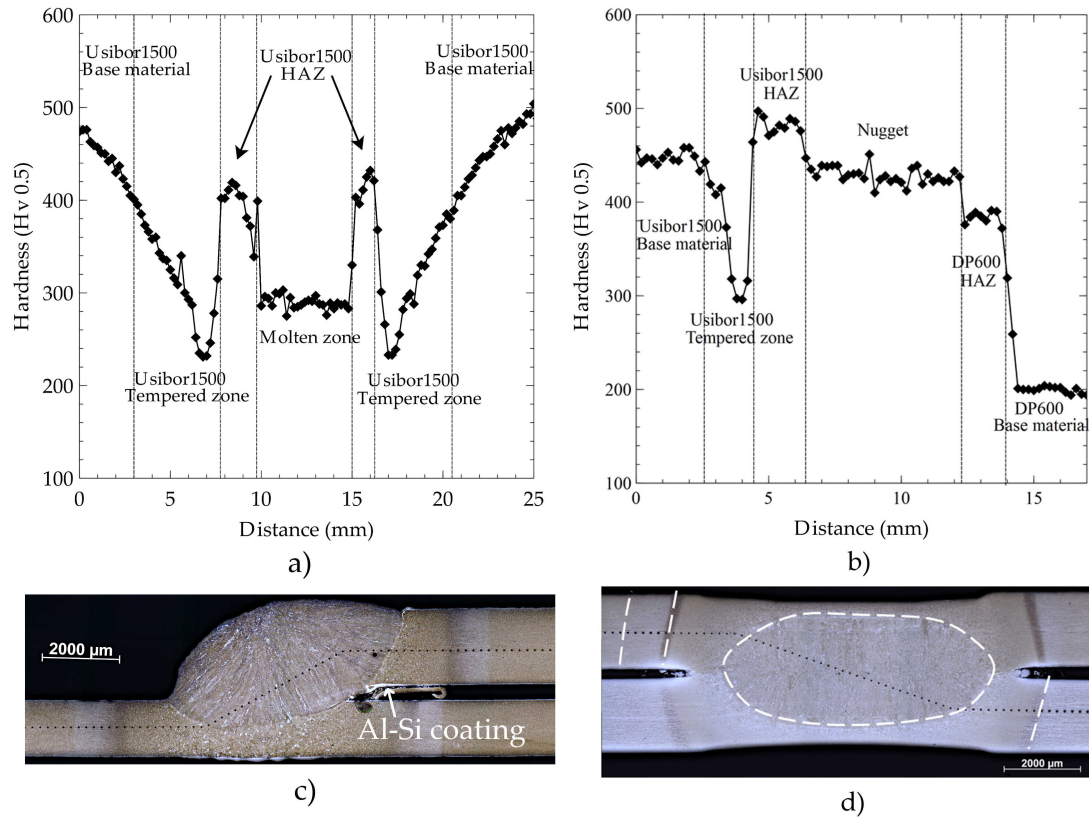


Figure 5.20: Hardness profiles of Usibor1500 2.0 mm/Usibor1500 1.5 mm arc weld and Usibor1500 2.0 mm/DP600 2 mm spot weld: a) and b) hardness profiles, c) and d) metallographic cross-sections.

In fact, this is directly due to the welding process which allows a very long tempering time during arc welding. Thereby, the tempered zone was discretized in three zones with different mechanical behaviour in order to better represent the progressive hardness evolution. Thus, six zones with different mechanical behaviour need to be described:

- Usibor1500 base material, not affected by welding process,
- Usibor1500 soft tempered zone 1, where maximal temperature reached  $450^{\circ}\text{C}$ ,
- Usibor1500 soft tempered zone 2, where maximal temperature reached  $550^{\circ}\text{C}$ ,
- Usibor1500 soft tempered zone 3, where maximal temperature reached  $650^{\circ}\text{C}$ ,
- Usibor1500 HAZ, corresponding to the quenched HAZ of Usibor1500 steel, but with a small hardness than for RSW because of lower cooling rate.
- Fusion zone, quenched mixture of Usibor1500 and G3Si steels, the dilution effect leads to an harder zone than DP600.

In figure 5.21, two zones of Usibor1500 soft tempered zone 1 are discretized at the borders of tempered zone. The discretization was not applied on the lower right part of arc welds because no loading is applied here and there is no stress in this area.

Constitutive laws of each zone were identified as in chapter 4 using the SCCA martensite

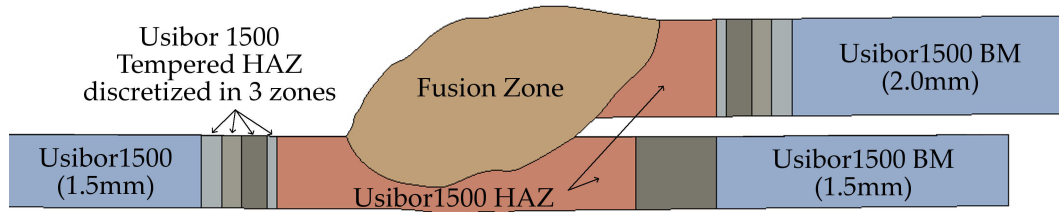


Figure 5.21: Discretization for dissimilar Usibor1500 (2.0 mm/1.5 mm) arc weld FE model.

model. However, the Fusion Zone mechanical response is not as easy as in spot welding because the quantity of filler wire (G3Si) provided is not known. In fact, the only way to estimate the filler wire quantity is to observe the Fusion Zone hardness value. Therefore, Fusion Zone constitutive law was established reproducing the hardness values ratio between the zones on elastic plastic laws by homothety. Constitutive laws of each zones are given in figure 5.22.

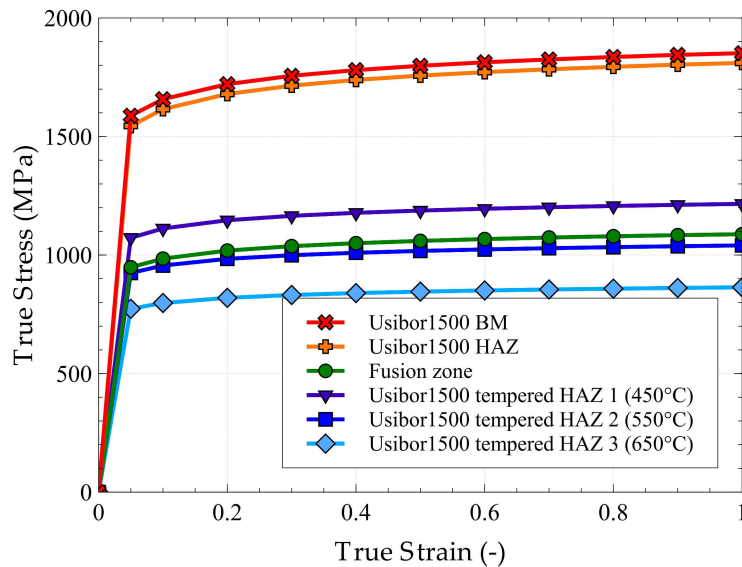


Figure 5.22: Elastic-plastic strain hardening law for each zones of Usibor1500 2.0 mm/1.5 mm arc weld established by SCCA model [ARL 13].

Concerning ductile damage parameters, the identification method is the same as in chapter 4, using the Considere strain as damage initiation and a corresponding effective plastic displacement as damage evolution. Damage initiation criteria were found in table 5.5.



Zones	Usibor1500 BM	Usibor1500 HAZ	Usibor1500 tempered 1	Usibor1500 tempered 2	Usibor1500 tempered 3	Fusion zone
$\bar{\varepsilon}_0^{pl}$	0.070	0.071	0.048	0.046	0.044	0.054
$\bar{u}_f^{pl}$ (mm)	0.02	0.02	0.2	0.2	0.2	0.2

Table 5.5: Identified damage initiation strain using Considere criterion and effective plastic displacement at fracture for the different zones of a Usibor1500 arc weld.

Moreover, damage evolution description (effective plastic displacement) identified for each zone is collected in table 5.5. Effective plastic displacement of zones are split in two categories following their hardness.

A mesh size of 0.1 mm and boundary conditions are chosen in order to reproduce the experimental quasi-static mechanical test.

### 5.2.2.2 Modelling results

In this section, the FE simulation results of 2.0 mm/1.5 mm and 1.5 mm/2.0 mm arc weld assemblies will be presented. Investigations will focus on the failure modes and strengths.

Experimental and simulated Load-Elongation curves of the two configurations (depending on the thicker sheet position) are plotted in figure 5.23. Global behaviour of arc welds is well predicted (figures 5.23.a and 5.23.b), and the failure strength prediction is very accurate whatever the configuration.

In the case where thickest sheet (2.0 mm) is the upper sheet, relative error to an average of experimental failure strength is 7%. In the other case, when the thicker sheet is the lower sheet, relative error is 5%.

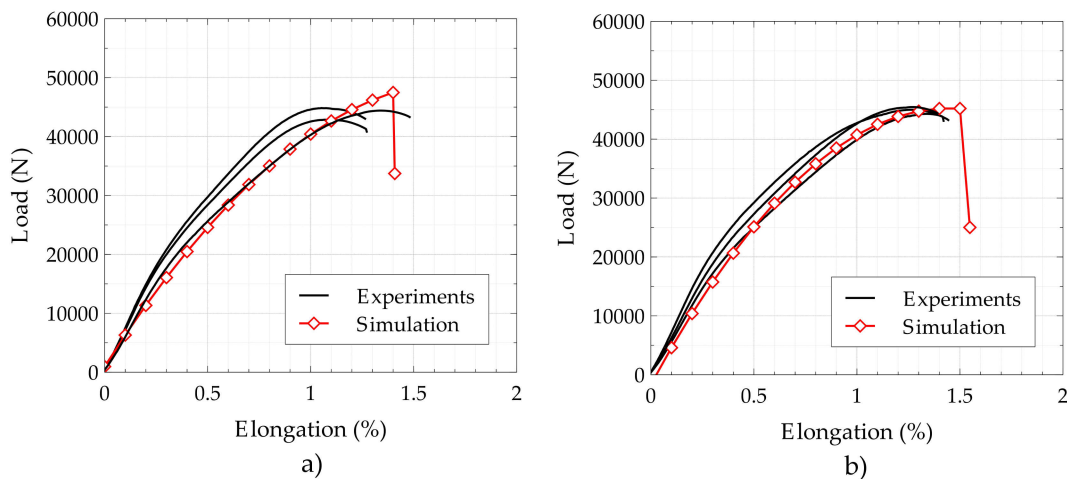


Figure 5.23: Experimental and simulated Load-Elongation responses of dissimilar thicknesses Usibor1500 arc welds: a) 2.0 mm/1.5 mm configuration and b) 1.5 mm/2.0 mm configuration.

Concerning the failure modes in both configurations, simulated failure occurs in the same zone as in the experiments (figure 5.24). When the thickest sheet is above, failure



occurs in the tempered HAZ of the thinnest sheet (figures 5.24.a and 5.24.c). When the thickest sheet is the lower one in the overlap assembly, failure occurs in the Fusion Zone very close to the interface with the quenched HAZ of the thinnest sheet (figures 5.24.b and 5.24.d).

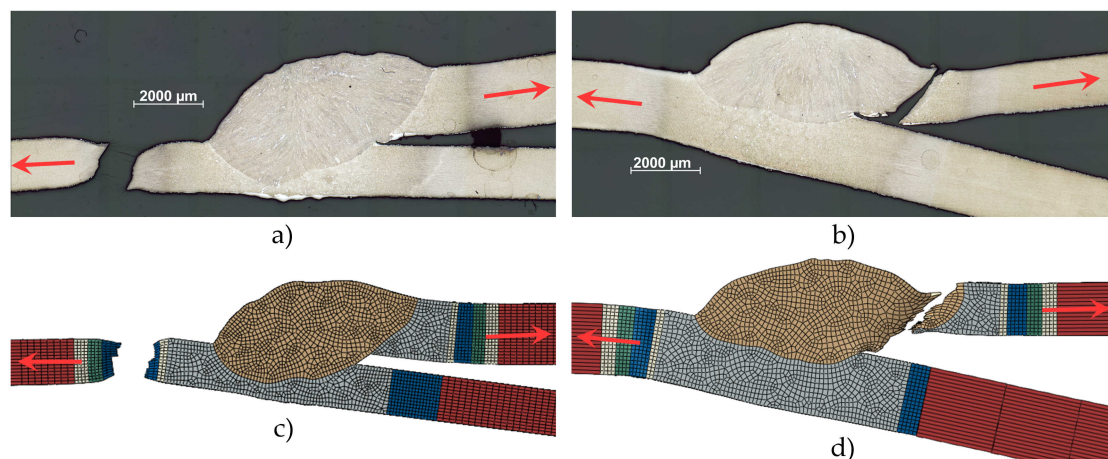


Figure 5.24: Failure modes comparison between experiments and FE simulation of dissimilar thicknesses Usibor1500 arc welds: a) and b) 2.0 mm/1.5 mm and 1.5 mm/2.0 mm configurations experimental failure modes, c) and d) 2.0 mm/1.5 mm and 1.5 mm/2.0 mm configurations simulated failure modes.

In this last configuration, a close competition between weak zones is observable in the experiments as well as in the FE models: in figures 5.24.b and 5.24.d, necking is observed in the tempered zone with an important cross section reduction. Observing the failed tempered zone in the first configuration (5.24.a), strain is comparable to tempered HAZ zone in the second configuration (5.24.b), even if this zone did not fail. Besides, experimental and simulated failure strengths confirm this hypothesis because they are similar in both configurations.

### 5.3 Conclusion

In this section, the FE model for spot weld mechanical testing previously introduced in chapter 4 was discussed. First, limitations of FE model and necessary precautions were highlighted. These limitations were investigated by using the model on previous configurations (chapter 4) but modifying solver, mesh size, or boundary conditions.

Using the Implicit solver is very efficient to verify that no disruptive dynamic effects occurred during the Explicit solver calculation. Moreover, the load-displacement curve has a mesh size dependence because total plastic displacement is function of mesh size. Indeed, it is recommended to have around ten elements in the sheet thickness, and if refinement is needed, the effective plastic displacement should be corrected to counterbalance the displacement loss before damage initiation.

Moreover, special caution is needed concerning boundary conditions and in particular for the velocity used to apply the displacement during test in FE model. The easiest

solution to check for disruptive dynamic effect is to compare the Explicit response to the Implicit one before failure initiation. This allows to chose the appropriate velocity to be applied on the assembly. Comparing Internal and Kinetic energies also gives a good indication about dynamic effects. The mass scaling method could be used to improve calculation time without affecting too much the quasi-static nature of loading.

Despite these limitations, this FE methodology could be extended to more complex configurations. It was successfully applied on a Usibor2000/DP780 triple-sheet spot weld assembly. Failure modes and strengths of FE models obtained for three intensities were in agreement with experimental ones. In addition, modelling methodology was applied to a different welding process: arc welding. Usibor1500 arc weld FE model results could predict the failure modes and strengths of two overlap configurations. However, when brittle interfacial or dome failures occur, it is necessary to introduce cohesive zones. The cohesive zone parameters need to be fitted by inverse method on an experimental case because, there is no other simple case of identification. However, when ductile failure occurs, a FE model without cohesive zone is enough to predict failure mode and strength.

In conclusion, the greatest strength of this FE model is its versatility as it can be used in many welding types and on complex configurations. It gives accurate failure modes and strengths prediction, provided that the model has been carefully built especially with regard to quasi-static boundary conditions and mesh size.

# Conclusion and outlooks

The objective of this PhD was to understand the fracture mechanisms of heterogeneous welded assemblies during cross tension and tensile shear mechanical tests and to propose a Finite Element (FE) model allowing to predict failure modes and strength of these assemblies.

In the first part of this work, an experimental study was carried out about several heterogeneous configurations. Different base materials and different configurations were welded. First, the martensitic Usibor1500 steel was welded to ferritic-martensitic DP600 steel with four thickness configurations (similar and dissimilar). Then, ferritic-austenitic Duplex steels were weld to DP600 steel. These experimental studies allow to highlight many special points permitting to get a better understanding of the mechanical behaviour of heterogeneous spot welds.

First, influential parameters on the failure mode transition were highlighted such as sheet thicknesses and nugget diameter. It was also shown that cautions need to be taken for upper end intensity because of appearance of splash which could decrease weld strength and modify the failure mode. A positive deviation was observed for dissimilar thickness configurations presenting higher performance than similar configurations in cross tension but not in tensile shear. Then, in a highly heterogeneous welding case (Duplex/DP600), the negative effect of the ferrite layer at the interface between the DP600 HAZ and the fusion zone was highlighted, in particular, its effect on the failure strength and mode leading to dome failure. Hypothesis on the ferrite layer formation was proposed, depending on the aluminium content, and its weakness was mainly described by intergranular  $\delta$ -ferrite fracture in this zone.

Moreover, an elaboration methodology including hot and cold rolling as well as thermal treatments was established in order to obtain the final Duplex steel to weld. Many tests were carried out in order to find the optimized parameters for hot and cold rolling, but also for heat treatments which are essential to allow the cold rolling of the Duplex steels.

On the other hand, a FE modelling approach was built to predict the failure mode and strength of heterogeneous spot weld assemblies. Thanks to the important experimental data obtained in the different welded configurations, the FE model has been validated, in particular for the failure mode transition prediction. Whatever the configurations, experimental failure modes and strengths were mainly well predicted, even in the highly heterogeneous case (Duplex/DP600). Moreover, to our knowledge, it was the first time a FE modelling methodology was successfully applied on arc weld and triple sheets spot weld assemblies. In the triple sheets case, partial dome failures were for the first time observed in the simulation (as in experimental).

However, this work underlined the precautions to be taken into account in the FE modelling process which constitute some perspectives of this PhD. First, and such as all FE models, the mesh size dependency needs to be verified in order to not disturb the model response, in particular for the ductile damage criterion. Then, boundary conditions need to be wisely chosen in order to minimize dynamic effects which could disturb the mechanical response of spot welds. Moreover, the cohesive zone parameters identification is a weak point in the model, because no mechanical test was done to identify precisely the parameters. Even if, a test was available, many couple of zone cohesive parameters could work to well predict the failure mode and strength of spot welds. This issue highlights another particularities of the heterogeneous welding: fusion zone microstructure and mechanical behaviour. The fusion zone is a mixture of the two steel grades with dilution varying a lot as a function of welding intensity and its microstructure is very particular because of the oriented cooling conditions and solidification. Moreover, the fusion zone geometry does not allow to extract representative sample to test mechanically which is a limiting point of FE modelling.

Thus, the determination of strain hardening law also needs precaution. First, concerning the fusion zone, which is a mixture of the two steels. A new experimental technique should be set up to be able to get a realistic mechanical response of the FZ. Then, SCCA model predicts fairly the elastic-plastic behaviour of martensitic/ferritic steels but for a given chemical composition in a particular range. This model could take into account more chemical elements, such as Aluminium, which could allow to obtain Duplex strain hardening law otherwise that using experimental data.

For a given material, effective plastic displacement at fracture as a function of mesh size could be established, which could allow to minimize the effect of mesh size and obtain a mesh independent ductile damage criterion.

Robustness of FE models has been proved through many configurations varying in particular sheet thicknesses and nugget diameter. FE model could allow to predict material and process parameters in order to obtain an optimal spot weld for a given configuration. A parametric study with FE model could be considered to establish a kind of Ashby graph giving the failure mode as a function of sheet thickness and nugget diameter of spot weld. This graph would permit to optimize process parameters like welding intensity in order to obtain an acceptable failure mode.

In figure 5.25, similar Usibor1500/DP600 spot weld experimental failure modes are given. The low amount of experimental data does not allow to precisely describe the zone borders. In figures 5.25.a and 5.25.b, two different possible discretizations are presented. A parametric study with the FE model could be considered to enrich the data in these graphs in order to precisely identify the borders of failure mode transition for a given configuration.

For a given configuration, FE model could thus give failure mode in all thickness and nugget diameter range. Then, after the thicknesses of steel grades were optimized and after the best failure mode was chosen, welding process parameters could be predicted to obtain the best compromise, and could be verified experimentally which could be very cost-effective.

At last, on a long term, one could imagine to use this methodology to design new materials with enhanced properties in welds. The FE modelling could find the optimized

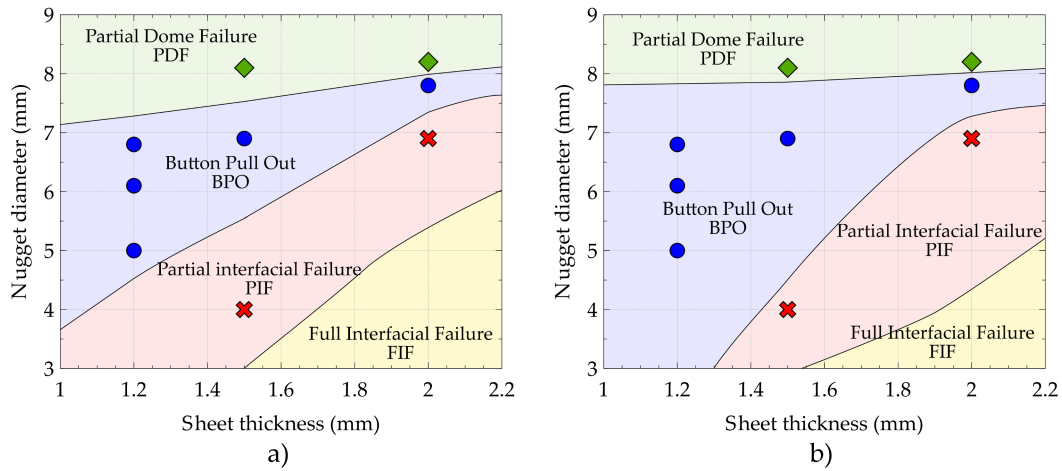


Figure 5.25: Experimental data and failure mode zones as function as nugget diameter and sheet thickness: a) First proposed discretization and b) another example of discretization.

mechanical properties of the zones to get the higher strength and the good failure mode. Then thanks to a link with a software predicting the microstructure and mechanical properties from the composition (such like JMatPro [JMA 11]), the best material could be find.

It is clear that this last perspective still need a lot of work but it is very promising and it is situated in the heart of the Materials by design concept.





# References

- [AA 15] VAN DER AA E. M., AMIRTHALINGAM M., WINTER J., HANLON D. N., HERMANS M. J. M., RIJNDERS M., RICHARDSON I. M.  
Improved resistance spot weldability of 3rd generation AHSS for automotive applications. *11th International Seminar on Numerical Analysis of Weldability, Austria, Graz*, 2015.
- [ABA 14] ABADI M. M. H., POURANVARI M.  
Failure-mode transition in resistance spot welded DP780 advanced high strength steel: effect of loading conditions. *Materials and Technology*, vol. 48, 2014, p. 67-71.
- [ADI 04] ADIB H., JEAONG J., PLUVINAGE G.  
Three-dimensional finite element analysis of tensile-shear spot-welded joints in tensile and compressive loading conditions. *Strength of Materials*, vol. 36, 2004, p. 353-364.
- [AHM 06] AHMAD Z.  
Principles of corrosion engineering and corrosion control. *Elsevier, Cited page 181*, 2006.
- [ALI 14] ALIZADEH-SH M., MARASHI S. P. H., POURANVARI M.  
Microstructure properties relationships in martensitic stainless steel resistance spot welds. *Science and Technology of Welding and Joining*, vol. 19, 2014, p. 595-602.
- [ALL 12] ALLAIN S., BOUAZIZ O., TAKAHASHI M.  
Toward a new interpretation of the mechanical behaviour of as-quenched low alloyed martensitic steels. *ISIJ International*, vol. 52, 2012, p. 717-722.
- [AND 01] ANDERSON K.  
Stick vs. MIG vs. TIG: which process is right for you? *Welding supplies from IOC*, 2001.
- [ARL 13] ARLAZAROV A., BOUAZIZ O., HAZOTTE A., GOUNÉ M., ALLAIN S.  
Characterization and modeling of manganese effect on strength and strain hardening of martensitic carbon steels. *ISIJ International*, vol. 53, 2013, p. 1076-1080.
- [BAB 02] BABU S., ELMER J., VITEK J., DAVID S.  
Time-resolved X-ray diffraction investigation of primary weld solidification in Fe-C-Al-Mn steel welds. *Acta Materialia*, vol. 50, 2002, p. 4763-4781.
- [BAR 14] BARGES P.  
Le Grand Bleu - Optical metallography of Fe-Mn-Al-C low density Duplex steel - Klemm II reagent. *Prix Jacquet SF2M*, 2014.
- [BIR 12] BIRO E., CRETTEUR L., DUPUY T.  
Higher than expected strengths from dissimilar configuration advanced high strength

- steel spot welds. *Proceedings of Sheet Metal Welding Conference XV, USA, Livonia Michigan*, 2012.
- [BLO 01] BLONDEAU R.  
Procédés et applications industrielles du soudage. *Hermès Science Publications, Paris*, 2001.
- [BOR 12] BORHANA A. A., MOHAMAD A. T., ABDUL-LATIF A., AHMAD Z., AYOB A., TAMIN M. N.  
Ductile failure prediction of spot welded lap joint. *Applied Mechanics and Materials*, vol. 165, 2012, p. 285-289.
- [BOU 09] BOUAFIA F., BOUTABOUT B., MECIRDI M. A.  
Analyse par éléments finis du comportement en rupture des structures assemblées par soudage par points. *Matériaux et Techniques*, vol. 97, 2009, p. 339-345.
- [BOU 10] BOUZEKRI M., DANCETTE S., DUPUY T., LENS A., NAIT-OUTIT B., MAS-SARDIER V., FABRÈGUE D., KLÖCKER H.  
An investigation of failure types in high-strength steel resistance spot welds. *Welding in the World*, vol. 54, 2010, p. 3-14.
- [BUR 13] BURGET S., SOMMER S.  
Modeling of deformation and failure behavior of dissimilar resistance spot welded joints under shear, axial and combined loading conditions. *13th International Conference on Fracture, China, Beijing*, 2013.
- [CAV 05] CAVALLI M. N., THOULESS M. D., YANG Q. D.  
Cohesive-zone modelling of the deformation and fracture of spot-welded joints. *Fatigue and Fracture of Engineering Materials and Structures*, vol. 28, 2005, p. 861-874.
- [CAZ 89] CAZES R.  
Soudage par résistance. *Techniques de l'ingénieur, TI B7720*, 1989.
- [CHA 03a] CHAO Y. J.  
Ultimate strength and failure mechanism of resistance spot weld subjected to tensile, shear, or combined tensile/shear loads. *Journal of Engineering Materials and Technology*, vol. 125, 2003, p. 125-132.
- [CHA 03b] CHAO Y.  
Failure mode of spot welds: interfacial versus pullout. *Science and Technology of Welding and Joining*, vol. 8, n° 2, 2003, p. 133-137.
- [CHA 17] CHABOK A., VAN DER AA E., DE HOSSON J. T. M., PEI Y. T.  
Mechanical behavior and failure mechanism of resistance spot welded DP1000 dual phase steel. *Materials and Design (In Press, Accepted Manuscript)*, vol. xxx, 2017.
- [CHE 03] CHENG W. C., LIU C. F., LAI Y. F.  
The role carbon plays in the martensitic phase transformation of an Fe-Mn-Al alloy. *Scripta Materialia*, vol. 48, 2003, p. 295-300.
- [CHE 16] CHEN J., YUAN X., HU Z., SUN C., ZHANG Y., ZHANG Y.  
Microstructure and mechanical properties of resistance-spot-welded joints for A5052 aluminum alloy and DP 600 steel. *Materials Characterization*, vol. 120, 2016, p. 45-52.
- [CHO 10] CHOI H. S., KIM B. M., PARK G. H., LIM W.  
Optimization of resistance spot weld condition for single lap joint of hot stamped

- 22MnB5 by taking heating temperature and heating time into consideration. *Materials Transactions*, vol. 52, 2010, p. 1367-1375.
- [CHO 11] CHOI H. S., PARK G. H., LIM W., KIM B. M.  
Evaluation of weldability for resistance spot welded single-lap joint between GA780DP and hot-stamped 22MnB5 steel sheets. *Transactions of the Korean Society of Mechanical Engineers. A*, vol. 25, 2011, p. 1543-1550.
- [CHU 02] CHUKO W. L., GOULD J. E.  
Development of appropriate resistance spot welding practice for transformation-hardened steels. *Supplement of the Welding Journal*, , 2002.
- [CHU 16] CHUNG K., NOH W., YANG X., HAN H. N., LEE M. G.  
Practical failure analysis of resistance spot welded advanced high-strength steel sheets. *International Journal of Plasticity*, vol. xxx, 2016, p. 1-26.
- [CON 85] CONSIDÈRE A.  
Annales des Ponts et Chaussées 9. *pages 574-775*, 1885.
- [CRE 02] CRETTEUR L., KORUK I., TOSAL-MARTINEZ L.  
Improvement of weldability of TRIP steels by use of in-situ pre- and post-heat treatments. vol. 73, 2002.
- [DAN 09] DANCETTE S.  
Comportement mécanique des soudures par points: mécanismes et stratégies de prédiction dans le cas des tôles en acier pour automobile. PhD thesis, Université de Lyon, 2009.
- [DAN 11a] DANCETTE S., FABRÈGUE D., MASSARDIER V., MERLIN J., DUPUY T., BOUZEKRI M.  
Experimental and modeling investigation of the failure resistance of advanced high strength steels spot welds. *Engineering Fracture Mechanics*, vol. 78, 2011, p. 2259-2272.
- [DAN 11b] DANCETTE S., MASSARDIER V., FABRÈGUE D., MERLIN J., DUPUY T., BOUZEKRI M.  
HAZ microstructures and local mechanical properties of high strength steels resistance spot welds. *Iron and Steel Institute of Japan International*, vol. 51, 2011, p. 99-107.
- [DAN 12] DANCETTE S., FABRÈGUE D., ESTEVEZ R., MASSARDIER V., DUPUY T., BOUZEKRI M.  
A finite element model for the prediction of advanced high strength steel spot welds fracture. *Engineering Fracture Mechanics*, vol. 87, 2012, p. 48-61.
- [DAN 15] DANG W.  
Finite element modelling of hybrid (spot welded/bonded) joints under service conditions. PhD thesis, Université technologique de Compiègne, 2015.
- [DAR 48] DARKEN L.  
Diffusion of carbon in austenite with a discontinuity in composition. *Transactions of the American Institutetute of Mining, Metallurgical and Petroleum Engineers*, vol. 180, 1948, p. 430-438.
- [DEN 00] DENG X., CHEN W., SHI G.  
Three-dimensional finite element analysis of the mechanical behavior of spot welds. *Finite Elements in Analysis and Design*, vol. 35, 2000, p. 17-39.

- [EIS 10] EISAZADEH H., HAMED M., HALVAEE A.  
New parametric study of nugget size in resistance spot welding process using finite element method. *Materials and Design*, vol. 31, 2010, p. 149-157.
- [ESH 14] ESHRAGHI M., TSCHOPP M. A., ASLE ZAEEM M., FELICELLI S. D.  
Effect of resistance spot welding parameters on weld pool properties in a DP600 dual-phase steel: a parametric study using thermo mechanically-coupled finite element analysis. *Materials and Design*, vol. 56, 2014, p. 387-397.
- [FER 98] FERRASSE S., VERRIER P., MEESEMAECKER F.  
Resistance spot weldability of high strength steels for use in car industry. *Welding in the World*, vol. 41, 1998, p. 177-195.
- [GAD 12] GADALLAH R., FAHMY R., KHALIFA T., A. S.  
Influence of shielding gas composition on the properties of flux-cored arc welds of plain carbon steel. *International Journal of Engineering and Technology Innovation*, vol. 2, n° 1, 2012, p. 1-12.
- [GOL 97] GOLOGANU M., LEBLOND J. B., PERRIN G., DEVAUX J.  
Recent extensions of Gurson's model for porous ductile metals. *Continuum Micromechanics*, P. Suquet, ed., CISM Courses and Lectures No. 377, 1997.
- [GOU 98] GOULD J. E., WORKMAN D.  
Fracture morphologies of resistance spot welds exhibiting hold time sensitivity behavior). *Sheet Metal Welding Conference VIII, USA, Detroit, Michigan*, 1998.
- [GOU 03] GOURGUES A. F.  
Microtexture induced by the bainitic transformation in steels during welding. Effect on the resistance to cleavage cracking. *Materials Science Forum*, vol. 426-432, 2003, p. 3629-3634.
- [GOU 05] GOULD J., PETERSON W.  
Advanced materials require advanced knowledge - understanding resistance spot weld performance on AHSS. *The Fabricator*, 2005.
- [GUR 77] GURSON A. L.  
Continuum theory of ductile rupture by void nucleation and growth: part I-Yield criteria and flow rules for porous ductile media. *Journal of Engineering Materials and Technology*, vol. 99, 1977, p. 2-15.
- [HAY 10] HAYAT F.  
The effects of the welding current on heat input, nugget geometry, and the mechanical and fractural properties of resistance spot welding on Mg/Al dissimilar materials. *Materials and Design*, vol. 32, 2010, p. 2476-2484.
- [HER 08] HERNANDEZ V. H. B., KUNTZ M. L., KHAN M. I.  
Influence of microstructure and weld size on the mechanical behaviour of dissimilar AHSS resistance spot welds. *Science and Technology of Welding and Joining*, vol. 13, 2008, p. 769-776.
- [HIL 76] HILLEBORG A., MODEER M., PETERSSON P. E.  
Analysis of crack formation and crack growth in concrete by means of fracture mechanics and finite elements. *Cement and Concrete Research*, vol. 6, 1976, p. 773-782.
- [HUI 16] HUIN T., DANCETTE S., FABRÈGUE D., DUPUY T.  
Investigation of the failure of advanced high strength steels heterogeneous spot welds.

- International Journal of Fracture*, vol. 6, n° 5, 2016.
- [IIS 06] IISI  
AHSS application guidelines - Version 3. 2006.
- [ISO 04] ISO  
Resistance welding-weldability-Part 2: alternative procedures for the assessment of sheet steels for spot welding NF EN ISO 18278-2. *Copyright office, Switzerland, Geneva*, 2004.
- [JMA 11] JMatPro  
JMatPro: Practical software for materials properties. *Sente Software Ltd*, 2011.
- [JON 81] JONES T. B., WILLIAMS N. T.  
Resistance spot welding of high strength steels. *Institution of Mechanical Engineers Journal*, vol. 16, 1981, p. 123-130.
- [JON 11] JONG Y. S., LEE Y. K., KIM D. C., KANG M. J., HWANG I. S., LEE W. B.  
Microstructural evolution and mechanical properties of resistance spot welded ultra-high strength steel containing boron. *Materials Transactions, JIM*, vol. 52, 2011, p. 1330-1333.
- [JSA 89] JSA J. S. A.  
Method of inspection for spot weld. *JIS Z 3140*, 1989.
- [KEE 04] KEELER S., KIMCHI M.  
Advanced high-strength steels application guidelines V5.0. *WorldAutoSteel*, 2004.
- [KHA 08] KHAN M. I., KUNTZ M. L., Y. Z.  
Effects of weld microstructure on static and impact performance of resistance spot welded joints in advanced high strength steels. *Science and Technology of Welding and Joining*, vol. 13, 2008, p. 49-59.
- [KIM 15] KIM E., EAGAR T. W.  
Interfacial temperature profiles in simulated resistance spot welding of bare and zinc coated steel. *Welding Journal*, vol. 94, 2015, p. 35-43.
- [KON 08] KONG X., YANG Q., LI B., ROTHWELL G., ENGLISH R., REN X. J.  
Numerical study of strengths of spot-welded joints of steel. *Materials and Design*, vol. 29, 2008, p. 1554-1561.
- [KOS 14] KOSNAN M. S. E., AHMAD Z., BORHANA A. A., TAMIN M. N.  
Finite element simulation of ductile failure process of spot welded joint under tensile loading. *Applied Mechanics and Materials*, vol. 660, 2014, p. 623-627.
- [KRA 10] KRAJCARZ F., GOURGUES A. F., BOCHARD V., LUCAS E., BOBADILLA M.  
Formation et solidification de la zone fondue en soudage par point: influence des paramètres de soudage. *Fédération française des matériaux. Matériaux 2010*, , 2010.
- [KRA 13] KRAJCARZ F., GOURGUES A. F., LUCAS E., PINEAU A.  
Fracture toughness of the molten zone of resistance spot welds. *International Journal of Fracture*, vol. 181, 2013, p. 209-226.
- [KUO 04] KUO M., CHIANG J.  
Weldability study of resistance spot welds and minimum weld button size methodology development for DP steel. *Journal of Materials and Manufacturing*, vol. 113, 2004, p. 67-77.

- [LAC 15] LACROIX R., KERMOUCHE G., LENS A., BERGHEAU J. M., KLÖCKER H.  
Original test device for crack propagation in the weld nugget of advanced high strength steels. *Engineering Fracture Mechanics*, vol. 138, 2015, p. 156-168.
- [LAM 04a] LAMBERT-PERLADE A., GOURGUES A. F., BESSON J., STUREL T., PINEAU A.  
Mechanisms and modeling of cleavage fracture in simulated heat-affected zone microstructures of a high-strength low alloy steel. *Metallurgical and materials Transactions A*, vol. 35a, 2004, p. 1039-1053.
- [LAM 04b] LAMBERT-PERLADE A., GOURGUES A. F., PINEAU A.  
Austenite to bainite phase transformation in the heat-affected zone of a high strength low alloy steel. *Acta Materialia*, vol. 52, 2004, p. 2337-2348.
- [LAM 07] LAMOUREUX E. H. J.  
Modélisation détaillée des soudures par point et Laser pour simuler la rupture des assemblages automobiles. PhD thesis, Université de Valenciennes et du Hainaut-Cambrésis, 2007.
- [LAN 04] LANGRAND B., COMBESURE A.  
Non-linear failure behaviour of spotwelds: a global finite element and experiments in pure and mixed modes I/II. *International Journal of Solids and Structures*, vol. 41, 2004, p. 6631-6646.
- [LEE 05a] LEE H., KIM N., LEE S.  
Overload failure curve and fatigue behavior of spot-welded specimens. *Engineering Fracture Mechanics*, vol. 72, 2005, p. 1203-1221.
- [LEE 05b] LEE H., KIM N., LEE S.  
Overload failure curve and fatigue behavior of spot-welded specimens. *Engineering Fracture Mechanics*, vol. 72, 2005, p. 1203-1221.
- [LEM 07] LEMOINE X.  
Behavior laws and their influences on numerical prediction. *10th ESAFORM conference, Spain, Zaragoza*, 2007.
- [LIA 10] LIAO X., WANG X., GUO Z., WANG M., WU Y., RONG Y.  
Microstructures in a resistance spot welded high strength dual phase steel. *Materials Characterization*, vol. 61, 2010, p. 341-346.
- [LIN 02] LIN S. H., PAN J., WU S. R., AL.  
Failure loads of spot welds under combined opening and shear static loading conditions. *International Journal of Solids and Structures*, vol. 39, 2002, p. 19-39.
- [LIN 03] LIN S. H., PAN J., TYAN T., AL.  
A general failure criterion for spot welds under combined loading conditions. *International Journal of Solids and Structures*, vol. 40, 2003, p. 5539-5564.
- [LIU 16] LIU C., ZHENG X., HE H., WANG W., WEI X.  
Effect of work hardening on mechanical behavior of resistance spot welding joint during tension shear test. *Materials and Design*, vol. 100, 2016, p. 188-197.
- [LON 16] LONG H., HU Y., JIN X., SHAO J., ZHU H.  
Effect of holding time on microstructure and mechanical properties of resistance spot welds between low carbon steel and advanced high strength steel. *Computational Materials Science*, vol. 117, 2016, p. 556-563.



- 
- [LUO 09] LUO Y., LIU J., XU H., XIONG C., LIU L.  
Regression modeling and process analysis of resistance spot welding on galvanized steel sheet. *Materials and Design*, vol. 30, 2009, p. 2547-2555.
- [MAH 07] MAHELLE P.  
Caractérisation expérimentale et numérique du comportement d'assemblages soudés soumis à des sollicitations quasi-statiques et dynamiques. PhD thesis, Valenciennes, Université de Valenciennes et du Hainaut-Cambrésis, 2007.
- [MAR 05] MARYA M., GAYDEN X. Q.  
Development of requirements for resistance spot welding Dual-Phase (DP600) steels Part 1 - The causes of interfacial fracture. *Welding Journal*, vol. 84, 2005, p. 172-182.
- [MAR 10] MARASHI S., POURANVARI M., SALEHI M., ABEDI A., KAVIANI S.  
Overload failure behavior of dissimilar thickness resistance spot welds during tensile shear test. *Materials Science And Technology*, vol. 26, 2010, p. 1220-1225.
- [MIL 10] MILLION K., BURBA H., DATTA R., ZIMMERMANN H.  
Root causes of disbonding in austenite-ferrite dissimilar joint welds and prevention approach. *Welding and Cutting*, vol. 4, 2010, Page 210.
- [MIM 04] MIMER M., SVENSSON E., JOHANSSON R.  
Process adjustments to improve fracture behaviour in resistance spot welds of EHSS and UHSS. *Welding in the World*, vol. 48, 2004, p. 14-18.
- [MIN 07] MINNICK W.  
Weld joints and weld types. *Gas Metal Arc Welding Handbook, Goodheart-Willcox*, 2007.
- [MOO 89] MOORE L. G., JAFFREY D., KERR H. W.  
Failure mechanisms in rephosphorised sheet steel spot welds. *Materials Science and Technology*, vol. 5, 1989, p. 492-498.
- [MOS 12] MOSHAYEDI H., SATTARI-FAR I.  
Numerical and experimental study of nugget size growth in resistance spot welding of austenitic stainless steels. *Journal of Materials Processing Technology*, vol. 212, 2012, p. 347-354.
- [NAI 08] NAIT-OUTIT B.  
Endommagement des soudures d'aciers à Très Haute Résistance pendant l'essai de Trac-tion en Croix : analyse mécanique et métallurgique de la fissuration dans la zone fondue. PhD thesis, Saint-Etienne, Mines, 2008.
- [NIE 08] NIELSEN K. L.  
3D modelling of plug failure in resistance spot welded shear-lab specimens (DP600-steel). *International Journal of Fracture*, vol. 153, 2008, p. 125-139.
- [NIE 10] NIELSEN K. L.  
Predicting failure response of spot welded joints using recent extensions to the Gurson model. *Computational Materials Science*, vol. 48, 2010, p. 71-82.
- [NIE 15] NIELSEN C. V., MARTINS P. A. F., ZHANG W., BAY N.  
Numerical method in simulation of resistance welding. *VI International Conference on Computational Methods for Coupled Problems in Science and Engineering*, 2015.
-

- [NIS 82] NISHI T., SAITO T., YAMADA A., TAKAHASHI Y.  
Evaluation of spot weldability of high-strength sheet steels for automotive use. *Nippon Steel Technical Report*, 1982.
- [NOH 17] NOH W., KIM W., YANG X., KANG M., LEE M. G., CHUNG K.  
Simple and effective failure analysis of dissimilar resistance spot welded advanced high strength steel sheets. *International Journal of Mechanical Sciences*, vol. 121, 2017, p. 76-89.
- [PAR 84] PARKER S. F., GRUNDY P. J., JONES G. A.  
The microstructure and magnetic properties of a permanent magnet alloy in the FeAlC system. *IEEE Transactions on Magnetics*, vol. 20, 1984, p. 1630-1632.
- [PET 96] PETERSON W.  
A method of eliminating interfacial fractures in high and ultra high strength steels. *Sheet Metal Welding Conference VII, USA, Troy, Michigan*, 1996.
- [PET 02] PETERSON W.  
Methods to minimize the occurrence of interfacial fractures in HSS spot welds. *Sheet Metal Welding Conference X, USA, Sterling Heights Michigan*, 2002.
- [PET 06] PETERSON W., ACCORSI I., COON T.  
Review of weld mechanical property specification requirements in AWS D8.1 (Proposed). *Sheet Metal Welding Conference XII, USA, Livonia Michigan*, 2006.
- [POO 75] POOK L. P.  
Fracture mechanics analysis of the fatigue behaviour of spot welds. *International Journal of Fracture*, vol. 11, 1975, p. 173-176.
- [POO 79] POOK L. P.  
Approximate stress intensity factors obtained from simple plate bending theory. *Engineering Fracture Mechanics*, vol. 12, 1979, p. 505-522.
- [POU 07] POURANVARI M., ASGARI H., MOSAVIZADCH S., MARASHI P., GOODARZI M.  
Effect of weld nugget size on overload failure mode of resistance spot welds. *Science and Technology of Joining*, vol. 12, 2007, p. 217-225.
- [POU 09] POURANVARI M., MARASHI S. P. H.  
Similar and dissimilar RSW of low carbon and austenitic stainless steels: effect of weld microstructure and hardness profile on failure mode. *Materials Science and Technology*, vol. 25, 2009, p. 1411-1416.
- [POU 10a] POURANVARI M., MARASHI P.  
Resistance spot welding of unequal thickness low carbon steel sheets. *Advanced Materials Research*, vol. 83, 2010, p. 1205-1211.
- [POU 10b] POURANVARI M., MARASHI S., MOUSAVIZADEH S.  
Failure mode transition and mechanical properties of similar and dissimilar resistance spot welds of DP600 and low carbon steels. *Science and Technology of Welding and Joining*, vol. 15, 2010, p. 625-631.
- [POU 11] POURANVARI M., MARASHI S. P. H.  
Failure mode transition in AHSS resistance spot welds. Part I. Controlling factors and Part II: Experimental investigation and model validation. *Materials Science and Engineering*, vol. 528, 2011, p. 8337-8343.

- 
- [POU 12] POURANVARI M., MARASHI S. P. H.  
On failure mode of resistance spot welded DP980 advanced high strength steel. *Canadian Metallurgical Quarterly, the Canadian Journal of Metallurgy and Materials Science*, vol. 51, 2012, p. 447-455.
- [QIU 09a] QIU R., IWAMOTO C., SATONAKA S.  
The influence of reaction layer on the strength of aluminum/steel joint welded by resistance spot welding. *Materials Characterization*, vol. 60, n° 2, 2009, p. 156-159.
- [QIU 09b] QIU R., IWAMOTO C., SATONAKA S.  
Interfacial microstructure and strength of steel/aluminum alloy joints welded by resistance spot welding with cover plate. *Journal of Materials Processing Technology*, vol. 209, 2009, p. 4186-4193.
- [RAD 08] RADAKOVIC J., TUMULURU M.  
Predicting resistance spot weld failure modes in shear tension tests of advanced high-strength automotive steels. *Welding Journal*, vol. 87, 2008, p. 96-105.
- [RAD 12] RADAKOVIC D. J., TUMULURU M.  
An evaluation of the cross-tension test of resistance spot welds in high-strength dual-phase steels. *Welding Journal*, vol. 91, 2012, p. 8-15.
- [RIC 69] RICE, TRACEY  
On the ductile enlargement of voids in triaxial stress fields. *Journal of the Mechanics and Physics of Solids*, vol. 17, 1969, p. 201-217.
- [RIV 04] RIVAS S., SERVENT R., BELDA J.  
Automated spot weld inspection in the automotive industry. *16th World Conference on Non Destructive Testing (WCNDT), Canada, Montreal, 2004.*
- [RUS 15] RUSSO SPENA P., DE MADDIS M., LOMBARDI F.  
Mechanical strength and fracture of resistance spot welded advanced high strength steels. *Materials and Manufacturing Processes*, vol. 109, 2015, p. 450-456.
- [RUS 16] RUSSO SPENA P., DE MADDIS M., LOMBARDI F., ROSSINI M.  
Dissimilar resistance spot welding of Q and P and TWIP steel sheets. *Materials and Manufacturing Processes*, vol. 31, 2016, p. 291-299.
- [SAD 16] SADASUE T., IGI S., TANIGUSHI K., IKEDA R., OI K.  
Fracture behaviour and numerical study of resistance spot welded joints in high-strength steel sheet. *Welding International*, vol. 30, 2016, p. 602-613.
- [SAK 03] SAKUMA Y., OIKAWA H.  
Factors to determine static strengths of spot weld for high strength steel sheets and developments of high strength steel sheets with strong and stable welding characteristics. *Nippon Steel Technical Report N°88*, 2003.
- [SAT 04] SATONAKA S., KAIEDA K., OKAMOTO S.  
Prediction of tensile-shear strength of spot welds based on fracture modes. *Welding in the World*, vol. 48, 2004, p. 39-45.
- [SAW 14] SAWANISHI C., OGURA T., TANIGUCHI K., IKEDA R., OI K., YASUDA K., HIROSE A.  
Mechanical properties and microstructures of resistance spot welded DP980 steel joints using pulsed current pattern. *Science and Technology of Welding and Joining*, vol. 19, 2014, p. 52-59.
-

- [SCH 05] SCHNEIDER A., ZHANG J.  
Orientation relationship between a ferritic matrix and k-phase ( $\text{Fe}_3\text{AlC}_x$ ) precipitates formed during metal dusting of Fe-15Al. *Intermetallics*, vol. 13, 2005, p. 1332-1336.
- [SEV 06] SEVIM I.  
Effect of hardness to fracture toughness for spot welded steel sheets. *Materials and Design*, vol. 27, 2006, p. 21-30.
- [SHE 10] SHEN J., ZHANG Y. S., LAI X. M.  
Influence of initial gap on weld expulsion in resistance spot welding of dual phase steel. *Science and Technology of Welding and Joining*, vol. 15, 2010, p. 386-392.
- [SHI 04] SHI G., WESTGATE S. A.  
Resistance spot welding of high strength steels. *International Journal for the Joining of Materials*, vol. 16, 2004, p. 9-14.
- [SMI 80] SMITH R. A.  
Sizing of spot welds by elastic/plastic analysis. *3rd European Colloquium on Fracture, Oxford*, 1980.
- [SOM 10] SOMMER S.  
Modeling of the fracture behavior of spot welds using advanced micro-mechanical damage models. *Materials Science and Engineering*, vol. 10, 2010.
- [SON 11] SONG J. H., HUH H.  
Failure characterization of spot welds under combined axial-shear loading conditions. *International Journal of Mechanical Sciences*, vol. 53, 2011, p. 513-525.
- [SRI 03] SRIKUNWONG C., DUPUY T., BIENVENU Y.  
Numerical simulation of resistance spot welding process using FEA technique. *In Proceedings of 13th international conference on computer technology in welding, Orlando, Florida*, 2003.
- [SRI 05] SRIKUNWONG C.  
Modélisation du soudage par points. PhD thesis, Paris, Mines, 2005.
- [SUN 06] SUN X., STEPHENS E. V., KHALEL M. A.  
Effects of fusion zone size and failure modes of advanced high strength steel spot welds. *Sheet Metal Welding Conference XII, USA, Livonia Michigan*, 2006.
- [SUN 08] SUN X., AL.  
Effects of fusion zone size and failure mode on peak load and energy absorption of advanced high strength steel spot welds under lap shear loading conditions. *Engineering Failure Analysis*, vol. 15, 2008, p. 356-367.
- [TAD 85] TADA H.  
The stress analysis of cracks handbook. *Saint Louis: Paris Productions and (Del Research Corp.)*, 1985.
- [TAO 08] TAO W., LI Q., CHEN B., WU L.  
Joint strength and failure mechanism of laser spot weld of mild steel sheets under lap shear loading. *Science and Technology of Welding and Joining*, vol. 13, 2008, p. 754-759.
- [TVE 84] TVERGAARD V., NEEDLEMAN A.  
An analysis of ductile rupture in notched bars. *Journal of the Mechanics and Physics of Solids*, vol. 32, 1984, p. 461-490.

- [TWE 87] TWEED J. H., KNOTT J. F.  
Micromechanisms of failure in C-Mn weld metals. *Acta Metallurgica*, vol. 35, 1987, p. 1401-1414.
- [WAN 16] WANG X. P., ZHANG Y. Q., JU J. B., ZHANG J. Q., YANG J. W.  
Characteristics of welding crack defects and failure mode in resistance spot welding of DP780 steel. *Journal of Iron and Steel Research*, vol. 23, 2016, p. 1104-1110.
- [WEI 16] WEI S. T., LV D., LIU R. D., LIN L.  
Similar and dissimilar resistance spot weldability of galvanised DP1000 and TWIP980 steels. *Science and Technology of Welding and Joining*, vol. 1, 2016, p. 1-8.
- [WIL 79] WILLIAMS N. T., JONES T. B.  
Spot weld size and fracture mode in low carbon mild steel. *Metal Construction*, vol. 11, 1979, p. 541-546.
- [WU 91] WU C. C., CHOU J. S., LIU T. F.  
Phase transformation in an Fe-10.1Al-28.6Mn-0.46C alloy. *Metallurgical and Materials Transactions A*, vol. 22A, 1991, p. 2265-2276.
- [XU 14] XU F., SUN G., LI G., LI Q.  
Failure analysis for resistance spot welding in lap-shear specimens. *International Journal of Mechanical Sciences*, vol. 78, 2014, p. 154-166.
- [YAN 08] YANG Y. P., BABU S. S., ORTH F., PETERSON W.  
Integrated computational model to predict mechanical behaviour of spot weld. *Science and Technology of Welding and Joining*, vol. 13, 2008, p. 232-239.
- [YUA 17] YUAN X., LI C., CHEN J., LI X., LIAND X., PAN X.  
Resistance spot welding of dissimilar DP600 and DC54D steels. *Journal of Materials Processing Technology*, vol. 239, 2017, p. 31-41.
- [ZHA 99] ZHANG S.  
Stress intensities derived from stresses around a spot weld. *International Journal of Fracture*, vol. 99, 1999, p. 239-257.
- [ZHA 06] ZHANG H., SENKARA J.  
Resistance welding : fundamentals and applications. *CRC Press*, 2006.
- [ZHA 14] ZHANG H., QI X., XING F., BAI J., CHEN J.  
Failure analysis of dissimilar thickness resistance spot welded joints in dual-phase steels during tensile shear test. *Materials and Design*, vol. 55, 2014, p. 366-372.
- [ZUN 97] ZUNIGA S., SHEPPARD S. D.  
Resistance spot weld failure loads and modes in overload conditions. *Fatigue and Fracture Mechanics*, vol. 27, 1997, p. 469-489.



## FOLIO ADMINISTRATIF

### THESE DE L'UNIVERSITE DE LYON OPEREE AU SEIN DE L'INSA LYON

NOM : HUIN

DATE de SOUTENANCE : le 04 juillet 2017

Prénom : Thibaut

TITRE : Experimental and numerical investigation of the mechanical behaviour of dissimilar arc and spot welds of advanced high strength steels

NATURE : Doctorat

Numéro d'ordre : 2017LYSEI055

Ecole doctorale : ED 34 Matériaux de Lyon

Spécialité : Matériaux

RESUME : Nowadays, ecological policy encourages carmakers to reduce the global vehicle weight. Fine steel sheets assemblies with different thickness optimizing each part of the assembly are used and steelmakers develop steels which are more and more resistant namely Advanced High Strength Steel (AHSS). During the mechanical tests of heterogeneous AHSS welding, unusual fracture modes are observed, in particular along the interface between the Heat Affected Zone (HAZ) and the Fusion Zone or molten zone (FZ). These fractures generally occur with lower strength than expected for these welding.

The objectives of the study are to understand fracture mechanisms during mechanical testing and create a mechanical FE model is developed to be able to predict mechanical strength of the welded assemblies.

Firstly, a study of heterogeneous welding constituted of two well-known steel grades aims at understanding failure mechanism and parameters affecting the failure modes. FE model is built with mechanical response identified of each zone (base materials, heat affected zones and fusion zone). Failure criteria based on ductile damage taking into account the influence of the triaxiality are used and some cohesive elements are used to simulate interfacial failure. Two configurations of mechanical testing in the case of Resistance Spot Welding (cross tension and tensile shear tests) are considered.

Then, this modelling method was successfully applied to a highly heterogeneous spot welding case including a new third generation low density AHSS concept with high aluminum and manganese content. Moreover, FE modelling method was applied on more complex configurations, in particular on a triple thick spot welded assembly. The robustness of the model has been demonstrated.

In addition, modelling methodology was extended to another welding type: arc welding. In this case, two sheets are welded in an overlap configuration. FE model allows predicting the failure zone and strength of welded assembly.

MOTS-CLÉS : resistance spot welding, arc welding, dissimilar welding, automotive high strength steel, cross tension, tensile shear, failure mode, ductile damage, FE modelling, microstructure, low density steel, martensitic steel.

Laboratoire (s) de recherche : MATEIS - UMR CNRS  
INSA de Lyon  
25 avenue Jean Capelle  
69621 VILLEURBANNE Cedex

Directeur de thèse : Damien FABREGUE (MATEIS), Sylvain DANCETTE (MATEIS)

Président de jury : Aude SIMAR (Professeur)

Composition du jury : Anne-Françoise GOURGUES-LORENZON (Professeur)  
Jean-Michel BERGHEAU (Professeur)  
Julien ZOLLINGER (Enseignant chercheur)  
Thomas DUPUY (Ingénieur Docteur)